Cr(VI)-free pre-treatments for adhesive bonding of aerospace aluminium alloys

Abrahami, Shoshan

DOI
10.4233/uuid:d5850b96-ec5b-4639-aac0-e05f81681800

Publication date
2016

Document Version
Final published version

Citation (APA)
Abrahami, S. (2016). *Cr(VI)-free pre-treatments for adhesive bonding of aerospace aluminium alloys*. [Dissertation (TU Delft), Delft University of Technology]. https://doi.org/10.4233/uuid:d5850b96-ec5b-4639-aac0-e05f81681800

Cr(VI)-free pre-treatments for adhesive bonding of aerospace aluminium alloys

Ph.D. thesis

Shoshan Tamar Abrahami

This research was performed in Delft University of Technology
Department of Materials Science and Engineering
Mekelweg 2, 2628 CD Delft,
The Netherlands

This research was carried out under the project number M11.6.12473 in the framework of the Research Program of the Materials innovation institute (M2i) in the Netherlands (www.m2i.nl).

Cr(VI)-free pre-treatments for adhesive bonding of aerospace aluminium alloys

Proefschrift

ter verkrijging van de graad van doctor
aan de Technische Universiteit Delft,
op gezag van de Rector Magnificus Prof. Ir. K.C.A.M Luyben,
voorzitter van het College voor Promoties,
in het openbaar te verdedigen op woensdag 7 december 2016 om 15:00 uur

door

Shoshan Tamar ABRAHAMI
Master of Science in Materials Science and Engineering,
Delft University of Technology, Delft, the Netherlands
geboren te Haifa, Israël.

This dissertation has been approved by the

Promotor:	Prof. Dr. H. Terryn
Copromotor:	Dr. J.M.C Mol

Composition of the doctoral committee:

Rector Magnificus	chairman
Prof. dr. H. Terryn	Delft University of Technology, promotor
Dr. J.M.C. Mol	Delft University of Technology, copromotor
Dr. J.M.M de Kok	Fokker Aerostructures, The Netherlands

Independent members:

Prof. dr. B.J. Thijsse	Delft University of Technology, The Netherlands
Prof. dr. J.F. Watts	University of Surrey, United Kingdom
Prof. dr. P. Marcus	École Nationale Supérieure de Chimie de Paris, France
Dipl. Ing. T. Hack	Airbus Group Innovations, Germany
Prof. dr. J. Sietsma	Delft University of Technology, The Netherlands (reserve member)

Keywords: Aluminium, Cr(VI)-free, Surface pretreatments, Anodizing, Adhesive bonding, Adhesion, Durability.

ISBN 978-94-91909-43-6

Cover design: Visual Essence, Utrecht, NL

Printed by Proefschriftmaken.nl

Content

Summary

For more than six decades, chromic acid anodizing (CAA) has been the central process in the surface pre-treatment of aluminium for adhesively bonded aircraft structures in Europe. Unfortunately, this electrolyte contains hexavalent chromium (Cr(VI)), a compound known for its toxicity and carcinogenic properties. The approaching ban on the use of hexavalent chromium (Cr(VI)) makes its elimination a high-priority R&D topic within the aerospace industry and the Cr(VI)-era will soon have to come to an end.

Anodizing aluminium in acid electrolytes produces a self-ordered porous oxide layer with a thin barrier layer underneath. This special type of oxide readily adheres to the organic resin and provides protection against corrosion. Although Cr(VI)-free candidates such as sulphuric acid- (SAA), phosphoric acid- (PAA) and mixtures of phosphoric-sulphuric acid anodizing (PSA) can be used to create this type of structure, the excellent adhesion and corrosion resistance that is currently achieved by the Cr(VI)-based process is not easily matched.

To gain a better understanding of the underlying physical and chemical mechanisms that contribute to the adhesion and durability in these structures, this study investigates the correlation between the oxide's chemical and morphological characteristics, as influenced by the anodizing electrolyte, and bond performance. The major challenge in the mechanistic understanding of the adhesion in bonded components is to differentiate between the different forces acting at the oxide/resin interface.

In the first part of this PhD thesis, studies focus on the role of surface chemistry. To exclude the contribution of mechanical interlocking between the oxide and the resin, featureless oxides were prepared by stopping the anodizing during the formation of the barrier layer. Surface characterization of the different anodic oxides by means of Fourier transform infrared (FTIR) and X-ray Photoelectron Spectroscopy (XPS) revealed no significant net change in the acid-base properties of the different anodic oxides. It was found that local chemical changes were introduced due to the incorporation of electrolyte-driven anions. Therefore, a model was developed to quantify the relative amounts of O^{2-}, OH^{-}, PO_4^{3-}, and SO_4^{2-}, showing significant changes in the type and amount of surface species. Consequently, measurements showed that the pretreatments and the molecule type affected oxide/molecule interfacial interactions. To evaluate the contribution of adsorptive interaction in practice, peel tests were performed on featureless oxides bonded with commercial aerospace adhesives. Results showed that significant initial dry adhesion is achieved with FM 73 epoxy without mechanical interlocking, and independent of the type of pretreatment. However, the formed bonding was not water resistant, with the amount of applied stress needed for peeling linearly increasing with the amount of surface hydroxyls. Moreover, the application of a thin γ-APS silane layer before bonding with epoxy has confirmed that the stability of

the interface is also determined by the nature of the bond, showing much more stable interfaces in the presence of covalent interactions. When peel tests were performed with a phenolic-based adhesive (Redux 775), no correlation to the surface chemistry was found. Nevertheless, the bonded joints on the basis of the weakly acidic character of the phenolic adhesive showed better resistance to corrosion in salt spray tests, compared to those on the basis of the epoxy adhesive. Therefore, we conclude that both oxide surface- and adhesive chemistries play a role in the formation and long-term stability of the oxide/resin interface.

In the second part of this thesis industrial porous oxides were applied. Fundamental investigations show that changing the voltage during anodizing can produce morphological variations across the oxide thickness. The effect of the initial voltage sweeps, however, was limited by the oxide dissolution action of phosphoric acid in PSA, since prolonged anodizing in this electrolyte not only leads to an increase of the pore diameter, but also completely dissolves the upper most part of the oxide. Morphological changes were distinguished between geometrical modifications that affect the pore size and changes in the surface roughness that was caused by extended chemical dissolution at higher anodizing temperatures and/or phosphoric acid concentration. Measured carbon concentration profiles within the pores using high-resolution transmission electron microscopy (TEM) coupled with energy-dispersive X-ray spectroscopy (EDS) indicated that resin penetration is affected by both aspects. Moreover, mechanical performance in peel tests indicates that these parameters, rather than the oxide layer thickness are critical for moisture-resistant adhesion. Both adhesion mechanisms: adsorption and mechanical interlocking seem to contribute to the adhesion in these structural bonds. A higher degree of dissolution during anodizing is beneficial for the adhesion, facilitating a composite-like interphase. Too much dissolution, however, reduces the resistance to bondline corrosion. Overall, the presented results illustrate the need to consider both chemical and morphological changes in the selection of Cr(VI)-free alternatives for structural adhesive bonding.

Samenvatting

Al meer dan zes decennia lang is chroomzuur anodiseren (CAA) de belangrijkste stap in de oppervlakte-voorbehandeling van aluminium panelen in de Europese vliegtuigbouw. Helaas bevat chroomzuur zeswaardig chroom (Cr(VI)), een zeer giftige en kankerverwekkende stof. Het aanstaande verbod op het gebruik van deze stof maakt de eliminatie ervan een hoge prioriteit binnen de luchtvaartindustrie en het Cr(VI)-tijdperk zal op afzienbare termijn tot een einde moeten komen.
Het anodiseren van aluminium in zure elektrolyten resulteert in een poreuze oxidelaag met daaronder een dunne barrièrelaag. Dit type oxide is uitermate geschikt voor lijmhechting en beschermt bovendien het substraat tegen corrosie. Hoewel anodiseren in Cr(VI)-vrije alternatieven zoals zwavelzuur (SAA), fosforzuur (PAA) en mengsels van fosfor- en zwavelzuur (PSA) kunnen worden gebruikt om een dergelijke structuur te creëren, is de uitzonderlijk goede hechting en corrosiebestendigheid van CAA moeilijk te evenaren.
Om een beter begrip van de onderliggende fysische en chemische mechanismen die bijdragen aan de hechting en de duurzaamheid van deze structuren te verkrijgen, is in deze studie het verband tussen de kwaliteit van adhesie en de chemische en morfologische kenmerken van het oxide onderzocht. De nadruk is gelegd op de invloed van het elektrolyt op de hechting en duurzaamheid van lijmverbindingen. De grootste uitdaging bestaat erin de verschillende bijdragen aan hechting in deze gelijmde panelen te onderscheiden.
Het eerste deel van dit proefschrift richt zich erop de rol van de oppervlaktechemie te bestuderen. Om de bijdrage van de mechanische hechting tussen het oxide en de lijm uit te sluiten, is gebruik gemaakt van modeloxiden. Deze zijn bereid door het anodisatie-proces te stoppen tijdens de vorming van de barrièrelaag. Oppervlaktekarakterisering door middel van Fourier transform infrared (FTIR) spectroscopie en X-ray photoelectron spectroscopie (XPS) vertoonde geen significante veranderingen in de zuur-base eigenschappen van de verschillende anodische oxiden. Lokale chemische veranderingen komen echter voort uit de opname van elektrolyt-afhankelijke anionen. Het ontwikkelde model om de relatieve hoeveelheden van O^{2-}, OH^{-}, PO_4^{3-} en SO_4^{2-} te kwantificeren, bracht significante verschillen in type en hoeveelheid anionen aan het licht. Aanvullende metingen hebben aangetoond dat de voorbehandeling en het type organisch molecuul de interacties aan het grensvlak tussen molecuul en oxide sterk beïnvloeden. Om de bijdrage van adsorptie in de praktijk te evalueren, zijn pelproeven met commerciële lijmen uitgevoerd. Resultaten toonden aan dat een goede initiële (droge) hechting met FM 73 epoxy lijm kan worden bereikt zonder mechanische verankering en onafhankelijk van het type elektrolyt. Desalniettemin, de gevormde binding is niet waterbestendig en de mechanische belasting nodig voor het doen bezwijken van de lijmverbinding neemt lineair toe met de hydroxylfractie aan het oppervlak. Wanner

een dunne γ-APS silaanlaag wordt aangebracht alvorens de epoxy-lijmverbinding wordt gemaakt is de stabiliteit van de hechting veel hoger. Een veel stabieler grensvlak wordt dus gevormd in aanwezigheid van covalente bindingen. Dezelfde pelproeven uitgevoerd met fenol gebaseerde lijm (Redux 775), vertonen geen correlatie tussen oppervlaktechemie en pelsterkte. Toch vertonen de fenol verlijmde panelen een hogere weerstand tegen corrosie in zoutsproeitesten ten opzichte van epoxy gelijmde panelen. Dit komt door de eerder zwakke zure aard van deze lijm. Samenvattend kunnen we concluderen dat zowel de chemie van de oxiden als die van de lijm een rol spelen bij de vorming en de langetermijn stabiliteit van de hechting.

In het tweede deel van dit proefschrift worden industriële poreuze oxides bestudeerd. Fundamenteel onderzoek toont aan dat variaties in anodiseerspanning verschillen in poriegrootte kunnen opleveren. Het effect van het spanningsregime is echter beperkt door het oplossingseffect van fosforzuur in PSA. Langdurig anodiseren in dit elektrolyt leidt niet alleen tot een toename van de poriediameter, maar ook tot de oplossing van het buitenste gedeelte van de oxidelaag. Morfologische verschillen werden onderscheiden tussen modificaties aan de poriegrootte en verschillen in de oppervlakteruwheid, veroorzaakt door uitgebreide chemische oplossing bij hogere anodisatietemperaturen en/of fosforzuurconcentratie. Koolstofconcentratie-profielen, gemeten middels een hoge-resolutie transmissie elektronenmicroscoop (TEM) met gekoppelde chemische analyse toonden aan dat lijmpenetratie wordt beïnvloed door beide aspecten. Bovendien gaven mechanische peltesten aan dat deze parameters, meer dan de oxidelaagdikte, cruciaal zijn voor vochtbestendige lijmverbindingen. Het type elektrolyt en de anodisatietemperatuur zijn dus van groot belang voor een sterke en vochtbestendige hechting. Beide hechtingmechanismen, adsorptie en mechanische verankering, lijken bij te dragen tot de hechting in deze typen lijmverbindingen. Tevens is een hogere mate van oplossing tijdens het anodiseren gunstig voor de hechting daar het een stabieler grensvlak door diepere lijmpenetratie in de opener poriën bevordert. Echter teveel oplossing van de oxiden vermindert de corrosieweerstand van de lijmverbinding daarentegen. Uit de in het onderzoek beschreven resultaten is af te leiden dat voor robuuste constructieve lijmverbindingen zowel chemische als morfologische effecten in rekening gebracht moeten worden bij de selectie van Cr(VI)-vrije alternatieven.

Abbreviations and acronyms

4-EP	4-ethylphenol
4-HbA	4-hydroxybenzyl
AA	Aluminium Alloy
AC	Alternating current
AES	Auger electron spectroscopy
Alk.	Alkaline
APS	Aminopropyltriethoxy
at. %	Atomic percent
BE	Binding energy
BSAA	Boric-sulphuric acid anodizing
BTSE	1,2 Bis(triethoxysilyl)ethane
CAA	Chromic acid anodizing
Cr(VI)	Hexavalent chromium
CSA	Chromic sulphuric acid
DC	Direct current
DETA	Diethylenetriamine
EDS	Energy dispersive X-ray spectroscopy
EPAD	Electrolytic phosphoric acid deoxidizer
FPL	Forest Products Laboratory
FTIR	Fourier transform infrared spectroscopy
FWHM	Full-width at half-maximum
GDOES	Glow discharge optical emission spectroscopy
HcPSA	High concentration Phosphoric-Sulphuric acid Anodizing
Hydro.	Hydrothermal
ISO	International Organization for Standardization
NLR	Nederlands Lucht- en Ruimtevaartcentrum (Netherlands Aerospace Center)
OSHA	Occupational Safety and Health Administration
PAA	Phosphoric acid anodizing
PSA	Phosphoric-sulphuric acid anodizing
PVF	polyvinyl formal
R&D	Research and development
REACH	Registration, Evaluation, Authorization and Restriction of Chemicals
RT	Room temperature
SAA	Sulphuric acid anodizing
SEM	Scanning Electron Microscopy
TEM	Transmission Electron Microscopy
THF	Tetrahydrofuran
TSA	Tartaric sulphuric acid anodizing

UK	United Kingdom
US	United States
wt. %	Weight percent
XPS	X-ray photoelectron spectroscopy

CHAPTER 1

Introduction

1.1 Industrial Relevance and Research Aim

The preparation of metal-to-metal adhesive bonding is a major processing step in the manufacturing of structural components for the aviation industry. The formation of a strong and durable bond between the aluminium alloy substrates and the adhesive requires a carefully controlled, multi-step pre-treatment. This pre-treatment (Fig. 1.1) currently contains hexavalent chromium (Cr(VI)) in every major step of the process.

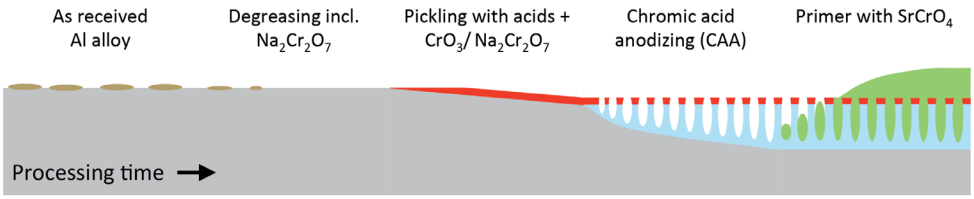

Figure 1.1: Schematic illustration of the current pre-treatment steps of aluminium alloys for structural adhesive bonding at Fokker Aerostructures, and the corresponding surface changes that take place.

Unfortunately, Cr(VI) is a highly hazardous and carcinogenic substance [1]. Employees working with chromate-containing compounds risk exposure through skin contact and by inhalation of vapour or dust particles [2]. This mostly occurs in the production stage, when the parts are pretreated and painted, during their maintenance or at the end-of life, when these coatings and paints are removed. In 2006, the Occupational Safety and Health Administration (OSHA) in the U.S. [3] and the European REACH (EC n°1907/2006) policies both introduced new regulations that strictly limit the use of hexavalent chromium and announced its near future ban. Accordingly, there is an urgent need to develop and qualify an alternative pre-treatment that will consistently provide the required level of performance, while being acceptable in terms of strict health and environmental standards.

Gaining confidence in the lasting robustness of new systems requires a fundamental understanding of the forces that provide this system its excellent adhesion and durability properties. This demands knowledge on both microscopic and macroscopic levels [5]. On a microscopic level, adhesion is achieved by atomic and molecular interactions between the oxide and the resin (primer/adhesive) [6]. This is generally described by the adsorption theory [7]. On a macroscopic level, mechanical interlocking between the substrate and the adhesive also promote adhesion. This type of interactions are introduced when the resin is able to interlock with rough features (e.g. cavities and oxide pores) at the substrate surface [8]. It appears from reviewing the literature (Chapter 2) that so far most studies tried to reproduce the morphological characteristics of the CAA process, as shown in Fig. 1.1, using different types of acids and/or process combination. The fact that both adsorption and mechanical interlocking will contribute to adhesion

in these structural bonds is not yet reflected in adhesion research. This is especially surprising, since it is well known that the most popular candidate alternative electrolytes (*phosphoric- (PAA), sulphuric- (SAA) and phosphoric- sulphuric acid (PSA)* anodizing) introduce chemical changes to the oxides. It is therefore of great interest to understand how chemical and morphological changes to the anodic oxides affect bond adhesion and durability performance.

1.2 Experimental Approach

In this study, we investigate how the oxide/adhesive interface (Fig. 1.2 (a)) is affected by the nature of the electrolyte and the anodizing conditions. Since industrial oxides that are used for structural bonding are porous, two main adhesion mechanisms are generally working simultaneously: adsorption and mechanical interlocking [7]. In order to differentiate between these individual contributions, two types of oxides are applied in this study: featureless and porous oxides. The first part of this thesis (Chapters 3-6) applies a model system with relatively flat and featureless oxides (Fig. 1.2 (b)). This allows focusing on the effect of oxide surface chemistry by excluding the contribution of mechanical interlocking. The second part, (Chapter 7 and 8) includes industrial anodic

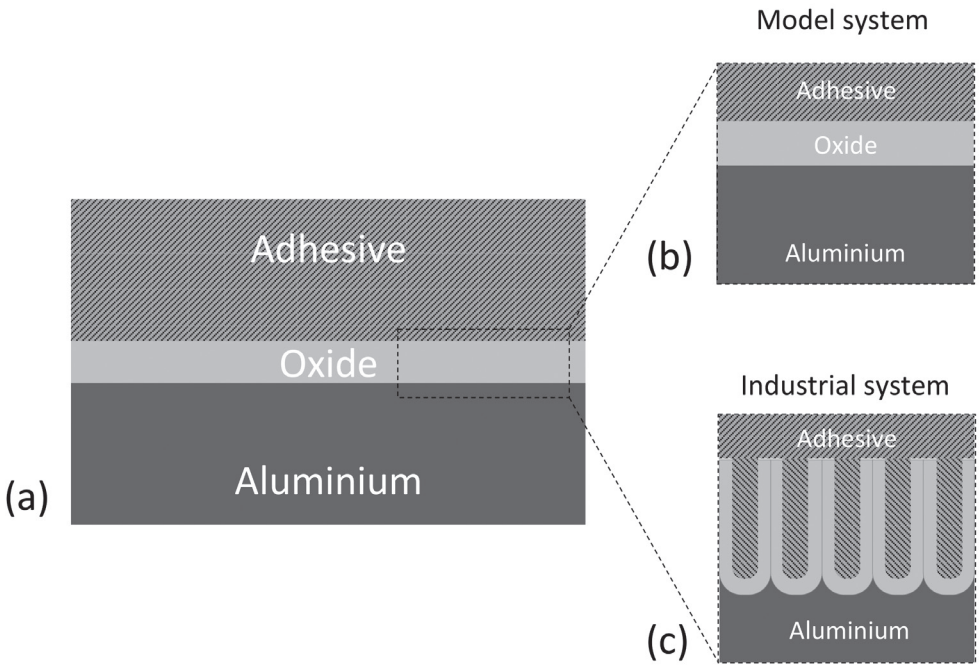

Figure 1.2: Schematic illustrations of (a) the components of the adhesive bond, showing the region of interest at the oxide/adhesive interface, (b) the model system used to study the effect of oxide chemistry and (c) the industrial system used to study the effect of oxide morphology.

oxides, which are porous and therefore involves both adhesion mechanisms (Fig. 1.2 (c)). In order to evaluate the link between fundamental principles of adhesion and bond performance, the work in this PhD thesis is presented in terms of the modifications to the oxide properties, such as morphological features (e.g. pore size, barrier layer thickness) and surface chemistry.

1.3 Outline of the Thesis

A graphical illustration for the structure of this PhD thesis is shown in Fig. 1.3. A general introduction and research approach are given in Chapter 1. An extensive literature review is presented in Chapter 2. This chapter provides background information about structural bonding and surface pre-treatments, including the history of the Cr(VI)-based process and the state-of-the-art in its replacement. Experimental results are presented in the form of scientific papers throughout chapters 3 to 8. These results can be generally divided into two parts; studying the effect of *oxide chemistry* and *oxide morphology*. Chapter 3 and 4 study the influence of electrolyte on different aspects of the oxide chemistry and its effect on the interactions with model molecules that are typically present in aerospace adhesives. In Chapters 5 and 6, the influence of oxide chemistry is tested on practical bond adhesion and durability with industrial adhesive films. Investigations into the influence of electrolyte on the oxide morphology are presented in Chapter 7. Finally, the results obtained regarding adhesion performance and durability of the industrial oxides upon adhesive bonding is presented in Chapter 8. General overview and conclusions, relating the two types of modifications on molecular bonding and adhesion performance of industrial systems is given in the last part, Chapter 9.

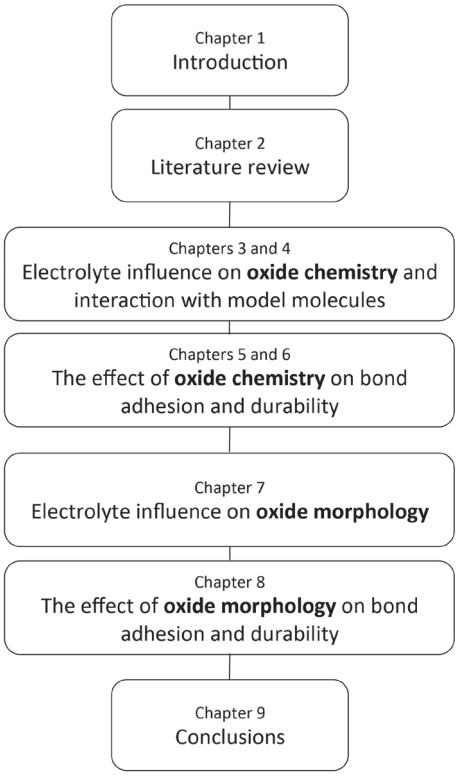

Figure 1.3: Graphical outline of this PhD thesis.

References

1. ATSDR, *Toxicologica Profile for Chromium*, P.H.S. U.S. Department of Health and Human Services, Editor. 2012: Atlanta, GA.
2. Alexander, B.H., et al., *Lung Cancer in Chromate-Exposed Aerospace Workers.* Journal of Occupational and Environmental Medicine, 1996. **38**(12): p. 1253-1258.
3. OSHA, *Toxic and Hazardous Substances* in *Occupational Exposure to Hexavalent Chromium*. 2006, United States Department of Labor.
4. European Parliament, C.o.t.E.U. 2006.
5. Brockmann, W., O.D. Hennemann, and H. Kollek, *Surface properties and adhesion in bonding aluminium alloys by adhesives.* International Journal of Adhesion and Adhesives, 1982. **2**(1): p. 33-40.
6. Brockmann, W., et al., *Adhesion in bonded aluminium joints for aircraft construction.* International Journal of Adhesion and Adhesives, 1986. **6**(3): p. 115.
7. Packham, D., *Theories of Fundamental Adhesion*, in *Handbook of Adhesion Technology*, L.M. da Silva, A. Öchsner, and R. Adams, Editors. 2011, Springer Berlin Heidelberg. p. 9-38.
8. McBain, J.W. and D.G. Hopkins, *On Adhesives and Adhesive Action.* The Journal of Physical Chemistry, 1925. **29**(2): p. 188-204.

CHAPTER 2

Literature review

Part of this chapter was submitted as a scientific journal paper: Abrahami, S. T., de Kok, J.M.M., Terryn, H., and Mol, J.M.C. (2016), Front. Chem. Sci. Eng.

ABSTRACT

For more than six decades, chromic acid anodizing (CAA) has been the central process in the surface treatment of aluminium for adhesively bonded aircraft structures. Unfortunately, this electrolyte contains hexavalent chromium (Cr(VI)), a compound known for its toxicity and carcinogenic properties. To comply with the new strict international regulations, the Cr(VI)-era will soon have to come to an end. Anodizing aluminium in acid electrolytes produces a self-ordered porous oxide layer. Although different acids can be used to create this type of structure, the excellent adhesion and corrosion resistance that is currently achieved by the complete Cr(VI)-based process is not easily matched. This chapter provides a critical overview and appraisal of proposed alternatives, including combinations of multiple anodizing steps, pre- and post anodizing treatments. The work is presented in terms of the modifications to the oxide properties, such as morphological features (e.g. pore size, barrier layer thickness) and surface chemistry, in order to evaluate the link between fundamental principles of adhesion and bond performance.

2.1 Introduction

For many years, hexavalent chromium has been used for the corrosion protection of metals in many industries; aerospace, automotive, maritime and architectural structures are just a few examples of the wide spectrum of applications in which Cr(VI)-based coatings can guarantee the life-long integrity of metallic parts. Excellent corrosion protection can be achieved in the form of a passive oxide layer or pigments in sealing and painting that provide an active 'self-healing' mechanism to repair local damage.
Unfortunately Cr(VI) is regarded to be extremely toxic and carcinogenic [1]. Employees working with chromate-containing compounds risk exposure through skin contact and by inhalation of vapour or dust particles [2]. This mostly occurs in the production stage, when the parts are pretreated and painted, during their maintenance or at the end-of life, when these coatings and paints are removed. In 2006, the Occupational Safety and Health Administration (OSHA) in the U.S. [3] and the European REACH (EC n°1907/2006) policies both introduced new regulations that strictly limit the use of hexavalent chromium and announced its near future ban. As a consequence, chromates are no longer used in most applications, except for some high-demanding applications such as in the aerospace industry.
In the aerospace industry, Cr(VI) is generally incorporated in every major step of the pre-treatment, coating and bonding processes. The corrosion sensitivity of aerospace aluminium alloys and the required level of performance and safety make its overall replacement a very challenging task. In addition, the time it takes to test and qualify new systems for aviation is much longer compared to that in other industries.
This chapter reviews the literature available to date on the replacements of Cr(VI) in the aerospace industry. It focuses on the replacement of chromic acid anodizing (CAA), which is typically used for the pre-treatment of aluminium alloys for structural adhesive bonding. Although other parts of the aircraft are also prepared using chromates, structural components are part of the principal load-carrying structure of the aircraft and they are typically not accessible for maintenance during their lifetime. Consequently, they are subject to the most critical performance standards [4]. In order to understand the recent progress toward Cr(VI)-free alternatives, this study aims to identify the key factors in the adhesion and durability of these structures.

2.2 Structural adhesive bonding in aircraft structures

Adhesive bonding is one of the oldest techniques to join different components, often of dissimilar nature [5]. It was already used in the first aircrafts, which were made from wood and continued in the 1940s, when manufacturers started using aluminium instead [6]. Modern aircraft are designed using a semi monocoque construction. This means that the fuselage (the main body of the aircraft) shell is carrying most of the loads together

with the help of reinforcing frames, longerons and stringers. From a technical point of view, adhesive bonding offers several benefits over mechanically fastened joints. The first is an advantageous strength-to-weight ratio, potentially leading to a reduction of up to 15% in structural weight [7]. When well prepared, bonds are capable of efficient stress transfer, distributing it over a large area to improve the fatigue resistance. Also, they provide a simplified and smooth design and the ability to join dissimilar materials [8]. Bonding is established when the adhesives undergoes physical or chemical hardening reaction (curing) to join the two panels together through surface adherence (adhesion) and internal strength (cohesion) [9]. Since then adhesive bonding has become a standard technique to produce the main body (fuselage), wings and other parts of many modern aircrafts [8]. Fig, 2.1 shows the main steps in the production of adhesively bonded components at *Fokker Aerostructures* in the Netherlands.

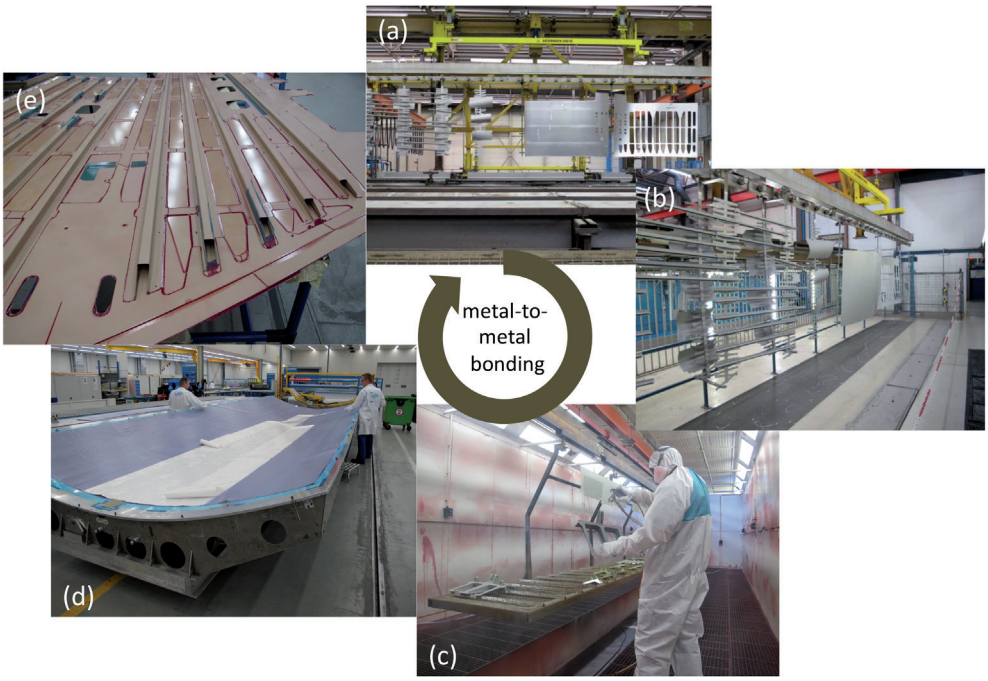

Figure 2.1: The production of metal-to-metal bonding at Fokker Aerostructures: (a) during surface pre-treatment, above the anodizing bath, (b) parts drying on the rack after pre-treatment, (c) primer application, (d) adhesive application, (e) a bonded part.

2.2.1 Components of the adhesive bond

2.2.1.1 The aluminium substrates

The most commonly employed types of aluminium in the aerospace industry belong to the 2xxx and 7xxx alloy series. Within these families, AA2024-T3 and AA7005-T6 are

the most used ones to date. Their main alloying elements in the two alloys include copper (Cu), magnesium (Mg) and manganese (Mn) in AA2024 and zinc (Zn), magnesium (Mg), copper (Cu) and silicon (Si) in AA7075. [10]. These are heat-treatable alloys that develop their strength by precipitation hardening. The microstructure of these alloys is complex, presenting several second phase and intermetallic particles. The formation of fine precipitates create the desired hardening effect, producing an alloy with a high strength-to-weight ratio at relatively low costs [11]. However, particles differing in size and nature, even across different batches of the same manufacturer are typically found [12].

Further, the surface of the substrate in its 'as-received' state is not suitable for bonding. Metallurgical processing, including heat treatment and rolling, modifies the uppermost layers of the alloy surface. Fig. 2.2 presents a schematic illustration these layers [13]. It displays compositional changes in the structure, including refined grains and enrichments of secondary particles (dispersoids). As a result of diffusion during tempering, the surface oxide is typically enriched in Mg and Zn [14, 15]. Additionally, the high shear forces applied during rolling are able to break and fold some of these surface oxides into the substrate. As a consequence, many fragments from the surface oxide, in addition to broken intermetallic particles are found underneath the surface. These so-called 'near-surface deformed layers' (NSDL) have a significant impact on the mechanical and electrochemical properties compared to the bulk material. [16].

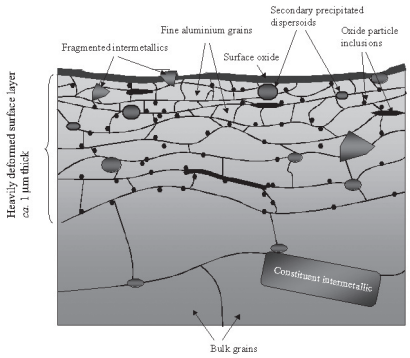

Figure 2.2: Schematic illustration of the modified composition of the aluminium alloy surface present after metallurgical processing [13].

2.2.1.2 Aerospace adhesives

The first adhesives for metal-to-metal bonding were based on a combination of phenol with polyvinyl formal (PVF). PVF is a thermoplastic polymer that serves as a plasticizer to the brittle phenol. Together they form an adhesive that is commercially known as *Redux* (Research at Duxford) [6]. By curing at high temperatures (above 150°C) the PVF melts and the two precursors polymerize by a polycondensation reaction. To avoid

the formation of bubbles and defects caused by water vapour that is released during the reaction, pressure is applied on the joint area during hardening. This process requires an autoclave furnace, providing surface pressures in the order of 0.5 to 1 MPa for a period of about half an hour. Redux adhesives are known for their excellent deformation and crack controlling properties. It is a high modulus adhesive which is able to produce high strength bonds, suitable for load-bearing constructions [8]. Its high curing temperature, however, also has a disadvantage. The relatively high heat is affecting the fatigue strength of the alloy. This has to be overcome by overdesigning, using a thicker substrate, which leads to an increased weight. In addition, the high PVF content also set serious limitations on the bonds heat resistance, while at lower amounts of PVF, the adhesive retains the brittle nature of the phenolic resins [17].
Therefore, a new type of adhesive was developed in the early 1960s. It is based on a polyether resin that contains more than one epoxy group capable of being converted into the thermoset form [6]. Since the most common curing process for epoxy is based on the addition reaction (polyaddition) of a hardener molecule such as an amine, curing can be completed at lower temperatures and pressures (about 120°C and 0.1 MPa), reducing processing costs and the negative temperature effects that were mentioned earlier [7]. Furthermore, the final properties of the epoxy network can be tailored, depending on the crosslinking agents, plasticizers, and carrier materials providing stronger adhesives.
Nowadays both types of adhesives are still applied. Epoxy adhesives are often preferred for their better wetting ability, mechanical properties, and high chemical and thermal resistance. However, their durability has often been unsatisfactory without the help of a corrosion inhibiting primer. Phenolic adhesives, on the other hand, have excellent water-resistant properties. They retain a weakly acid character that stabilizes the aluminium oxide against hydration, which is one of the main reasons for its prolonged use in this industry [18].

2.2.2 Adhesion theories

A fundamental understanding of adhesively bonded joints requires an understanding on both microscopic and macroscopic levels. Numerous theories including adsorption, mechanical, electrostatic and diffusion theories have been suggested to describe adhesion. Amongst these theories, adsorption and mechanical models are most relevant for a metal/polymer bonding [19].
Firstly, to achieve any form of adhesion, the adhesive must come within molecular or atomic contact with the molecules of the adhered surface (the substrate). Hence, physical absorption is a prevailing requirement for both models. Obtaining such intimate contact requires appropriate wetting of the surface. This is why the adhesive or primer is applied in liquid form. A measure of how well a liquid wets a solid surface is the contact angle θ. This is the angle that is formed between the solid/liquid interface and the liquid/ vapour interface when these three phases are in equilibrium (Fig. 2.3 (a)).

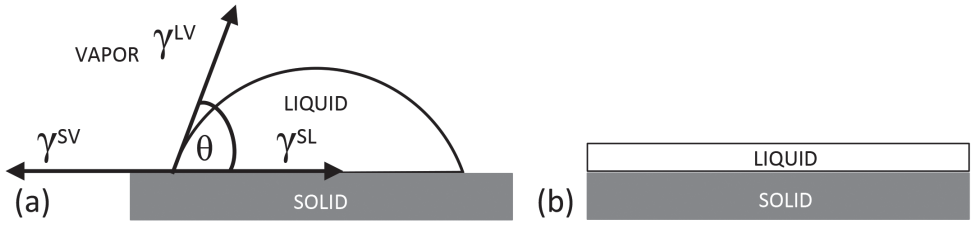

Figure 2.3: Contact angle (θ) and surface tension (γ) for a liquid drop on a solid surface at partial wetting (a) and complete wetting (θ =0), *(b).*

Young's equation (2.1) is used to describe the interactions between the forces of cohesion and adhesion and measure what is referred to as the surface free energy (or surface tension).

$$\gamma^{SV} = \gamma^{SL} + \gamma^{LV} cos\theta \qquad \text{Eq. 2.1}$$

In terms of surface tension, γ^{SL} is the solid/liquid interface tension, γ^{SV} is the solid surface tension and γ^{LV} is the liquid surface tension. Complete wetting (Fig. 2.3 (b)) is achieved whenever the critical surface tension of the substrate is larger than the surface tension of the adhesive, so that the contact angle is 0°.
While good wetting is necessary for good contact, it does not guarantee adhesion. Initial and long-term adhesion strength depends on the type of forces holding the two phases together.

2.2.2.1 Adsorption theory

The adsorption theory states that adhesion between two materials can only occur when their atoms and molecules are brought sufficiently close to establish some kind of attractive forces. The type of forces (or bonds) will vary according to the nature of the atoms. Bonds are generally divided into primary (chemical-) and secondary (physical-) bonds (Table 2.1). Secondary bonds include van der Waals and hydrogen bonds, which are relatively weak intermolecular forces. Van der Waals bonds result from dipole-dipole interactions and dispersion forces of atoms or molecules. These forces become important in the adhesion of nonpolar and chemically inert surfaces. Hydrogen bonds are slightly stronger, involving the attractive interaction between polar proton and an electronegative atom (e.g. oxygen) across the interface. This is a special type of acid-base interactions [4] that are often accounted for the adhesion between alumina (in both hydrated or dehydrated forms) and polymeric resins [20, 21].
Primary or chemical bond types exhibit much larger bond energies and are therefore much more stable. Amongst the three primary bonds in Table 2.1, only covalent bonds are relevant in the case of oxide-polymer adhesion. Covalent bonds involve sharing of electron pairs between adjacent atoms. This can, for example, be achieved by the use

of organosilane coupling agents that improve adhesion by forming a covalent Si-O-Al bond across the interface [22].

Table 2.1: Bond types and typical bond energies [23]

Bond type		Bond energy kJ/mol
Primary	Ionic	600 - 1100
	Covalent	60 – 700
	Metallic	110 - 350
Secondary	Hydrogen	10 – 40
	Van der Waals	1 - 20

2.2.2.2 Mechanical adhesion

On a macroscopic level, mechanical interlocking between the substrate and the adhesive also promotes adhesion. This type of interaction is introduced by surface topography such as cavities, voids and pores on the surface [24]. According to the mechanical theory, adhesion occurs as a result of the adhesive penetrating into these open cavities. When the adhesive hardens, it adheres to the substrate [25]. The interface is then seen as a composite layer that enables better stress distribution and arrests the propagation of cracks during mechanical stress.

This theory is supported by experimental results that show an increase in joint strengths after mechanical roughening of the surface using grit blasting or mechanical abrasion [26]. Further, even higher strengths were measured in the presence of an open porous structure formed by anodizing aluminium in acid electrolytes that leads to nanometre size pores [17, 27, 28]. Too much roughness, however, also has its disadvantages as it can lead to incomplete initial wetting of the surface and to the creation of voids that can act as stress concentrations points that can initiate failure [29].

There is an on-going discussion about the nature of such mechanical contribution to bond strength. Since good adhesion can also occur between smooth adherent surfaces, opponents to the mechanical theory claim that the increased strength can be attributed to an increase in the contact area between the oxide and the adhesive, resulting in a larger amount of interfacial bonds. In either way, years of practical experience has led to a general application of macro- and micro-rough surfaces [30].

2.2.3 Durability of the substrate and the adhesive bond

Pure aluminium metal has an inherent corrosion resistance due to the presence of a relatively uniform and thin oxide layer that protects the underlying metal [31]. This is caused by the high affinity of aluminium towards oxygen. Whenever the fresh metal surface is exposed to the atmosphere as, for example, in case of mechanical damage a new oxide layer will be formed. In dry conditions, this oxide film is typically a dense

barrier layer of amorphous alumina (Al_2O_3) that is only 2 to 3 nm thick. In humid environments, this oxide will be covered by a more permeable hydrated aluminium hydroxide ($Al_2O_3 \cdot xH_2O$) at the outer surface. In that case the thickness of this layer can reach up to 10 nm [31].
These thin oxide layers are stable over a fairly broad range of pH ($4 < pH < 8.5$), providing aluminium with sufficient protection for various commercial purposes. Unfortunately this layer is not stable at both lower and higher pH values. The Pourbaix diagram in Fig. 2.4 illustrates this behaviour. The diagram indicates which state of aluminium is thermodynamic stable in the presence of water, under different pH and potential conditions. At acidic environments when $pH < 4$, aluminium dissolves to Al^{3+} ions. Above pH 8.5 aluminium dissolves into aluminate (AlO^{2-}) ions. These two situations lead to an on going corrosion, which is the attack of the metal by a reaction with its environment [32].

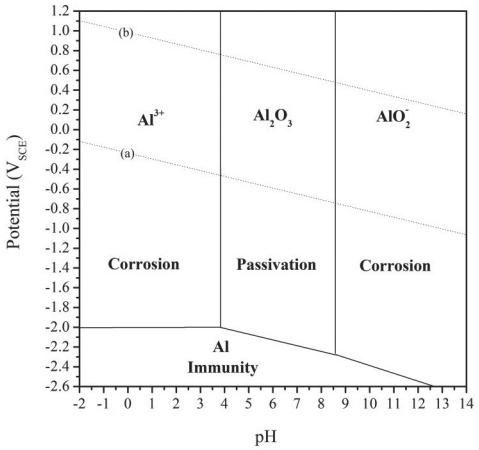

Figure 2.4: E-pH diagram for pure Al at 25˚C in aqueous solution [32]. The lines (a) and (b) correspond to water stability and its decomposed product.

This metal attack is coupled to a reduction reaction. The dashed lines (a) and (b) in Fig. 2.4 represent the water stability limits, which will determine the nature of the cathodic reaction. In the upper region (above line (a)), water can be oxidized to produce oxygen while in the lower region (below line (b)) water is reduced to form hydrogen gas.
As previously mentioned, aluminium in aerospace applications is mainly used in its alloy form. The addition of alloying elements, though essential for mechanical properties, can have detrimental consequences on its corrosion behaviour. The (electro-)potential differences between (local) areas of compositional differences can lead to galvanic coupling and selective dissolution of the more active element. The localized presence of second phases makes these alloys very susceptible to localized corrosion attacks. The most common type of corrosion in aluminium alloys is pitting corrosion due to second

phase particles in the matrix acting as cathodes or grain boundary precipitation causing precipitate-free zones with different electrochemical potential. These phenomena are especially pronounced in AA2024-T3, which contains relatively high amounts of copper, a much nobler element than aluminium. These localized attacks can proceed to considerable depths within the substrate and may lead to grain fallout when proceeding along grain boundaries. They present an extremely high risk of failure. Detailed mechanisms of localized corrosion of AA2024-T3 under chloride conditions can be found elsewhere in the literature [33-35].

Another crucial parameter in maintaining the long-term integrity of the assembly is durability of adhesion under various environmental conditions. Aircraft structures are frequently subjected to temperature extremes at varying atmospheric pressures, moisture content and types of aggressive species (e.g. anti-freeze and chlorine ions). These, in combination with the varying mechanical stresses, may lead to early failure [36]. Fig. 2.5 illustrates the different possible failure mechanisms that can occur within an adhesive joint. They are generally characterized as predominantly cohesive- or adhesive in nature. Cohesive failures take place within the same phase, whereas adhesive failures occur at their interfaces.

Industrial standards generally demand higher adhesion than cohesion strengths. This is desired from an engineering point of view. Cohesive failure related to bulk material properties can be readily considered by design. In the case of metal-to-metal bonding, this refers to a cohesive failure within the polymeric adhesive (Fig. 2.5 (A)). Other failure mechanisms (Fig. 2.5 (B)-(F)) are the result of poor bond preparation (processing) and effects of environmental conditions.

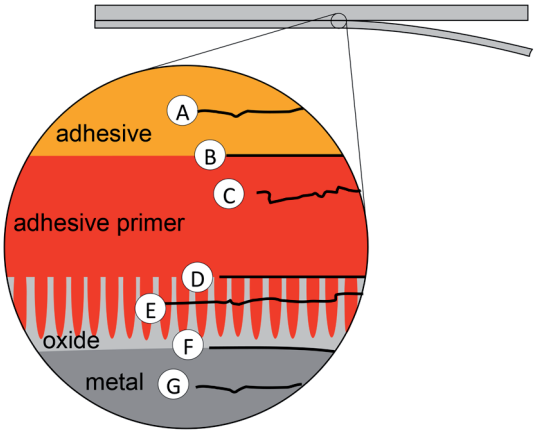

Figure 2.5: Schematic illustration of the possible failure modes in structural adhesive joint: (A) cohesive fracture of the adhesive film, (B) interfacial disbonding between adhesive and primer, (C) cohesive fracture of primer layer, (D) interfacial disbonding between primer and anodic coating, (E) fracture within anodic oxide coating and (F) corrosion of aluminium substrate at metal/oxide interface.

One of the key issues concerning bond durability is the permeability of water molecules. Moisture from the environment can enter the bonded system by bulk diffusion through the adhesive, by interfacial diffusion along the interface between the adhesive and the oxide, and by capillary action through cracks or defects. Zanni-Deffarges and Shanahan [37] compared diffusion rates in bulk and bonded epoxy adhesive to show that capillary effects near the oxide-polymer interface can significantly enhance the diffusion rate of water in bonded joints. Once reaching the bond line, moisture can hydrate the oxide. This leads to the formation of oxyhydroxydes, a weaker form of oxide with a larger volume [38]. Ultimately, this can lead to cohesive fracture within the hydrated oxide (Fig. 2.5 (E)). Alternatively, the presence of water at the interface can displace the previously formed bonds between the oxide and the resin, leading to delamination by de-adhesion (Fig. 2.5 (D)).
Another dangerous failure mode is bondline corrosion (Fig. 2.5 (F)). This is facilitated by the diffusion of water and other corrosion-initiating species (e.g. chlorine ions). Once bondline corrosion is initiated, it is characterized by disbonding at the interface followed by localized corrosion. In order to avoid these types of failures and ensure long-term safety, bonded metal-to-metal assemblies must be carefully prepared. The preparation of such surfaces is the subject of this thesis and therefore, is addressed in detail in the following section.

2.3 Key Methods to Enhance Adhesion and Durability

The previous section illustrates the problem arising from the use of high strength alloys. Maintaining their long-term strength and integrity under loading and various environmental conditions requires the help of some protective systems. Four general types of surface protection methods are relevant to adhesive bonding: cladding, surface pre-treatment, primer application and corrosion inhibition. These are detailed in the following sections.

2.3.1 Cladding

One method to overcome localized corrosion attack on bare alloys is by cladding it with a thin layer of relatively pure aluminium [32]. The uniform composition and excellent corrosion resistance of pure aluminium is then used to protect the underlying heterogeneous substrate. In a corrosive environment the clad layer will serve as a sacrificial anode. Metal dissolution will then proceed evenly over the surface, preventing localized damage that would lead to an early failure. One of the drawbacks of cladding is its additional weight. Ironically, the presence of cladding is reported to enhance corrosion instead of delaying it in some cases. This occurs when the joint edges are exposed, leading to galvanic coupling between the two different layers. Accelerated failure and disbonding then proceeds along the bond-line towards the interior of the bond [8].

2.3.2 Chromate-based surface pre-treatments

Surface pre-treatment has emerged as the most important step to provide the desired surface characteristics for bonding and minimize the effect of surface heterogeneities. The main process steps that are currently applied in the aerospace industry are illustrated in Fig. 2.6. It consists of four major steps: degreasing, pickling (or etching), anodizing, and primer application, all currently including Cr(VI)-based chemicals. In between two steps the surface is thoroughly rinsed in water. The following sections describe each step of this pre-treatment scheme in terms of how it modifies the surface and its properties in its historical context.

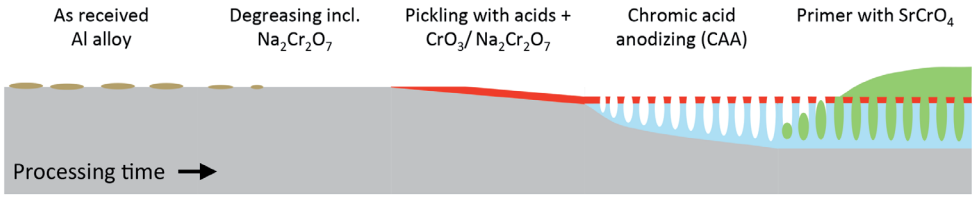

Figure 2.6: Schematic representation of the process steps and the modifications that take place during the complete chromate-based pre-treatment that is currently applied in the European aerospace industry.

2.3.2.1 Degreasing

Degreasing is the first step in the pre-treatment process and normally the minimum preparation that is carried out prior to any type of metal bonding. Degreasing removes any oils, grease and contaminations that might have been introduced during aluminium manufacturing and processing [39]. This preliminary cleaning is necessary in order to assure the efficiency of the following steps. Failing to remove organic material at the surface will lead to poor wetting. If the organic layer is effectively removed the contact angle will be reduced to zero (full wetting) and the following steps will work evenly across the substrate surface [31].

2.3.2.2 Pickling (or etching)

After superficial contaminations have been removed, the modified surface layers on the as-received substrate are chemically removed. According to the Pourbaix diagram, as shown in Fig. 2.4, this can be performed in either acidic or alkaline solutions. The distinction between pickling and etching is not always well defined in the literature and both terms are can be used to describe the same process. According to one definition [31], however, etching and pickling differ in the severity of their attack on the surface, with pickling been slightly milder than etching.

The classical etching solutions are often composed from mixtures of chromic and sulphuric acids. They are generally divided into two types: the FPL- and the CSA etch (Table 2.2). The first is the Forest Products Laboratory (FPL) process that was developed in the 1950s in the U.S. It consists of immersing the substrate in sodium dichromate

($Na_2Cr_2O_7$) and sulphuric acid solution for 9-15 min at 65°C [40]. The European version of this etch, the CSA pickling uses lower concentrations of either chromium trioxide (CrO_3) or sodium dichromate ($Na_2Cr_2O_7$) with sulphuric acid at similar temperatures, but longer times (30 min.) [41].

Table 2.2 Classical chromate-based etching solutions [40]

Parameter	FPL [a)]	CSA [a)]
$Na_2Cr_2O_7$ (wt.%)	5.0	6.4 [b)]
H_2SO_4 (wt.%)	26.7	23.3
H_2O (wt. %)	68.3	70.3
Temperature (°C)	65	60-65
Time (min.)	10	30

[a)] Both solutions are optimized by the additions of 1.5g/l AA2024 for its Al and Cu content. [b)] Readily replaced by CrO_3.

Both methods follow the two-step reaction mechanism in eq. 2.1 and 2.2. First, hexavalent chromium catalyses aluminium oxidation to alumina (eq. 3.1). Next, the alumina product is dissolved by sulphuric acid (reaction 3.2) [31].

$$2Al + 4H_2SO_4 + Na_2Cr_2O_7 \leftrightarrow Al_2O_3 + Na_2SO_4 + Cr_2(SO_4)_3 + 4H_2O \qquad \text{Eq. 2.1}$$

$$Al_2O_3 + 3H_2SO_4 \leftrightarrow Al_2(SO_4)_3 + 3H_2O \qquad \text{Eq. 2.2}$$

Since the second step is slower than the first one, a thin oxide layer (about 5 nm thick) is produced on the surface. This oxide is indicated by the red layer in Fig. 2.6. It is amorphous, with a composition corresponding to alumina (Al_2O_3) and some minor concentrations (~0.5%) of Cr and S impurities. Venables et al. [28] reported that due to surface energy interactions, whiskers-like protrusions extending from the triple grain boundary points extend up to 40 nm from the surface. They suggested that these branched protrusions already provide sufficient interlocking with the adhesive surface, resulting in an improved adhesion.

Unfortunately, various early in-service failures (mostly of non-bonded structures) occurred in the early 1960s, as aircrafts manufacturers started using epoxy adhesives instead of phenols [41]. The failure was followed by corrosion of the part, accelerated by the creation of a crevice by the delamination. This corrosion was especially pronounced in the presence of clad layers. As explained earlier, the difference in electrochemical

potential between the cladding and the bare metal enhanced the corrosion along the bond line (hence, bondline corrosion). The simple pre-treatment procedure was thus insufficient to provide reproducible durable bond performances.
An important result from studies on bond-line corrosion is the '*optimized FPL*' etch. Researches reported that there is an important relationship between the content of pre-dissolved aluminium and copper in the pre-treatment bath and bond performance [41]. Joints made after the substrate were prepared in solutions that contained some pre-dissolved AA2024- T3 alloy (hence, 'aged solutions') persistently performed better than joints treated in freshly prepared solutions. This was attributed to stabilizing the surface reaction rate that helped to improve reproducibility and provide a more porous and thicker surface oxide. Consequently, industrial standards now prescribe minimum amounts of aluminium and copper in the bath for both FPL (now, "optimized FPL") and CSA solutions, as well as for anodizing baths.

2.3.2.3 Anodizing

Anodizing is an electrochemical process in which the aluminium substrate is artificially oxidized to grow a thick oxide film (up to several μm) [31]. The process derives its name from the fact that the aluminium substrate is used as the anode in an electrolytic cell (Fig. 2.7). The anode (substrate) is connected to the positive terminal of a DC power supply while a cathode (e.g. Al, stainless steel) is connected to the negative terminal. When the circuit is closed, electrons are withdrawn from the aluminium anode, which facilitate the oxidation of aluminium atoms to cations (Al^{3+}) at the metal/oxide interfaces of the anode and the break down of water at the oxide/electrolyte interface. This process is accompanied by hydrogen reduction at the cathode.

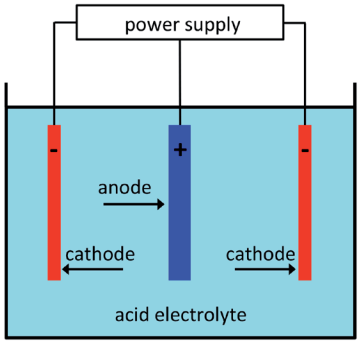

Figure 2.7: Schematic illustration of an anodizing bath.

The mechanism of anodic film growth during anodizing is illustrated in Fig. 2.8. Since the electronic conductivity of aluminium oxide is very low, the anodizing voltage that is applied on the anodic cell encounters a resistance by the existing (natural) oxide film. This leads to a potential drop over the metal/electrolyte interface, which give rise to high

electric field over the oxide layer. These electric fields are typically in the order of 10^6 to 10^7 V/m [42], which is high enough to enable oxide growth by ionic migration through the oxide [43]. Since aluminium is anodized in an aqueous electrolyte, adsorbed water at the anode will break down forming negatively charged O^{2-} and OH^-. These anions migrate towards the positively charged anodic substrate. A reaction between Al^{3+} and O^{2-} will leads to the formation of alumina, Al_2O_3, at the metal/oxide interface. Since not all the produced Al^{3+} is consumed by this interface, excess Al^{3+} cations will migrate away from the positively charged anode. Upon reaching the oxide/electrolyte interface, Al^{3+} can react with available O^{2-} forming additional alumina at the oxide/electrolyte interface. Under certain conditions, alumina ions will be directly ejected into the electrolyte. The conversion efficiency and, hence, final film morphology will depend on the balance between oxide growth and oxide dissolution (through direct ejection and chemical attack by an aggressive electrolyte). This in turn, is determined by the nature of the electrolyte and the process conditions, as discussed later.

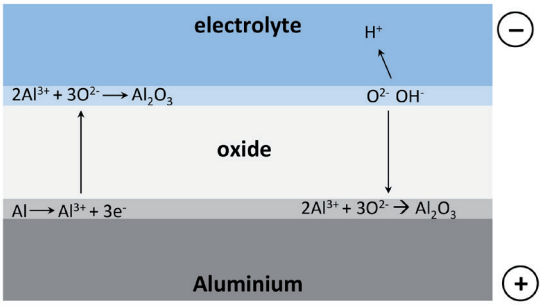

Figure 2.8: Schematic representation of the aluminium/electrolyte interface, showing the ionic processes involved in oxide growth during anodizing.

Chromic acid anodizing (CAA) was incorporated into the pre-treatment schedule in the 1960s. It mainly aimed to improve the overall corrosion resistance by producing a thicker physical barrier between the metal and its environment. Although anodizing can produce different oxide morphologies (see section 2.4), porous-type anodic films are preferred for bonding purposes. As illustrated in Fig. 2.9, porous anodic oxides consist of a compact barrier layer on the bottom and a relatively regular porous structure on top [44-47]. These films are created when the anodic oxide is sparingly soluble in the anodizing electrolyte [44, 48]. In Europe, the 40/50V Bengough-Stuart process was adapted, using 2.5-3.0 wt.% chromic acid (CrO_3) at 40 °C [49]. The voltage across the electrolytic bath is initially raised to 40V in the first 10 minutes. This voltage is then maintained for 20 more minutes before it is raised to 50V, where it is kept constant during the last 5 minutes [50]. The higher voltage at the end results in a thicker barrier layer and wider pores just above the barrier layer, providing an extra thick barrier for corrosion [51].

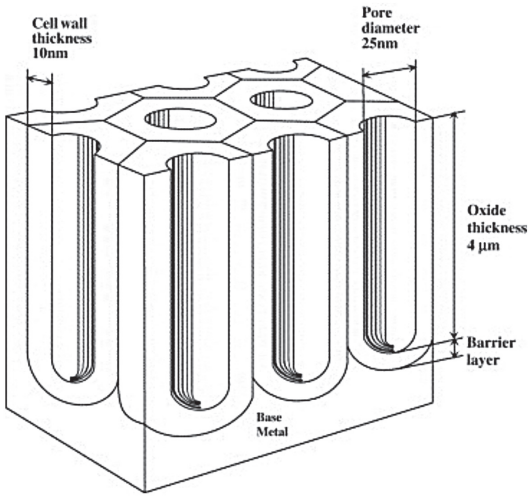

Figure 2.9: An idealized illustration of the anodic oxide structure formed on clad alloys following the 40/50 V CAA process [49].

This process produces 3-4 μm thick oxide layers on both AA2024-T3 and AA7075-T6 (bare and clad). It is a relatively ductile oxide with very low (0.1-0.3 wt.%) chromium content in the oxide. The oxide is moderately resistant to attack by moisture, although hydration has been reported [39]. This treatment, combined with prior CSA etching, was soon established as an effective pre-treatment for adhesive bonding and become an industrial standard.

For economic reasons, anodizing was initially rejected in the US until in 1975 Boeing introduced phosphoric acid anodizing (PAA) after the FPL etch. The PAA process applies 10 wt.% phosphoric acid at 21-24 °C. Anodizing is conducted at constant voltage of 10-15 V for 25 minutes. The PAA oxide is considerably thinner (typically 0.5 to 2 μm) and more porous than the CAA film [52]. The composition of the oxide corresponds to non-hydrated Al_2O_3 with $AlPO_4$ in the outer part of the film, which provides an excellent stability in humid environments with higher resistance to hot water sealing. This resistance is attributed to the stability of the chemical bonds between aluminium and phosphate [53] [54]. PAA anodizing is reported effective in increasing the environmental stability of adhesively bonded aluminium structures in service [55]. This process was developed together with the introduction of chromate inhibiting primers and, if used separately, is reported to yield insufficient corrosion resistance. Together with the FPL etch, PAA is generally considered competitive to CAA [56].

2.3.3 Primer application

In regular manufacturing operations, a certain time interval (several hours up to several months) usually passes between substrate pre-treatment and bonding. During this time, the freshly prepared oxide is very active and therefore susceptible to damage,

contaminations, and environmental degradation [57]. This is prevented by the application of a thin layer of primer to seal the oxide immediately (within two hours) after the pre-treatments, when surface activity is maximal.

Primers are diluted polymeric coatings, usually matching the chemistry of the adhesive. The primer functions as a physical barrier between the pretreated surface and its surrounding. Except for surface protection, primers are also used to promote adhesion. Two contributing mechanisms can be distinguished; (1) improved surface wetting and (2) providing stronger adsorption interactions. The first mechanism is driven by the primer's lower viscosity (compared to the adhesive) and the addition of wetting agents. As a result, the primer is able to penetrate deep and completely fill the pores [58]. The second mechanism uses coupling agents to form a covalent bond across the inorganic-organic interface. Coupling agents are molecules with dual functionality. They contain organic end- groups such as methoxy (CH_3O-), ethoxy (CH_3CH_2O-) or hydroxyl (HO-) attached to a metallic central atom (e.g. silicon, zirconium or titanium) [59]. Organosilane coupling agents are the predominant chemical type of adhesion promoters. These groups are able to adsorb on the metal oxide surface through hydrogen bonds. Upon curing, a metallosiloxane bonds (Al-O-Si) are formed with the surface oxide [60]. Recalling from the previous section, these type of bonds are much more stable than hydrogen bonds. Any remaining silanol groups will condense with themselves, forming a dense Si-O-Si network. Since Al-O-Si bond can be hydrolysed, the durability of these bonds will be determined by the extent of cross-linking of the Si-O-Si bonds, which will determine the hydrophobicity of the covering siloxane film. Hence, adjusting the chemical composition to tailor the desired film properties is essential. It is important to also match the reactivity of the coupling agent with that of the adhesive [59]. Different studies have demonstrated that silanes are capable to improve interfacial adhesion [58, 61-63], as well as corrosion resistance of coated aluminium [64, 65]. Song and van Ooij [66], for example, have shown that by combining two types of silanes, namely 1,2-bis(triethoxysilyl)ethane (BTSE) and ϒ-aminopropyltriethoxy (ϒ-APS), it is possible to design a dual functionality interface that would give good corrosion protection and will be compatible with an epoxy adhesive. Since silanes connect via the OH- groups on the substrate, maximizing their amount on the substrate is desired. A study by Franquet et al. [67], showed that chemical pre-treatments affecting the amount of surface hydroxyl groups will in turn affect the silane film uniformity and thickness. Therefore, when silanes are applied, prior surface pre-treatment is still needed.

2.3.4 Corrosion inhibition

It is incorrect to assume that a primer completely seals the oxide from its environment. Similarly to adhesives, water and other aggressive ions can still penetrate into a cured primer. Therefore, the additions of corrosion-inhibiting species are used to provide an active corrosion protection [8]. The protection mechanism is then provided by the

adsorption and reaction of corrosion inhibiting species with water, preventing it from reaching the metal surface and preventing the rupture of sensible bonds at the organic-inorganic interface or degradation of the aluminium surface.

Chromate pigments (e.g. as $SrCrO_4$ pigments) are one of the most effective corrosion inhibitors for a wide range of environmental conditions. These are important not only for surface protection during storage, but also for the durability of the joint during service. In case of a local damage, chromate ions will leach from the coating, migrating to the exposed metal surface to react with ambient water and form a new protective oxide film [68]. This additional protection mechanism, often referred to as 'self-healing', is a valuable active corrosion inhibition that has made hexavalent chromium prominent and so difficult to replace [69]. Various environmentally friendlier alternatives to chromates have been studied over the years. While search for suitable alternatives is still ongoing, there are numerous reports concerning their protection mechanism, efficiency and compatibility with different metal substrates and coating systems. For more details readers are referred to Hughes et al. [53].

In addition, components of the adhesive may leach out after the adhesive reacts with water. Hence, the nature of the adhesive can also influence the durability of the bond. The alkaline environment that is, for instance, formed by epoxies can attack the aluminium oxide and negatively affect its durability (thus the need for corrosion inhibitors). Phenolic resins, on the other hand, were found to retain a weakly acidic character that stabilizes the aluminium oxide against hydration and provide it its excellent water-resistant properties [17].

2.4 Fundamentals of anodizing

2.4.1 Barrier anodic oxide films

Barrier anodic oxide films are highly uniform and compact. Such films are grown when the electrolyte is relatively unreactive towards the anodic film. Hence, no aluminium species are lost to the electrolyte and all the oxidized aluminium atoms are contributing to film growth, resulting in 100% conversion efficiency. Studies using inert markers indicate that the transport numbers (hence, the relative migration rate of the different ions within the oxide) are 0.4 for Al^{3+} and 0.6 for OH^- and O^{2-} [70]. As a consequence, the relative contributions to oxide growth are, respectively 60% and 40% at the metal/oxide and the oxide/electrolyte interface. Barrier type film formation occurs in multivalent anion solutions (e.g. borate and tartrate), with near-neutral electrolyte pH and at ambient temperatures.

Anodizing in general can be performed under (constant voltage, U) or (constant current density, j) conditions. Under galvanostatic conditions, the constant current density induces oxide growth at constant electric field strength. In order to maintain constant field strength while compensating for the increasing electrical resistance of the

thickening oxide, the anodizing voltage increases as the film thickens (Figure 2.10 (a)). Eventually, the oxide will prevent the current from reaching the anode and the reaction will stop at a characteristic potential [70]. At this stage, sparking may be observed. This phenomenon is reflected by irregular oscillations in the voltage-time curve that can be seen in Fig. 2.10 (a) [71].

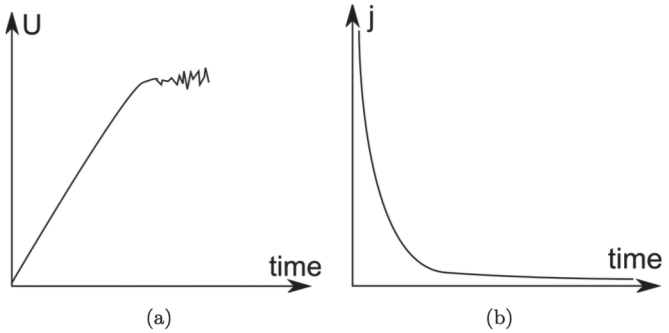

Figure 2.10 Schematic illustration of the potential (U) and current density (j) evolution with time under galvanostatic (a) and potentiostatic conditions (b) [71].

Anodizing under constant voltage shows similar, but inverse characteristics (Figure 10 (b)). Initially very high current density is measured, which steeply declines due to the rapid thickening of the oxide. Finally, the current density drops to a relatively low value where it remains stationary. The origin of this remaining current is suspected to be either an electronic leakage current (through defects in the oxide) or related to corrosion [31].

2.4.2 Porous anodic films

Porous anodic alumina films are formed in acid (and some alkaline) electrolytes that facilitate some solubility of the reaction products [31]. This process leads to the formation of a regular array of an hexagonal structure with central pores perpendicular to the metal surface (Fig. 2.11). A thin barrier layer is also present at the base of each pore, physically separating the substrate from the electrolyte. As opposed to the uniform barrier oxide film, this barrier under a porous oxide displays a scalloped morphology (Fig. 2.11 (C)). Because of the continuous oxide dissolution during anodizing, the barrier layer never approaches the maximal possible value and a continuous ionic current flow allows the pores to extend. This type of anodizing process facilitates the growth of much thicker films (a few up to some tens of micrometres), depending on the nature of the electrolyte and the process conditions. Commonly applied electrolytes include inorganic acids like chromic-, sulphuric- and phosphoric acids, organic acids (oxalic-, and tartaric-), and alkaline (di-sodium tetraborate, also called borax) solutions [31].

The mobile species involved in the process of porous oxide growth are again Al^{3+} and O^{2-} moving in opposite directions. An important difference in this process is, however,

that the oxide is only growing at the metal/oxide interface. The specific conditions obtained in these aggressive electrolytes result in direct ejection of the Al^{3+} cations into the electrolyte. This corresponds to total conversion efficiency of about 60%. Also here, anodizing under galvano- or potentiostatic conditions is possible with a corresponding current-time and voltage-time characteristic behaviours shown in Figure 2.11 (A) and (B). For anodizing at constant voltage, high initial current is observed followed by a rapid fall to a minimum value and a subsequent increase to the steady-state value. This behaviour contains four characteristic stages (Fig. 2.11 (B) a-d). Anodizing under constant current density follows these same characteristic stages (Figure 2.11 (A)). During the initial phase (stage a) a relatively uniform barrier film is grown. Since the top layer of the oxide is in continuous contact with the aggressive electrolyte, some penetration paths eventually develop over the outer surface. At a certain moment (stage b), the presence of these penetration paths through the barrier layer will provide lower resistance paths for current flow. This will affect the potential over the film and potential lines will now concentrate at the thinner oxide regions. As a consequence the rate at which the potential increases will decline. Since all outwardly mobile Al^{3+} species are lost to the electrolyte without forming a solid film, no mechanism exists to "heal" the initial penetration paths, which eventually will develop into pores. After a maximum potential is attained (stage c), the rearrangement of pores is observed. Some pores will terminate while others will continue to grow until the steady-state structure is obtained. With progressing concentration of the electric field at major pores, local scalloping of the aluminium/oxide interface occurs. Additionally, with the redistribution of the current and the development of the porous structure a thinning of the original barrier layer takes place, corresponding to a decreasing potential. This trend continues until a stationary anodic film morphology is created. In this stage of the anodizing process (stage d) the current (and electric field) is completely concentrated in the curved barrier layer in the middle of each pore and oxide growth leads to the deepening of the pores at constant

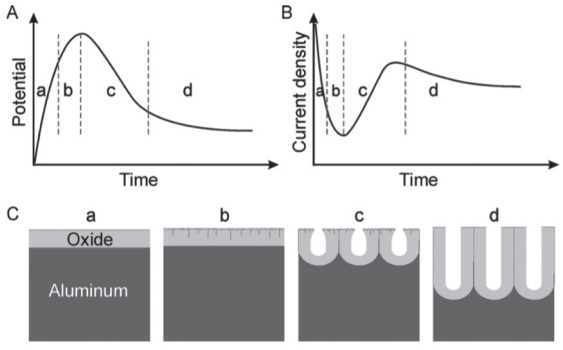

Figure 2.11 Schematic illustration of the kinetics of porous oxide growth in galvanostatic (A) and potentiostatic (B) regimes, together with stages of anodic porous oxide development (C) [72].

potential. The final thickness of the anodic film is, thus, primarily determined by the anodizing time [72].

In addition to direct ejection of Al^{3+}, oxide thinning can occur through chemical dissolution of the oxide or field assisted dissolution at the pore base. The latter used to be thought of as the principal mechanism contributing to the formation of pores and their shape. Recent experimental results, however, show that this is not always the case. In a series of studies at the university of Manchester in the UK, e.g. [73-75] researches have shown that the development of a porous structure in certain electrolytes is better explained by a model based on stress-induced plastic deformation. This was concluded based on experiments using a fine band of tungsten that was deposited in the aluminium substrate. The observed displacements of the marker species on the oxide after anodizing in phosphoric- and sulphuric acids conflicted with expectations according to the field assisted dissolution model. The tungsten marker, observed by transmission electron microscopy (TEM), remained evenly distributed within the film, indicating oxide displacement from the barrier layer region to the pore walls. This plastic flow is believed to originate from strong electrostriction stresses that develop as a result of volume changes. When the same experiment was conducted with borax electrolyte (which shows, according to the authors, similar behaviour to chromate) growth behaviour complied with the dissolution model [75].

2.4.3 Parameters affecting the anodic oxide film properties

Before covering the range of Cr(VI)-free alternatives to CAA, it is important to understand which key parameters control the anodizing process and how these, in turn, affect the oxide properties.

2.4.3.1 Pre-texturing

Studies have shown that surface features produced by prior steps are related to pore initiation and development. Following the previously discussed growth mechanism, geometrical (near-)surface features like the rolling lines, scratches and rolled-in oxides locally increase the curvature and therefore present preferential regions for pore initiation and development. It has been shown by Terryn [76] that such features can even pre-impose the alignment of pores to develop certain orientation. This is especially relevant when the previous step produces characteristic surface features. If a highly-regular pore arrangement is required, as in the production of alumina template for nanostructure fabrication, a two-step anodizing (with intermediate dissolution of the oxide) is used to produce a well-ordered structure, in which the first anodizing step is used to texture the surface [72]. Since this method is both time-consuming and expensive, pre-texturing by anodizing is generally not applied in the aerospace industry.

2.4.3.2 Incorporation of anions

Besides the ionic species that are responsible for oxide growth, any ion species that is present in the solution may be affected by the electric field. Since the anode is positively charged during anodizing, negatively charged species from dissociating acids will migrate towards the oxide, leading to the incorporation of small amounts of impurities into the oxide. The extent of incorporation is determined by the nature of the electrolyte solution, the applied conditions and the film type. A range of surface analysis techniques, including Auger electron spectroscopy (AES), X-ray photoelectron spectroscopy (XPS) and glow discharge optical emission spectroscopy (GDOES) [77, 78] have been applied to measure the concentration and distribution of electrolyte-derived impurities in the film. These studies show that the migration of electrolyte species varies from one electrolyte to the other. Table 2.3 lists the concentration of anions within the most common anodizing electrolytes. It demonstrates that almost anion-free films are formed in chromic acid, while other anions of alternative electrolytes contribute to a much higher relative composition. Since most electrolyte anions migrate at slower rates than the O^{2-} ions, a relatively pure alumina region is formed close to the aluminium/oxide interface [79]. This is indicated in Fig. 2.12 that displays a comparison of the resulting oxide composition in SAA and PAA. Sulphate anions can migrate into the inner most part of the cell wall, resulting in a duplex oxide composition. Phosphate anions, on the other hand, exhibit a triplex structure with maximal concentration in the region near the interface with the electrolyte. Additionally, the amount of incorporation also varies.

Table 2.3: Percentage of incorporated anions in the porous oxide layer [72].

Electrolyte	H_2CrO_4	H_3PO_4	$H_2C_2O_4$	H_2SO_4
Anion concentration (at.%)	0.1 – 0.3	6 - 8	2 - 3	10 - 13

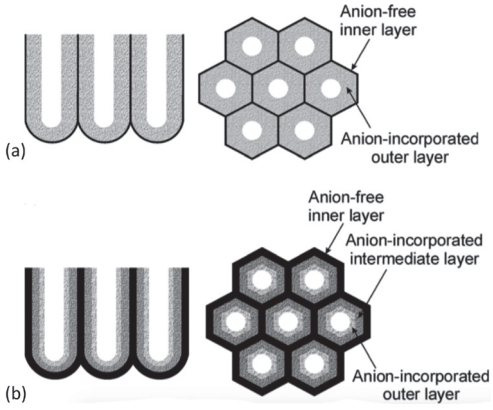

Figure 2.12: Schematic representations of the sectional and plan views of, respectively, the duplex (a) and triplex (b) structures of porous alumina cell walls formed in sulphuric and phosphoric acids [72].

Porous film formation generally supports a higher anion content in the oxide structure. This is explained by the fact that the electric field at the barrier layer is not uniform, so that the semi-spherical shape of the pore base results in a much higher electric field close to the electrolyte/oxide interface, which in turn supports easier incorporation of anions [72]. In addition, the long-term exposure of the oxide walls also allows active penetration of the acid.

Anion incorporation has an effect on the properties of the oxide film, such as the mechanical (e.g. flexibility and hardness) and chemical properties, and the space charge [80]. Thompson and Wood [81] reported a transition from solid to gel-like material moving across the cell walls towards the pore interior, with the thickness of this layer depends on the electrolyte, the voltage or current density, and the temperature. Another example is the resistance to hydration that is provided by oxides produced in phosphoric acid. This resistance has been contributed to the presence of $H_2PO_4^-$ ions in the anodic films. These anions can be further decomposed to proton, H^+, and HPO_4^{2-}, thereby restraining the hydration of alumina [82].

Moreover, the applied electrolyte seems to have an influence on the water content of the film. Although no water is found in the bulk of oxides formed in acid electrolytes, chemical adsorption (chemisorption) of OH^- groups and water molecules at the outer layer is reported [83]. This can, according to findings on chemically grown aluminium oxides, affect the extent in which the oxide interact with organic molecules and resins [84].

2.4.3.3 Potential / current density

At steady state growth, a dynamic equilibrium exists between pore base dissolution at the oxide/electrolyte interface and oxide growth at the metal/oxide interface. Studies have shown that the major film characteristics (pore diameter *d*, cell diameter *c* and barrier layer thickness *b*, as indicated in Fig. 2.13) are directly related to the applied potential [85, 86]. This is explained by the fact that stationary film formation occurs at a constant rate, which is determined by the average field over the oxide [87]. Higher potential values will result in thicker barrier layers, larger cells, and wider pores. The thickening of the barrier layer was found to show an almost universal relation, growing at 1.3-1.4 nm/V for barrier-type films and about 1.2 nm/V for the barrier under porous films, with only small deviations as a function of the temperature and the electrolyte characteristics [72].

Any tendency of a pore to become too big or too small will be compensated by its curvature that will, accordingly, adjust field strength [70]. If during the anodizing process, a large variation in potential is induced, the oxide film will adapt itself to the new applied conditions. This observations, together with a 'recovery effect' was reported by Curioni et al. [88], using cyclic polarization measurements. Therefore, varying the anodizing

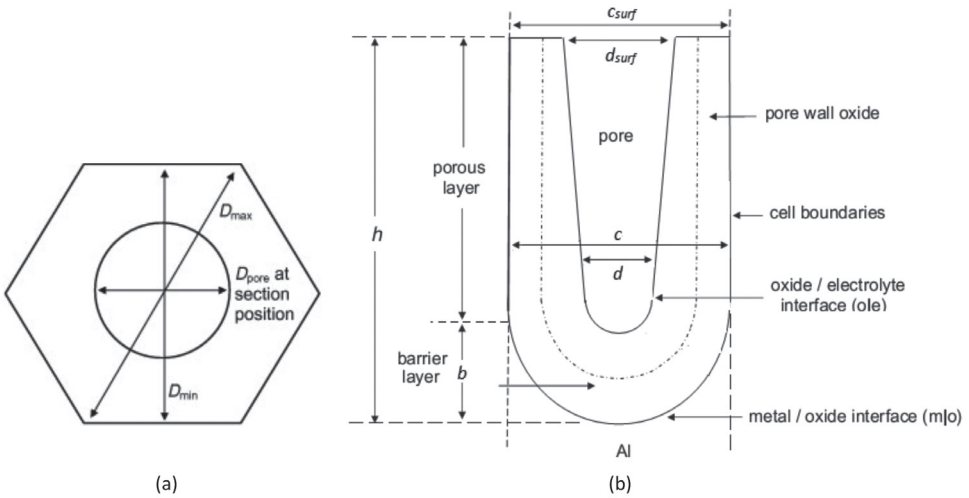

Figure 2.13: Schematic representation of an ideally hexagonal columnar cell of a porous anodic alumina film [87].

potential during the treatment will produce an oxide with varying morphology across its thickness. The recovery effect is the elapsed time before the steady-state characteristic conditions of the new voltage are attained. It will depend on the potential variance, as well as the bath conditions (electrolyte, temperature). This may explain the gradient of voltage that is applied during the conventional 40/50V CAA anodizing process, providing wider pores at the bottom of the film and thickening the barrier layer. This is an interesting observation that can be used as opportunity in developing new processes.

2.4.3.4 Temperature

Another significant variable in the anodizing conditions is the electrolyte temperature. Generally, temperature effects are negligible on the barrier layer and its thickness under barrier-forming anodizing conditions, but this is not the case for porous oxides. A higher bath temperature will enhance local dissolution at the pore base. This, in turn, will result in an increased local current density, which will increase the ionic transfer and oxide formation rates [89].

Aerts et al. [90] have shown that a higher rate of oxide dissolution, due to the aggressiveness of the electrolyte at higher temperatures, have increased the porosity in sulphuric acid anodizing (with a constant convection) from 4% at 5 ℃ to 32% at 55 ℃. Dissolution effects are mainly noticeable at the outer layer of the oxide, leading to pore broadening (but generally not affecting the interpore distance) [91]. This is explained by the longer contact times of the outer layers with the electrolyte. This is why cone-shaped pores are often reported; with the pore diameter at the pore base (d in Fig. 2.13 (b)) generally exhibiting a linear correlation to the anodizing voltage, while pores at the surface (d_{surf} *in* Fig. 2.13 (b)) are frequently larger than expected. Interestingly,

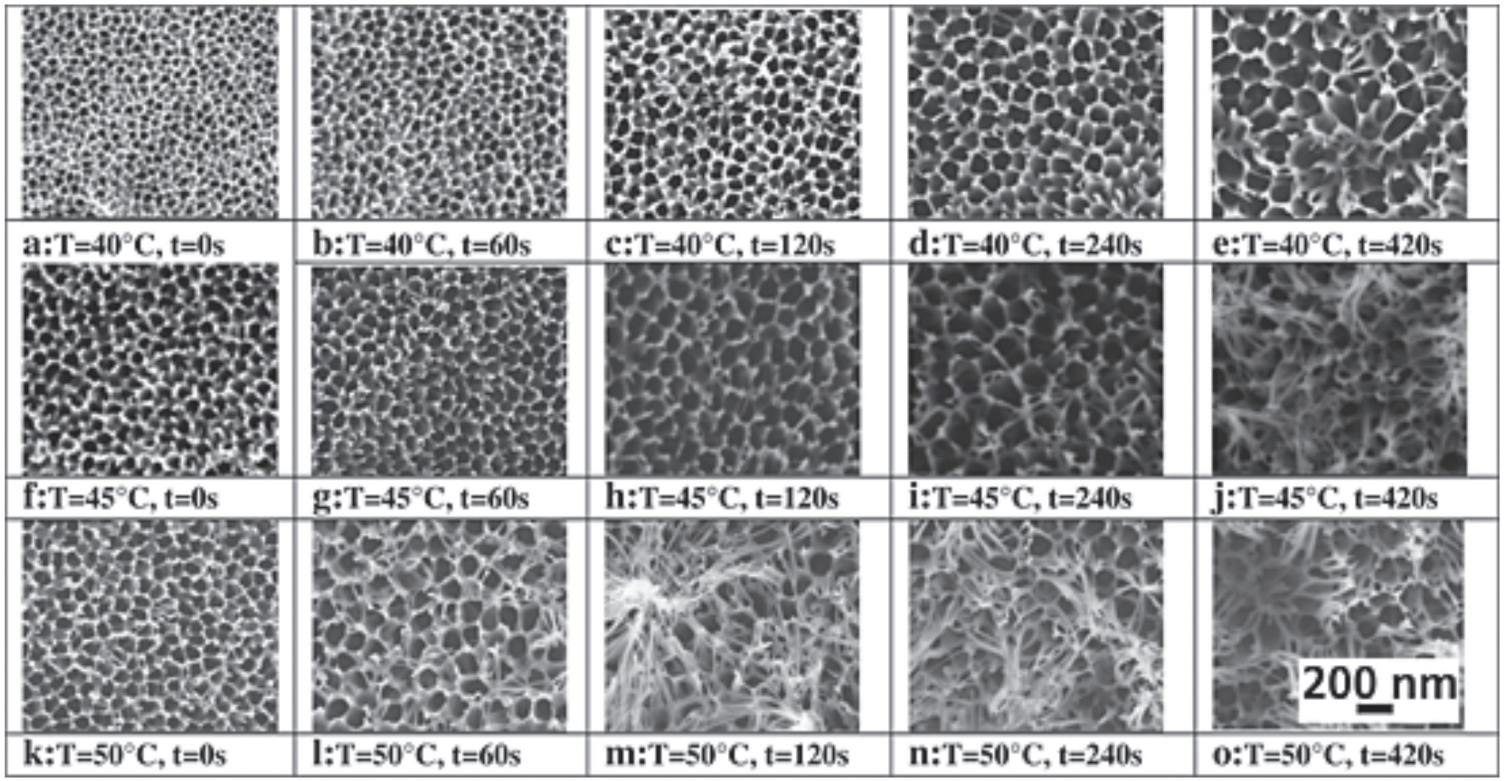

Figure 2.14: SEM of the oxide layer depending on the bath temperature and the dwell time - surface views (anodizing potential E = 50 VSCE) [93]. Whiskers are formed at longer anodizing times. Longer time and higher temperatures lead to their collapse and the formation of a 'bird's nest'.

controlling the electrode temperature can have a larger influence on oxide formation than changing the electrolyte temperature [92]. Hence, physical bath properties, such as convection-based heat transfer should be considered.
At high anodizing temperatures and longer times, dissolution has an even larger influence on oxide morphology. An example is shown in Fig. 2.14 where whisker formation on top of the oxide can be observed. These are created by extended dissolution of the pore walls. At some critical point, these filaments are so long and thin, that they will collapse, forming a so-called 'bird's nest' structure on top of the oxide film (Fig. 2.14 m-o).

2.4.3.5 Electrolyte

In addition to determining the type and extent of anion incorporation, the nature of the electrolyte will also affect the geometrical dimensions of the oxide [85]. Moreover, similarly to a higher anodizing temperate, the nature and concentration of the electrolyte will determine the rate of oxide dissolution. Upon extended anodizing times, aggressive electrolytes will cause excessive chemical dissolution. Since the oxide is only growing from within the metal, the outer part of the film is in contact with eh electrolyte for a longer time period and therefore suffers from the most chemical attack. This phenomenon induces pore widening at the outer surface, which affects the general shape of the pores. In aggressive electrolytes, pores become cone-shaped, having a larger diameter at the surface. As previously discussed and shown in Fig. 2.13, in extreme cases this excessive dissolution may lead to a collapse of the top structure and the creation of a structure that resembles a 'bird's nest'.

2.4.3.6 Alloy composition

The presence of alloying elements has an effect on the anodizing potential, as well as the oxide morphology. Since elements in solid solution will change the resistance to current flow, the purer the aluminium, the more resistance to ionic transport [94].
It is generally also observed that the same process conditions can yield completely different forms of anodic films on bare and clad substrates. Fig. 2.15 shows a comparison between the CAA 40/50V anodic oxide on clad and bare AA20204-T3. The high purity clad alloy shows a relatively regular columnar structure while no evidently regular structure is observed on the bare substrate, which resembles a sponge-like structure. This difference is attributed to the presence of second phase particles and alloying elements with a different potential than that of the matrix [27, 95, 96]. Alloying elements with more negative potential will oxidize with aluminium and enter the anodic oxide, while nobler alloying elements like Cu do not. Cu concentration will then rise, leading to enrichment at the metal/oxide interface, immediately beneath the oxide film [97, 98]. It has been shown by Garcia-Vergara et.al [99] that cyclic oxidation of copper in the enriched layer below the barrier layer results in oxygen generation that leads to gas evolution and lateral porosity, resulting in the irregular anodic oxide structure that is produced on

bare A2024-T3. Correspondingly, similar process conditions may lead to different oxide weight and morphology on different aluminium alloys.

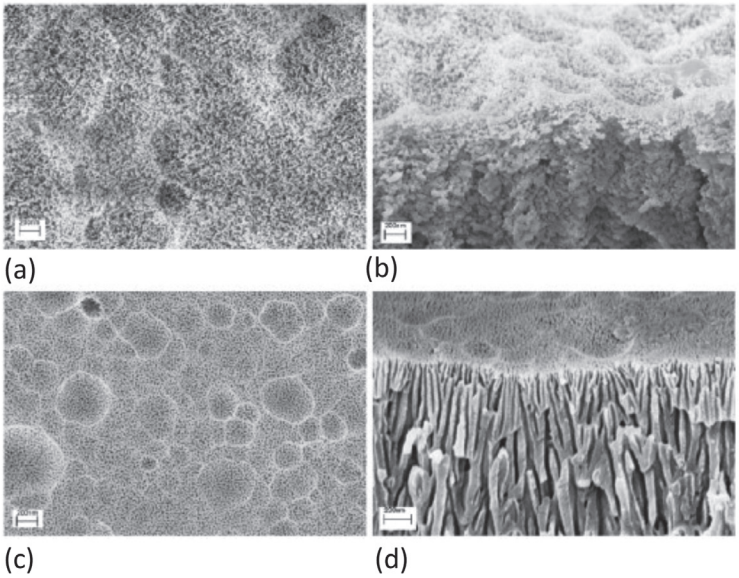

Figure 2.15: CAA 40/50 V processed, 2024-T3 bare: plan view (a) and cross-section (b), 2024-T3 clad: plan view (c) and cross-section (d). Reprinted from [27].

2.5 Cr(VI)-free alternatives to CAA

Health and environmental issues, together with the increasing costs associated with the treatment and disposal of solutions containing hexavalent chromium initiated a large number of studies over the past decades. More often than not, researchers applied commercial products, evaluating their success by a comparison to the chromate-based benchmark (FPL etch or CAA). As understood from the previous section, these pre-treatments are often sensitive to changes in the processing conditions, including the use of different alloys. To avoid an exhaustive comparison of the different process parameters, this section will focus on the methods rather than specific outcomes of the most relevant alternative Cr(VI)- free pre-treatments for structural adhesive bonding. For a detailed list of the specific pre-treatments and evaluation techniques, readers are encouraged to consult the review published by Critchlow and Brewis [39].

2.5.1 Mixed electrolytes anodizing

The most popular alternative electrolytes are phosphoric- and sulphuric acids. As mentioned earlier, phosphoric acid anodizing (PAA) which is used by Boeing typically creates a thinner and very porous oxide layer that is suitable for adhesion, but is lacking sufficient corrosion resistance and, hence, requires the application of an active corrosion

inhibiting primer. Conversely, sulphuric acid anodizing (SAA) that is used for decorative and corrosion protection applications produces a thick and dense oxide films that result in poor bonding with the primer/adhesive [100]. Additionally, the high relative weights of these thick coatings render their fatigue resistance, and poor durability is reported in hot and humid environments. A possible method to overcome these limitations is to mix the two acids in the anodizing bath. The resulting process, named phosphoric-sulphuric acid (PSA) anodizing was developed by Kock et al. [101]. The first PSA process contains equal amounts of sulphuric- and phosphoric acids (100 g/l), yielding a morphology that is similar to CAA. However, similarly to PAA, the PSA oxide cannot be sealed by hot water treatment.

Recent investigations at the Adhesion Institute of Delft, together with NLR and Fokker covered a broad range of process parameters: different concentrations, together with various temperature, time and aging conditions, were investigated in the search for the optimal PSA conditions [102-105]. According to the final structure, and industrial adhesion and corrosion tests, modified conditions were chosen for further development on a commercial scale with all different types of alloys.

Alternatively, a mixture of tartaric and sulphuric acid anodizing (TSA) was suggested by Kape [106] in the 1960s. Unfortunately, the resulting porosity is relatively low and adhesives cannot easily permeate into the oxide layer. Hence, the process is mainly used in non-structural applications. The role of tartaric acid, according to a study by Curioni et al. [107] is reducing the current density and thereby reducing the oxide growth rate, so that the of the final film thickness is lower than for normal SAA. More interestingly, however, a resulted improved corrosion resistance is observed. This resistance is explained by a "buffering effect" that tartarate ions remnants are providing. During anodizing, tartaric acid can combine with aluminium cations to produce aluminium tartrate, a compound that is highly soluble in the acidic anodizing solution but with relatively low solubility in water. During subsequent rinsing, the pH is rapidly increased and relatively large amounts of aluminium tartrate may precipitate at the pore walls. As a consequence, if the oxide is exposed to a corrosive environment during its use, aluminium tartrate may re-dissolve, producing a local buffer, thereby limiting the susceptibility to localized corrosion. Relying on this TSA advantage, a combination of PSA and TSA anodizing was suggested by Kock [108]. The resulting structure shown in Fig. 2.16 is reported to be suitable for structural components.

Another process is the boric-sulphuric acid anodizing (BSAA) that has been patented by Boeing as an alternative to CAA [109]. The oxide structure resembles SAA, but with finer pores and more uniform hexagonal arrangement compared to CAA, showing promising results [110]. Zhang et al. [82] report an improvement in bonding and durability of panels created by the BSAA process by the addition of phosphoric acid to the anodizing electrolyte. The process is reported to result in bigger pores, improving

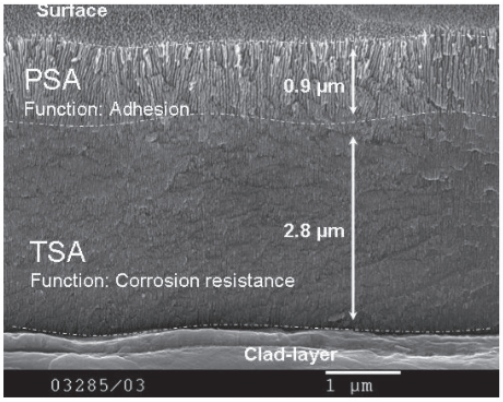

Figure 2.16: Cross section of the anodic oxide produced by TSA+PSA process on 2024-T3 clad [108]

primer penetration and extending oxide durability. However, since boric acid is also hazardous, using it as a replacement is less favourable.

2.5.2 Electrolytic deoxidation

As mentioned earlier, Venables [28] assigned the fine oxide protrusions produced by the FPL etch on top of the PAA oxide for the high strength. This is considered desired from adhesion point of view, where such protrusions, even at the nanometre scale, can interlock with the resin to create an additional reinforcement. Likewise, Yendall and Critchlow [27] suggests a method that applies electrolytic phosphoric acid deoxidizer (EPAD) before anodizing. In that respect EPAD replaces the FPL etch in producing an open top layer that comes into contact with primer/adhesive (Fig. 2.17). They found that this method improves the mechanical properties of the bond depending, however, also on the anodizing temperature used for SAA.

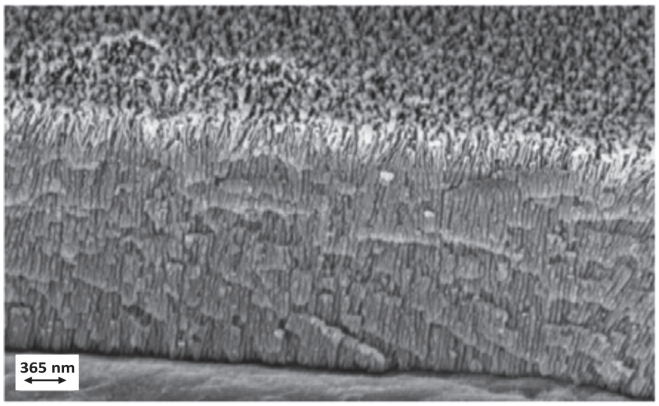

Figure 2.17 Cross section of AA2024-T3 clad after EPAD and SAA [27].

2.5.3 AC Anodizing

An interesting alternative applies alternating current (AC) instead of the traditional direct current (DC) for anodizing. AC anodizing was originally developed for high-speed coil applications in the automotive industry. Relatively elastic oxide layers are developed by treatment at higher temperatures and higher anodizing currents. Both sulphuric- and phosphoric acid processes have been reported, with the conditions listed in Table 2.4. Though developed as a continuous process, batch operation is also possible.

Table 2.4 Anodizing parameters [111].

Parameter	H_3PO_4	H_2SO_4
Acid concentration, wt.%	10	15
Temperature, °C	50	80
Time, min.	12	30
Current, A/dm^2	4	10

As in other AC processes, hydrogen evolves on the surface of the anode during the cathodic cycle. This is sufficient to remove organic contaminants and the natural oxides, so that separate steps for cleaning and deoxidizing prior to anodizing are not required, drastically reducing the amount of tanks needed [111]. Since the resulted oxides are thin, their performance is comparable to the etching rather than anodic oxides [112]. Hence, in a U.S. patent by Critchlow et al. [113] suggested a method for the formation of a duplex oxide film by applying a two-step process that includes subsequent AC and DC anodizing in the same bath. This combination produces an oxide film that has a thin porous outer layer (less than 1 μm) and a relatively thick (up to 8 μm) uniform inner layer to yield an optimal combination of corrosion protection by the inner barrier layer, and adhesion provided by the porous outer layer. The electrolyte solution contains equal ratios of phosphoric and sulphuric acids.

2.5.4 Anodizing with post-treatments

Alternatively, a post-treatment immersion of the relatively dense anodic oxide in a dilute acidic or alkaline solution will chemically attack the oxide to partly dissolve it and open the pores to produce the desired morphology. Both Arrowsmith and Clifford [114] and Yendall and Critchlow [27] applied phosphoric acid dip after SAA (or BSAA) anodizing to report an improved short and long-term durability. The narrow pores close to the substrate are considered to provide the corrosion resistance, while the etched top layer is able to interlock with the primer/adhesive. The time, nature and concentration of the etching solution is important to control, in order to avoid over-etching [115]. Such post-anodizing step is not new to the aviation industry, which frequently applies post-

anodizing immersion in boiling water to seal the porous oxide layer when it serves as a protective coating against corrosion and not as a receptive surface for bonding.
An interesting alternative to a post-treatment dip concerns anodizing combining positive and small-negative voltages. The negative charge at the end of the normal anodizing cycle causes the dissolution of the oxide by hydrogen ions that are attracted to the temporary negative pole [116]. In this case, the dissolution is done in the same bath as anodizing, reducing the need for an extra process and rinsing bath.

2.5.5 Non-anodizing processes

As previously mentioned, immersion in hot water is often used to seal off the anodic pores. Treatment in boiling water (and even water at 40 and 50 °C, [117]) leads to hydration of the aluminium and changes from an Al_2O_3 to a pseudoboehemite (AlOOH) type oxide structure. Although sealing the pores is not desired from a bonding perspective, boiling water treatment has been suggested as a stand-alone treatment to replace anodizing. The hydrated form of oxide has been reported to provide many benefits, besides it being an inexpensive alternative: a highly-porous morphology with a large surface area [118], increased number of surface hydroxyl groups [119] and a low contact angle [120]. Oxide morphology will depend on the temperature and the duration of the treatments. Three representative morphologies are presented in Fig. 2.18. After just 30 s of immersion the surface oxide exhibits a cellular structure with thin ridges (approx. 10 nm wide) that provide large porosity. As the treatment time is extended, cell walls develop into distinct plates (of increased thickness) that are oriented normal to the surface. When the time is extended up to 4 hours, the cell walls significantly thickness, producing a distinctive and much less porous structure [121]. Unfortunately, this type of oxide is brittle and, mechanical tests often show an early cohesive failure within this pseudoboehemite layer [118, 120]. Although in some cases, the combination of prior grit blasting and the addition of a silane layer was shown to reproduce results comparable to the benchmark

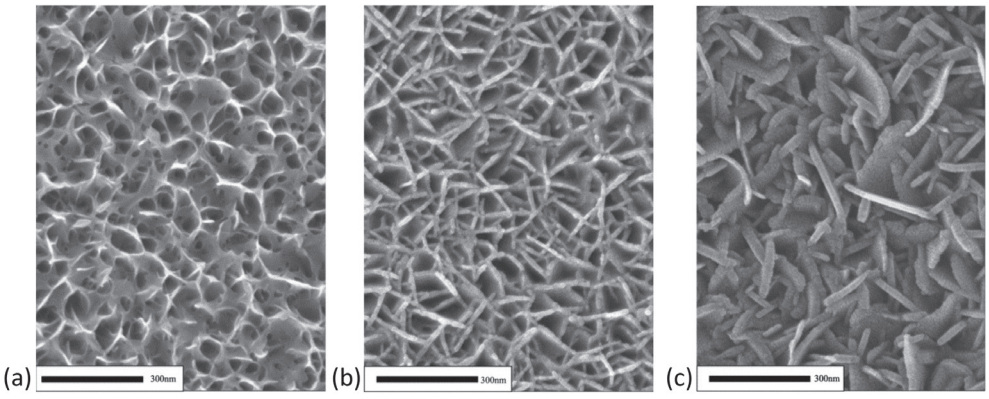

Figure 2.18: High-resolution SEM micrograph after boiling water treatment on AA2024-T3 clad for 30 s (a), 60 min (b) and 240 min (c), figure edited from [121].

used (CSA+PAA), its level of success is highly sensitive to alloy composition [121]. Hence, it generally does not compare with the durability of anodized-based oxide layers.

A similar option consists of a steam treatment [122, 123]. Studies have shown that oxide layers with thicknesses comparable to the anodic oxide can be produced (from a few nanometre up to 3 μm), depending on treatments parameters and steam chemistry. The addition of acidic components (citric or phosphoric acids) to the steam enables the growth of thicker layers and help in the corrosion protection (especially due to incorporation of phosphates) [124].

2.6 Conclusions

The corrosion sensitivity of aerospace aluminum alloys, together with the required bond performance and durability, have led to the development of a multi-step pre-treatment process that is carefully designed to minimize the effect of the heterogeneous nature of the metal surface and provide the desired surface characteristics for bonding and corrosion resistance. In this pretreatment, hexavalent chromium currently takes crucial role, generally being incorporated in every major step of the process.
The importance of finding a replacement for hexavalent chromium is evident by the large amount of literature available on this subject. It is, however, also clear that the success and versatility of chromate application is one that is very difficult to duplicate. Although there have been many claims for chromate free alternatives, as of yet, there aren't any complete chromate free functioning systems which meet the specifications that have been set by chromate processes.
It appears that the main aim in the development of Cr(VI)-free processes so far is to reproduce the CAA morphological features using different chemicals. One of the main challenges is to provide a high level of corrosion resistance with no Cr(VI). Consequently, many studies combine the production of an open structure at the outer layer that will be receptive for the primer or adhesives, while providing enough corrosion protection by a dense inner layer and thick barrier layer. The fact that both adsorption and mechanical forces are declared important for adhesion in structural bonds is not yet reflected in practical research. It is therefore of great interest to understand how these two adhesion mechanisms contribute to the final bond performance.

2.7 References

1. ATSDR, *Toxicologica Profile for Chromium*, P.H.S. U.S. Department of Health and Human Services, Editor. 2012: Atlanta, GA.
2. Alexander, B.H., et al., *Lung Cancer in Chromate-Exposed Aerospace Workers.* Journal of Occupational and Environmental Medicine, 1996. **38**(12): p. 1253-1258.
3. OSHA, *Toxic and Hazardous Substances* in *Occupational Exposure to Hexavalent Chromium*. 2006, United States Department of Labor.
4. Ebnesajjad, S., *1 - Introduction and Adhesion Theories*, in *Handbook of Adhesives and Surface Preparation*, S. Ebnesajjad, Editor. 2011, William Andrew Publishing: Oxford. p. 3-13.
5. Brockmann, W., et al., *Adhesive Bonding*. 2009: Wiley-VCH Verlag GmbH & Co. KGaA. I-XVIII.
6. Bishopp, J., *13 - Adhesives for Aerospace Structures*, in *Handbook of Adhesives and Surface Preparation*, S. Ebnesajjad, Editor. 2011, William Andrew Publishing: Oxford. p. 301-344.
7. Potter, D.L., *Primary Adhesively Bonded Structure Technology (PABST). Design Handbook for Adhesive Bonding*. 1979, Douglas Aircraft Co Long Beach Ca.
8. Higgins, A., *Adhesive bonding of aircraft structures.* International Journal of Adhesion and Adhesives, 2000. **20**(5): p. 367-376.
9. Marshall, S.J., et al., *A review of adhesion science.* Dental Materials, 2010. **26**(2): p. e11-e16.
10. Lyle, J.P., D.A. Granger, and R.E. Sanders, *Aluminum Alloys*, in *Ullmann's Encyclopedia of Industrial Chemistry*. 2000, Wiley-VCH Verlag GmbH & Co. KGaA.
11. Hughes, A.E., et al., *High Strength Al-Alloys: Microstructure, Corrosion and Principles of Protection*, in *Recent Trends in Processing and Degradation of Aluminium Alloys*, Z. Ahmad, Editor. 2011, InTech. p. 223-262.
12. Boag, A., et al., *How complex is the microstructure of AA2024-T3?* Corrosion Science, 2009. **51**(8): p. 1565-1568.
13. Afseth, A. 1999, NTNU Trondheim: Norway.
14. Yu, Q.S., et al., *Improved Corrosion Protection of Aluminum Alloys by System Approach Interface Engineering: Part 2—AA2024-T3.* Corrosion, 2000. **56**(9): p. 887-900.
15. Moffitt, C.E., D.M. Wieliczka, and H.K. Yasuda, *An XPS study of the elemental enrichment on aluminum alloy surfaces from chemical cleaning.* Surface and Coatings Technology, 2001. **137**(2–3): p. 188-196.
16. Zhou, X., et al., *Near-Surface Deformed Layers on Rolled Aluminum Alloys.* Metallurgical and Materials Transactions A, 2011. **42**(5): p. 1373-1385.
17. Brockmann, W., et al., *Adhesion in bonded aluminium joints for aircraft construction.* International Journal of Adhesion and Adhesives, 1986. **6**(3): p. 115.
18. Packham, D.E., *Work of adhesion: contact angles and contact mechanics.* International Journal of Adhesion and Adhesives, 1996. **16**(2): p. 121-128.
19. Kollek, H., *Some aspects of chemistry in adhesion on anodized aluminium.* International Journal of Adhesion and Adhesives, 1985. **5**(2): p. 75-80.
20. van den Brand, J., et al., *Interaction of Ester Functional Groups with Aluminum Oxide Surfaces Studied Using Infrared Reflection Absorption Spectroscopy.* Langmuir, 2004. **20**(15): p. 6318-6326.

21. Fauquet, C., et al., *Adsorption of monoethanolamine on clean, oxidized and hydroxylated aluminium surfaces: a model for amine-cured epoxy/aluminium interfaces.* Applied Surface Science, 1994. **81**(4): p. 435-441.
22. Packham, D., *Theories of Fundamental Adhesion*, in *Handbook of Adhesion Technology*, L.M. da Silva, A. Öchsner, and R. Adams, Editors. 2011, Springer Berlin. p. 9-38.
23. Israelachvili, J.N., *Intermolecular and Surface Forces* Third Edition ed. 2011, San Diego: Academic Press.
24. Packham, D.E. *The mechanical theory of adhesion - A seventy year perspective and its current statuis*. in *First International Congress on Adhesion Science and Technology*. 1995. Amsterdam: VSP.
25. McBain, J.W. and D.G. Hopkins, *On Adhesives and Adhesive Action.* The Journal of Physical Chemistry, 1925. **29**(2): p. 188-204.
26. Rider, A.N., C.L. Olsson-Jacques, and D.R. Arnott, *Influence of adherend surface preparation on bond durability.* Surface and Interface Analysis, 1999. **27**(12): p. 1055-1063.
27. Yendall, K.A. and G.W. Critchlow, *Novel methods, incorporating pre- and post-anodising steps, for the replacement of the Bengough–Stuart chromic acid anodising process in structural bonding applications.* International Journal of Adhesion and Adhesives, 2009. **29**(5): p. 503-508.
28. Venables, J.D., et al., *Oxide morphologies on aluminum prepared for adhesive bonding.* Applications of Surface Science, 1979. **3**(1): p. 88-98.
29. Packham, D.E., *Theories of Fundamental Adhesion*, in *Handbook of Adhesion Technology*, L.F.M. Da Silva, A. Öchsner, and R.D. Adams, Editors. 2011, Springer-Verlag: Berlin Heidelberg.
30. Awaja, F., et al., *Adhesion of polymers.* Progress in Polymer Science, 2009. **34**(9): p. 948-968.
31. Sheasby, P.G. and R. Pinner, *Surface Treatment and Finishing of Aluminium and its Alloys*. 6th ed. 2001., England: Finishing Publications Ltd.
32. Sukiman, N.L., et al., *Durability and Corrosion of Aluminium and Its Alloys: Overview, Property Space, Techniques and Developments*, in *Aluminium Alloys - New Trends in Fabrication and Applications*. 2012, InTech. p. 47- 97.
33. Boag, A., et al., *Corrosion of AA2024-T3 Part I: Localised corrosion of isolated IM particles.* Corrosion Science, 2011. **53**(1): p. 17-26.
34. Hughes, A.E., et al., *Corrosion of AA2024-T3 Part II: Co-operative corrosion.* Corrosion Science, 2011. **53**(1): p. 27-39.
35. Glenn, A.M., et al., *Corrosion of AA2024-T3 Part III: Propagation.* Corrosion Science, 2011. **53**(1): p. 40-50.
36. Sargent, J.P., *Durability studies for aerospace applications using peel and wedge tests.* International Journal of Adhesion and Adhesives, 2005. **25**(3): p. 247-256.
37. Zanni-Deffarges, M.P. and M.E.R. Shanahan, *Diffusion of water into an epoxy adhesive: comparison between bulk behaviour and adhesive joints.* International Journal of Adhesion and Adhesives, 1995. **15**(3): p. 137-142.
38. Posner, R., O. Ozcan, and G. Grundmeier, *Water and Ions at Polymer/Metal Interfaces*, in *Design of Adhesive Joints Under Humid Conditions*, M.L.F. Silva and C. Sato, Editors. 2013, Springer Berlin Heidelberg: Berlin, Heidelberg. p. 21-52.

39. Critchlow, G.W. and D.M. Brewis, *Review of surface pre-treatments for aluminium alloys.* International Journal of Adhesion and Adhesives, 1996. **16**(4): p. 255-275.
40. Wegman, R.F. and J. Van Twisk, *2 - Aluminum and Aluminum Alloys*, in *Surface Preparation Techniques for Adhesive Bonding (Second Edition)*, R.F. Wegman and J.V. Twisk, Editors. 2013, William Andrew Publishing. p. 9-37.
41. Pocius, A.V., *The Electrochemistry of the FPL (Forest Products Laboratory) Process and its Relationship to the Durability of Structural Adhesive Bonds.* The Journal of Adhesion, 1992. **39**(2-3): p. 101-121.
42. Carter, E.A., *High current anodization of magnesium and magnesium alloys*. 1996, The University of Auckland.
43. Su, Z. and W. Zhou, *Porous Anodic Metal Oxides.* Science Foundation in China, 2008. **16**(1): p. 36.
44. Thompson, G.E., *Porous anodic alumina: fabrication, characterization and applications.* Thin Solid Films, 1997. **297**: p. 192-201.
45. O'Sullivan, J.P. and G.C. Wood, *Morphology and mechanism of formation of porous anodic films on aluminum.* Proceedings of the Royal Society of London Series A - Mathematical and Physical Sciences, 1970. **317**: p. 511-543.
46. Setoh, S. and A. Miyata, Sci. Pap. Inst. Phys. Chem. Res., 1932. **189**.
47. Keller, F., M.S. Hunter, and D.L. Robinson, *Structureal features of oxide coatings on aluminum.* Journal of The Electrochemical Society, 1953. **100**: p. 411-419.
48. Wernick, S., R. Pinner, and P.G. Sheasby, *The surface treatment and finishing of aluminium and its alloys*. 5 ed. Vol. 1. 1987, Ohio and Middlesex: ASM International and Finishing Publications LTD.
49. Critchlow, G.W., et al., *Strategies for the replacement of chromic acid anodising for the structural bonding of aluminium alloys.* International Journal of Adhesion and Adhesives, 2006. **26**(6): p. 419-453.
50. Brockmann, W., O.D. Hennemann, and H. Kollek, *Surface properties and adhesion in bonding aluminium alloys by adhesives.* International Journal of Adhesion and Adhesives, 1982. **2**(1): p. 33-40.
51. Oosting, R., *Toward a new durable and environmentally compliant adhesive bonding process for aluminum alloys*. 1995, Delft University of Technology: The Netherlands
52. Park, S.Y., et al., *Recent Trends in Surface Treatment Technologies for Airframe Adhesive Bonding Processing: A Review (1995–2008).* The Journal of Adhesion, 2010. **86**(2): p. 192-221.
53. Hughes, A.E., et al., *Designing green, self-healing coatings for metal protection.* NPG Asia Mater, 2010. **2**: p. 143-151.
54. Marceau, J.A., R.H. Firminhac, and Y. Moji, *Method for providing environmentally stable aluminum surfaces for adhesive bonding and product produced*. 1978, Google Patents.
55. Kinloch, A.J., L.S. Welch, and H.E. Bishop, *The Locus of Environmental Crack Growth in Bonded Aluminium Alloy Joints.* The Journal of Adhesion, 1984. **16**(3): p. 165-177.
56. McGarel, W., H.A. Farnham, and R. McGuckin, *Influence of pre-treatment rinse waters on the durability of adhesive-bonded aluminium alloys.* International Journal of Adhesion and Adhesives, 1986. **6**(2): p. 89-92.
57. Olsson-Jacques, C.L., et al., *Effect of Contaminant on the Durability of Epoxy Adhesive Bonds with Alclad 2024 Aluminium Alloy Adherends.* Surface and Interface Analysis, 1996. **24**(9): p. 569-577.

58. Kinloch, A.J., M.S.G. Little, and J.F. Watts, *The role of the interphase in the environmental failure of adhesive joints.* Acta Materialia, 2000. **48**(18–19): p. 4543-4553.
59. G. Pape, P., *15 - Adhesion Promoters*, in *Handbook of Adhesives and Surface Preparation*, S. Ebnesajjad, Editor. 2011, William Andrew Publishing: Oxford. p. 369-386.
60. Abel, M.-L., et al., *Evidence of specific interaction between γ-glycidoxypropyltrimethoxysilane and oxidized aluminium using high-mass resolution ToF-SIMS.* Surface and Interface Analysis, 2000. **29**(2): p. 115-125.
61. Tchoquessi Doidjo, M.R., et al., *Influence of silane-based treatment on adherence and wet durability of fusion bonded epoxy/steel joints.* Progress in Organic Coatings, 2013. **76**(12): p. 1765-1772.
62. Ooij, W., et al., *Overview: The Potential of silanes for chromate replacement in metal finishing industries.* Silicon Chemistry, 2006. **3**(1-2): p. 11-30.
63. Thiedmanu, W., et al., *Silane Coupling Agents as Adhesion Promoters for Aerospace Structural Film Adhesives.* The Journal of Adhesion, 1987. **22**(3): p. 197-210.
64. Cabral, A., et al., *Analytical characterisation and corrosion behaviour of bis-[triethoxysilylpropyl] tetrasulphide pre-treated AA2024-T3.* Corrosion Science, 2005. **47**(3): p. 869-881.
65. Cabral, A.M., et al., *A comparative study on the corrosion resistance of AA2024-T3 substrates pre-treated with different silane solutions: Composition of the films formed.* Progress in Organic Coatings, 2005. **54**(4): p. 322-331.
66. Song, J. and W.J. Van Ooij, *Bonding and corrosion protection mechanisms of γ-APS and BTSE silane films on aluminum substrates.* Journal of Adhesion Science and Technology, 2003. **17**(16): p. 2191-2221.
67. Franquet, A., H. Terryn, and J. Vereecken, *Study of the effect of different aluminium surface pre-treatments on the deposition of thin non-functional silane coatings.* Surface and Interface Analysis, 2004. **36**(8): p. 681-684.
68. Clark, W.J., et al., *A Galvanic Corrosion Approach to Investigating Chromate Effects on Aluminum Alloy 2024-T3.* Journal of The Electrochemical Society, 2002. **149**(5): p. B179-B185.
69. Frankel, G.S. and R.L. McCreery, *Inhibition of Al Alloy Corrosion by Chromates.* The Electrochemical Society Interface, 2001. **10**(4): p. 34-40.
70. Thompson, G.E., *Porous anodic alumina: fabrication, characterization and applications.* Thin Solid Films, 1997. **297**(1–2): p. 192-201.
71. Aerts, T., I. De Graeve, and H. Terryn, *Anodizing of aluminium under applied electrode temperature: Process evaluation and elimination of burning at high current densities.* Surface and Coatings Technology, 2010. **204**(16–17): p. 2754-2760.
72. Sulka, G.D., *Highly Ordered Anodic Porous Alumina Formation by Self-Organized Anodizing*, in *Nanostructured Materials in Electrochemistry*. 2008, Wiley-VCH Verlag GmbH & Co. KGaA. p. 1-116.
73. Skeldon, P., et al., *A Tracer Study of Porous Anodic Alumina.* Electrochemical and Solid-State Letters, 2006. **9**(11): p. B47-B51.
74. Garcia-Vergara, S.J., et al., *Stress generated porosity in anodic alumina formed in sulphuric acid electrolyte.* Corrosion Science, 2007. **49**(10): p. 3772-3782.
75. Garcia-Vergara, S.J., et al., *Compositional Evidence for Flow in Anodic Films on Aluminum under High Electric Fields.* Journal of The Electrochemical Society, 2007. **154**(9): p. C540-C545.

76. Terryn, H., *Electrochemical investigation of AC electrograining of aluminium and its porous anodic oxidation*, in *Facultiet Toegepaste Wetenschappen, Dienst Metallurgie*. 1987, Vrije Universiteit Brussel: Brussel.
77. Parkhutik, V.P., *The initial stages of aluminium porous anodization studied by Auger electron spectroscopy.* Corrosion Science, 1986. **26**(4): p. 295-310.
78. Xu, Y., et al., *Anion incorporation and migration during barrier film formation on aluminium.* Corrosion Science, 1987. **27**(1): p. 83-102.
79. González-Rovira, L., et al., *Direct sub-nanometer scale electron microscopy analysis of anion incorporation to self-ordered anodic alumina layers.* Corrosion Science, 2010. **52**(11): p. 3763-3773.
80. Ono, S., H. Ichinose, and N. Masuko, *The high resolution observation of porous anodic films formed on aluminum in phosphoric acid solution.* Corrosion Science, 1992. **33**(6): p. 841-850.
81. Thompson, G.E. and G.C. Wood, *5 - Anodic Films on Aluminium*, in *Treatise on Materials Science and Technology*, S. J.C, Editor. 1983, Elsevier. p. 205-329.
82. Zhang, J.-s., et al., *The bonding strength and corrosion resistance of aluminum alloy by anodizing treatment in a phosphoric acid modified boric acid/sulfuric acid bath.* Surface and Coatings Technology, 2008. **202**(14): p. 3149-3156.
83. Alexander, M.R., G.E. Thompson, and G. Beamson, *Characterization of the oxide/hydroxide surface of aluminium using x-ray photoelectron spectroscopy: a procedure for curve fitting the O 1s core level.* Surface and Interface Analysis, 2000. **29**(7): p. 468-477.
84. van den Brand, J., et al., *Interaction of Anhydride and Carboxylic Acid Compounds with Aluminum Oxide Surfaces Studied Using Infrared Reflection Absorption Spectroscopy.* Langmuir, 2004. **20**(15): p. 6308-6317.
85. Keller, F., M.S. Hunter, and D.L. Robinson, *Structural Features of Oxide Coatings on Aluminum.* Journal of The Electrochemical Society, 1953. **100**(9): p. 411-419.
86. Wood, G.C. and J.P. O'Sullivan, *The anodizing of aluminium in sulphate solutions.* Electrochimica Acta, 1970. **15**(12): p. 1865-1876.
87. Patermarakis, G. and K. Moussoutzanis, *Transformation of porous structure of anodic alumina films formed during galvanostatic anodising of aluminium.* Journal of Electroanalytical Chemistry, 2011. **659**(2): p. 176-190.
88. Curioni, M., P. Skeldon, and G.E. Thompson, *Anodizing of Aluminum under Nonsteady Conditions.* Journal of The Electrochemical Society, 2009. **156**(12): p. C407-C413.
89. Han, X.Y. and W.Z. Shen, *Improved two-step anodization technique for ordered porous anodic aluminum membranes.* Journal of Electroanalytical Chemistry, 2011. **655**(1): p. 56-64.
90. Aerts, T., et al., *Influence of the anodizing temperature on the porosity and the mechanical properties of the porous anodic oxide film.* Surface and Coatings Technology, 2007. **201**(16–17): p. 7310-7317.
91. Stępniowski, W.J. and Z. Bojar, *Synthesis of anodic aluminum oxide (AAO) at relatively high temperatures. Study of the influence of anodization conditions on the alumina structural features.* Surface and Coatings Technology, 2011. **206**(2-3): p. 265-272.
92. Aerts, T., et al., *Comparison between the influence of applied electrode and electrolyte temperatures on porous anodizing of aluminium.* Electrochimica Acta, 2010. **55**(12): p. 3957-3965.

93. Schneider, M., et al., *Interplay between parameter variation and oxide structure of a modified PAA process.* Surface and Interface Analysis, 2013. **45**(10): p. 1503-1509.
94. Zaraska, L., et al., *Porous anodic alumina formed by anodization of aluminum alloy (AA1050) and high purity aluminum.* Electrochimica Acta, 2010. **55**(14): p. 4377-4386.
95. Curioni, M. and F. Scenini, *The Mechanism of Hydrogen Evolution During Anodic Polarization of Aluminium.* Electrochimica Acta, 2015. **180**: p. 712-721.
96. Curioni, M., et al., *Macroscopic and Local Filming Behavior of AA2024 T3 Aluminum Alloy during Anodizing in Sulfuric Acid Electrolyte.* Journal of The Electrochemical Society, 2008. **155**(8): p. C387-C395.
97. Schneider, M., O. Yezerska, and M.M. Lohrengel, *Anodic oxide formation on AA2024: electrochemical and microstructure investigation.* Corrosion Engineering, Science and Technology, 2008. **43**(4): p. 304-312.
98. Saenz de Miera, M., et al., *The behaviour of second phase particles during anodizing of aluminium alloys.* Corrosion Science, 2010. **52**(7): p. 2489-2497.
99. Garcia-Vergara, S.J., et al., *Influence of copper on the morphology of porous anodic alumina.* Corrosion Science, 2006. **48**(10): p. 2937-2946.
100. Arrowsmith, D.J. and A.W. Clifford, *Morphology of anodic oxide for adhesive bonding of aluminum.* International Journal of Adhesion and Adhesives, 1983. **3**(4): p. 193-196.
101. Kock, E., et al., *Verfahren zur anodischen oxidation*, E.P. Office, Editor. 1993.
102. de Regt, P.A. and A. van den Berg, *Phosphoric – Sulphuric Acid anodizing (Exploratory phase)*. 2002, Adhesion Institute, TU Delft.
103. Kwakernaak, A. and P.A. de Regt, *Phosphoric-Sulphuric Acid Anodising of AA7075-T6 Clad*. 2004, Adhesion Institute, TU Delft.
104. de Ruijter, C. and A. Kwakernaak, *Cost Reduction Glare part 2: Cost-effective and environmental friendly pre-treatment process PSA Test plan*. 2009, Adhesion Institute, TU Delft.
105. de Wit, F.M. and J. Sinke, *Cost Reduction Glare part 2: Cost-effective and environmental friendly pre-treatment process Results Phase 1*. 2012, Adhesion Institute, TU Delft.
106. Kape, J.M., Electroplating Met. Finish., 1961. **11**: p. 407-415.
107. Curioni, M., et al., *Role of Tartaric Acid on the Anodizing and Corrosion Behavior of AA 2024 T3 Aluminum Alloy.* Journal of The Electrochemical Society, 2009. **156**(4): p. C147-C153.
108. Kock, E. *Design of a novel anodic film to meet the requirements of aircraft applications*. in *Anodisation Workshop*. 2004. Bremen, Germany
109. Boeing, *Process Spec. Boric Acid -- Sulfuric Acid Anodizing, Revision D*. 2004, Boeing.
110. Domingues, L., et al., *Anodising of Al 2024-T3 in a modified sulphuric acid/boric acid bath for aeronautical applications.* Corrosion Science, 2003. **45**(1): p. 149-160.
111. Bjørgum, A., F. Lapique, and J. Walmsley, *AC anodising as pre-treatment prior to adhesive bonding of aluminium*. 2004, SINTEF Materials and Chemistry.
112. Critchlow, G.W., K.A. Yendall, and J. Lu, *Friendlier Surface Treatments – For Metals*, in *Society for Adhesion and Adhesives in conjunction with BASA*. 2007: London.
113. Critchlow, G., et al., *Anodising aluminum alloy*. 2011.

114. Arrowsmith, D.J. and A.W. Clifford, *A new pre-treatment for the adhesive bonding of aluminium.* International Journal of Adhesion and Adhesives, 1985. **5**(1): p. 40-42.
115. Digby, R.P. and D.E. Packham, *Pre-treatment of aluminium: topography, surface chemistry and adhesive bond durability.* International Journal of Adhesion and Adhesives, 1995. **15**(2): p. 61-71.
116. Chung, C.K., et al., *Effects of temperature and voltage mode on nanoporous anodic aluminum oxide films by one-step anodization.* Thin Solid Films, 2011. **520**(5): p. 1554-1558.
117. Underhill, P.R. and A.N. Rider, *Hydrated oxide film growth on aluminium alloys immersed in warm water.* Surface and Coatings Technology, 2005. **192**(2–3): p. 199-207.
118. Rider, A.N., *The influence of porosity and morphology of hydrated oxide films on epoxy-aluminium bond durability.* Journal of Adhesion Science and Technology, 2001. **15**(4): p. 395-422.
119. Özkanat, Ö., et al., *Scanning Kelvin Probe Study of (Oxyhydr)oxide Surface of Aluminum Alloy.* The Journal of Physical Chemistry C, 2011. **116**(2): p. 1805-1811.
120. Özkanat, Ö., et al., *Influence of pre-treatments and aging on the adhesion performance of epoxy-coated aluminum.* Surface and Coatings Technology, 2013. **215**(0): p. 260-265.
121. Rider, A.N. and D.R. Arnott, *Boiling water and silane pre-treatment of aluminium alloys for durable adhesive bonding.* International Journal of Adhesion and Adhesives, 2000. **20**(3): p. 209-220.
122. Din, R.U., et al., *Steam assisted oxide growth on aluminium alloys using oxidative chemistries: Part I Microstructural investigation.* Applied Surface Science, 2015. **355**: p. 820-831.
123. Din, R.U., M.S. Jellesen, and R. Ambat, *Steam assisted oxide growth on aluminium alloys using oxidative chemistries: Part II corrosion performance.* Applied Surface Science, 2015. **355**: p. 716-725.
124. Din, R.U., M.S. Jellesen, and R. Ambat, *Role of acidic chemistries in steam treatment of aluminium alloys.* Corrosion Science, 2015. **99**: p. 258-271.

CHAPTER 3

The role of acid-base properties in the interactions across the oxide-primer interface in aerospace applications

This chapter is published as a scientific paper:
Abrahami, S.T., Hauffman, T., de Kok, J.M.M., Terryn, H., and Mol, J.M.C.,
Surf. Interface Anal. (2016), 48(8): p. 712-720.

ABSTRACT

In the transition to environmentally friendly production, chromic acid anodizing (CAA) is being replaced by sulphuric acid (SAA), phosphoric acid (PAA) or phosphoric-sulphuric acid (PSA) anodizing. While it is known that using these acids leads to the incorporation of anions into the oxide, little is known on how they affect the nature of the oxide and how this, in turn, affect the interactions across the oxide-primer interface. In the current work we investigate these changes in the interactions, especially the acid-base bonding, across the interface as a function of the pre-treatment. To exclude contribution of surface roughness, oxides with no surface features were prepared in the above-mentioned anodizing solutions by stopping the oxide growth during the formation of the barrier layer. Treatments in alkaline solution and boiling water were also included. XPS and FTIR were first used to probe the acid-base properties of the oxide before its interactions with 4-ethylphenol (4-EP) and 4-hydroxybenzyl alcohol (4-HbA), were measured. These two molecules represent functional groups of phenolic-based thermoset resins with different acidities. Results show that both the pre-treatments and the choice of molecule play a role in the interactions across the interface. While 4-HbA showed no preference, thin films of 4-EP were not detected on oxides that were prepared in phosphoric acid.

3.1 Introduction

Various structures in the aerospace industry are manufactured by adhesive bonding of aluminium and its alloys, as it provides lightweight structures with a high fatigue resistance and good aerodynamic properties [1]. To perform successfully, the metal-adhesive assembly must form a strong and durable bond. This is typically achieved with a pre-treatment that modifies the aluminium surface, creating a porous anodic oxide with a thin barrier layer underneath [2].

Pre-treatments in the European aerospace industry are based on hexavalent chromium, Cr(VI), a highly carcinogenic substance. Recent international legislations require its replacement in the coming years. Candidate alternatives include *sulphuric acid-*, (SAA), *phosphoric acid-*, (PAA) and mixtures of *phosphoric-sulphuric acids* (PSA) for anodizing and alkaline solutions for etching. Up to now, most research efforts focused on controlling the film morphology, such as the pore diameter, oxide-, and barrier layer thickness. However, numerous studies [3-7] provide evidence for the significance of the oxide chemistry in the interfacial bonding with an organic coating.

Phenolic-based adhesives and primers are among the first synthetic compounds developed for bonding. These hot-cured resins set by a condensation reaction between phenol and formaldehyde, yielding 4-hydroxylbenzyl alcohol and water [8]. Due to an advantageous combination of high-strength, good temperature resistance and long-term stability, these longstanding formulations (e.g. Redux 101 primer, Redux 775) are still regularly used for metal-to-metal bonding in the aerospace industry [9]. Since most analysis techniques are not able to probe interactions at the buried interface, adhesion is often modelled by the adsorption of functional molecules representing the resin on the metal surfaces [4, 10, 11]. This type of measurements offers valuable information about bonding on a molecular level. Additionally, the adsorption of various molecules on different surface oxides provides an indication of the nature of the oxide, such as its activity and its acid-base properties [12].

In the current work we investigate the changes in the interactions, especially the acid-base bonding, across the interface as a function of the pre-treatment. To exclude the contribution of mechanical interlocking and surface roughness, oxides with no morphological features were prepared using anodizing in phosphoric, sulphuric and a mix of phosphoric and sulphuric acids by stopping the oxide growth during the formation of the barrier layer. The physical and chemical properties of these oxides, along with these of the oxides prepared by alkaline and boiling water immersion, were characterized by Fourier transform infrared (FTIR) and X-ray Photoelectron Spectroscopy (XPS). Next, the ability of these oxides to establish acid–base interactions with two types of phenol molecules were studied by means of FTIR. The two phenolic molecules, 4-ethylphenol (4-EP) and 4-hydroxybenzyl alcohol (4-HbA) represent two different components of a phenolic resin [13].

3.2 Experimental

3.2.1 Materials and Pre-treatments

Samples were cut from a 0.3 mm thick sheet of commercially pure aluminium (99.99%) and ultrasonically cleaned in ethanol. To remove imperfections and provide a flat substrate, specimens were electropolished. This was done after the substrate was etched in an aqueous solution of 25 g/L NaOH at 70 °C for 1 min., followed by rinsing for 15 s with deionized water and then ultrasonically rinsed for 3 additional minutes. The substrate was then electropolished in a solution of 80 vol.% (absolute) ethanol and 20 vol.% perchloric acid, at current density of 70mA/cm^2 and 10 °C for 6 min. Subsequently, it was rinsed according to procedure described above, dried with compressed air and stored in a sealed plastic bag. Later, each sample was given one of the pre-treatments listed in Table 3.1.

Table 3.1: Summary of the different surface pre-treatments.

Abbreviation	Pre-treatment	Conditions	Max. Voltage (V)	Estimated thickness (nm) [14]
PAA	Phosphoric Acid Anodizing	25g/l H_3PO_4 4s, *0.2A, RT	22 ± 6	26 ± 3
SAA	Sulphuric Acid Anodizing	10g/l H_2SO_4, 4s, *0.2A, RT	16 ± 6	27 ± 2
PSA	Phosphoric-Sulphuric Acid Anodizing	25g/l H_3PO_4 and10g/l H_2SO_4, 4s, *0.2A, RT	18 ± 4	24 ± 2
CAA	Chromic Acid Anodizing	40g/l CrO_3, 4s, *0.2A, RT	21 ± 10	35 ± 4
Alkaline	Alkaline immersion	25g/l NaOH, 30s, RT	-	2 ± 1
Hydrothermal	Boiling water immersion	Boiling (demi-) water, 30s	-	53 ± 13

*Corresponds to approx.10 mA/cm^2, RT = Room Temperature (22 °C ± 3)

Galvanostatic anodizing was performed in a three-electrode cell with two AA1050 cathodes. Current was applied with SM120-25 power-supply (Delta Elektronika) equipped with an Ethernet interface connection to monitor the cell voltage. After each of the described treatment steps, the substrate was thoroughly rinsed with de-ionized water and subsequently ultrasonically rinsed for 3 more minutes. Anodizing conditions

were pre-selected to yield featureless anodic oxides by stopping the oxide growth at the end of the part in which the voltage raised linearly with time, hence the part associated with barrier layer formation [1].

3.2.1.1 Molecular interactions across the metal/organic interface

Molecular interactions across the oxide-phenolic resin interface were modelled by the adsorption of phenolic molecules. After pre-treatments, the substrates were placed in a tetrahydrofuran (THF) solution containing 10 g/l of 4-EP or 4-hydroxylbenzyl alcohol (Sigma-Aldrich). These two molecules have methyl and alcohol end-groups Fig. 3.1 (a) and (b), respectively, with a different pKa values (pKa =10.3 and 15.2 for 4-EP and 4-HbA [14]). After 30 min of immersion, substrates were withdrawn from the solution and allowed to dry in the lab atmosphere for 3 minutes before they were analysed in the "*non-rinsed*" condition. Thereafter, the substrates were rinsed using a fresh THF solvent and dried before they were analysed in the "*rinsed*" condition.

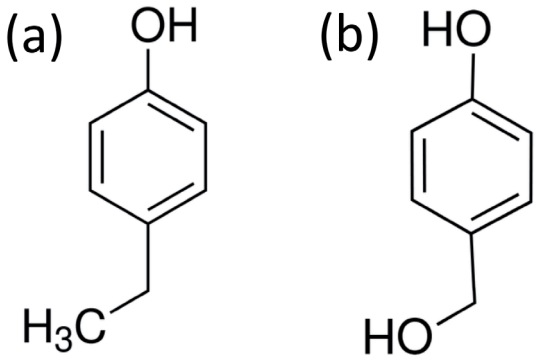

Figure 3.1: Chemical structure of (a) 4-ethylphenol and (b) 4-hydroxybenzyl alcohol.

3.2.2 Surface Characterization

3.2.2.1 X-Ray Photoelectron Spectroscopy

Normal XPS spectra were collected using a PHI5600 photoelectron spectrometer (Physical Electronics) with an Al *K*α monochromatic X-ray source (1486.71 eV of photons). To minimize ageing and contamination effects, samples were put in the pre-vacuum chamber no longer than 20 minutes after preparation.

The vacuum in the analysis chamber was approximately $5x10^{-9}$ Torr during measurements. High-resolution scans of the peaks were recorded at a take-off angle of 45°, using pass energy of 23.5 eV and 0.1 eV step size.

For the Auger parameter, X-ray excited photoelectron and Auger lines had to be generated in the same spectra. This was not possible for the Al contribution with the above-described equipment. Therefore, a PHI 5400 ESCA instrument with Mg (*K*α 1253.6 eV) X-ray source was applied. Using a Beryllium window, the Bremsstrahlung radiation [15] was generated to enable the detection of the high-energy Al(KLL) line. After a survey scan, high-resolution Al2p, O1s, C1s, S2p, P2s and O(KLL) and Al(KLL) photo- and Auger lines, respectively, were recorded at a take-off angle of 45°, constant analyser pass energy of 35.75 eV and step size of 0.2 eV.
XPS data was analysed with PHI Multipak software (V9.5.0.8). The energy scale of the spectra was calibrated relative to the binding energy of advantageous hydrocarbons (C-C/C-H) in the C1s peak at 284.4eV. Curve fitting and decomposition were performed after a Shirley-type background removal. A mixed Gauss (80–100%) – Lorentz shape for the different components was used.

3.2.2.2 Fourier-Transform Infrared Spectroscopy

FTIR spectra were obtained by Thermo-Nicolet Nexus FTIR apparatus, equipped with a liquid-nitrogen cooled MCT-A (mercury-cadmium-tellurium) detector and a SAGA grazing angle accessory at an incident angle of 80°C with respect to the normal of the surface. FTIR measurements of the bare oxides were conducted versus a background collected from an electropolished sample (which is the prior surface treatment step). Prior to adsorption, an infrared background spectrum was obtained from the freshly prepared oxide and the final spectra were measured against this background. Each spectrum is the average of 128 scans taken with a resolution of 4 cm^{-1}.

3.3 Results

3.3.1. Bare Anodic Oxides Characterization in FTIR

The FTIR spectra in Fig. 3.2 reveal the modifications of the aluminium surface as a result of the different pre-treatments. A summary of the bands and their assignments is also given in Table 3.2. All anodized samples show a strong band at 950 cm^{-1}. This results from stretching of the Al-O bond, originating from the thickened oxide layer. Additionally, small shoulders can be seen at 1143, 1158 and 1157 cm^{-1} for SAA, PSA and PAA oxides, respectively. These correspond to the stretching vibrations of the S-O and P-O bonds (or both), as a result of anion incorporation into the oxide [16, 17]. No such feature is observed for the CAA oxide.
The hydrothermal oxide appears intrinsically different from the anodic oxides. Bands are observed at 790, 1060, 1600 and 3430 cm^{-1}. The development of these bands indicates the hydration of the surface [18]. The bands at 790 and 1060 cm^{-1} are attributed to the Al-OH [19]. These bands are bending and twisting OH vibrations, respectively, and their positions are characteristic for a pseudoboehemite-type aluminium oxide. The

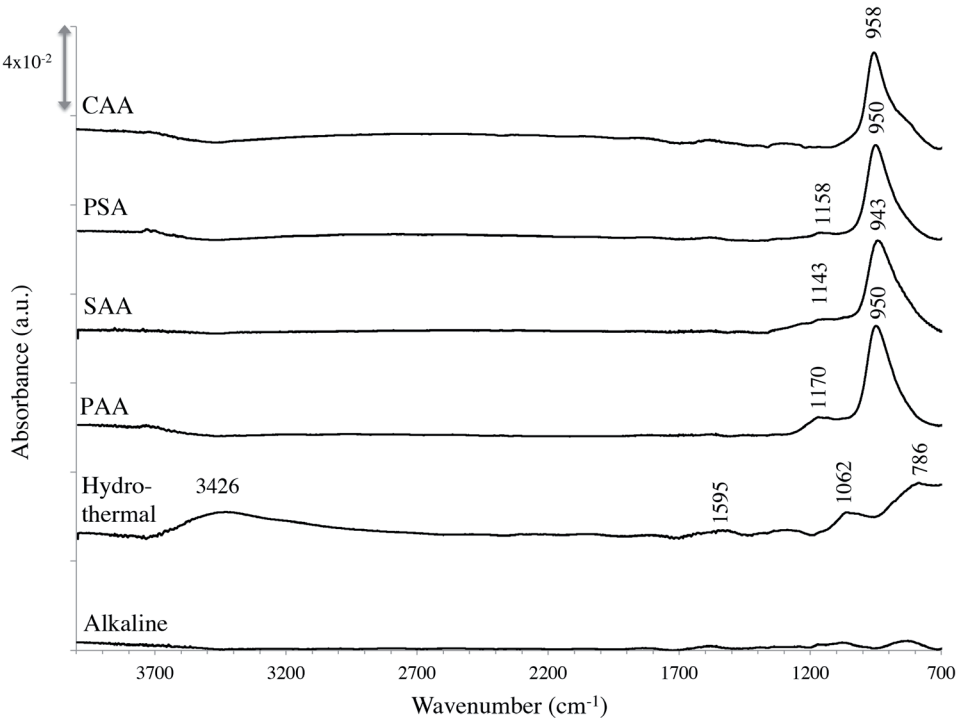

Figure 3.2: FTIR spectra of the bare oxides after pre-treatments (measured vs. the electropolished background).

presence of hydroxyls in this oxide is also evidenced from the development of the broad, asymmetric band at 3450 cm^{-1}. This band is partially due to the corresponding stretching vibrations of hydroxyls in AlO-H and partially due to the OH of water molecules [20]. Although the alkaline treatment seems to introduce no significant difference, minuscule bands at similar regions to those observed for the hydrothermal oxide can be seen.

It is striking that no hydroxyl bands can be distinguished for the anodised oxides, while these have been previously reported for porous anodic oxides [17]. This observation can be explained by Dorsey [19] who reported a shift of the Al-OH stretching band to lower frequencies (900-1000 cm^{-1}) in barrier anodic oxides. Hence, the presence of hydroxyls in these barrier-type oxides cannot be determined by FTIR.

Table 3.2: Infrared peak positions and assignments for the various infrared peaks.

Approx. infrared band position (cm-1)	Assignment
790	(OH) bend, aluminium oxyhydroxide region
950	(Al–O) stretch, aluminium oxide
1060 – 1070	(OH) twist, aluminium oxyhydroxide region
1140	(S–O) stretch
1170	(P–O) stretch
1390	(OH) bend, adsorbed contamination
1590 – 1650	Adsorbed water
3450	(OH) hydroxyl stretch, adsorbed water and aluminium oxyhydroxide region

3.3.2 Bare Anodic Oxides Characterization with XPS

XPS, being a surface-sensitive technique, can assist in the detection of more subtitle chemical changes at the top layers of the oxides, such as the presence of surface hydroxyls. These are reflected in the spectra showing the binding energy of the different atoms. A representative XPS survey spectrum is shown in Fig. 3.3 for a PSA oxide. Oxygen, aluminium and carbon are the main elements. These were also the major detected elements in all the other oxides. Phosphorus, sulphur and chromium were also detected in the relevant oxides. An example of a high-resolution XPS spectra of the O1s and the Al2p photopeaks from a PAA oxide is shown in Fig. 3.4. The binding energy (BE) and full-width at half-maximum (FWHM) of the envelope of these peaks at the different oxides are listed in Table 3.3.

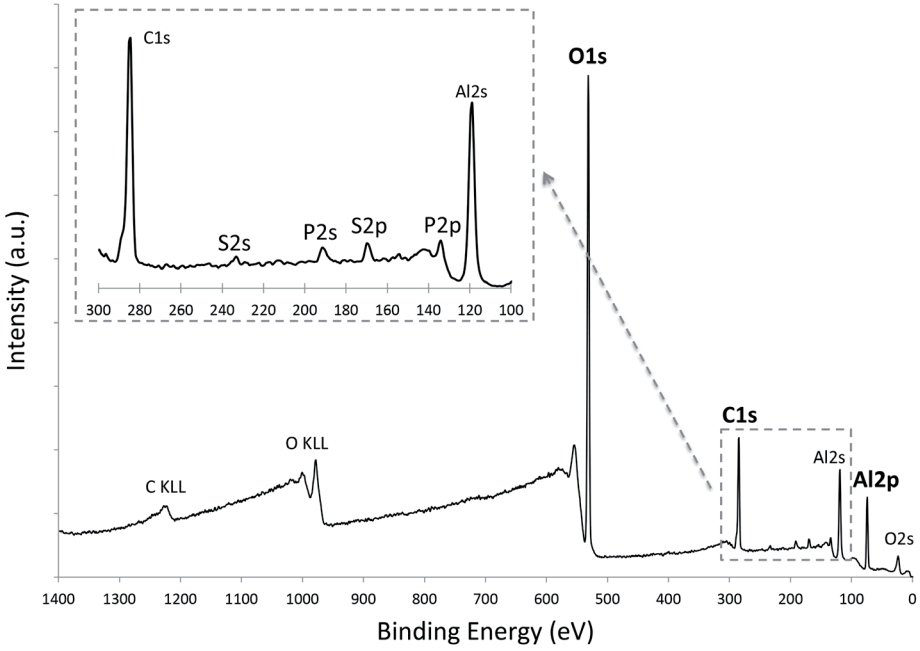

Figure 3.3: XPS survey spectra of a PSA oxide.

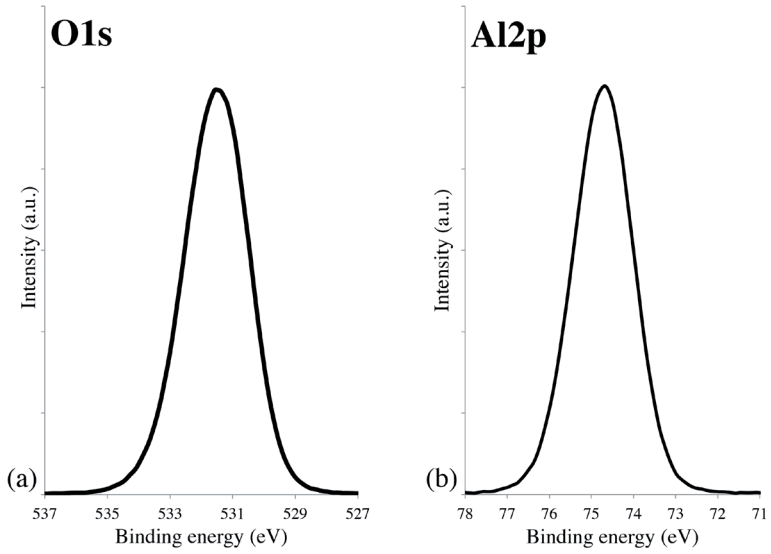

Figure 3.4: High-resolution XPS spectra of the O1s and Al2p from a PAA oxide.

Table 3.3: Summary of XPS envelope O1s and Al2p peaks, generated by Al X-ray source (all in eV).

Abbreviation	*O1s (envelope)*		O^{2-}	OH^-	*Al2p (oxide)*		*Al2p (metal)*		*E(Al2p(ox.)-OH⁻)*
	BE	FWHM	BE	BE	BE	BE	BE	FWHM	
PAA	531.4	2.4	530.9	532.0	74.3	1.7	-	-	457.7
PSA	531.4	2.6	531.0	532.2	74.5	1.7	-	-	457.7
SAA	531.4	2.8	530.7	531.9	74.4	1.7	-	-	457.5
CAA	531.4	2.9	530.6	532.0	74.1	1.7	-	-	457.9
Alkaline	531.9	2.8	531.0	532.2	74.2	1.7	70.9	0.8	458
Hydrothermal	531.2	3.0	530.0	531.4	74.1	2.0	-	-	457.3

Generally, an increase in the FWHM of the O1s peak gives an indication of the amount of hydroxyl groups present in the oxide. A higher amount of hydroxyls leads to broadening of the O1s peak and its shift to a higher BE, resulting from the more covalent character of the Al-OH bond, relative to the Al-O bond [21]. This effect is clearly observed in Table 3.3. The FWHM is increased in the order PAA < PSA < SAA, Alkaline < CAA < hydrothermal. According to Cordier and Ollivier [22], the same trend should be visible in the Al2p peak. However, in this study only the hydrothermal oxide exhibits a wider FWHM (2.0 eV), with the FWHM of all the other oxides equal to 1.7 eV, showing no direct relation to different environments around the Al atoms.

According to Mullins and Averbach [23], shifts in the Al2p and O1s core electrons are related to changes in the Fermi level. These changes also reflect the acid-base nature of the oxides [24]. An increase in the BE of both the Al2p and the O1s is related to an increase in the Lewis acidity of the oxide [22]. Fig. 3.5 presents a plot of the oxide component of the Al2p and the OH component in the O1s (curve-fitting parameters are addressed in our previous manuscript [25]). Consequently, the most acidic oxides in this group are the ones prepared in phosphoric acid (PSA and PAA), followed by SAA, alkaline and CAA while the hydrothermal oxide exhibits the most basic character in the group. These results are consistent with previous works done on porous anodic oxides [22, 24]. It is important to mention that the energy resolution of the equipment (a hemispherical analyser and monochromatized Al Kα x-ray source) is in the order of 0.25 eV [26]. Although this method provides a consistent way to analyse the differences between the electronic structures of the different oxides, most shifts measured between the pre-treatments are minor (<0.3 eV) and fall within this resolution limit.

Moreover, Cordier and Ollivier [22] noted that the shift between the Al2p (oxide peak) and the OH component in the O1s peaks to be (nearly) constant and equal to 457.5 eV.

This value is in agreements with the shifts found in here. After curve fitting, a separation of 457.7 ±0.3 eV was registered (Table 3.3), even though our fitting parameters were different.

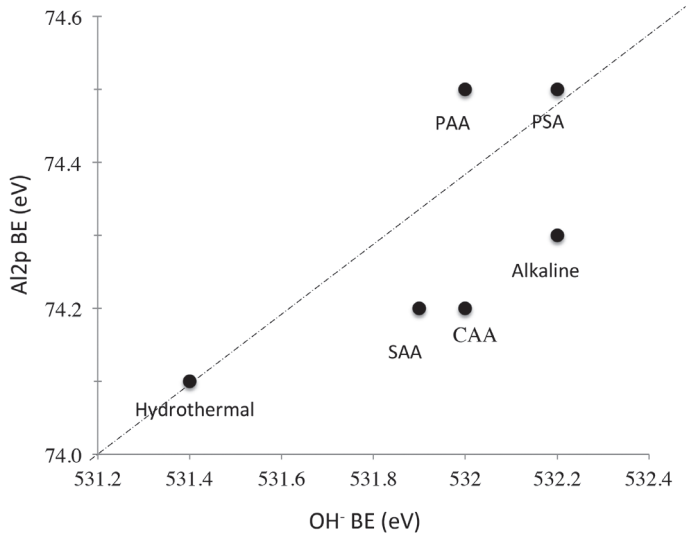

Figure 3.5: XPS binding energy of Al2p oxide vs. OH^- component in O1s for the different oxides after correction for constant separation between O^{2-} and OH^- of 1.1 eV. An increase in the BE corresponds to an increase in the acidity of the oxide.

3.3.3. Auger Parameter

The Auger parameter, as first demonstrated by Wagner [27], is another useful quantity to detect chemical differences, such as a change in the acid-base properties of metal oxides. The modified Auger parameter, α', is the sum of the Auger kinetic energy, E_K, and the binding energy of a photoelectron, E_B, (Eq. 3.1), acquired on the same spectra. Consequently, it does not depend on the absolute measurement energy, such as the XPS data in the previous section and it is independent of the photon energy used for the excitation [28]

$$\propto' = E_B + E_K \qquad \text{Eq. 3.1}$$

The calculated Auger parameters in Table 3.4 are similar for all oxides. α'Al = 1461.4 (±0.1eV) and α'O = 1039.6 (±0.4eV). These values correspond well to previous findings [29], and match to fall in the octahedral aluminium oxide and hydroxides region [27]. Consequently, the differences in the nature of these oxides are too small to be reflected in the Auger parameter.

3.3.4. Interaction with Model Molecules

3.3.4.1 Surface Interaction with 4-Ethylphenol

After the adsorption of 4-EP, FTIR measurements revealed thin organic films on the surface of the oxides prepared by hydrothermal, alkaline and CAA treatments. Their spectra contain many absorption bands that correspond with that of the pure molecule. The interpretation of the spectra for such a hydroxyl-containing compound is complicated by the occurrence of hydrogen bonding, since these can occur both at the interface between the molecule and the aluminium and between the molecules

Table 3.4: Summary of the position of XPS and AES lines generated with Mg X-Ray source and the modified Auger parameter calculated for the different oxides (all in eV).

Abbreviation	O1s BE (FWHM)	Al 2p (ox.) BE (FWHM)	Al 2p (metal) BE (FWHM)	O (KL23L23) KE (FWHM)	Al (KL23L23) KE (FWHM)	α'Al	α'O
PAA	531.6 (2.6)	74.6 (1.9)	-	507.9 (8.4)	1386.8 (2.2)	1461.4	1039.9
PSA	531.7 (2.8)	74.7 (2.0)	-	508.1 (7.4)	1386.7 (2.3)	1461.5	1039.8
SAA	531.2 (2.8)	74.3 (2.0)	-	507.9 (8.9)	1387.0 (2.3)	1461.3	1039.4
CAA	531.3 (2.6)	74.4 (1.9)		508.2 (7.5)	1387.1 (2.2)	1461.3	1039.4
Alkaline	531.4 (2.9)	74.6 (2.0)	71.4 (1.1)	508.0 (8.3)	1387.0 (2.5)	1461.4	1039.2
Hydrothermal	531.4 (3.3)	73.8 (2.0)	-	508,0 (9,8)	1387.6 (2.6)	1461.5	1039.7

themselves due to the high surface coverage. Generally, the lower the acidity of the surface site, the lower its OH band frequency for a hydrogen bonding with the surface (and vice versa) [30]. The observed OH band frequencies are 3280, 3304 and 3331 cm^{-1} for hydrothermal, alkaline and CAA, respectively, indicating of an increased acidity of the surface sites. No interactions were detected on PAA and very small bands were detected on PSA and SAA oxides (Fig. 3.6) Hence, there is a selectivity for interaction with 4-EP based on the pre-treatments.

After rinsing most of the bands disappear and the intensity of the remaining bands is substantially decreased, though some are still visible (Fig. 3.7, illustrated for the CAA oxide). The remaining bands in Fig. 3.7 indicate a phenolate species, bonded at one (1296 cm-1) and two (1248 cm-1) aluminium cation (Al^{3+}) sites [31]. Evidently, very

few of these sites are present since the intensity of these two peaks is substantially low. In light of this behaviour, the mechanism in Fig. 3.8 is proposed for the adsorption of 4-EP. Most of the molecules are attached to the surface by hydrogen bonds, Fig. 3.8 (a), also stabilized through intermolecular hydrogen bonding (not illustrated). Upon rinsing in pure solvent (Fig. 3.8 (b)), weak hydrogen bonds with the surface are broken, indicating of a reversible adsorption that leaves the surface uncharged (Fig. 3.8 (c)).

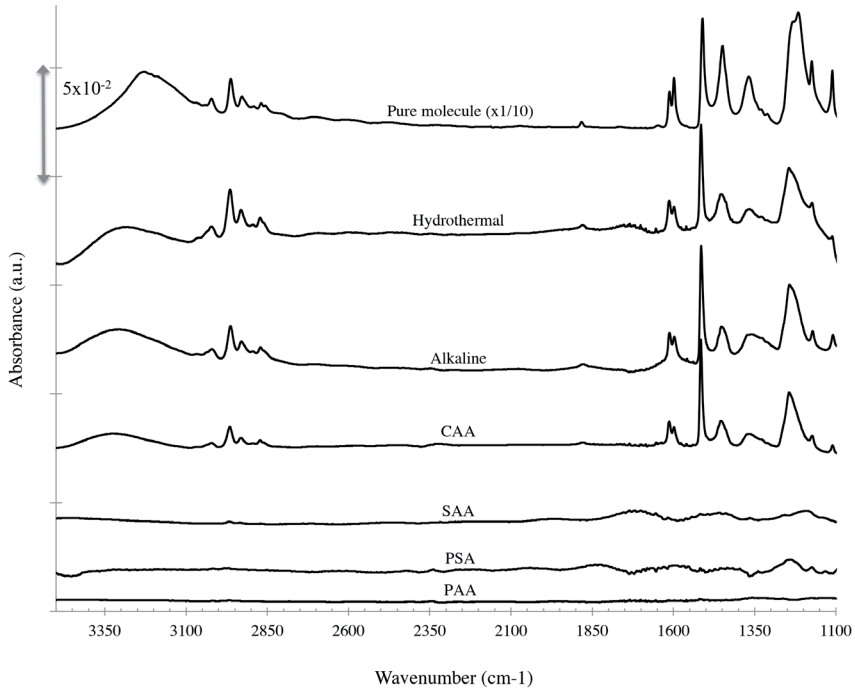

Figure 3.6: FTIR spectra of pure 4-ethylphenol (top curve) and the spectra obtained after its adsorption on the differently pretreated aluminium substrates (not rinsed). Spectra were measured with respect to a background of the corresponding oxide prior to adsorption.

3.3.4.2 Surface Interaction with 4-Hydroxybenzyl Alcohol

Upon the adsorption of 4-HbA, thin white films were visually observed on the surface of all the different oxides and similar FTIR spectra were recorded (Fig. 3.9, non-rinsed condition), displaying no preference for the adsorption to certain oxides surfaces. The spectra in Fig. 3.9 are composed of many bands, which are typical of this molecule and in line with previous observations [13, 32]. Also in here, due to the high concentration that was used, a high surface coverage was attained and many possible coordination states can be expected.

Among the previously reported interactions are hydrogen bonding to surface oxygen, Lewis acid–Lewis base coordination at Al^{3+} and Brønsted acid protonation by the surface OH [33]. According to Kollek [13], the absorption at 1292 cm^{-1} indicates the

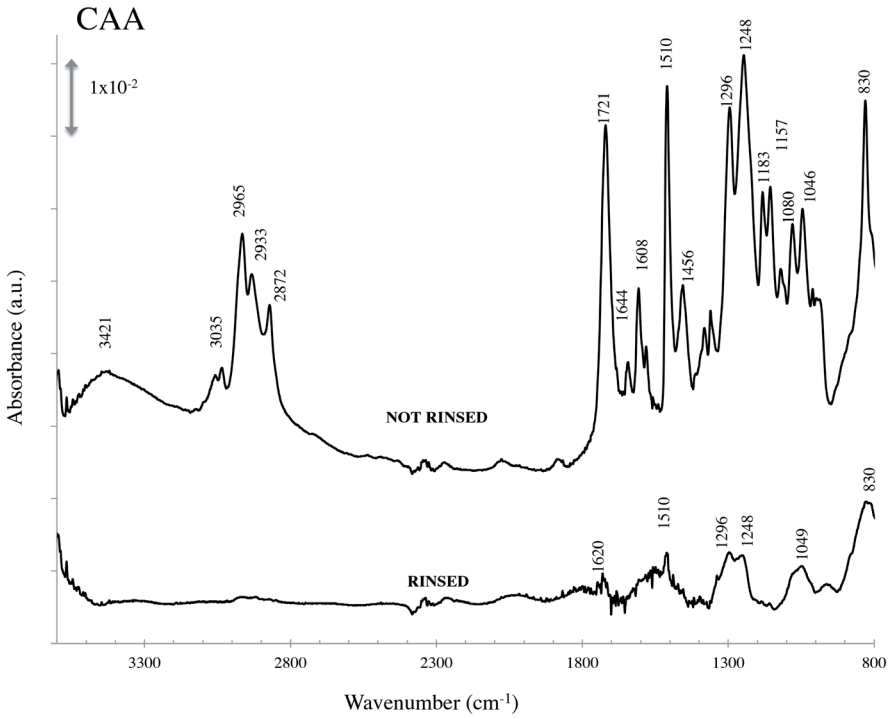

Figure 3.7: FTIR spectra for the interaction of 4-ethylphenol with CAA before and after rinsing in pure THF.

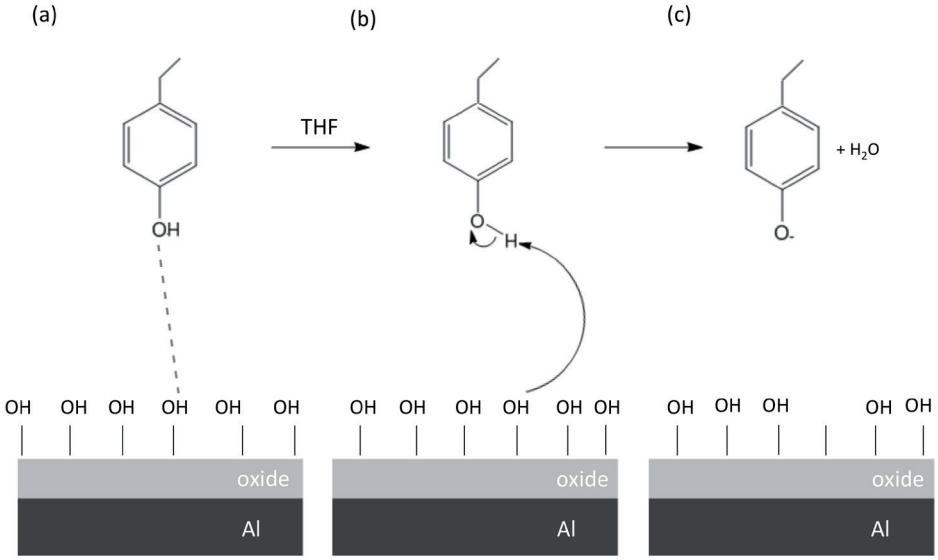

Figure 3.8: Proposed mechanism of the adsorption (a) and desorption (b) and (c) of 4-ethylphenol on CAA, alkaline and hydrothermal oxide.

formation of a phenolate and a peak at 1253 cm^{-1} is caused by a free phenol. Only the former is visible in the spectra in Fig. 3.9. The bands at 3380 cm^{-1} and 3130 cm^{-1} can be assigned to the O-H stretching vibration of the alcoholic hydroxyl group which is engaged in a hydrogen bond to surface hydroxyl and surface oxygen, respectively, with both reversibly adsorbed [32]. This supported by our observation that after rinsing in pure solvent no clear bands can be distinguished in the spectra (not shown). A strong displacement of the hydroxyl stretching bands towards lower wavenumbers (3130 cm^{-1}) and the appearance of multiple diffused bands ranging from 3100 to 2500 cm^{-1} is generally contributed to (laterally) coordinated alcohol molecules [34].

According to Knözinger and Stüebner [32], irreversible adsorption of an alcohol group onto alumina takes place, similar to phenol, at unsaturated aluminium cations sites. Since irreversible adsorption is negligible in here, we, again, conclude, that these surface sites are very limited in these types of oxides. Instead, the relatively weak acceptor properties of the alcohol group are contributing to interactions with the surface, through coordination reactions. Assuming, as shown by Knözinger and Stüebner, [32], that the alcohol group typically is the electron donor in the interaction with alumina, we can conclude that its reduced acidity (compared to the phenol group in 4-EP) contributes to this variety of bonding mechanisms and, as a result, acid-base interactions are established with all oxides.

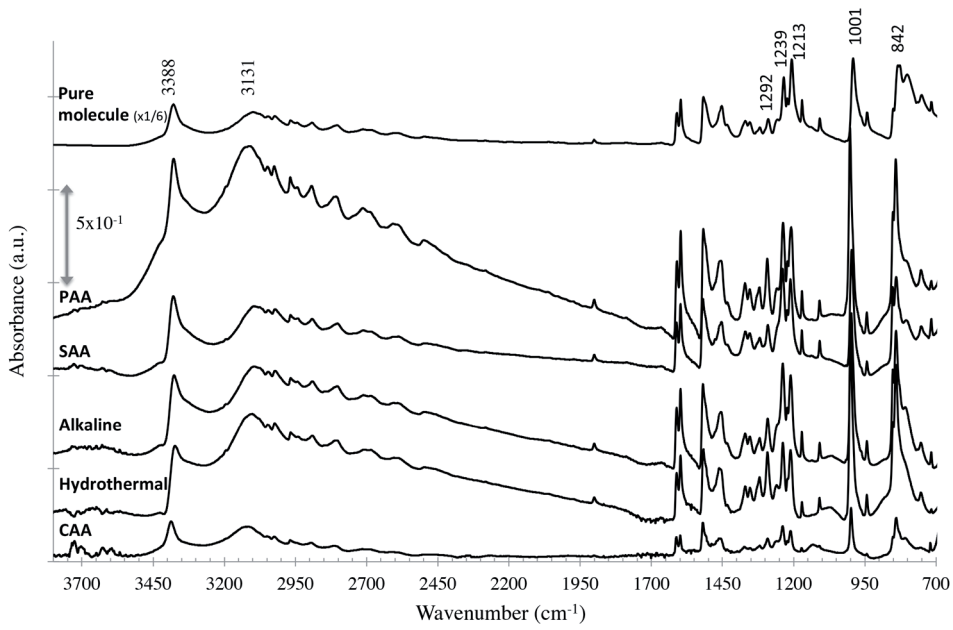

Figure 3.9: FTIR spectra of pure 4-hydroxylbenzyl alcohol (top curve) and the spectra obtained after its adsorption on the differently pretreated aluminium substrates (not rinsed). Spectra were measured with respect to a background of the corresponding oxide prior to adsorption.

3.4 Discussion

In the first part of this chapter, the chemical properties of the different oxides were probed using FTIR, XPS and the Auger parameter. Similar FTIR features were seen for all the bare anodic oxides. Surface-sensitive XPS measurements show that the most acidic oxides in this group are the ones prepared in phosphoric acid (PSA and PAA), while the hydrothermal oxide exhibits the most basic character. While shifts in the binding energies between the two extremes (PAA and hydrothermal oxides) are substantial, differences between the various anodic oxides are generally minor. Hence, we conclude that the net changes in the acid-base nature of the different anodic oxides are also minor. This is supported by the similar Auger parameter that was found.
In the second part, acid-base properties were probed by the interactions between the oxides and two types of phenolic molecules. Results show that interfacial interactions varied according to the pre-treatment and the choice of molecule. FTIR measurements of 4-EP and 4-HbA revealed the presence of thin films of the former only after CAA, hydrothermal and alkaline pre-treatments, while the latter showed no selectivity to certain oxides. This different behaviour can be attributed to the different degree of acidity of their phenol and alcohol end-groups. The phenol end-group on 4-ethylphenol is weakly acidic due to delocalization of the negative charge around the benzen-ring. It therefore has a higher affinity to weak basic hydroxyls, which are found on the hydrothermal, alkaline and CAA oxides. Since the oxides prepared in phosphoric acid are relatively more acidic than the other oxides, they supress the adsorption of 4-EP. Clarification to the more acid character of oxides prepared in phosphoric acid can be given by the incorporation of phosphate anions into the oxide [35]. In 4-HbA, on the other hand, both phenol and alcohol groups are present. This results in a less acidic nature, which results in multiple molecular interactions. Since both 4-EP and 4-HbA films can be washed off using fresh solvent, no irreversible (chemisorption) occurs.

3.5 Conclusions

XPS results show that the different pre-treatments cause no significance net change in the acid-base nature of the (anodic) oxides. Yet, interactions with the two phenolic molecules varied with the pre-treatment and the choice of molecule. Consequently, we believe that it is local changes in the type of surface sites that affects bonding. This is most probably caused by the incorporation of acidic phosphates into the oxides prepared in phosphoric acid. The results give a qualitative indication that changing the chemistry of the oxide by using phosphoric acid will also affect adhesion.

References

1. Sheasby, P.G. and R. Pinner, *Surface Treatment and Finishing of Aluminium and its Alloys*. 6th ed. 2001., England: Finishing Publications Ltd.
2. Critchlow, G.W. and D.M. Brewis, *Review of surface pretreatments for aluminium alloys.* International Journal of Adhesion and Adhesives, 1996. **16**(4): p. 255-275.
3. Affrossman, S. and S.M. MacDonald, *Adsorption of a Model Epoxy Resin, N-Propyl-2-hydroxybutylamine, on Aluminum Surfaces Studied by Static Secondary Ion Mass Spectroscopy.* Langmuir, 1994. **10**(7): p. 2257-2261.
4. Wielant, J., et al., *Influence of the Iron Oxide Acid–Base Properties on the Chemisorption of Model Epoxy Compounds Studied by XPS.* The Journal of Physical Chemistry C, 2007. **111**(35): p. 13177-13184.
5. van den Brand, J., et al., *Interaction of Anhydride and Carboxylic Acid Compounds with Aluminum Oxide Surfaces Studied Using Infrared Reflection Absorption Spectroscopy.* Langmuir, 2004. **20**(15): p. 6308-6317.
6. Brown, N.M.D. and G.M. Taggart, *A study of the chemisorption of a series of aminophenols on plasma-grown aluminium and magnesium oxides by IETS.* Spectrochimica Acta Part A: Molecular Spectroscopy, 1990. **46**(11): p. 1569-1579.
7. Salgin, B., et al., *Role of Surface Oxide Properties on the Aluminum/Epoxy Interfacial Bonding.* The Journal of Physical Chemistry C, 2013. **117**(9): p. 4480-4487.
8. Ebnesajjad, S., *Characteristics of Adhesive Materials*, in *Handbook of Adhesives and Surface Preparation*, S. Ebnesajjad, Editor. 2011, William Andrew Publishing: Oxford. p. 137-183.
9. Higgins, A., *Adhesive bonding of aircraft structures.* International Journal of Adhesion and Adhesives, 2000. **20**(5): p. 367-376.
10. Taheri, P., et al., *A comparison of the interfacial bonding properties of carboxylic acid functional groups on zinc and iron substrates.* Electrochimica Acta, 2011. **56**(4): p. 1904-1911.
11. van den Brand, J., et al., *Interaction of Ester Functional Groups with Aluminum Oxide Surfaces Studied Using Infrared Reflection Absorption Spectroscopy.* Langmuir, 2004. **20**(15): p. 6318-6326.
12. Barthés-Labrousse, M.G., *Acid–base characterisation of flat oxide-covered metal surfaces.* Vacuum, 2002. **67**(3–4): p. 385-392.
13. Kollek, H., *Some aspects of chemistry in adhesion on anodized aluminium.* International Journal of Adhesion and Adhesives, 1985. **5**(2): p. 75-80.
14. Wiley, I., *Ullmann's encyclopedia of industrial chemistry*. 2003, Wiley-VCH: Weinheim, Germany :.
15. Wagner, C.D. and J.A. Taylor, *Generation of XPS Auger lines by bremsstrahlung.* Journal of Electron Spectroscopy and Related Phenomena, 1980. **20**(1): p. 83-93.
16. Johnsen, B.B., F. Lapique, and A. Bjørgum, *The durability of bonded aluminium joints: a comparison of AC and DC anodising pretreatments.* International Journal of Adhesion and Adhesives, 2004. **24**(2): p. 153-161.
17. Johnsen, B.B., et al., *The effect of pre-bond moisture on epoxy-bonded sulphuric acid anodised aluminium.* International Journal of Adhesion and Adhesives, 2004. **24**(3): p. 183-191.

18. Underhill, P.R. and A.N. Rider, *Hydrated oxide film growth on aluminium alloys immersed in warm water.* Surface and Coatings Technology, 2005. **192**(2–3): p. 199-207.
19. Dorsey, G.A., *The Characterization of Anodic Aluminas: I . Composition of Films from Acidic Anodizing Electrolytes.* Journal of The Electrochemical Society, 1966. **113**(2): p. 169-172.
20. van den Brand, J., et al., *Ageing of aluminium oxide surfaces and their subsequent reactivity towards bonding with organic functional groups.* Applied Surface Science, 2004. **235**(4): p. 465-474.
21. McCafferty, E. and J.P. Wightman, *Determination of the concentration of surface hydroxyl groups on metal oxide films by a quantitative XPS method.* Surface and Interface Analysis, 1998. **26**(8): p. 549-564.
22. Cordier, F. and E. Ollivier, *X-ray photoelectron spectroscopy study of aluminium surfaces prepared by anodizing processes.* Surface and Interface Analysis, 1995. **23**(9): p. 601-608.
23. Mullins, W.M. and B.L. Averbach, *Bias-reference X-Ray photoelectron spectroscopy of sapphire and yttrium aluminum garnet crystals.* Surface Science, 1988. **206**(1–2): p. 29-40.
24. Mullins, W.M. and B.L. Averbach, *The electronic structure of anodized and etched aluminum alloy surfaces.* Surface Science, 1988. **206**(1–2): p. 52-60.
25. Abrahami, S.T., et al., *XPS Analysis of the Surface Chemistry and Interfacial Bonding of Barrier-Type Cr(VI)-Free Anodic Oxides.* The Journal of Physical Chemistry C, 2015.
26. Tougaard, S., *Quantification of Surface and Near-Surface Composition by AES and XPS*, in *Handbook of Surface and Interface Analysis*. 2009, CRC Press. p. 223-244.
27. Wagner, C.D. and A. Joshi, *The auger parameter, its utility and advantages: a review.* Journal of Electron Spectroscopy and Related Phenomena, 1988. **47**(0): p. 283-313.
28. Moretti, G., *Auger parameter and Wagner plot in the characterization of chemical states by X-ray photoelectron spectroscopy: a review.* Journal of Electron Spectroscopy and Related Phenomena, 1998. **95**(2–3): p. 95-144.
29. van den Brand, J., et al., *Acid–Base Characterization of Aluminum Oxide Surfaces with XPS.* The Journal of Physical Chemistry B, 2004. **108**(19): p. 6017-6024.
30. Hair, M.L. and W. Hertl, *Acidity of surface hydroxyl groups.* The Journal of Physical Chemistry, 1970. **74**(1): p. 91-94.
31. Popov, A., et al., *IR study of the interaction of phenol with oxides and sulfided CoMo catalysts for bio-fuel hydrodeoxygenation.* Catalysis Today, 2011. **172**(1): p. 132-135.
32. Knözinger, H. and B. Stüebner, *Adsorption of alcohols on alumina. 1. Gravimetric and infrared spectroscopic investigation.* The Journal of Physical Chemistry, 1978. **82**(13): p. 1526-1532.
33. Knözinger, H. and A.A. Davydov, *Infrared Spectroscopy of Adsorbed Species on the Surface of Transition Metal Oxides*. Berichte der Bunsengesellschaft für physikalische Chemie. Vol. 95. 1991: Wiley-VCH Verlag GmbH & Co. KGaA. 543-543.
34. Brown, N.M.D., et al., *Inelastic electron tunnelling spectroscopy of selected alcohols and amines on plasma-grown aluminium oxide.* Journal of the Chemical Society, Faraday Transactions 1: Physical Chemistry in Condensed Phases, 1980. **76**(0): p. 2335-2346.
35. Abrahami, S.T., et al., *XPS Analysis of the Surface Chemistry and Interfacial Bonding of Barrier-Type Cr(VI)-Free Anodic Oxides.* The Journal of Physical Chemistry C, 2015. **119**(34): p. 19967-19975.

CHAPTER 4

XPS analysis of the surface chemistry and interfacial bonding of barrier-type Cr(VI)-free anodic oxides

This chapter is published as a scientific paper:
Abrahami, S.T., Hauffman, T., de Kok, J.M.M., Terryn, H., and Mol, J.M.C.,
J. Phys. Chem. C, (2015), 119 (34) 19967-19975.

ABSTRACT

In the transition to environmental friendly pre-treatment of aerospace aluminium alloys, chromic acid anodizing (CAA) is being replaced by sulphuric acid (SAA), phosphoric acid (PAA) or phosphoric-sulphuric acid (PSA) anodizing. While generally the main concern is controlling the film morphology, such as the pore diameter, oxide-, and barrier layer thickness, little is known on how the anodic oxide chemistry affects the interactions at the interface upon adhesive bonding. To study the link between surface chemistry and interfacial bonding, featureless oxides were prepared by stopping the anodizing during the formation of the barrier layer. A model was developed to quantify the relative amounts of OH^-, PO_4^{3-} and SO_4^{2-} by curve-fitting the XPS data. Calculations showed that almost 40% of the surface species in PAA oxide are phosphates (PO_4^{3-}), while about 15% are sulphates (SO_4^{2}) in SAA. When both anions were present in the electrolyte, phosphate incorporation was inhibited. Studies of the interaction between this set of Cr(VI)-free oxides and diethylenetriamine (DETA) – an amine curing-agent for epoxy resin, showed that all oxides interact with the nitrogen of DETA. However, larger ratios of Lewis-like acid-base bonding between the amine electron pair and the acidic hydroxyl on phosphate surface sites were observed.

4.1 Introduction

The controlled electrochemical oxidation of aluminium, better known as anodizing, is commonly used to enhance the metal's durability by creating a protective oxide layer on its surface [1]. Suitable for finishing or as a pre-treatment, anodizing has a myriad of utilities. One major application is adhesive bonding in the aerospace industry, in which prolonged anodizing in an acid electrolyte is used to produce an aluminium surface oxide with a compact barrier layer at the bottom and a relatively regular porous structure on top. This duplex surface oxide contributes to the enhanced adhesion to an organic resin and the corrosion resistance of the anodized components [2].

In the transition towards an environmental friendly production, replacements are desired for *chromic acid anodizing* (CAA), which is still largely used for this purpose, but recognized to pose severe health and environmental risks during processing [3]. Cr(VI)-free candidate replacements include *sulphuric acid anodizing* (SAA), *phosphoric acid anodizing* (PAA) and *phosphoric-sulphuric acid anodizing* (PSA) mixtures. While research efforts are often directed towards controlling the film morphology, such as the pore diameter, oxide-, and barrier layer thickness, various studies show that the oxide surface chemistry can play an essential role in the subsequent interfacial bonding with an organic coating [4-6].

So far, changes in the oxide chemistry on aluminium have been explained in terms of changes in the acid-base properties [7, 8], the surface charge [9-11] and the hydroxyl fraction [12, 13]. It is interesting to note that although the incorporation of anions during anodizing in sulphuric and phosphoric acids has been extensively reported (e.g. [14], [15], [16]), studies including these type of pre-treatments did not explicitly account for their presence [5, 7, 8]. Since it is mostly the outer region of the oxide, the part that comes into contact with the organic resin, that is contaminated by these anions [17, 18], their consideration seems vital to understand how electrolyte variations will affect interfacial bonding with organic resins on a molecular and atomic level.

To focus on interfacial chemistry and exclude the effect of (and variations in) surface roughness, anodizing in phosphoric-, sulphuric, chromic- and a mix of phosphoric and sulphuric acids was stopped during the formation of the barrier layer, resulting in featureless anodic oxides. Additional chemical pre-treatments in alkaline and boiling water were also included in this study for broadening the range of hydroxyl fractions. Oxide chemistry was studied by Auger electron spectroscopy (AES) and angle-resolved X-ray Photoelectron Spectroscopy (XPS). High-resolution O1s, C1s, P2s and S2p photopeaks were curve-fitted. The relative amounts of hydroxyls, phosphates and sulphates were then calculated using an extended model, based on the one developed by McCafferty and Wightman [19]. Furthermore, we examined the interaction between the oxides and diethylentriamine (DETA) – an amine curing-agent that is typically used in commercially epoxy adhesive primers.

4.2 Experimental

4.2.1 Materials and Pre-treatments

Samples were cut from a 0.3 mm thick sheet of pure aluminium (99.99%, Hydro). To remove imperfections and provide a flat substrate, all specimens were electropolished. This was done after the substrate was etched in an aqueous solution of 25g/L NaOH at 70 °C for 1 minute, followed by rinsing for 15s with deionized water and then ultrasonically rinsed for additional 3 minutes. The substrate was then electropolished for 6 min in a solution of 80 vol.% (absolute) ethanol and 20 vol.% perchloric acid, at current density of 70 mA/cm^2 and 10 °C. Subsequently, it was rinsed following the above procedure, dried with compressed air and stored separately. Later, each sample was given one of the aqueous pre-treatments listed in Table 4.1.

Galvanostatic anodizing was performed with SM120-25 power-supply (Delta Elektronika) equipped with an Ethernet interface connection to monitor the cell voltage. A three-electrode cell filled with 400 mL solution and two AA1050 cathodes was used. After each of the described pre-treatments, the substrate was thoroughly rinsed (as described above). Anodizing conditions were pre-selected to yield featureless anodic oxides by stopping the oxide growth at the end of the region in which the voltage was increasing linearly with time, the part which is associated with the formation of the barrier layer [1].

Table 4.1: Summary of the type and process conditions of the different surface pre-treatments.

Abbreviation	*Treatment*	*Conditions*
PAA	Phosphoric Acid Anodizing	25g/l H_3PO_4 4s, *0.2A, RT
SAA	Sulphuric Acid Anodizing	10g/l H_2SO_4, 4s, *0.2A, RT
PSA	Phosphoric-Sulphuric Acid anodizing	25g/l H_3PO_4 and 10g/l H_2SO_4, 4s, *0.2A, RT
HcPSA	High concentration Phosphoric-Sulphuric Acid anodizing	80g/l H_3PO_4 and 50 g/l H_2SO_4, 4s, *0.2A, RT
CAA	Chromic Acid Anodizing	40g/l CrO_3, 4s, *0.2A, RT
Alkaline	Alkaline immersion	25g/l NaOH, 30s, RT
Hydrothermal	Boiling water immersion	Boiling Boiling demineralized water (conductivity of 0.9 μS/cm), 30s

*Corresponds to approx.10 mA/cm^2, RT= Room Temperature (22 °C ± 3)

4.2.2 Adsorption of DETA

Molecular interactions across the interface were modelled by the adsorption of DETA. Soon after the pre-treatments, the substrates were placed in a tetrahydrofuran (THF) solution containing 0.1 wt.% DETA (Sigma-Aldrich). After 30 min of immersion, substrates were withdrawn from the solution and rinsed using a clean solvent before they were placed in the analysis chamber.

4.2.3 Surface Characterization

4.2.3.1 Auger Electron Spectroscopy

Auger Electron Spectroscopy (AES) measurements were performed using a PHI 650(SAM) with a LaB6 cathode and a cylindrical mirror analyser (CMA). A primary electron beam of 5 keV and an emission current of 1 μA were applied on 0.24 mm^2 of the sample surface at 30 degrees incident angle. A depth profile was taken with a PHI 04-303 ion gun at 5 keV. Ion sputtering at intervals of 1 minute was performed using argon ions with emission current of 20 mA and Ar pressure of 10 mPa, impinging the surface at 50 degrees to its normal. Atomic concentrations in AES were determined using the sensitivity factors provided by the manufacturer.

4.2.3.2 X-Ray Photoelectron Spectroscopy

X-ray photoelectron spectroscopy (XPS) spectra were collected using a PHI5600 photoelectron spectrometer (Physical Electronics) with an Al *K*α monochromatic X-ray source (1486.71 eV of photons). The vacuum in the analysis chamber was approximately $5x10^{-9}$ Torr during measurements. High-resolution scans of the Al2p, O1s, C1s, P1s, S2p and N1s photopeaks were recorded from a spot diameter of 0.8 mm using pass energy of 23.5 eV and step size 0.1 eV. Measurements were performed with take-off angles of 45° and 15° with respect to the sample surface. Electron gun was deliberately not used to avoid vertical differential charging. The reproducibility of the AES and XPS measurements was verified by triplication of the measurements.

AES and XPS data was analysed with PHI Multipak software (V9.5.0.8). Before curve fitting, the energy scale of the XPS spectra was calibrated relative to the binding energy of advantageous hydrocarbons (C-C/C-H, Fig. 4.2 (e)) in the C1s peak at 284.4 eV. Curve fitting was done after a Shirley-type background removal, using mixed Gaussian (80–100%) – Lorentzian shapes.

4.3 Results and Discussion

4.3.1 AES Depth Profiles

Auger electron spectroscopy (AES) depth profiles were used to estimate the oxide thickness and to obtain an in-depth composition analysis. Fig. 4.1 displays representative

AES profiles for the different oxides. To make the plots, the Al KLL signal was separated into its metal (1396 eV) and oxide (1387 eV) components using Target Factor Analysis (TFA). Only the Al metal signal is displayed in the plots. Depth profiles are expressed as a function of the sputter time due to the dependence of the effective sputter rate on the matrix properties [20]. We can estimate the oxide thickness by the time it takes the Al KLL signal to reach 50% of its maximum intensity [21]. These values are summarized in Table 4.2. Under the applied conditions, silicon oxide films are removed at a rate of 1 nm/min. According to Baer et al. [20], the same conditions used on (pure) aluminium oxides will result in a sputter rate of approximately 4.6 nm/min. Hence, the studied oxides are between 2 (for alkaline) and 53 nm (hydrothermal). The different anodic oxides have comparable thicknesses of about 30 nm.

Table 4.2: Sputter time to 50% Al_{KLL} intensity (average from at least 3 measurements with standard deviation) and the estimated oxide thickness [20].

Pre-treatment Abbreviation	Sputter time to 50% Al_{KLL} intensity (min.)	Estimated thickness (nm)
PAA	5.6 ± 0.6	26 ± 3
SAA	5.9 ± 0.5	27 ± 2
PSA	5.2 ± 0.4	24 ± 2
CAA	7.7 ± 0.8	35 ± 4
Alkaline	0.4 ± 0.2	2 ± 1
Hydrothermal	11.6 ± 2.8	53 ± 13

It is especially interesting to learn how phosphor and sulphur are distributed in the oxides and what types of species are present. From the profiles in Fig. 4.1 (d-f), we can follow the trends for the incorporation of phosphor and sulphur. Chrome signal was below the detection limit of AES and, therefore, could not be recorded. The sulphur Auger peak is located around 150 eV, indicating the presence of sulphate (SO_4^{2-}) species [22]. Sulphates are incorporated throughout the oxide thickness, as seen in Fig. 4.1 (d). The phosphor Auger peak is located at 110 eV during the first two sputter cycles (after a survey scan has been taken). No peak is seen at the third cycle before a new peak at 120 eV appears. This is a known phenomenon that is related to an interaction with the electron beam rather than to a change in the oxidation state of phosphor [23, 24] (it was also confirmed by following its position during the survey scans). Hence, only one

peak at 120 eV is present. This peak is characteristic to phosphate (PO_4^{3-}) species [23]. The two peaks are, therefore, co-added to create the PAA profile in Fig. 4.1(e), showing incorporation of phosphates in about two-thirds of the oxide thickness.

In contrast to the above results, phosphor in PSA is only observed at the outer most part of the oxide, while sulphur is incorporated almost throughout the oxide thickness (similar to SAA). Also in here, an Auger phosphor peak shift was registered after the first two sputter cycles. Subsequently however, the concentration of phosphor drops and completely diminishes after just a few extra sputter cycles Fig. 4.1(f).

The ratio of oxygen to aluminium in the oxide layer is generally constant and equal to 1.5, indicating of an Al_2O_3 stoichiometry. Atomic concentrations of sulphur and

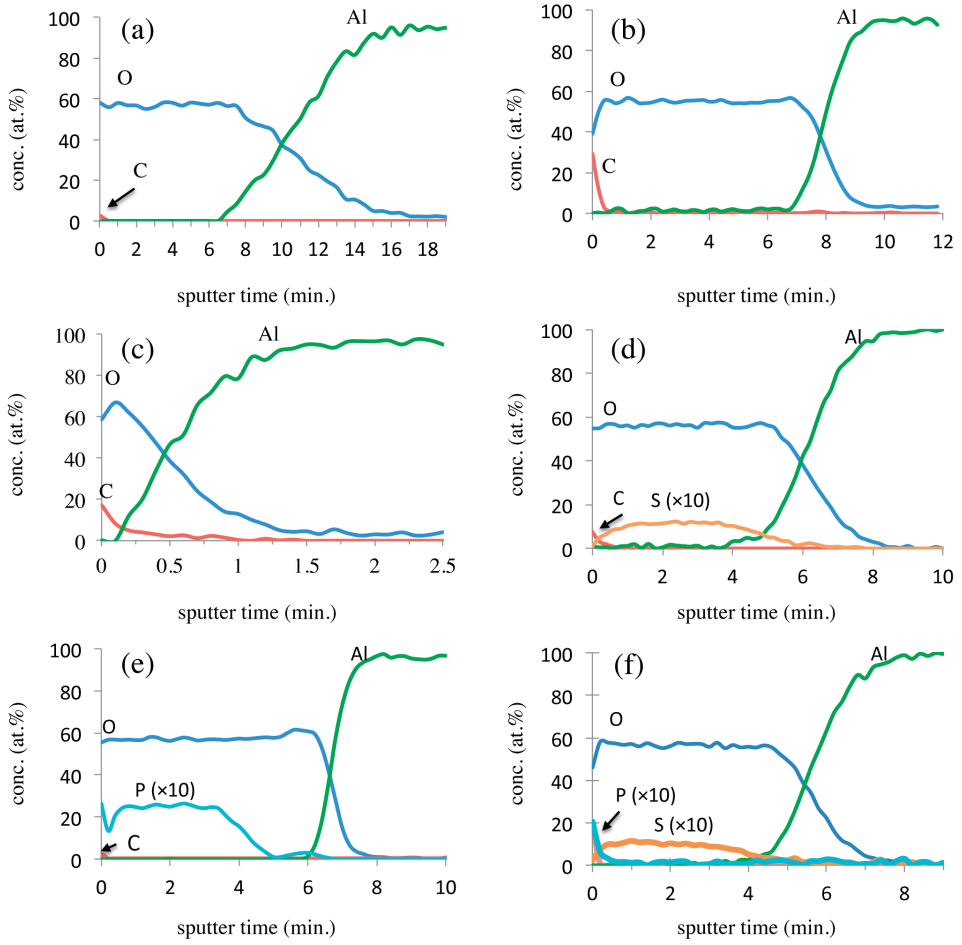

Figure 4.1: AES depth profiles after the following pre-treatments: (a) Hydrothermal, (b) CAA, (c) Alkaline, (d) SAA, (e) PAA and (f) PSA. Only the Al metal signal is displayed in the plots. For illustration purposes Phosphor (P) and sulphur (S) concentrations were multiplied by a factor of 10.

phosphor are ranging from 1-2 and 1-4 at. %, respectively. These are lower than the amounts normally reported for porous anodic oxides, which ranges from 6-10 and 10-13 at. % for PAA and SAA, respectively [17, 25]. This higher concentration in porous anodic oxides is generally attributed to its long-term exposure to the electrolyte [22, 25]. It is also proposed that the higher anion incorporation in those oxides is enabled by field-assisted adsorption due to the semi-spherical shape of the barrier-layer at the pore base [25].

4.3.2 Qualitative Characterization of the Oxides by XPS

A typical survey XPS scan is shown in Fig. 4.2 (a) for a PSA oxide. The main elements detected in all oxides are oxygen, aluminium and carbon. Phosphor, sulphur and chromium were also detected in the corresponding oxides. Typical high-resolution spectra are also shown in Fig. 4.2 (b) - (e). A summary of peak envelope positions and the full width half-maximum (FWHM) of the peak intensities (for O1sand Al2p) is given in Table 4.3. An increase in charging of the spectra is related to oxide thickness, as indicated by the shift in the BE of C1s before charge correction.

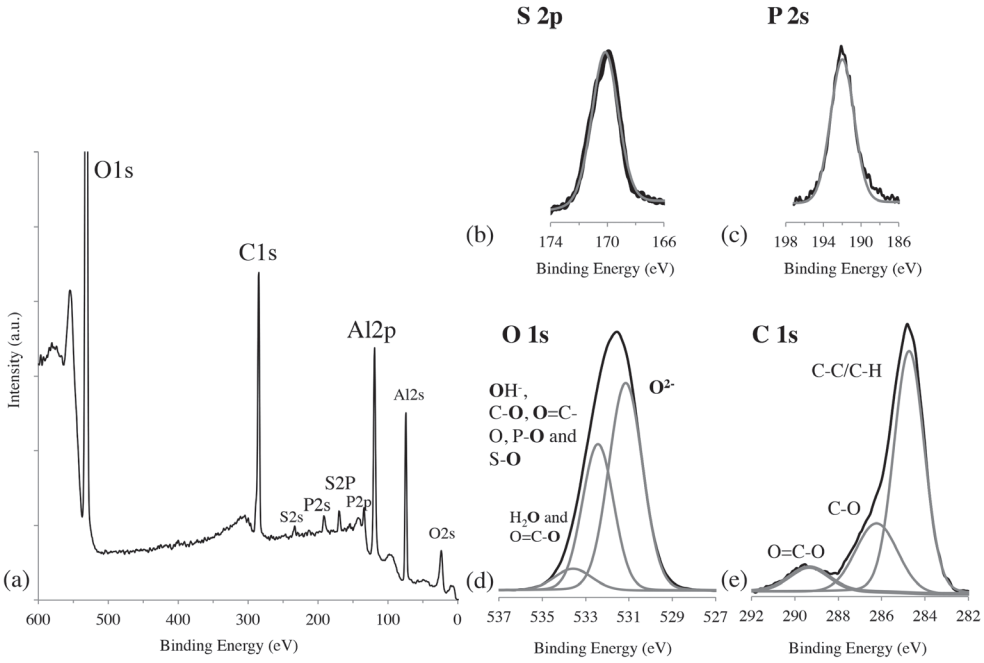

Figure 4.2: Survey-scan (a) and high-resolution XPS spectra for S2p (b), P2s (c), O1s (d) and C1s (e) photopeaks.

The binding energies for phosphor and sulphur, as derived from the P2s and S2p photopeaks, are 191.6 (±0.3) eV and 169.7(±0.4) eV (Table 4.3). Only one specie is present for each element, with a position that corresponds to P in PO_4^{3-} [26] and S in SO_4^{2-} [27] states, confirming our previous AES observations. The oxidation state of chromium is predominantly Cr(VI) detected at 579.4 (±0.1) eV and 587.8 (±0.2) eV for, $Cr2p_{3/2}$ and $Cr2p_{1/2}$, respectively (not shown) [28]. The Al2p metal peak was only detected after alkaline pre-treatment. All other oxides were thicker than the analysis depth so only the Al2p oxide component has been observed.

Changes in the chemical environment of the elements are often assigned by changes in the BE and the FWHM of their photopeaks [8, 13]. The different oxides in this study have very similar O1s and Al2p binding energies, but the FWHM of the O1s is significantly increased from PAA to hydrothermal oxide. This broadening is often attributed to changes in the extent of hydration, since the OH bond has a higher binding energy than O^{2-} (as in Al-O-Al) bond [29]. However, this is not the only effect present in here, since contributions of PO_4^{3-}, SO_4^{2-} and COOX are also present. The FWHM of pure $AlPO_4$ is very narrow (1.8 eV) in comparison to other alumina compounds that typically ranges from 2.2 to 3.1 eV [30]. Hence, in the following paragraph (section 3.3) these contributions are quantified.

Table 4.3: Summary of XPS (envelope-) peak positions and FWHM measured at 45° take-off angle.

	C1s	*O1s*		*Al 2p (oxide)*		*Al 2p (metal)*	*S2p*	*P2s*	*Cr 2p*
	BE * (eV)	BE (eV)	FWHM (eV)	BE (eV)	FWHM (eV)	BE (eV)	BE (eV)	BE (eV)	BE (eV)
SAA	287.4	531.4	2.8	74.4	1.7	-	169.4	-	-
PAA	287.2	531.4	2.4	74.3	1.7	-	-	191.5	-
PSA	287.1	531.4	2.6	74.5	1.7	-	169.8	191.8	-
HcPSA	287.3	531.5	2.7	74.6	1.8	-	169.8	191.9	
CAA	287.4	531.4	2.9	74.1	1.7	-	-	-	579.5
Alkaline	286.8	531.9	2.8	74.2	1.7	70.9	-	-	-
Hydro	289.6	531.2	3.0	74.1	2.0	-	-	-	-

*Before charge correction.

4.3.3 Quantification of Surface Species with XPS

Quantitative analysis can be performed by curve fitting the C1s and O1s photopeaks into their sub-components. Different methods have been reported for the curve-fitting of these peaks, with most researchers following the three-component deconvolution of the oxygen into the O^{2-}, OH^- and adsorbed H_2O peaks and carbon into the C-C/C-H,

CO and COOX components, as shown in Fig. 4.2 (d) and (e) [31]. This method is also applied in this study, using the constraint parameters that are listed in Table 4.4. Since the FWHM of the sub- components in O1s were constrained, the distance between the O^{2-} and OH^- components was allowed to vary from 1.1 to 1.4 eV, taking into account the higher complexity of these oxides. The resulting binding energies that correspond to the different components after fitting are listed in Table 4.5.

Table 4.4: Parameters applied for a constrained curve fitting the O1s and C1s high-resolution XPS peaks. Peak shapes and background subtraction are given in the experimental section.

O1s			C1s		
Component	FWHM (eV)	Position lock (eV)	Component	FWHM (eV)	Position lock (eV)
O^{2-}	1.80 – 1.84	0	CC/CH	1.6	0
OH^-	1.68 – 1.72	1.1 – 1.4	CO	2.0	1.5
H_2O	2.03 – 2.07	2.43	COOX	1.4 - 2.0	3.8 – 4.8

Table 4.5: Summary of fitting results for the O1s XPS photopeak.

	Angle	*O^{2-} BE (eV)*	*OH^- BE (eV)*	*H_2O BE (eV)*	*E (O^{2-} - OH^-) (eV)*
PAA	15	531.4	532.6	533.8	1.1
	45	530.9	532.0	533.3	1.1
PSA	15	530.9	532.3	533.3	1.2
	45	531.0	532.2	533.5	1.2
HcPSA	15	531.1	532.3	533.6	1.2
	45	530.7	532.3	533.5	1.3
SAA	15	530.6	531.9	533.1	1.3
	45	530.7	531.9	533.1	1.3
CAA	15	530.2	531.5	532.6	1.3
	45	530.6	532.0	532.8	1.4
Alkaline	15	531.1	532.2	533.5	1.1
	45	531.0	532.2	533.4	1.2
Hydro	15	529.9	531.3	532.4	1.4
	45	530.0	531.4	533.4	1.3

To calculate the hydroxyl fraction, other oxygen-containing components with similar binding energies as the OH component have to be subtracted. A method to account for the contribution of CO and COOX has been developed by McCafferty and Wightman [19] and successfully applied by others (e.g. [12, 13, 32, 33]). In this study, we extend their model in order to account for the contribution of phosphates and sulphates, since the binding energies of both P-O and S-O bonds overlap with the hydroxide component in Fig. 4.2 (d)) [26, 34]. Their contribution is taken from the area of the P2s and S2p peaks (Fig. 4.2 (a) and (b)).
Using the peak intensity, *I*, which is the area of the fitted (sub-)peak of each component, the atomic concentration of a specie, c(x), can be determined using Eq. 4.1 [19].

$$I = F\sigma \int c(x)\, e^{\left(\frac{-x}{\lambda \sin\theta}\right)} dx \qquad \text{Eq. 4.1}$$

In which F represents all the instrumental factors, λ the inelastic mean free path (IMFP), σ the photo-ionization cross-section and θ is the angle between the sample and the analyser. The applied λ and σ values are listed in Table 4.6.
Since the freshly prepared oxides contain no carbon species, the measured carbon signal comes entirely from ambient contamination. This includes the oxygen-containing groups CO-, COOX- in Fig. 4.2 (e)) [19]. We account for the organic contamination by solving the integral for the intensity of the organic signal from the top layer in Fig. 4.3, which has a certain confined thickness, t_{cont}. Hence, solving the integral in Eq. (1) from x=0 to x=t_{cont} yields the carbon intensity as in Eq. (4.2) [31]

$$I_n = F\sigma_m c_n \lambda_m \sin\theta \left(1 - e^{\left(\frac{-t_{cont}}{\lambda_m \sin\theta}\right)}\right) \qquad \text{Eq. 4.2}$$

Where *n* refers to the component of interest and *m* is the corresponding elemental property in the relevant environment. For species in the oxide layer of thickness t_{ox}, the solution accounts for intensity attenuation by the covering organic layer (Fig. 4.3). Assuming that all elements are homogenously distributed through the oxide in the limited probed depth with respect to the oxide thickness, their concentration can be calculated using Eq. (4.3).

$$I_n = F\sigma_m c_n \lambda_m \sin\theta \left(e^{\left(\frac{-t_{cont}}{\lambda_m \sin\theta}\right)}\right) \qquad \text{Eq. 4.3}$$

Since multiple oxygen atoms are involved in bonding to carbon in COOX, phosphor in PO_4^{3-} and sulphur in SO_4^{2-}, their concentration is multiplied by the stoichiometric factor.

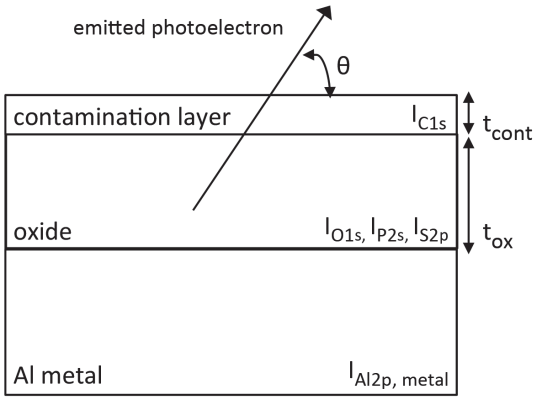

Figure 4.3: Schematic representation of the multi-layer system in this study, showing the aluminium covered by the anodic oxide and the contamination carbon layer at the top.

Table 4.6 Inelastic Mean Free Paths (IMFP, λ) [12, 31] and Cross Sections (σ) [35] for C, O, P and S used in the used for quantitative analysis. IMFP values for P and S are approximated by the calculated value for O1s, given the fact that the oxide layer is mainly composed of alumina.

Element	*σ*	*λ (nm)*
C	0.16	2.3
O	0.46	2.4 (cont.)
		1.8 (oxide)
P	0.33	1.8
S	0.41	1.8

An equation is then written for each component (CO-, COOX-, PO_4^{3-}, SO_4^{2-}, OH^- and O^{2-}) and the set of six equations (given in Eq. 4 (a-f) in Appendix A) are simultaneously solved for an estimated $t_{cont,}$ of 2 nm [12]. The relative fractions of OH^-, PO_4^{3-} and SO_4^{2-} are then independent of the instrumental factors and can be calculated with Eq. (4.5) (shown for OH^-).

$$\frac{C_{OH^-}}{C_{OH^-}+C_{O^{2-}}+(4\times C_{PO_4^{3-}})+(4\times C_{SO_4^{2-}})} \quad \text{Eq. 4.5}$$

Results are displayed in Fig. 4.4 (a) and (b) for measurements taken at take-off angles of 15° and 45°, respectively. The hydroxyl fraction, ranging from 0 to almost 50% varies significantly and is increased in the order; PAA < PSA < HcPSA < SAA < CAA < Alkaline < hydrothermal (Table 4.7). Calculations show that almost 40% of the surface species in PAA oxide are phosphates (PO_4^{3-}), while about 15% are sulphates (SO_4^{2-}) in SAA. Phosphates concentration is significantly higher close to the surface, while sulphates concentration is more constant. This effect is seen in PAA and SAA, as well

as in the mixed electrolyte oxides (PSA and HcPSA) and is generally in agreement with the observations in section 4.3.1. When both anions are present in the electrolyte, the relative amount of phosphates (PO_4^{3-}/OH^-, Table 4.7) is much lower (about 4 times) than for PAA, while the relative incorporation of sulphates (SO_4^{2-}/OH^-, Table 4.7) remains the same as in SAA. This is also consistent with our previous AES findings in section 4.3.1.

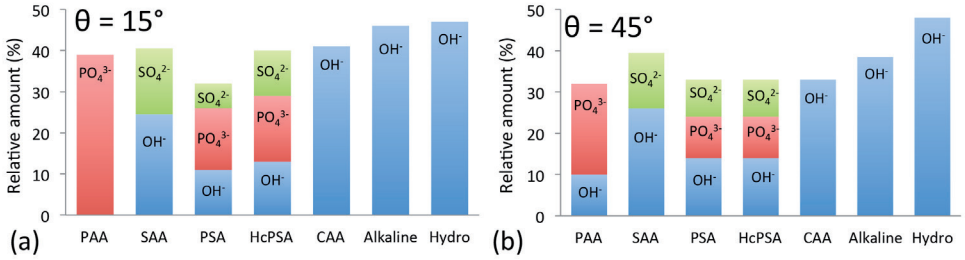

Figure 4.4: Calculated per cent of OH^-, SO_4^{2-} and PO_4^{3-} species at the surface of the different oxides. Results were acquired by curve-fitting the XPS data at (a) 15° and (b) 45° take-off angles.

Table 4.7: Calculated present of OH^-, SO_4^{2-} and PO_4^{3-} species and their relative fraction at the surface of the different oxides. Results were acquired by curve-fitting the XPS data.

	Angle	*OH^- (%)*	*$(PO_4)^{3-}$ (%)*	*$(SO_4)^{2-}$ (%)*	*$(PO_4)^{3-}/OH^-$*	*$(SO_4)^{2-}/OH^-$*
PAA	15	0	39	-	N.A	-
	45	10	22	-	2.2	-
SAA	15	25	-	16	-	0.6
	45	26	-	14	-	0.5
PSA	15	11	15	6	1.4	0.5
	45	14	10	9	0.7	0.6
HcPSA	15	13	16	11	1.2	0.8
	45	18	7	8	0.4	0.4
CAA	15	41	-	-	-	-
	45	33	-	-	-	-
Alkaline	15	46	-	-	-	-
	45	39	-	-	-	-
Hydro	15	47	-	-	-	-
	45	48	-	-	-	-

The detected amount of phosphor in PAA is so high that calculations yield no hydroxyls at the outer surface. Although we assume in the calculations that all P and S species are in the form of phosphates and sulphates, different complexes might be present. It is possible, for example, that hydrated forms of aluminium phosphate (e.g. AlH_2PO_4 ion) are present at the surface. Since the (Pauling) electronegativity of phosphor, sulphur and hydrogen is similar [36], this differences are not readily distinguished by XPS.

4.3.4 Surface Interaction with DETA

Adsorption experiments were followed by Fourier transform infrared spectroscopy (FTIR) and XPS measurements. Representative spectra of FTIR and XPS survey are shown in Fig. A1 and Fig. A2 in Appendix A. Both reveal the presence of nitrogen on all oxides, indicating chemisorption. However, the type of interaction cannot be extracted from these data. Therefore, high-resolution XPS spectra for Al2p, O1s, C1s and N1s have been recorded. The relative intensities of the different peaks suggest a comparable amount of chemisorbed molecules on the surfaces.

The asymmetric shape of the N1s peak in Fig. 4.5 clearly indicates that multiple components are present. Although the binding energies cannot be assigned to specific bonding, the type of interaction and surface sites can be estimated by their relative position, since the higher the partial charge on nitrogen, the higher its binding energy. Hence, Brønsted interactions that involve charge generally correspond to a higher binding energy than dipole-dipole Lewis interactions [37].

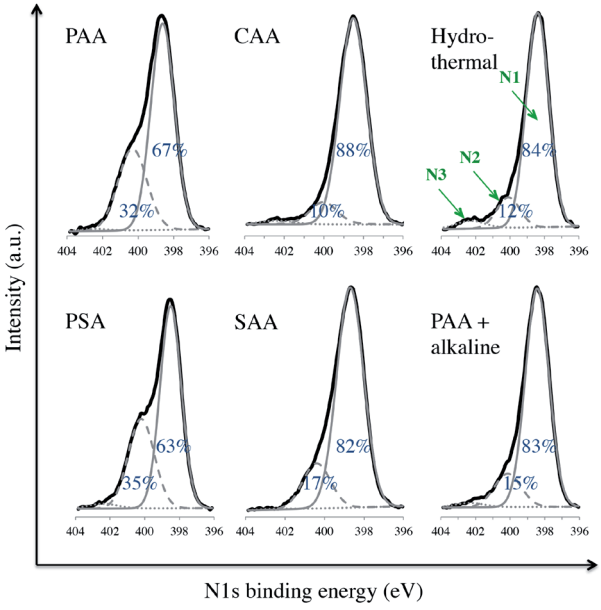

Figure 4.5: High-resolution XPS spectra of N1s after adsorption of DETA on barrier-type anodic oxides. N3 area is 4 area-% for the hydrothermal oxide and 1-2 area-% for all the other oxides.

The N1s spectra was fitted using three components of similar full width at half-maximum (FWHM) of 1.6 ±0.2 eV. Fitting shows that the three components have similar binding energies of 398.6 ±0.3, 400.2 (±0.2) and 402.4 (±0.2) eV for all oxides. These are assigned N1, N2 and N3, respectively (as indicated in Fig. 4.5).

A significant difference between the pre-treatments is observed for the second component, N2. Oxides prepared in phosphoric acid (PSA and PAA, Fig. 4.5) exhibit a significantly larger relative amount of this component. Its binding energy of 400.2 (±0.2) eV corresponds to values reported for a Lewis acid-base interaction and associated hydrogen bonding to a more acidic surface hydroxyl group [38]. Since hydroxylated aluminium is known for its amphoteric nature [39], hydroxyl groups on its surface can function as both acid and basic sites for interaction. This double functionality may explain why all oxides are able to interact with the basic nitrogen. However, the higher ratio of bonding to oxides with phosphates clearly suggests that these more acidic surface sites facilitate bonding, as illustrated in Fig. 4.6 (2) - (a) and (b).
However, the main component in all oxides is N1. Bolouri et al. [40] and Watts et al [41] assigned it to a non-interacting amine nitrogen, while Affrossman et al. [5] assigned it to a weak Brønsted or Lewis acid site. Since each DETA molecule has one secondary and two primary nitrogen atoms, this large component is likely to represent excessive, unbound, nitrogen atoms. Assuming that only one nitrogen-atom is bound to the surface of the oxide, the ratio between N1 and N2 should be 2:1. While this is true for PAA and PSA, the other oxides exhibit much larger ratios. Since the surface has been rinsed in pure solvent and only attached molecules are left, it is possible that some nitrogen atoms are coordinated to the surface by weak hydrogen bonding to surface hydroxyls (Fig. 4.6 (1)). Such interactions will have a binding energy that is close to the unbound molecules [38] .
The component with the highest binding energy, N3, represents the highest partial charge. Hence, N3 can be attributed to protonation of the nitrogen atom, resulting in Brønsted type interaction. The contribution of this component is relatively low and

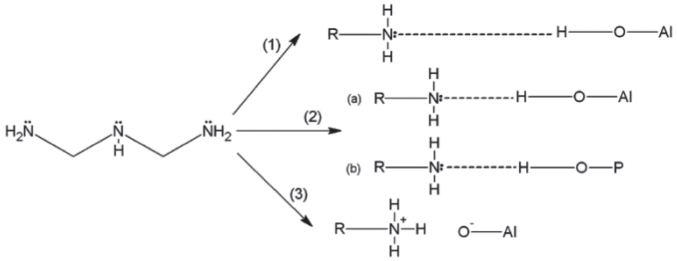

Figure 4.6: Proposed molecular interactions between DETA and surface sites of increasing acidity on barrier-type anodic oxides. Interactions (1), (2) and (3) correspond to components N1, N2 and N3 in Fig.4.5.

was previously found to increase with the hydroxyl fraction [42]. This is also a minor component in this study, with the largest contribution for the hydrothermal oxide (4 area-%) and 1-2 area-% for all the other oxides. Although we assumed that bonding exclusively occurs with surface hydroxyls, other types of bonding are also possible. For example, incompletely coordinated surface cationic sites (Al^{3+}) are also acidic sites that can facilitate Brønsted interactions with a similar binding energy as N3.

4.4 Conclusions

We investigated the surface chemistry of barrier-type anodic oxides from Cr(VI)-free electrolytes, and the effect of anion incorporation on the interaction with DETA.
A model was developed to calculate the relative amounts of surface species, accounting for the incorporation of phosphates and sulphates anions from the electrolytes. It then followed that the hydroxyl fraction varied from 0 to 50 %, increasing in the order PAA < PSA < HcPSA < SAA < CAA < Alkaline < Hydrothermal. Calculations showed that almost 40% of the surface species in PAA oxide are phosphates (PO_4^{3-}), while about 15% are sulphates (SO_4^{2}) in SAA, with a phosphate concentration significantly higher close to the surface, while the sulphate concentration remains relatively constant. AES and XPS results both indicate that the incorporation of phosphates is somewhat inhibited when anodizing is performed in a mixture of phosphoric- and sulphuric acids, however, the reason for this behaviour is not yet understood.
Decomposition of the XPS N1s signal indicated that interaction between the amine and the surface oxides is mainly Lewis in nature. The larger extent of interaction for oxides prepared by phosphoric acid strongly suggests that the incorporation of acidic anions from the electrolyte is affects the interaction with a basic amine hardener. These results illustrate the need to consider changes in the surface chemistry in the selection of Cr(VI)-free alternatives in terms of subsequent polymer-oxide interaction, especially since both adhesion and delamination processes are often initiated on a molecular level.

4.5 References

1. Sheasby, P.G. and R. Pinner, *Surface Treatment and Finishing of Aluminium and its Alloys*. 6th ed. 2001., England, : Finishing Publications Ltd.
2. Critchlow, G.W. and D.M. Brewis, *Review of surface pre-treatments for aluminium alloys.* International Journal of Adhesion and Adhesives, 1996. **16**(4): p. 255-275.
3. U.S. Department of Health and Human Services, Registry of Toxic Effects of Chemical Substances (RTECS, online database). National Toxicology Information Program, National Library of Medicine, Bethesda, MD. 1993.
4. van den Brand, J., et al., Interaction of Anhydride and Carboxylic Acid Compounds with Aluminum Oxide Surfaces Studied Using Infrared Reflection Absorption Spectroscopy. Langmuir, 2004. **20**(15): p. 6308-6317.
5. Affrossman, S., R. F. Comrie, and S. M. MacDonald, *Interaction of a model epoxy resin compound, diethanolamine, with aluminium surfaces studied by static SIMS and XPS.* Journal of the Chemical Society, Faraday Transactions, 1998. **94**(2): p. 289-294.
6. Alexander, M.R., et al., Interaction of carboxylic acids with the oxyhydroxide surface of aluminium: poly(acrylic acid), acetic acid and propionic acid on pseudoboehmite. Journal of Electron Spectroscopy and Related Phenomena, 2001. **121**(1–3): p. 19-32.
7. Mullins, W.M. and B.L. Averbach, *The electronic structure of anodized and etched aluminum alloy surfaces.* Surface Science, 1988. **206**(1–2): p. 52-60.
8. Cordier, F. and E. Ollivier, X-ray photoelectron spectroscopy study of aluminium surfaces prepared by anodizing processes. Surface and Interface Analysis, 1995. **23**(9): p. 601-608.
9. Lovreček, B., Z. Bolanča, and O. Korelić, *Surface charge and interaction with sulphate ions at the boehmitized aluminum.* Surface and Coatings Technology, 1987. **31**(4): p. 351-364.
10. Özkanat, Ö., et al., *Scanning Kelvin Probe Study of (Oxyhydr)oxide Surface of Aluminum Alloy.* The Journal of Physical Chemistry C, 2011. **116**(2): p. 1805-1811.
11. Bolanča, Z., O. Korelić, and B. Lovreček, *Surface charge at the oxide-covered aluminium-electrolyte interface.* Surface Technology, 1984. **22**(4): p. 323-329.
12. van den Brand, J., et al., Correlation between hydroxyl fraction and O/Al atomic ratio as determined from XPS spectra of aluminium oxide layers. Surface and Interface Analysis, 2004. **36**(1): p. 81-88.
13. Alexander, M.R., et al., *The distribution of hydroxyl ions at the surface of anodic alumina.* Surface and Interface Analysis, 2003. **35**(8): p. 649-657.
14. Solomon, J.S. and D.E. Hanlin, AES and SEM characterization of anodized aluminum alloy adherends for adhesive bonding application. Applications of Surface Science, 1980. **4**(3–4): p. 307-323.
15. Dorsey, G.A., The Characterization of Anodic Aluminas: I . Composition of Films from Acidic Anodizing Electrolytes. Journal of The Electrochemical Society, 1966. **113**(2): p. 169-172.
16. Murphy, O.J., et al., *Spectroscopic Investigations of Porous and Sealed Anodic Alumina Films.* Journal of The Electrochemical Society, 1989. **136**(11): p. 3518-3525.
17. González-Rovira, L., et al., Direct sub-nanometer scale electron microscopy analysis of anion incorporation to self-ordered anodic alumina layers. Corrosion Science, 2010. **52**(11): p. 3763-3773.

18. Ono, S., H. Ichinose, and N. Masuko, The high resolution observation of porous anodic films formed on aluminum in phosphoric acid solution. Corrosion Science, 1992. **33**(6): p. 841-850.
19. McCafferty, E. and J.P. Wightman, Determination of the concentration of surface hydroxyl groups on metal oxide films by a quantitative XPS method. Surface and Interface Analysis, 1998. **26**(8): p. 549-564.
20. Baer, D.R., et al., *Comparison of the sputter rates of oxide films relative to the sputter rate of SiO2.* Journal of Vacuum Science & Technology A, 2010. **28**(5): p. 1060-1072.
21. De Laet, J., et al., Determination of the depth resolution of Auger electron spectroscopy depth profiles of anodic barrier oxide films on differently pretreated aluminium substrates. Surface and Interface Analysis, 1994. **22**(1-12): p. 175-180.
22. Parkhutik, V.P., The initial stages of aluminium porous anodization studied by Auger electron spectroscopy. Corrosion Science, 1986. **26**(4): p. 295-310.
23. Sun, T.S., et al., *Interpretation of AES depth profiles of porous Al anodic oxides.* Applications of Surface Science, 1980. **5**(4): p. 406-425.
24. Ferrer, S., A.M. Baró, and J.M. Rojo, *Auger study of phosphorus and phosphorus compounds on a copper surface.* Surface Science, 1978. **72**(2): p. 433-443.
25. Sulka, G.D., Highly Ordered Anodic Porous Alumina Formation by Self-Organized Anodizing, in Nanostructured Materials in Electrochemistry. 2008, Wiley-VCH Verlag GmbH & Co. KGaA. p. 1-116.
26. Rotole, J.A. and P.M.A. Sherwood, *Aluminum Phosphate by XPS.* Surface Science Spectra, 1998. **5**(1): p. 60-66.
27. Treverton, J.A. and N.C. Davies, *XPS studies of dc and ac anodic films on aluminium formed in sulphuric acid.* Electrochimica Acta, 1980. **25**(12): p. 1571-1576.
28. Grzybowska, B., et al., *Chromium Oxide/Alumina Catalysts in Oxidative Dehydrogenation of Isobutane.* Journal of Catalysis, 1998. **178**(2): p. 687-700.
29. Alexander, M.R., G.E. Thompson, and G. Beamson, Characterization of the oxide/hydroxide surface of aluminium using x-ray photoelectron spectroscopy: a procedure for curve fitting the O 1s core level. Surface and Interface Analysis, 2000. **29**(7): p. 468-477.
30. Sherwood, P.M.A., *Introduction to Studies of Aluminum and its Compounds by XPS.* Surface Science Spectra, 1998. **5**(1): p. 1-3.
31. Hauffman, T., et al., Study of the Self-Assembling of n-Octylphosphonic Acid Layers on Aluminum Oxide. Langmuir, 2008. **24**(23): p. 13450-13456.
32. Wielant, J., et al., Influence of the Iron Oxide Acid–Base Properties on the Chemisorption of Model Epoxy Compounds Studied by XPS. The Journal of Physical Chemistry C, 2007. **111**(35): p. 13177-13184.
33. Blajiev, O.L., et al., XPS study of the assembling morphology of 3-hydroxy-3-phosphono-butiric acid tert-butyl ester on variously pretreated Al surfaces. Progress in Organic Coatings, 2008. **63**(3): p. 272-281.
34. Kim, B., et al., *The Effect of AlPO4-Coating Layer on the Electrochemical Properties in LiCoO2 Thin Films.* Journal of The Electrochemical Society, 2006. **153**(9): p. A1773-A1777.

35. Nefedov, V.I. and N.G. Shartse, *X-ray photoelectron spectroscopy of solid surfaces*. 1988, Utrecht :: VSP.
36. Burrows, A., *Chemistry3 : introducing inorganic, organic and physical chemistry*. 2009, Oxford; New York: Oxford University Press.
37. Marsh, J., et al., The nature of the surface acidity of anodised titanium: an XPS study using 1,2-diaminoethane. Applied Surface Science, 1996. **99**(4): p. 335-343.
38. Marsh, J., et al., Interaction of epoxy model molecules with aluminium, anodised titanium and copper surfaces: an XPS study. Applied Surface Science, 1998. **133**(4): p. 270-286.
39. Barthés-Labrousse, M.G., *Acid–base characterisation of flat oxide-covered metal surfaces.* Vacuum, 2002. **67**(3–4): p. 385-392.
40. Bolouri, H., R.A. Pethrick, and S. Affrossman, *Bonding of a simulated epoxy resin to aluminium surfaces studied by XPS.* Applications of Surface Science, 1983. **17**(2): p. 231.
41. Watts, J.F., A. Rattana, and M.-L. Abel, Interfacial chemistry of adhesives on hydrated aluminium and hydrated aluminium treated with an organosilane. Surface and Interface Analysis, 2004. **36**(11): p. 1449-1468.
42. Salgin, B., et al., *Role of Surface Oxide Properties on the Aluminum/Epoxy Interfacial Bonding.* The Journal of Physical Chemistry C, 2013. **117**(9): p. 4480-4487.

CHAPTER 5

Effect of anodic aluminium oxide chemistry on adhesive bonding of epoxy

This chapter is published as a scientific paper:
Abrahami, S.T., Hauffman, T., de Kok, J.M.M., Mol, J.M.C. and Terryn, H.,
J. Phys. Chem C, (2016) 120(35): p. 19670-19677.

ABSTRACT

The transition to Cr(VI)-free production is a great challenge in the global aerospace industry that currently still relies on Cr(VI)- based preparation of aluminium for bonding. Proper surface pre-treatment is a prerequisite for strong and durable adhesive joints. Despite decades of experience, the nature and contribution of the different adhesion forces between the aluminium and organic adhesive remain under discussion. Herein we studied the adhesion of epoxy resin as a function of the surface chemistry of barrier-type anodic oxides prepared in sulphuric acid (SAA), phosphoric acid (PAA) and mixtures of phosphoric-sulphuric acids (PSA) and chromic acid (CAA) at different anodizing temperatures. X-ray photoelectron spectroscopy (XPS) data measured on model specimens were curve-fitted to calculate the relative amounts of O^{2-}, OH^{-}, PO_4^{3-} and SO_4^{2-} species at the surface. The amounts of these species were then related to the mechanical performance of the joint measured by the floating roller peel test. Results show that significant initial adhesion is achieved without mechanical interlocking, and independent of the type of electrolytes used for the pre-treatment. Conversely, bonding stability under wet conditions is highly influenced by the surface chemistry. The wet adhesion strength increases with the hydroxyl concentration at the aluminium (oxide) surface, indicating that the interfacial bonding is established through these surface hydroxyls. Phosphate and sulphate anions were not found to contribute to interfacial bonding with this type of adhesive.

5.1 Introduction

Adhesive bonding is one of the oldest techniques used to join different components [1]. This type of structure is formed when an adhesive undergoes a physical or chemical hardening reaction to join two substrates through surface adherence (adhesion) and internal strength (cohesion) [2]. Since the 1940s, adhesive bonding has been used to prepare different structural parts of many commercial aircrafts [3].

To assure the life-long integrity of the structures, bonded panels are first subjected to a multistep pre-treatment. The surface is first degreased to remove superficial contaminations. In the American aerospace industry, this is followed by an etch that removes the natural oxide and produces a new oxide with finger like morphology [4]. Phosphoric acid anodizing (PAA) then follows. This electrochemical oxidation of aluminium under direct current (DC) conditions results in the formation of a porous oxide that is separated from the substrate by a thin and compact barrier layer [5]. The standard pre-treatment that has emerged in the European aerospace industry is based on CSA etching and chromic acid anodizing (CAA) which produces a more compact oxide than PAA, but offers an advantageous corrosion resistance.

A fundamental understanding of adhesively bonded joints requires an examination on both macroscopic and microscopic levels. On a microscopic level, adhesion is only achieved if the adhesive (or primer) comes in molecular contact with the substrate. Hence, physical absorption is a prevailing requirement. Obtaining such contact requires appropriate wetting of the surface. This is typically achieved by simple surface degreasing [5]. However, this alone does not guarantee adhesion. Initial- and long-term adhesion strength depends on the formation of physical and chemical bonds between the substrate and the adhesive [6]. Numerous studies have shown that bonding between aluminium oxides and organic resins often involves relatively weak intermolecular forces [7-10]. The kind of bond that is formed and its strength depend on the chemical nature of the substrate, the type of organic resin and their compatibility [11]. On a macroscopic level, mechanical forces originating from the hardening of the adhesive inside voids, cavities and pores at the surface promote adhesion [11, 12] . This is typically referred to as “mechanical interlocking” [4]. The interface can then be considered as a composite phase that enables better stress distribution and can arrest the propagation of cracks [13].

Strict international regulations on hexavalent chromium (Cr(VI) now encourage the transition to Cr(VI)-free surface pre-treatments, thereby eliminating this carcinogenic and hazardous substance [14]. Candidate replacements include anodizing in sulphuric acid (SAA), phosphoric acid (PAA) and mixtures of phosphoric-sulphuric acids (PSA). Pore formation during anodizing is controlled by the type of electrolyte, concentration, temperature and applied potential/current scheme. Depending on the combination of these parameters, oxides with different characteristic morphologies will develop. This

includes variations in the porosity, the pore size and interpore distance, barrier layer and oxide thickness. In addition, anodizing in phosphoric and sulphuric acids leads to the incorporation of phosphate and sulphate anions into the oxide, thereby also changing its chemistry [15-17].
In spite of its extensive commercial history, the nature and contribution of the different adhesion forces acting at the oxide/resin interface remain under discussion. In the present study we examine to what extent changes in the surface chemistry affect adhesion. We isolate the chemical contribution by stopping the anodizing during the formation of the barrier-layer, thereby avoiding the formation of a porous oxide that would lead to additional mechanical interlocking.

5.2 Experimental Section

Two types of specimens were used in this study. Model (laboratory) specimens were used for XPS surface analysis and industrial test specimens for floating roller peel tests. Both preparation methods are detailed below.

5.2.1 Model Specimens for XPS Analysis.

Samples were cut from a 0.3 mm thick sheet of pure aluminium (99.99%, Hydro). To remove imperfections and provide a flat substrate for analysis purposes, specimens were electropolished. This was done after the substrate was etched in an aqueous solution of 25 g/l NaOH at 70 °C for 1 minute, followed by rinsing for 15 s with deionized water and then ultrasonically rinsed for an additional 3 min. The substrate was then electropolished for 6 min in a solution of 80 vol.% (absolute) ethanol and 20 vol.% perchloric acid, at a current density of 70 mA/cm^2 and 10 °C. Subsequently, it was rinsed following the above procedure, dried with compressed air and stored in a sealed plastic bag. Later, each sample was given one of the anodizing pre-treatments listed in Table 5.1.

Galvanostatic anodizing with SM120-25 power-supply (Delta Elektronika) equipped with an Ethernet interface connection to monitor the cell voltage. Model specimens were anodized in a three-electrode cell filled with 400 mL solution and two AA1050 aluminium cathodes for 4s at constant current density of 10mA/cm^2. After each of the described pre-treatments, the substrate was thoroughly rinsed for 15s with deionized water and then ultrasonically rinsed for an additional 3 min. Anodizing conditions were pre-selected to yield featureless anodic oxides by stopping the oxide growth at the end of the region in which the voltage was increasing linearly with time, the part which is associated with the formation of the barrier layer [18]. In order to limit atmospheric contamination samples were placed in the pre-vacuum chamber for analysis no longer than 10 min after the pre-treatment was completed.

Table 5.1: Summary of the electrolyte composition for the different surface pre-treatments.

Abbreviation	*Pre-treatment*	*Electrolyte composition*
PAA	Phosphoric Acid Anodizing	0.3M H_3PO_4
SAA	Sulphuric Acid Anodizing	*0.1M H_2SO_4
PSA	Phosphoric-Sulphuric Acid anodizing	0.3M H_3PO_4 and 0.1M H_2SO_4
HcPSA	High concentration Phosphoric-Sulphuric Acid anodizing	0.8M H_3PO_4 and 0.5M H_2SO_4
CAA	Chromic Acid Anodizing	0.4M CrO_3

* 0.05M was used for the preparation of the industrial specimens.

5.2.2 Panels for floating roller peel test

AA2024-T3 alclad (clad layer AA1230) aluminium test panels of 250 x 95 x 1.6 mm and 300 x 95 x 0.5 mm were used for the thick and thin sheets, respectively. Before specimens were given one of the pre-treatments in Table 5.1, they were degreased, alkaline etched and desmutted. Degreasing was achieved by wiping the panels with ethanol. This was followed by a 2 min. alkaline etching with 40 g/l P3 Almeco 51 (from Henkel) at 35°C and a 1 min. pickling with 35 vol.% HNO_3 at RT. After each step, the panel was thoroughly rinsed with running demineralized water, followed by 1 min. immersion rinsing in an agitated beaker of fresh demineralized water. Then the panels were anodized in one of the electrolytes listed in Table 5.1. Anodizing at constant current density of 5 mA/cm^2 was performed for 8s. Although the current density is lower than for the model specimens, the time is doubled, so that the final barrier layer thickness should be similar [19]. After anodizing, the panels were rinsed and dried with compressed air. The panels were then bonded (without primer) with FM 73 epoxy film adhesive (from Cytec Engineering Materials) within 10 min after the pre-treatment of the thin panel was completed. After bonding, the panels were stored in a sealed plastic bag for up to 24 hours before curing. Curing following the manufacturer instructions was achieved using a Joos hot plate press at 6 bar and 120°C for 75 min.

5.2.3 Analysis Methods

5.2.3.1 X-Ray Photoelectron Spectroscopy

XPS spectra were collected using a PHI5600 photoelectron spectrometer (Physical Electronics) with an Al *K*α monochromatic X-ray source (1486.71 eV of photons). The vacuum in the analysis chamber was approximately 5x10^{-9} Torr during measurements. High-resolution scans of the Al 2p, O 1s, C 1s, P 1s and S 2p photopeaks were

recorded from a spot size of 0.8 mm using pass energy of 23.5 eV and step size 0.1 eV. Measurements were performed at take-off angles of 45° and 15° with respect to the sample surface. The reproducibility of the measurements was verified by (at least) two repetitions.
XPS data was analysed using PHI Multipak software (V9.5.0.8). Before curve fitting, the energy scale of the XPS spectra was calibrated relative to the binding energy of adventitious hydrocarbons in the C1s peak at 284.4 eV. Curve fitting was done after a Shirley-type background removal, using mixed Gaussian (80–100%) – Lorentzian shapes.

5.2.3.2 Mechanical Testing

Floating roller peel tests were executed according to ASTM D3167 - 03a [20]. Of each bonded panel, three strips of 25 x 250 mm were cut with a diamond saw. After fixing the test strips in the apparatus, the unbound end of the specimen was attached to the lower head of the testing machine. The thin aluminium panel was then peeled off the thick panel with a speed of 100 mm/min. The peeling load versus head movement (or load versus distance peeled) was recorded. All tests were performed at ambient temperature. The first half of the specimen was peeled under dry conditions. Water was then applied at the crack-tip and the second half was peeled under wet conditions. Since only clear cohesive or adhesive failures were observed, failure modes were assigned by visual inspection.

5.2.3.3 Atomic Force Microscopy (AFM)

A Bruker Dimension Edge atomic force microscope was used in force tapping-mode to measure the roughness of selected samples. Commercially available SCANASYST-AIR cantilevers (70 kHz resonance frequency and 0.4 N/m force constant) were employed. Images were analysed by NanoScope Analysis software 1.5 using the surface roughness mode.

5.3 Results

5.3.1 Anodic Oxidation

The plot in Fig. 5.1 displays the average anodizing voltage measured at 4 and 8 s for model and tests panels, respectively, vs. the electrolyte temperature. Although larger scatter in some of the data points is caused by slight variations in the exposed surface area, the plot illustrates the dependence of the voltage on three factors: the electrolyte temperature, the nature of electrolyte and the substrate composition. The higher solubility of the oxide at higher temperatures leads to a linear decrease in the final voltage. Alternatively, a lower voltage is reached when the solvent action of the electrolyte is higher, as is the case with additions of phosphoric acid [21].

The purity level of a substrate is affecting the final voltages by changing the resistance to ionic transport [22]. Therefore the voltage needed to maintain the same current density is higher for 99.99% pure aluminium, compared to the 99.31% of the AA1230 Clad layer on AA2024-T3 [23]. Since the oxide layer thickness is proportional to the voltage (according to the general 1.2 nm/V relationship [18]), a different oxide thickness is expected for the different substrate compositions (even though the total current that passed during anodizing is the same). In both cases, however, anodizing was stopped at the end of the part in which the voltage raised linearly with time (not shown), to ensure ending before pores start to form.

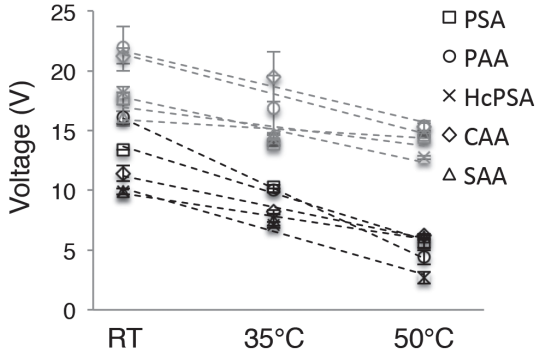

Figure 5.1: Average anodizing voltage vs. electrolyte temperature measured after 4 s and 8 s for pure (99.99%) aluminium (grey markers) and AA2024-T3 Clad (Clad layer AA1230, black markers), respectively. The dashed lines indicate trends.

5.3.2 Surface Roughness

AFM measurements were performed to check if there are significant variations in the surface roughness as a result of the anodizing temperature. Examples for typical AFM images are shown in Fig. 5.2 and Fig. 5.3 for PAA oxides prepared on AA2024-T3 clad. Although a scalloped morphology is observed due to prior etching, measurements show no significant difference between the surface roughness for anodizing at room temperature and at 50°C. Similar results were observed for the other pre-treatments.

For comparison, the surface roughness of a model specimen used for XPS measurements is given in Fig. 5.4 for a PSA oxide prepared at 35°C. Average results for the model specimens used for XPS surface analysis (electropolished and anodized) and the panels for floating roller peel test (etched, pickled and anodized) are listed in Table 5.2. Electropolished and anodized specimens can be considered relatively smooth. Although the surface is full of nanoscale etching pits that are caused by electropolishing, the average R_q, which is the root mean square of the surface roughness, is very low (4 nm) and is similar on localized (1x1 μm) and a larger surface area (10 x10 μm). This measured roughness is comparable to the roughness found after electropolishing under similar conditions [24].

Table 5.2: Average root mean-square (RMS) roughness as measured by AFM.

Sample	Image Rq (10 x 10 µm) (nm)	Image Rq (1 x 1 µm) (nm)
Electropolished and anodized	4	4
Etched, pickled and anodized	50	20

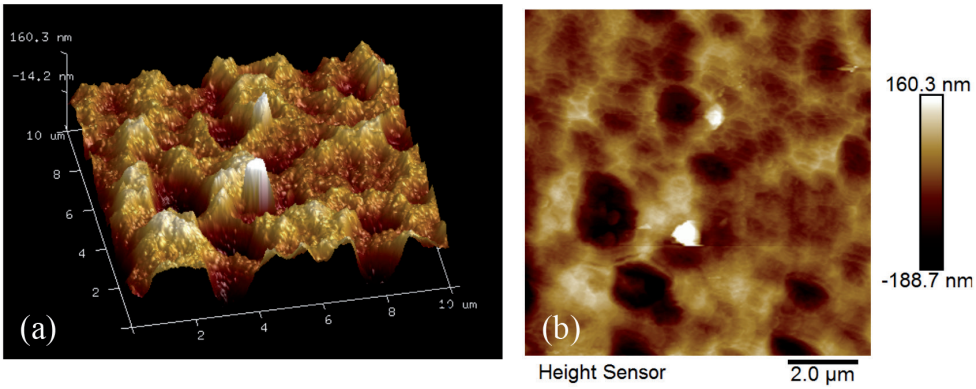

Figure 5.2: 3D (a) and height (b) AFM images of AA2024-T3 after alkaline etching and acid pickling and anodizing (PAA, RT). Image R_q = 48 nm, R_q 1µm x1µm = 18 nm.

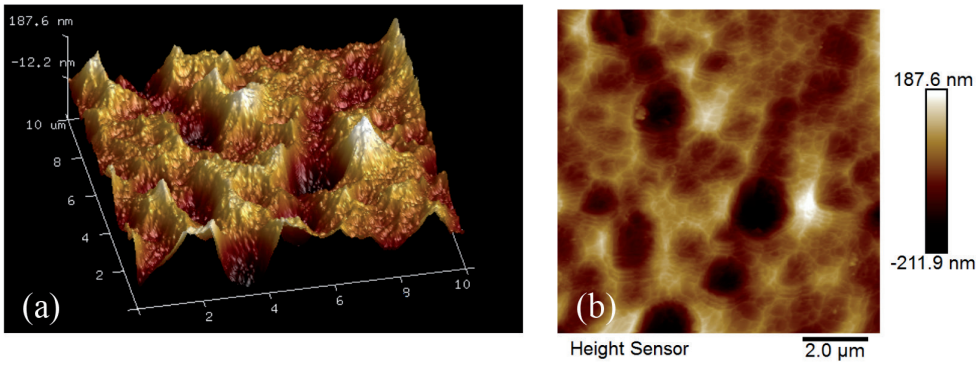

Figure 5.3: 3D (a) and height (b) AFM images of AA2024-T3 after alkaline etching, acid pickling and anodizing (PAA, 50°C). Image R_q = 52 nm, R_q 1µm x1µm = 14 nm.

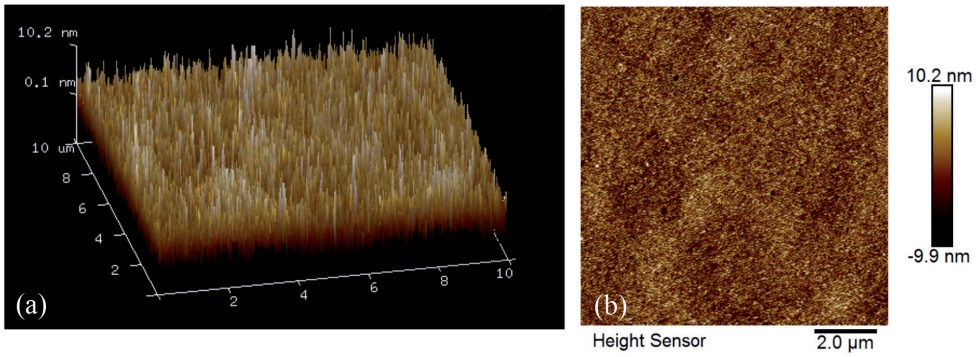

Figure 5.4: 3D (a) and height (b) AFM images of pure aluminium after electropolishing and anodizing (PSA, 35°C). Image R_q= 3 nm, R_q 1µm x1µm = 3 nm.

5.3.3 Surface chemistry analysis

Surface chemistry on model panels was characterized by angle-resolved X-ray photoelectron spectroscopy (XPS). To ensure that no other contaminations are present, a survey spectrum was acquired before each high-resolution spectrum. Typical XPS survey spectra of the different types of anodic oxides are shown in Fig. 5.5. Incorporation of electrolyte-derived anions is indicated by the presence of phosphor and sulphur in the corresponding oxides.

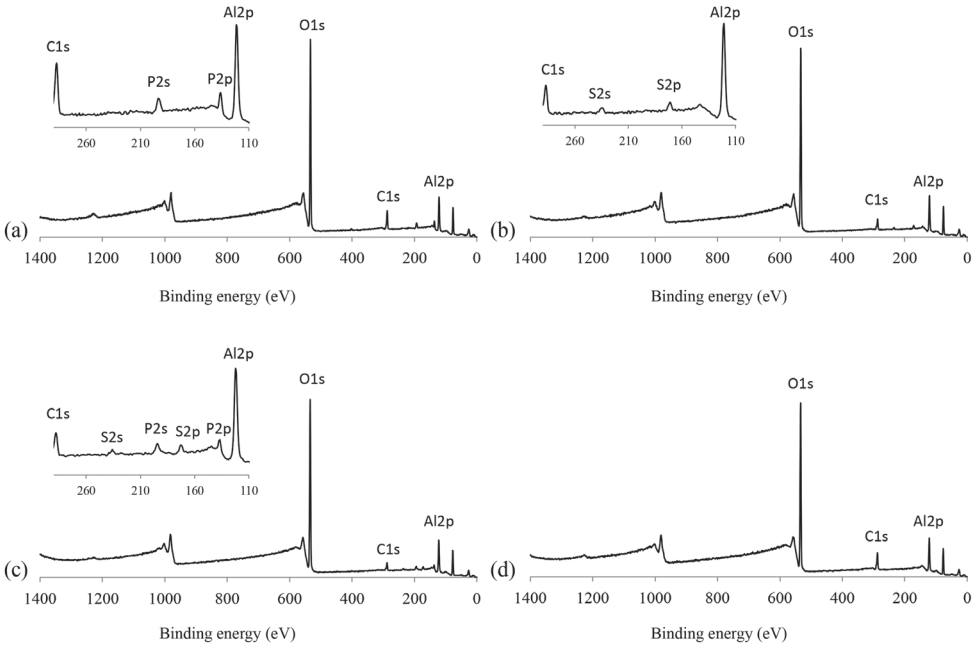

Figure 5.5: XPS survey spectra of (a) PAA, (b) SAA, (c) HcPSA, and (d) CAA barrier-type oxides on model panels.

Next, high-resolution spectra of O 1s, C 1s, Al 2p, S 2p and P 2s were measured (Fig. 5.6, black line). These were then curve-fitted using the method presented in detail in our previous work [25].

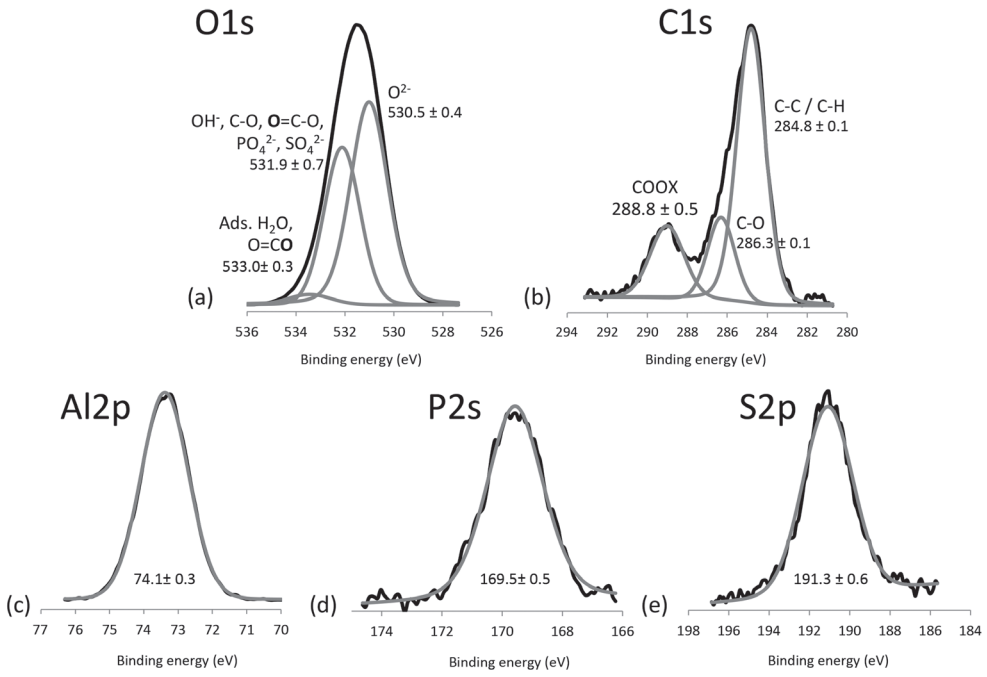

Figure 5.6: Fitted high-resolution XPS spectra with the deconvolution of the O1s and C1s peaks and the average measured binding energy. The measured spectrum is shown in black and the fitted spectrum/components are indicated with the grey lines, with the average measured binding energy (in eV).

The fitted intensity areas were then used to find a solution for the amount of OH^-, PO_4^{3-} and SO_4^{2}, while taking into account all the present species with an overlapping binding energy (CO-, COOX-, PO_4^{3-}, SO_4^{2-}, OH^- and O^{2-}) in the O 1s photopeak. The relative amounts of O^{2-}, OH^-, PO_4^{3-} and SO_4^{2-} (in %) were then determined by the ratio, as presented in eq. (1) for OH^-.

$$OH^-(\%) = \frac{C_{OH^-}}{C_{OH^-} + C_{O^{2-}} + (4 \times C_{PO_4^{3-}}) + (4 \times C_{SO_4^{2-}})} \times 100 \quad \text{Eq. (1)}$$

Calculation results for anodizing at room temperature (RT), 35°C and 50°C are summarized in Fig. 5.7, for take-off angles of θ =15° and 45°. All oxides are mainly composed of aluminium in the Al_2O_3 state, with different amounts of hydroxyls. Results show that anion incorporation has a significant effect on the chemical composition

of the corresponding anodic oxides. Incorporation of phosphate and sulphate anions from the respective electrolytes is the main cause for their reduced hydroxyl fraction. Since phosphate incorporation is relatively high, PAA anodizing results in the lowest amount of OH^-, followed by PSA, HcPSA, SAA and CAA. This trend is valid for all anodizing temperatures. More phosphates are found at the surface of the oxide in PAA than sulphates in SAA. However, when the two acids are used together (as in PSA and HcPSA), the incorporation of both anions is lower than in a single component electrolyte, with phosphates incorporation dropping more than sulphates.

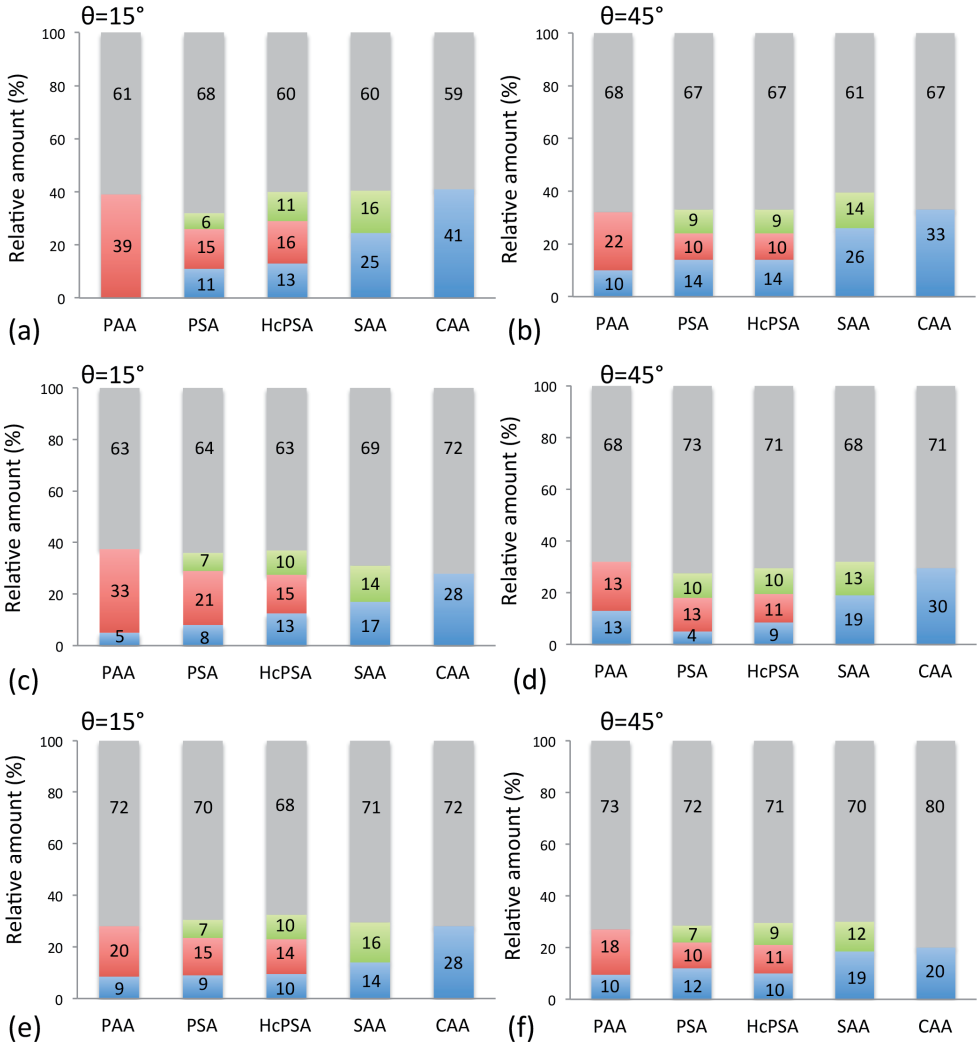

Figure 5.7: Calculated average percentage of O^{2-} (grey), OH^- (blue), SO_4^{2-} (green) and PO_4^{3-} (red) species on the differently prepared oxide layers at take-off angles of θ =15° and 45°. Anodizing was performed at room temperature (a, b), 35°C (c, d) and 50°C (e, f).

5.3.4 Floating Roller Peel Tests

Mechanical performance was evaluated by measuring two types of peel strengths: dry and wet peel. Dry peel represents the initial peel strength of the joint. Wet peel represents the performance under the presence of water at the interface by spraying water at the crack tip during testing. The measured (average) strengths for both tests are shown in Fig. 5.8, displayed as a function of the electrolyte temperature. As seen in Fig. 5.8 (a) the dry peel strength does not vary much between the different pre-treatments and although some increments are registered at higher temperatures, they are relatively small. On the other hand, there is a significant increase in the wet peel strength for anodizing at higher temperatures (Fig. 5.8 (b)). This trend is observed for all types of electrolyte. Moreover, there is a significant difference between the performances of the different types of oxides under wet conditions. The wet peel strengths after CAA anodizing is the best, while PAA and PSA oxides perform the worst.

Visual post inspection of the panels revealed a distinct behaviour. All panels exhibited a cohesive failure after dry peel testing (Fig. 5.9), with the yellow adhesive clearly visible on both sides of the joint. Surprisingly, despite a wide range of performances (maximum wet peel is 143 N/25 mm for CAA at 50 °*C* and minimum is 9 N/25 mm for PAA at RT), wet failure always occurred at the interface. This can be concluded by the shiny metal appearance of the aluminium substrate on one side of the thin peeled strip and what looks like an intact adhesive on the other side of the joint (Fig. 5.9). This distinctive behaviour was observed on all the tested panels, independent of the pre-treatment.

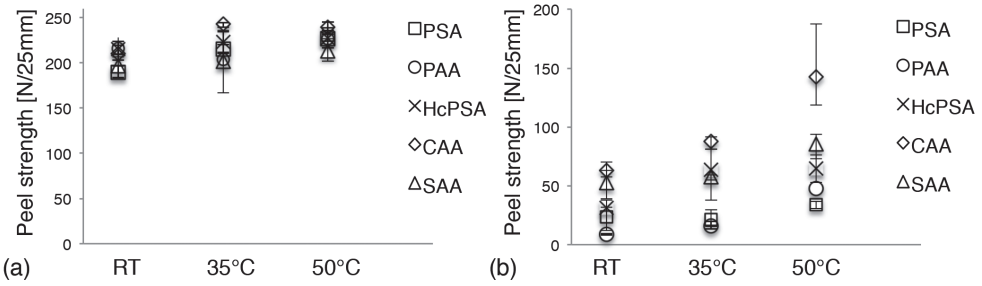

Figure 5.8: Average measured peel strength under dry (a) and wet (b) conditions. Range bars indicate the maximum and minimum measured values.

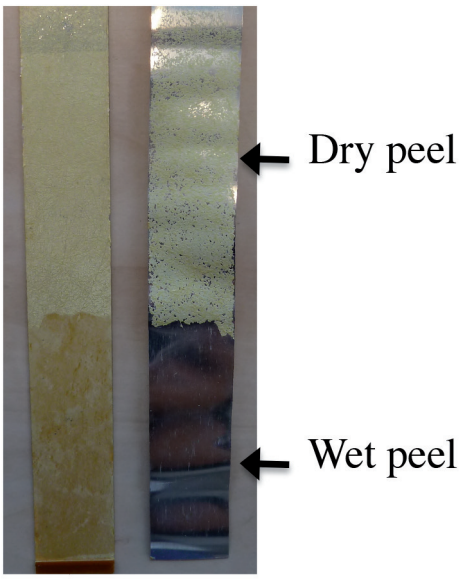

Figure 5.9: Representative macroscopic images of the peeled panels with the surfaces visible on the thick (left) and thin (right) adherends. The dry (top) part of the panel exhibits cohesive failure, with the yellow adhesive visible on both sides of the joint. On the bottom part, the aluminium substrate is fully visible on the thin panels that were peeled under wet condition, indicating an interface failure.

5.4 Discussion

Although the final anodizing voltage is different for model and peel panels, we presume that the incorporation of anions is not significantly affected by the short time and voltage (hence also thickness) variances. A comparison between the calculated hydroxyl percentage and the peel strengths is carried out in Fig. 5.10, for anodizing at RT, 35°C and 50°C (Fig. 5.7 (a), (b) and (c), respectively). At all temperatures, the dry peel strength of the different oxides is similar and independent of the amount of hydroxyls. Conversely, there is a positive linear correlation between an increased amount of hydroxyls and the wet peel strength. The dashed lines in Fig. 5.8 indicate this trend. Since the amount of surface hydroxyls depends on the electrolyte, the wet peel increases in the same trend as the calculated OH^-, namely increasing in the following order: PAA < PSA, HcPSA < SAA < CAA, at each temperature. These results indicate that interfacial bonding with epoxy proceeds through surface hydroxyls and that phosphate and sulphate anions do not contribute to interfacial bonding with this type of adhesive. These findings show that interfacial bonding between anodic oxides and epoxy proceeds similarly to that on native and chemically grown oxides that contain no "contamination" anions [26, 27]. Similarly to the finding by Rider et al. [28], we show that the amount of surface hydroxyls does not alter the failure mechanism. However, the results from both studies differ in the sense that in our study the hydroxyl fraction significantly affects bonding

with FM 73 adhesive, while the authors of the previous study did not find such effect. We suggest that the effect was concealed by large variation in the surface roughness. This affirms the need to study the effect of surface chemistry on the featureless oxides.

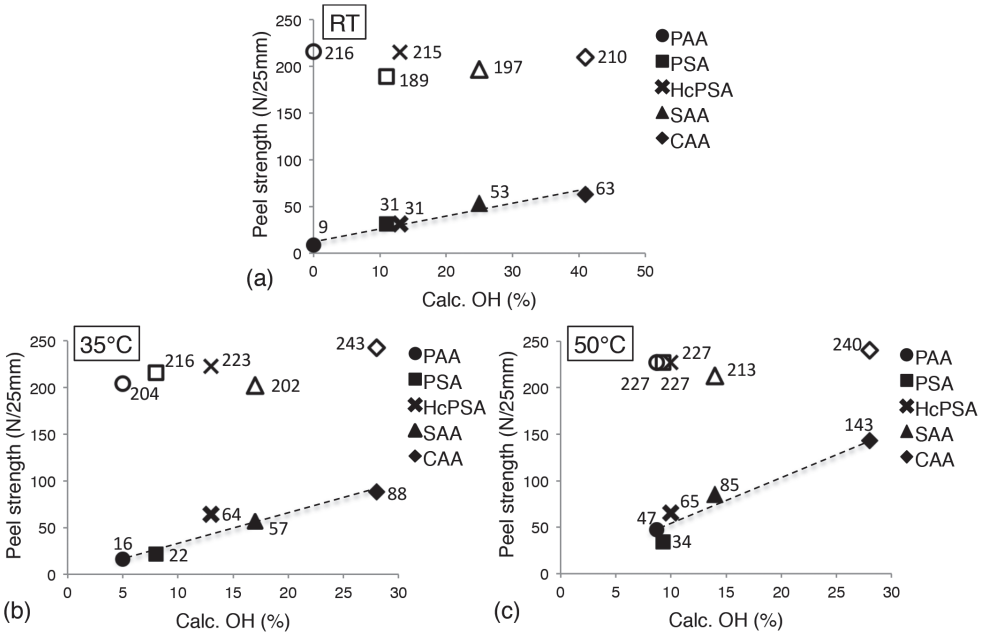

Figure 5.10: Average dry (empty markers) and wet (filled markers) peel strength vs the calculated hydroxyl percentage at the surface (θ=15°) on barrier-type oxides after anodizing at RT (a), 35°C (b) and 50°C (c).

These experimental results also confirm previous theoretical calculations. A modelled interaction using density functional theory (DFT) calculations by Semoto et al. [29] predicts that the hydroxyl groups on both the oxide and the epoxy sides are the reacting entities, typically forming hydrogen bonds across the interface. Since this type of bond is not stable in the presence of water, most of the adhesion is lost when water enters the interface, with the force necessary to separate the joint proportional to the amount of interactions and, hence, the amount of hydroxyls. Clearly the remaining peel strength in wet conditions indicates that some stable bonds are present, which increase proportionally with the fraction of surface hydroxyls.

Additionally, there is a clear positive effect between a higher anodizing temperature and mechanical performance. For PAA oxides, this can be linked to the increase in the amount of hydroxyls with temperature, leading to an approximately 5-fold increase in the wet peel strength. While the wet peel strength of the remaining pre-treatments also increases, their calculated hydroxyl fraction did not vary much with temperature (and even slightly decreased, as in the case of CAA and SAA oxides (Fig. 5.2)). As AFM

measurements confirm, this is not caused by an increased surface roughness at higher temperatures.

5.5 Conclusions

This is the first study in which the adhesion of anodic oxide films has been related to their surface chemistry. Experimental results verify that significant initial (dry) adhesion is achieved without mechanical interlocking and independent of the anodizing electrolyte. Conversely, we demonstrate that wet adhesion of featureless anodic oxides increases with anodizing temperature irrespective of the electrolyte and that the wet peel strength is highly influenced by the surface chemistry of the oxide. Since a clear correlation between the amount of hydroxyls and the wet peel strengths was found, it appears that interfacial bonding proceeds through the surface hydroxyls. Therefore, wet adhesion strength is also inversely correlated with the amount of phosphates and sulphates that are incorporated into the oxide by anodizing in phosphoric and sulphuric acids.

5.6 References

1. Brockmann, W., et al., *Adhesive Bonding*. 2009: Wiley-VCH Verlag GmbH & Co. KGaA. I-XVIII.
2. Brockmann, W., O.D. Hennemann, and H. Kollek, *Surface properties and adhesion in bonding aluminium alloys by adhesives.* International Journal of Adhesion and Adhesives, 1982. **2**(1): p. 33-40.
3. Higgins, A., *Adhesive bonding of aircraft structures.* International Journal of Adhesion and Adhesives, 2000. **20**(5): p. 367-376.
4. Venables, J.D., et al., *Oxide morphologies on aluminum prepared for adhesive bonding.* Applications of Surface Science, 1979. **3**(1): p. 88-98.
5. Critchlow, G.W. and D.M. Brewis, *Review of surface pre-treatments for aluminium alloys.* International Journal of Adhesion and Adhesives, 1996. **16**(4): p. 255-275.
6. Brockmann, W., et al., *Adhesion in bonded aluminium joints for aircraft construction.* International Journal of Adhesion and Adhesives, 1986. **6**(3): p. 115.
7. van den Brand, J., et al., Interaction of Ester Functional Groups with Aluminum Oxide Surfaces Studied Using Infrared Reflection Absorption Spectroscopy. Langmuir, 2004. **20**(15): p. 6318-6326.
8. van den Brand, J., et al., Interaction of Anhydride and Carboxylic Acid Compounds with Aluminum Oxide Surfaces Studied Using Infrared Reflection Absorption Spectroscopy. Langmuir, 2004. **20**(15): p. 6308-6317.
9. Mercier, D., J.C. Rouchaud, and M.G. Barthés-Labrousse, Interaction of amines with native aluminium oxide layers in non-aqueous environment: Application to the understanding of the formation of epoxy-amine/metal interphases. Applied Surface Science, 2008. **254**(20): p. 6495-6503.
10. Salgin, B., et al., *Role of Surface Oxide Properties on the Aluminum/Epoxy Interfacial Bonding.* The Journal of Physical Chemistry C, 2013. **117**(9): p. 4480-4487.
11. Packham, D.E., *Theories of Fundamental Adhesion*, in *Handbook of Adhesion Technology*, L.F.M. Da Silva, A. Öchsner, and R.D. Adams, Editors. 2011, Springer-Verlag: Berlin Heidelberg.
12. McBain, J.W. and D.G. Hopkins, *On Adhesives and Adhesive Action.* The Journal of Physical Chemistry, 1924. **29**(2): p. 188-204.
13. Kinloch, A.J., M.S.G. Little, and J.F. Watts, *The role of the interphase in the environmental failure of adhesive joints.* Acta Materialia, 2000. **48**(18–19): p. 4543-4553.
14. OSHA, Toxic and Hazardous Substances in Occupational Exposure to Hexavalent Chromium. 2006, United States Department of Labor.
15. Xu, Y., et al., Anion incorporation and migration during barrier film formation on aluminium. Corrosion Science, 1987. **27**(1): p. 83-102.
16. Takahashi, H., et al., Distribution of Anions and Protons in Oxide Films Formed Anodically on Aluminum in a Phosphate Solution. Journal of The Electrochemical Society, 1984. **131**(8): p. 1856-1861.
17. Parkhutik, V.P., The initial stages of aluminium porous anodization studied by Auger electron spectroscopy. Corrosion Science, 1986. **26**(4): p. 295-310.
18. Sheasby, P.G. and R. Pinner, *Surface Treatment and Finishing of Aluminium and its Alloys*. 6th ed. 2001., England: Finishing Publications Ltd.

19. Wood, G.C. and J.P. O'Sullivan, *The anodizing of aluminium in sulphate solutions.* Electrochimica Acta, 1970. **15**(12): p. 1865-1876.
20. ASTM, ASTM D3167-03a, Standard Test Method for Floating Roller Peel Resistance of Adhesives. 2003, ASTM International: West Conshohocken, PA.
21. van Put, M., et al., *Potentiodynamic anodizing of aluminum alloys in Cr(VI)-free electrolytes.* Surface and Interface Analysis, 2016. **48**(8): p. 946-952.
22. Sulka, G.D., Highly Ordered Anodic Porous Alumina Formation by Self-Organized Anodizing, in Nanostructured Materials in Electrochemistry. 2008, Wiley-VCH Verlag GmbH & Co. KGaA. p. 1-116.
23. Adeosun, S.O., et al., *Strength and hardness of directionally-rolled AA1230 aluminum alloy.* Journal of Emerging Trends in Engineering and Applied Sciences, 2011. **2**(3): p. 440-444.
24. Hauffman, T., et al., Study of the Self-Assembling of n-Octylphosphonic Acid Layers on Aluminum Oxide. Langmuir, 2008. **24**(23): p. 13450-13456.
25. Abrahami, S.T., et al., XPS Analysis of the Surface Chemistry and Interfacial Bonding of Barrier-Type Cr(VI)-Free Anodic Oxides. The Journal of Physical Chemistry C, 2015. **119**(34): p. 19967-19975.
26. Barthés-Labrousse, M.G., *Mechanisms of Formation of the Interphase in Epoxy-Amine/Aluminium Joints.* The Journal of Adhesion, 2012. **88**(8): p. 699-719.
27. Alexander, M.R., et al., Interaction of carboxylic acids with the oxyhydroxide surface of aluminium: poly(acrylic acid), acetic acid and propionic acid on pseudoboehmite. Journal of Electron Spectroscopy and Related Phenomena, 2001. **121**(1–3): p. 19-32.
28. Rider, A.N., et al., *The influence of hydroxyl group concentration on epoxy–aluminium bond durability.* Journal of Adhesion Science and Technology, 2004. **18**(10): p. 1123-1152.
29. Semoto, T., Y. Tsuji, and K. Yoshizawa, *Molecular Understanding of the Adhesive Force between a Metal Oxide Surface and an Epoxy Resin.* The Journal of Physical Chemistry C, 2011. **115**(23): p. 11701-11708.

CHAPTER 6

Interfacial bonding strength and stability of epoxy and phenol resins on different aluminium oxide and silane chemistries

Part of this chapter was submitted as a scientific journal paper:
Abrahami, S. T., Hauffman, T., de Kok, J.M.M., Terryn, H., and Mol, J.M.C. (2016)

Abstract

The long-term strength and durability of an adhesive bond is dependent on the stability of the oxide/adhesive interface. As such, changes in the chemistries of the oxide and/or the adhesive are expected to modify its interfacial properties and so to affect the joint performance. The upcoming transition to Cr(VI)-free surface pre-treatments makes it crucial to evaluate how the incorporation of electrolyte-derived sulfate and phosphate anions from, respectively, phosphoric acid- (PAA) and sulfuric acid- (SAA) anodizing are affecting the interfacial chemical properties. Hence, different types of featureless aluminum oxides with well-defined surface chemistries were prepared in this study. First, the relative amounts of O^{2-}, OH^{-}, PO_4^{3-} and SO_4^{2-} surface species were quantified using X-ray photoelectron spectroscopy (XPS). Next, bonding with two types of commercial aerospace adhesive films (FM 73 and Redux 775) was assessed by peel tests. The presented results indicate that the formation and the durability of the oxide/adhesive interface depends on the interplay between oxide and adhesive chemistries. Epoxy adhesion is highly affected by changes in the oxide surface chemistry, especially the amount of surface hydroxyls. Alternatively, the performance of anodic oxides with a lower hydroxyl fraction can be significantly enhanced by the presence of covalent bonds using a silane coupling-agent γ-amino propyl triethoxy (APS). On the contrary, results with Redux 775 adhesive exhibit very low sensitivity to variations in the surface chemistry.

6.1 Introduction

Structural adhesive bonding of aluminum is one of the principal techniques to produce aircraft components [1]. To prepare this type of joint, the aluminum substrate is first subjected to a multi-step pre-treatment. This pre-treatment produces a porous anodic oxide with a thin barrier layer at its bottom, providing the substrate with an increased adhesion and corrosion resistance [2]. In order to preserve its long-term strength, the produced oxide/adhesive interface must retain its properties during a life-long service that includes different mechanical loads, frequent changes in temperature and hostile environments [3].

In the transition to Cr(VI)-free production, aircraft manufacturers are looking to replace chromic acid anodizing (CAA) by alternative electrolytes. Candidates include phosphoric acid (PAA), sulfuric acid (SAA) and mixtures of phosphoric and sulfuric acid (PSA) anodizing [4]. It is well known that the nature of the electrolyte will affect the oxide properties, such as its morphological features and chemical composition [5]. Different studies have shown that bonding performance is affected by changing the oxide morphology [6-8]. This is often explained by changes in the extent of mechanical interlocking between the oxide and the resin [9]. Because bond formation (and degradation) is initiated on a molecular level [10, 11], changes in the chemical properties of the oxide are also expected to affect the initial adhesion, as well as its long-term performance.

Moreover, the chemical nature of the oxide, the type of organic resin and their compatibility will all affect the nature and extent of interfacial bonding [12]. Studies on natural and (electro) chemically grown oxides have shown that bonding between aluminum oxides and organic resins often involves various types of relatively weak interactions [13-15]. In a recent work we demonstrated that bonding between barrier-type anodic aluminum oxides and FM 73 epoxy resin is distorted by water [16]. This was postulated to occur due to the reversible nature of hydrogen bonds that are formed between the oxide and epoxy.

Covalent bonds exhibit much larger bond energy than hydrogen bonds and therefore are much more stable [17]. Numerous studies over the last decades have demonstrated the ability of silanes to form covalent bonds with an aluminum substrate [15, 18-20]. This is achieved using silane molecules that can form a covalent aluminosiloxane (Si-O-Al) bond [21]. By the right selection of the molecule chemical functionalities, silane films can be used as coupling agents, linking between organic and inorganic materials, or alternatively produce a thick corrosion-resistant coating [22]. Furthermore, using an amino silane like APS enables an additional interaction with epoxy. While the silane groups can form covalent bonds with the substrate, the amino group is able to act as an additional hardener for the epoxy matrix. This type of silanes are called coupling agents for this double functionality [23]. Since silanes react with metals via their OH groups,

maximizing the amount of these groups at the oxide surface is desired. In a study by Franquet et al. [24], it was shown that a pre-treatment increasing the amount of surface hydroxyls will in turn result in silane films of better uniformity and larger thickness.
This study investigates how changes in the oxide chemistry influence adhesion with two types of commercial aerospace resins: FM 73, an epoxy adhesive and Redux 775, a vinyl phenolic adhesive respectively. To exclude the contribution of mechanical interlocking, anodic oxide growth was stopped during the formation of the barrier layer, producing relatively thin and featureless oxides. Since the hydroxyl fraction is expected to play a crucial role in bonding with aluminum oxides, the classic alkaline and boiling water pre-treatments that produce the highest amount of surface hydroxyls [25] are included for comparison. To examine the different types of interfacial bonding, γ-amino propyl triethoxy (APS) silane was applied on some of the epoxy test panels.

6.2 Experimental

Two types of specimens were used in this study. Model (laboratory) specimens were used for surface characterization. These specimens were electropolished to produce a mirror-like smooth surface that is suitable for quantification purposes. Industrial test specimens were used for floating roller peel. Both preparation methods are detailed below.

6.2.1 Model Specimens for XPS Analysis

Samples were cut from a 0.3 mm thick sheet of commercially pure aluminum (99.99 %, Hydro). To remove imperfections and provide a flat substrate for analysis purposes, specimens were electropolished. This was done after the substrate was etched in an aqueous solution of 25 g/l NaOH at 70 °C for 1 minute, followed by rinsing for 15 s with deionized water and then ultrasonically rinsed for 3 additional minutes. The substrate was then electropolished for 6 min in a solution of 80 vol.% (absolute) ethanol and 20 vol.% perchloric acid, at a current density of 70 mA/cm^2 and 10 °C. Subsequently, it was rinsed following the above procedure, dried with compressed air and stored in a sealed plastic bag. Later, each sample was given one of the anodizing pre-treatments listed in Table 6.1.

Galvanostatic anodizing at 10 mA/cm^2 for 4 s was performed with SM120-25 power-supply unit (Delta Elektronika) equipped with an Ethernet interface connection to monitor the cell voltage. Model specimens were anodized in a three-electrode cell filled with 400 ml solution and two AA1050 aluminum cathodes. After each of the described pre-treatments, the substrate was again thoroughly rinsed as previously described. Anodizing conditions were preselected to yield featureless anodic oxides by stopping the oxide growth at the end of the region in which the voltage was increasing linearly with time, the part which is associated with the formation of the barrier layer [26]. In order

Table 6.1: Summary of the electrolyte composition for the different surface pre-treatments.

Abbreviation	Pre-treatment	Electrolyte composition
PAA	Phosphoric Acid Anodizing	25 g/l H_3PO_4
SAA	Sulphuric Acid Anodizing	*10g/l H_2SO_4
CAA	Chromic Acid Anodizing	40g/l CrO_3
Alkaline	Alkaline immersion	25g/l NaOH, 30s, RT
Hydrothermal	Boiling water immersion	Boling (demi-)water, 30s

* 5g/l was used for the preparation of the floating roller peel specimens instead.

to limit atmospheric contamination, samples were placed in the pre-vacuum chamber for analysis no longer than 10 minutes after the pre-treatment was completed.

6.2.2 Panels for Floating Roller Peel Test

For practical reasons, peel tests following aerospace protocol could not be made with the soft pure aluminum that was used for surface characterization. Therefore, AA2024-T3 alclad (clad layer AA1230) aluminum test sheets of 250x95x1.6 mm and 300x95x0.5 mm were used for the thick and thin panels, respectively. Before anodizing specimens were degreased, alkaline etched and desmutted. Degreasing was achieved by wiping the panels with ethanol. This was followed by a 2 min. alkaline etching with 40 g/L P3 Almeco 51 (from Henkel) at 35°C and a 1 min. pickling with 35 vol.% HNO_3 at RT. After each step, the panel was thoroughly rinsed with running demineralized water, followed by 1 min. immersion rinsing in an agitated beaker of fresh demineralized water. Then the panels were anodized in one of the electrolytes listed in Table 6.1. Anodizing at constant current density of 5 mA/cm^2 was performed for 8 s. Although the applied current density is lower than for the model specimens, the anodizing time is doubled so that the total amount of current passing is the same. After anodizing, the panels were rinsed and dried with compressed air. The panels were then bonded (without primer) with one of the selected adhesives, no longer than 10 minutes after the pre-treatment of the thin panel was completed. After bonding, the panels were stored in a sealed plastic bag for up to 24 hours before curing. Curing following the manufacturer instructions was performed using a Joos hot plate press. FM 73 curing was achieved at 6 bar and 120°C for 75 minutes. Redux 775 was cured at 9.9 bar and 155°C for 45 minutes. Measured adhesive thickness (after curing) corresponds to 0.1 ± 0.2 mm for epoxy/epoxy + silane and 0.2 ± 0.2 mm for Redux.

6.2.3 Adhesives Chemistries

Redux 775 and FM 73 are two typical aerospace structural adhesives. Redux 775 (Hexcel) is a vinyl phenolic resin. It is the first man-made adhesive that was used to bond aircraft structures [1]. The general building blocks of Redux are shown in Fig. 6.1. Its most basic unit is the phenol molecule (Fig. 6.1 (a)). A resole phenolic resin (Fig. 6.1 (c)) is produced by the reaction between phenol and formaldehyde (in excess, Fig. 6.1 (b)) using a basic catalyst [27]. Because phenolic resins are brittle, polyvinyl formal (PVF, Fig. 6.1 (d)) is added to improve the fracture toughness. PVF is made by acidic reaction between poly(vinyl alcohol) (PVA) and formaldehyde. The poly(vinyl alcohol) is, in turn, made by hydrolysis of polyvinyl acetate. Thus, residual alcohol and ester functionalities are usually present in PVF, as indicated in Fig, 6.1 (d). Phenolic adhesive provides a large amount of active sites on the phenol ring and residual hydroxyl methyl groups that enable its self-curing. Alternatively, it can condense with the phenolic hydroxyl of the residual hydroxyls of the PVA [3]. As a result, the adhesive can develop a high level of cross-linking.

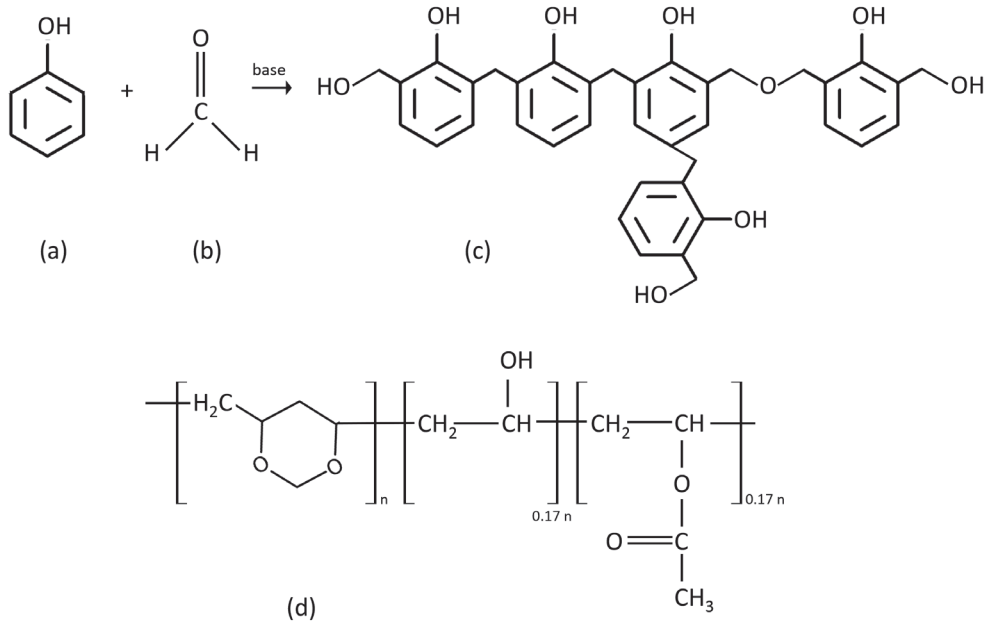

Figure 6.1: Molecular structure of the basic components of Redux 775 resin:(a) phenol, (b) formaldehyde, (c) a phenolic resole product and (d) formaldehyde polyvinyl formal (PVF, left) containing trace amounts (typically 0.1 to 0.17) of poly(vinyl alcohol), and poly(vinyl acetate).

FM 73 (Cytec Engineering Materials) is a typical epoxy structural adhesive that does not contain silanes. It is based on a DGEBPA (diglycidyl ether of bisphenol A, Fig. 6.2 (a)). The epoxide ring in DGEBPA is the reactive moiety in this molecule and, hence, a

schematic representation of epoxy curing is shown in Fig. 6.2 (b). The reaction proceeds by ring opening, which typically occurs by an amine addition [28].

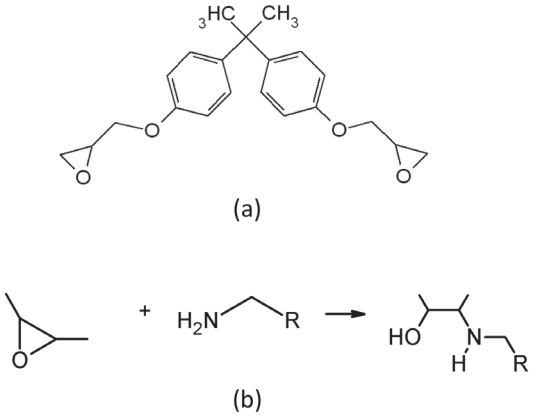

Figure 6.2: Molecular structure of DGEBPA (diglycidyl ether of bisphenol-A), (a) and representative reaction of epoxide ring opening reaction using an amine curing-agent, (b).

6.2.4 Silane Application

The silane applied in this study is γ-amino propyl triethoxy (APS), which is an amino silane with the molecular structure given in Fig. 6.3. Before its application the silane was hydrolyzed for 24 hours under continuous (magnetic) stirring. During this process the ethyl groups are converted to silanol (-SiOH) groups that can react with the aluminum. This was accomplished in a mixture of 2 vol.% APS in (distilled) water at pH 9 (adjusted with acetic acid).

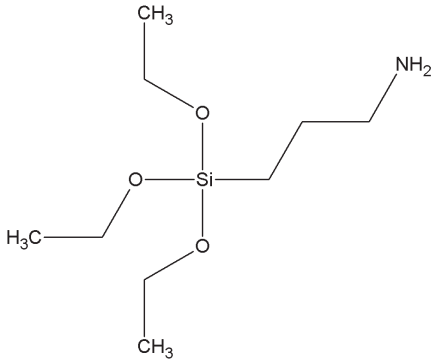

Figure 6.3: Molecular structure of APS.

After 24 hours, the mixture was ready and part of it was diluted to prepare a second mixture of 0.5 vol.% APS. For each concentration, a solution of pH 5.7 and pH 9 were made using acetic acid (when needed). Directly after the anodized panels were rinsed,

silanes were applied from the solution by dipping the panels for 30 s. Thereafter, the panels where air-blown dried and bonded with FM 73 epoxy. Silane-treated panels for floating roller peel tests were further prepared following the description in section 2.2.

6.2.5 Analysis Methods

6.2.5.1 X-Ray Photoelectron Spectroscopy (XPS)

XPS spectra were collected using a PHI5600 photoelectron spectrometer (Physical Electronics) with an Al *K*α monochromatic X-ray source (1486.71 eV of photons). The vacuum in the analysis chamber was approximately $5x10^{-9}$ Torr during measurements. The full elemental composition was initially determined by acquiring survey spectra on a spot size of 0.8 mm in diameter recorded in the full range (0–1400 eV) at analyzer pass energy of 187.85 eV and step size 0.5 eV. High-resolution scans of aluminum (Al 2p), oxygen (O 1s), carbon (C 1s), phosphorus (P 1s) and sulfur (S 2p) photopeaks were recorded using pass energy of 23.5 eV and step size 0.1 eV. Measurements were performed at takeoff angles of 45° and 15° with respect to the sample surface. The reproducibility of the measurements was verified by (at least) two repetitions.
XPS data was analyzed using PHI Multipak software (V9.5.0.8). Before curve fitting, the energy scale of the spectra was calibrated relative to the binding energy of adventitious hydrocarbons in the C1s peak at 284.8 eV. Curve fitting was done after a Shirley-type background removal, using mixed Gaussian (80–100%) – Lorentzian shapes.

6.2.5.2 Mechanical Testing

Floating roller peel tests were executed according to ASTM D3167 - 03a [29]. Of each bonded panel, three strips of 25x250 mm were cut with a diamond saw. After fixing the test strips in the apparatus, the unbound end of the specimen was attached to the lower head of the testing machine. The thin aluminum panel was then peeled off the thick panel with a speed of 100 mm/min while the peeling load versus head movement (or load versus distance peeled) was recorded. All tests were performed at ambient temperature. The first half of the specimen was peeled under dry conditions. Water was then injected at the crack-tip and the second half was peeled under wet conditions.

6.3. Results and Discussion

6.3.1 Oxide Chemical Characterization

The surface chemistry of model panels was characterized by angle-resolved XPS measurements. Before recording each high-resolution spectrum, a survey scan was taken. An example for a survey spectrum of the different oxides is shown in Fig. 6.4. The main elements detected in all oxides are oxygen, aluminum and carbon. Carbon is the only element that is not an integral part of the anodic oxide. It arises from ambient

contamination during sample processing. The amount of carbon on each sample varied somewhat according to handling procedure and processing time. Generally, however, carbon contamination on the hydrothermal specimens was much lower than on the other samples. Phosphor and sulfur were detected in the oxides that were prepared in phosphoric and sulfuric acids (Fig. 6.4 (a) and (b), respectively). Smaller amounts (almost negligible, hence not visible in the survey spectra in Fig. 6.4 (c)) of chromium were detected on CAA samples.

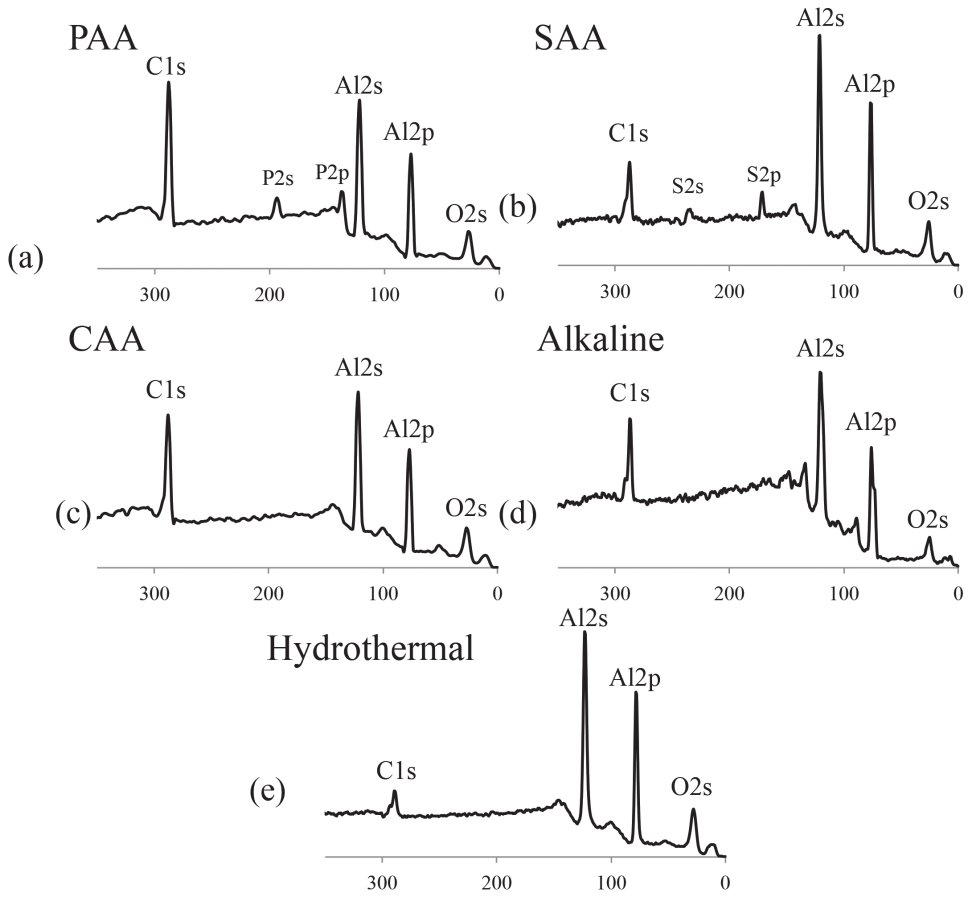

Figure 6.4: Relevant sections of the XPS survey spectra (0-350 eV) measured on the different oxides.

To link surface chemistry to bonding performance, the different surface species at the surface of the different oxides were quantified. This has already been completed for PAA, SAA and CAA in our previous publication [16]. These results are included in here, along with the quantification of the hydroxyl percentage on alkaline and hydrothermal treatments. Therefore, a short description of the analysis method is outlined in here: high-resolution spectra of O1s, C1s, Al2p, S2p and P2s were measured. The data was

fitted to resolve the CO-, COO-, PO_4^{3-}, SO_4^{2-}, OH^- and O^{2-} components using the constraint parameters that are provided in Abrahami et al. [16]. The fitted intensity areas were then used to find a solution for the concentration of the different surface species, while taking into account overlapping in the binding energy of different components in the O1s photopeak. Next, the relative amounts of O^{2-}, OH^-, PO_4^{3-} and SO_4^{2-} (in %) were determined by the ratio, as presented in Eq. 1 for OH^-.

$$OH^-(\%) = \frac{C_{OH^-}}{C_{OH^-} + C_{O^{2-}} + (4 \times C_{PO_4^{3-}}) + (4 \times C_{SO_4^{2-}})} \times 100 \quad \text{Eq. 6.1}$$

Results are summarized in Fig. 6.5, for takeoff angles of $\theta = 15°$ *and* $45°$. Calculations show that anodizing in PAA and SAA electrolytes modifies the anodic oxide chemistry by the incorporation of electrolyte-derived phosphate and sulfate anions. As a result, PAA and SAA oxides exhibit a much lower hydroxyl fraction compared to CAA. Since phosphate incorporation is the highest in the group, PAA oxide has the lowest surface OH fraction, followed by SAA and CAA. This trend is valid for both anodizing temperatures. As expected, oxides prepared by alkaline and hydrothermal treatments exhibited the highest hydroxyl percentage, between 40 and 50 %, in accordance with previous studies [14, 25].

Variations in the takeoff angle, θ, represent a different amount of detected volume under the surface. Since the interaction depth of the grazing angle of θ =15° *is much lower than for* θ =45°, *it provides* a rough indication for the in-depth distribution of the species within the oxide. The higher phosphate concentration at θ=15° *indicates* of a higher concentration in the top surface layers. Conversely, sulfur concentration is relatively constant in both measurements. These observations are in agreement with earlier in-depth study performed using Auger electron spectroscopy (AES) [30]. As oxide hydration is mostly dominant close to the surface, oxides other than SAA and PAA exhibit a higher hydroxyl fraction at θ =15° [31, 32].

6.3.2 The Effect of Oxide Chemistry on Bonding with Different Adhesives

6.3.2.1 Phenol-Base Adhesive (Redux 775)

To measure the quality of bonding as a result from adsorptive interactions, peel tests were carried out with barrier-type oxides bonded with Redux 775. Strength results are displayed in Fig. 6.6, as a function of the hydroxyl percentage at the surface (θ =15°). Results are divided into anodic oxides prepared at room temperature (Fig. 6.6 (a)) and at 50 °C (Fig. 6.6 (b)), with alkaline (prepared at room temperature) and hydrothermal (boiling water) treatments shown in both figures. As seen in Fig. 6.6, peel strengths are generally very low and show no particular trend in relation to the calculated amount of hydroxyls. Both dry (empty markers) and wet (filled markers) peel strengths seem to

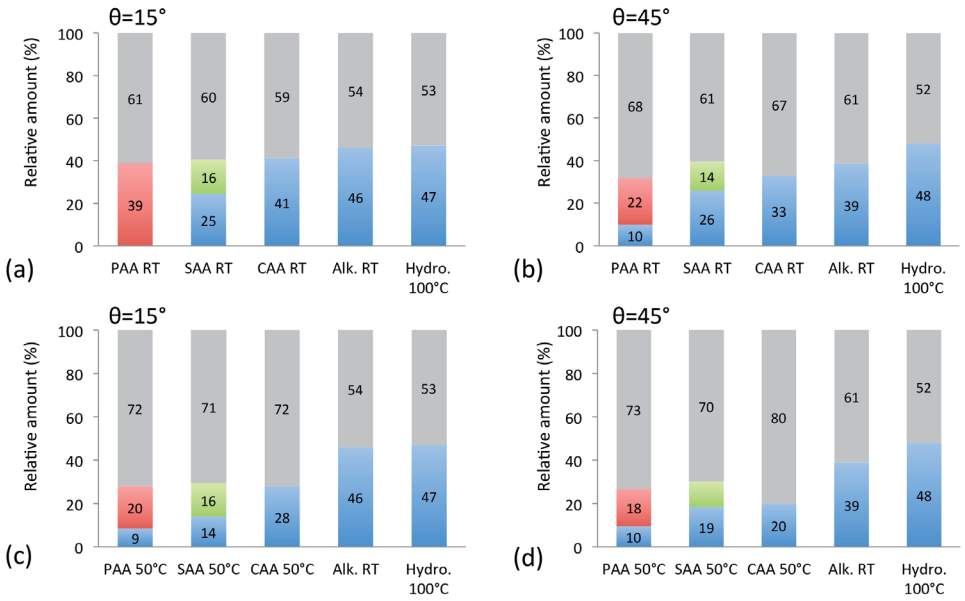

Figure 6.5: Calculated relative amounts of O^{2-} (grey), OH^{-} (blue), PO_4^{3-} (red) and SO_4^{2-} (green) on the different pretreated specimens anodized at room temperature (RT) (a) and (b) and 50 °C (c) and (d). Additional non-anodizing treatments, alkaline and hydrothermal (hydro), are added next to RT and 50 °C respectively.

be independent of the pre-treatments and the anodizing temperature. Yet, the wet peel strength of most oxides is slightly higher than the dry peel, indicating of a temporary improvement in adhesion. Images of some peeled panels are shown in Fig. 6.7. A thin layer of adhesive is visible on top of the thin aluminum panel, hence, failure appears to occur at or adjacent to the oxide/ adhesive interface. Also, no distinction is seen between the dry- and wet test conditions.

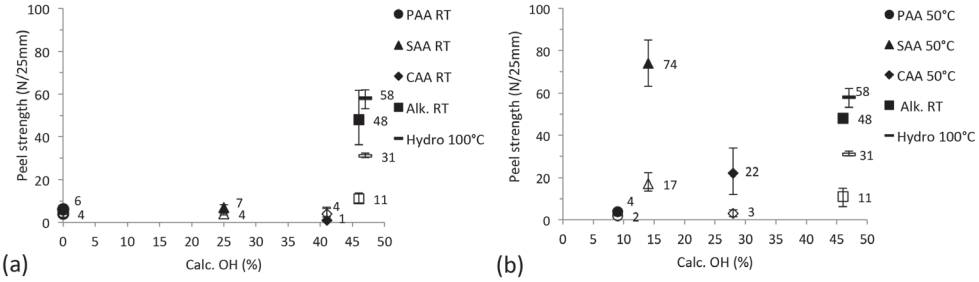

Figure 6.6: The average dry (empty markers) and wet (filled markers) peel strength vs. the calculated hydroxyl percentage (θ=15°) on barrier-type oxides for anodizing at RT (a) and 50°C (b) and adhesively bonded with Redux 775 phenolic adhesive (no primer). The error markers represent the minimum and maximum measured values.

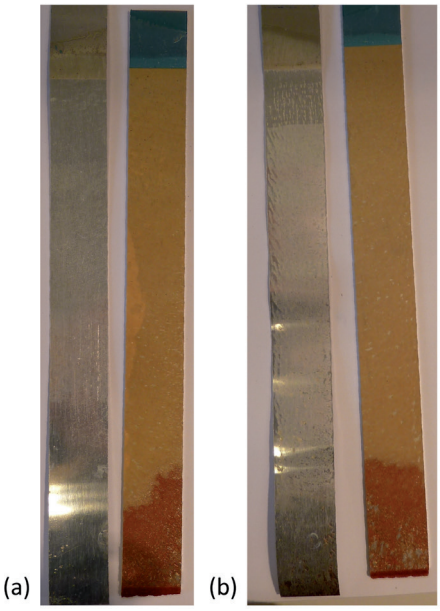

Figure 6.7: Visual images of the peeled panels after PAA RT (a), PAA 50 °*C and hydrothermal treatments (*b). The peeled area starting a few centimeters below the blue tape. The thin panel is peeled under dry- and then wet conditions.

Considering the chemical composition of Redux 775, adsorption to the substrate via phenol and alcohol functionalities can be expected according to our previous observations [33]. The highest peel strengths in here were achieved with the hydrothermal, alkaline and CAA oxides. These are the same oxides that were found to adsorb phenol molecules by the availability of weaker basic hydroxyl groups. The temporarily increase in peel strength after the transition from dry- to wet peel may be related to the weakly acid character of phenolic resin that stabilizes the aluminum oxide against hydration, which is, according to Brockmann et al. [34] as one of the main reasons of its prolonged industrial application. In both molecules and adhesive tests, however, interactions seem to be reversible.

6.3.2.2 Epoxy-Based Adhesive (FM 73)

Similar tests were performed with an epoxy adhesive, FM 73. Peel measurements with anodic oxides were reported previously [16]. The results in here (Fig. 6.8) compare the performance of anodic oxide versus simple chemical treatments in alkaline solution and boiling water (hydrothermal). As opposed to the previous results with Redux, the dry peel strength measured with epoxy is relatively high. The dry peel strength does not show a clear increase with the amount of hydroxyls (hence, to the type of anodizing electrolyte). Wet peel strength (filled markers in Fig. 6.8), on the other hand, linearly increases with the percentage of surface hydroxyls. This dependence indicates that

bonding is established via the hydroxyl groups at the surface. Additionally for the anodic oxides, wet peel strength increases with the anodizing temperature.

It is interesting to note that in this case the dry peel strength is much higher than the wet peel strength. Visual inspection of the peeled panels in Fig. 6.9 indicates that two different modes of failure occurred. Mainly cohesive failure occurred within the adhesive during dry peel. The adhesive is visible on both sides of the joint. Under wet conditions, the failure mode changes from cohesive to interface failure. This behavior was observed in all the tested panels, regardless of the measured wet peel strength. This indicates that interfacial interactions are stronger than the cohesive strength of the adhesive under dry conditions. Upon the ingress of water, the stability of the interface is the critical factor. It appears that water entering the interface between oxide and epoxy causes disbonding and the adhesion strength is reduced by a factor of at least two. These experimental measurements confirm previous predictions made by modeling the interface using density functional theory (DFT) calculations. Semoto et al. [35] have found that the main contribution to adhesion between epoxy and aluminum oxide originates from a network of hydrogen bonds with surface hydroxyls. Hence, the larger amount of hydroxyl groups available for interactions, the denser and stronger the resulting network of hydrogen bonds. Other studies that apply molecular and atomic simulations also predict disbonding and adhesion reduction in the presence of water molecules at the interface [36-38]. These predictions are also confirmed by the results showing interface failure and significant reduction in strengths of FM 73 epoxy joints peeled under wet conditions. In the absence of surface roughness that can retard interfacial diffusion of water, bonds stability is crucial for a durable adhesion.

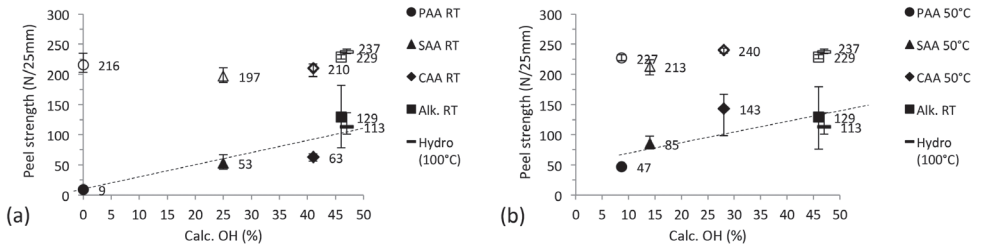

Figure 6.8: The average dry (empty markers) and wet (filled markers) peel strength vs. the calculated hydroxyl percentage at the surface (θ=15°) on barrier-type oxides for anodizing at RT (a) and 50°C (b) and adhesively bonded with FM 73 epoxy adhesive (no primer). The error markers represent the minimum and maximum measured values.

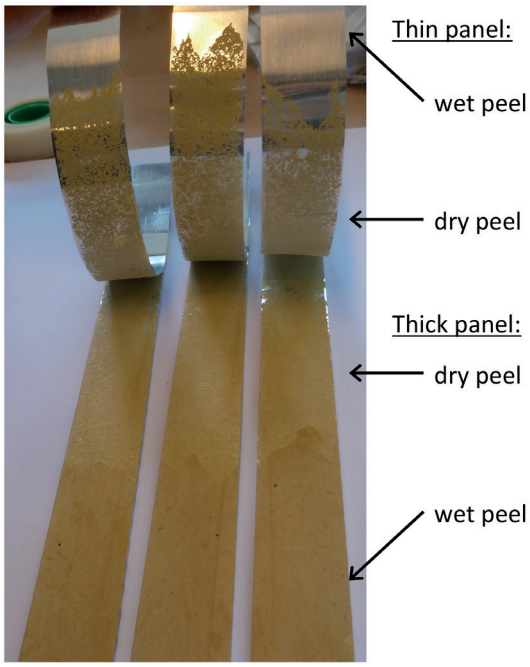

Figure 6.9: Visual impression of typical peeled panels (CAA RT) bonded with FM 73 epoxy. Dry conditions lead to cohesive failure, with the adhesive seen on both sides of the panels and interface failure under wet conditions, in which the substrate is revealed on the thin panel and an intact adhesive on the other panel (dark yellow).

6.3.3 Silane Effect on Adhesion

Results in the previous section indicate that adsorptive interactions between aluminum oxide and FM 73 epoxy are not stable under wet conditions. It is therefore of great interest to find out if interfacial stability and durability using only adsorptive adhesion mechanism can be increased by the presence of covalent bonds. Similar to epoxy, silanes first adsorb onto the aluminum surface through hydrogen bonds. Upon curing, hydrogen bonds are replaced by the covalent Al-O-Si bonds. To this aim two types of oxides, CAA and PAA, were chosen. These two anodic oxides present the best and worst mechanical performance, respectively, as shown in Fig. 6.8. A summary of the peel test results after silane post-treatments of PAA and CAA is listed in Table 6.2. For comparison, tests with barrier- and porous oxides without a silane layer (no primer) were also included. Results in Table 6.2 confirm that the interface stability is generally increased by the formation of covalent bonds. It is, however, interesting to note that dry adhesion after PAA silane treatment remains similar, while the dry peel of CAA oxides after silane post-treatment is worse than before.

Table 6.2: Average peel strength (of 3 repetitions) after silane post-treatment with FM 73 epoxy adhesive. Failure mode: C = cohesive, I = interface.

	Oxide type	Silane conditions	Dry peel (N/25mm)	Failure Mode	Wet peel (N/25mm)	Failure Mode
PAA, RT	Barrier	-	216 ± 14	C	9 ± 1	I
	Barrier	2 vol.%, pH 5.7	214 ± 10	C	208 ± 8	I
	Barrier	0.5 vol.%, pH 5.7	232 ± 9	C	60± 15	I
	Barrier	2 vol.%, pH 9	227 ± 7	C	92 ± 26	C/I
	Barrier	0.5 vol.%, pH 9	208 ± 5	C	18 ± 4	C/I
	Porous*	-	200± 10	C	262± 6	C
CAA, RT	Barrier	-	243 ± 9	C	88 ± 6	I
	Barrier	2 vol.%, pH 5.7	177 ± 23	C	225 ± 1	C
	Barrier	0.5 vol.%, pH 5.7	172 ± 13	C	227± 7	C
	Barrier	2 vol.%, pH 9	155 ± 27	C	83± 6	C/I
	Barrier	0.5 vol.%, pH 9	124 ± 20	C	203± 2	C
	Porous **	-	236 ± 4	C	244± 7	C

* Porous PAA was prepared by anodizing for 20 min. at 18V, ** Porous CAA was prepared by anodizing for 40 min. following the 40/50V scheme [7].

6.3.3.1 Solution pH Effect on Bonding

The deposited silane layers generally improve the wet adhesion of all barrier oxides bonded with epoxy. Both PAA and CAA oxides show the most pronounced improvements after treatment of 2 vol.% at lower pH of 5.7. In these cases, the wet adhesion approaches the value measured for the porous oxides (Table 6.2). The natural pH of APS is 10.5 [39]. At pH 5.7, the silanol groups are negatively charged (Si-OH → Si-O^-) [39] and are, therefore, expected to readily react with a positively charged surface hydroxyls. The solution pH will also affect the charge of the Alumina surface, as indicated by the zeta potential [40]. A zero zeta potential is called the isoelectric point (IEP), which is the point where the substrate is not charged. The isoelectric point of natural aluminum oxide is about 8.7. As a consequence, the silane solution at pH below this value is expected to carry a net positive charge that will support the formation of silanol bonds more than at pH 9.

6.3.3.2 Silane Concentration Effect on Bonding

Besides adhesion promotion through the formation of covalent bonds, the application of silanes was found to improve the overall durability of the interface through the formation of a highly cross-linked network [23]. This can only take place in the presence of excessive silanol groups. Upon curing, non-reacted neighboring silanol groups can condensate to form siloxane (Si-O-Si) bonds. Hence, a higher silane concentration will enable the formation of thicker layers that will allow for a higher cross-linking density.

Two different concentrations of silane solutions were applied: 0.5 and 2 vol.%. Since the present goal is to improve adhesion, the chosen concentrations are relatively low and were found to have no effect on the total thickness of the adhesive as measured after curing (section 2.2). Although the 2 vol.% is expected to provide better results, due to the presence of more excessive silanol groups, there is no significant effect of the concentration within this range.

6.3.3 Bondline Corrosion

Bondline corrosion tests were performed for anodizing at room temperature and for alkaline and hydrothermal treatments. A summary of the results is listed in Table 6.3. Images of the panels are shown in Fig. 6.10 and 6.11. Except for the hydrothermal oxide, all other joint bonded with epoxy already failed after just 1 week in the salt spray cabinet and could be easily opened by hand (represented by the – sign in Table 6.3). Visual inspection of the panels revealed extended corrosion on both sides of the joint. Similar observations were made after two and four weeks of testing.

An image of the hydrothermal oxide bonded with FM73 epoxy are shown in Fig. 6.10 (a) for 1, 2 and 4 weeks of aging in the salt spray cabinet. Corrosion starts from the edges of the panels and is already seen after 1 week, but it is then limited to about 2-3 mm from the edge (mostly at the bottom). The peel strength is still high and in the range of its initial dry peel. After two weeks, corrosion has already proceeded for about 5-10 mm from the edge. The corresponding peel strength is then also drastically lower. After four weeks, corrosion is covering a substantial part of the (thick) panel and the joint can be easily opened by hand. In Fig. 6.10 (b), the corresponding image of hydrothermal

Table 6.3 Summary of peel test results after different exposure periods in the salt spray cabinet. All tests were performed after room temperature anodizing in PAA, SAA and CAA (the - sign means that the joint was opened by hand).

1 week SST			**2 weeks SST**			**4 weeks SST**		
Adhes-ive	Treat-ment	Average peel (N)	Adhes-ive	Treat-ment	Average peel (N)	Adhes-ive	Treat-ment	Average peel (N)
Redux 775	NaOH	13	Redux 775	NaOH	10	Redux 775	NaOH	-
	Hydro.	43		Hydro.	28		Hydro.	-
	PAA	4		PAA	-		PAA	-
	SAA	12		SAA	-		SAA	-
	CAA	-		CAA	-		CAA	-
FM 73	NaOH	-	FM 73	NaOH	-	FM 73	NaOH	-
	Hydro.	252		Hydro.	148		Hydro.	-
	PAA	-		PAA	-		PAA	-
	SAA	-		SAA	-		SAA	-
	CAA	-		CAA	-		CAA	-

bonded with Redux 775 is shown. In this case, peel strength was much lower, but failure occurs as a result of de-adhesion at the interface rather than corrosion failure. After two weeks, peel strength is lower, but still no sign of corrosion. After four weeks the panel can be opened by hand, but there is still no sign of corrosion.

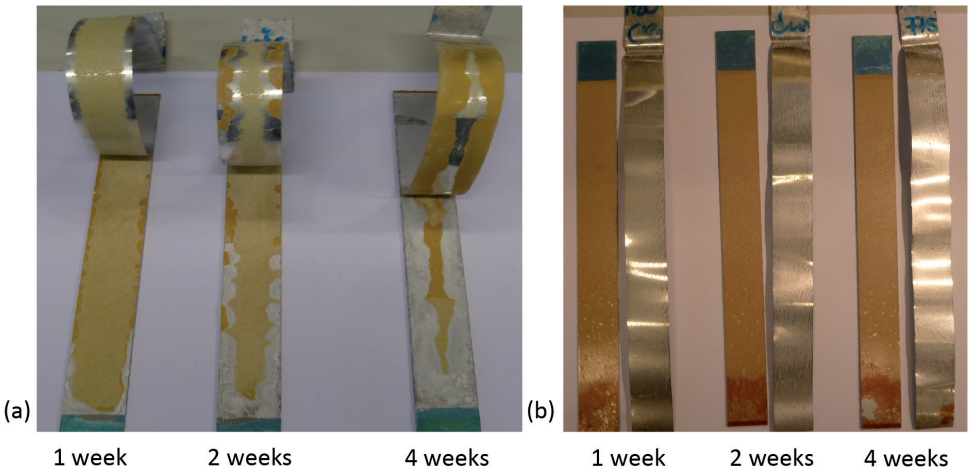

Figure 6.10: Macroscopic images of the peeled panels after various periods in the salt spray cabinet. Panels received hydrothermal pre-treatment with FM 73 (a) and Redux 775 adhesives (b), without any primer.

Except for the hydrothermal, all the other panels exhibited similar trends. There was clear distinction in the corrosion resistance of FM 73 and Redux 775 (e.g. in Fig. 6.11 (a) and (b), respectively). All FM 73 panels exhibit extensive corrosion while little to no corrosion has been observed on panels bonded with Redux 775. Although the bond strength of joint prepared with Redux 775 is substantially lower than for FM 73, the measured low peel strength is due interfacial failure since these are no signs of corrosion. Since components of the adhesive can leach out in an aqueous environment, the interface formed with Redux retain the weakly acidic character of the phenol, which stabilizes the aluminium oxide against hydration [33]. This is also the reason for its excellent protection against bondline corrosion. In addition, the alkaline environment that is formed by epoxies results in high susceptibility to bondline corrosion and leads to the attack of the aluminium oxide. Consequently, it is advised by the manufacturer to combine FM 73 with a corrosion inhibiting primer (typically BR 127).

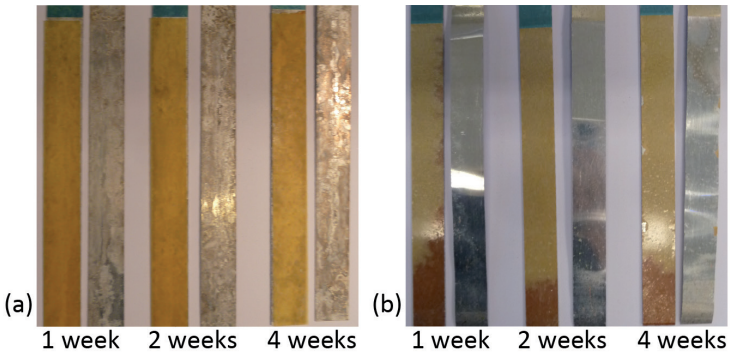

Figure 6.11: Macroscopic images of the SAA peeled panels after various periods in the salt spray cabinet: bonded with FM 73(a) and Redux 775(b).

6.4 Conclusion

This study compared the performance of oxides with ranging surface chemistries bonded with two types of aerospace adhesives: FM 73 epoxy and Redux 775. In the absence of surface features, mechanical peel tests measure the adhesion strength as a result of adsorptive interactions between the two phases. The presented results indicate that the formation, as well as the durability, of the oxide/adhesive interface depends on interplay between oxide and adhesive chemistries. Based on the above results, the following conclusions emerge:

- Interfacial bonding is influenced by the oxide surface- and the adhesive chemistry.
- Interfacial bond strength can change with the type and density of interactions.
- Interfacial bonding with both FM73 epoxy and Redux 775 appears to be based on relatively weak molecular interactions. However, the strength of these interactions differs.
- Maximizing the amount of surface hydroxyls is favorable for bonding with FM 73 epoxy adhesive since stable bonding proceeds through these surface species.
- Results generally confirm that the presence of covalent bonds, provided by a silane-coupling agent, improves the stability of the interface under wet conditions.

5. Acknowledgements

This research was carried out under the project number M11.6.12473 in the framework of the Research Program of the Materials innovation institute M2i (www.m2i.nl).

6. References

1. Higgins, A., *Adhesive bonding of aircraft structures.* International Journal of Adhesion and Adhesives, 2000. **20**(5): p. 367-376.
2. Thompson, G.E., *Porous anodic alumina: fabrication, characterization and applications.* Thin Solid Films, 1997. **297**(1–2): p. 192-201.
3. Bishopp, J., *13 - Adhesives for Aerospace Structures*, in *Handbook of Adhesives and Surface Preparation*, S. Ebnesajjad, Editor. 2011, William Andrew Publishing: Oxford. p. 301-344.
4. Critchlow, G.W. and D.M. Brewis, *Review of surface pretreatments for aluminium alloys.* International Journal of Adhesion and Adhesives, 1996. **16**(4): p. 255-275.
5. Sulka, G.D., *Highly Ordered Anodic Porous Alumina Formation by Self-Organized Anodizing*, in *Nanostructured Materials in Electrochemistry*. 2008, Wiley-VCH Verlag GmbH & Co. KGaA. p. 1-116.
6. Venables, J.D., et al., *Oxide morphologies on aluminum prepared for adhesive bonding.* Applications of Surface Science, 1979. **3**(1): p. 88-98.
7. Critchlow, G.W., et al., *Strategies for the replacement of chromic acid anodising for the structural bonding of aluminium alloys.* International Journal of Adhesion and Adhesives, 2006. **26**(6): p. 419-453.
8. Venables, J.D., *Adhesion and Durability of Metal/Polymer Bonds*, in *Adhesive Joints*, K.L. Mittal, Editor. 1984, Springer US. p. 453-467.
9. Kinloch, A.J., M.S.G. Little, and J.F. Watts, *The role of the interphase in the environmental failure of adhesive joints.* Acta Materialia, 2000. **48**(18–19): p. 4543-4553.
10. Davis, G.D., P.L. Whisnant, and J.D. Venables, *Subadhesive hydration of aluminum adherends and its detection by electrochemical impedance spectroscopy.* Journal of Adhesion Science and Technology, 1995. **9**(4): p. 433-442.
11. van den Brand, J., et al., *Changes in epoxy-coated aluminium due to exposure to water.* Progress in Organic Coatings, 2004. **51**(4): p. 351-364.
12. Packham, D.E., *Theories of Fundamental Adhesion*, in *Handbook of Adhesion Technology*, L.F.M. Da Silva, A. Öchsner, and R.D. Adams, Editors. 2011, Springer-Verlag: Berlin Heidelberg.
13. van den Brand, J., et al., *Interaction of Ester Functional Groups with Aluminum Oxide Surfaces Studied Using Infrared Reflection Absorption Spectroscopy.* Langmuir, 2004. **20**(15): p. 6318-6326.
14. Özkanat, Ö., et al., *Influence of pretreatments and aging on the adhesion performance of epoxy-coated aluminum.* Surface and Coatings Technology, 2013. **215**(0): p. 260-265.
15. Watts, J.F., A. Rattana, and M.-L. Abel, *Interfacial chemistry of adhesives on hydrated aluminium and hydrated aluminium treated with an organosilane.* Surface and Interface Analysis, 2004. **36**(11): p. 1449-1468.
16. Abrahami, S.T., et al., *Effect of Anodic Aluminum Oxide Chemistry on Adhesive Bonding of Epoxy.* The Journal of Physical Chemistry C, 2016. **120**(35): p. 19670-19677.
17. Packham, D., *Theories of Fundamental Adhesion*, in *Handbook of Adhesion Technology*, L.M. da Silva, A. Öchsner, and R. Adams, Editors. 2011, Springer Berlin. p. 9-38.

18. Abel, M.-L., et al., *Evidence of specific interaction between γ-glycidoxypropyltrimethoxysilane and oxidized aluminium using high-mass resolution ToF-SIMS.* Surface and Interface Analysis, 2000. **29**(2): p. 115-125.
19. Öhman, M. and D. Persson, *ATR-FTIR Kretschmann spectroscopy for interfacial studies of a hidden aluminum surface coated with a silane film and epoxy I. Characterization by IRRAS and ATR-FTIR.* Surface and Interface Analysis, 2012. **44**(2): p. 133-143.
20. Le Pen, C., et al., *In-situ characterisation of organosilane film formation on aluminium alloys by electrochemical quartz crystal microbalance and in-situ ellipsometry.* Thin Solid Films, 2005. **483**(1–2): p. 66-73.
21. Wegman, R.F. and J. Van Twisk, *2 - Aluminum and Aluminum Alloys*, in *Surface Preparation Techniques for Adhesive Bonding (Second Edition)*, R.F. Wegman and J.V. Twisk, Editors. 2013, William Andrew Publishing. p. 9-37.
22. Cabral, A.M., et al., *A comparative study on the corrosion resistance of AA2024-T3 substrates pre-treated with different silane solutions: Composition of the films formed.* Progress in Organic Coatings, 2005. **54**(4): p. 322-331.
23. Song, J. and W.J. Van Ooij, *Bonding and corrosion protection mechanisms of γ-APS and BTSE silane films on aluminum substrates.* Journal of Adhesion Science and Technology, 2003. **17**(16): p. 2191-2221.
24. Franquet, A., H. Terryn, and J. Vereecken, *Study of the effect of different aluminium surface pretreatments on the deposition of thin non-functional silane coatings.* Surface and Interface Analysis, 2004. **36**(8): p. 681-684.
25. van den Brand, J., et al., *Correlation between hydroxyl fraction and O/Al atomic ratio as determined from XPS spectra of aluminium oxide layers.* Surface and Interface Analysis, 2004. **36**(1): p. 81-88.
26. Sheasby, P.G. and R. Pinner, *Surface Treatment and Finishing of Aluminium and its Alloys*. 6th ed. 2001., England: Finishing Publications Ltd.
27. Pocius, A.V., *The Chemistry and Physical Properties of Structural Adhesives*, in *Adhesion and Adhesives Technology (Third Edition)*. 2012, Hanser. p. 219-258.
28. Pocius, A.V., *The Chemistry and Physical Properties of Elastomer-Based Adhesives*, in *Adhesion and Adhesives Technology (Third Edition)*. 2012, Hanser. p. 273-306.
29. ASTM, *ASTM D3167-03a, Standard Test Method for Floating Roller Peel Resistance of Adhesives*. 2003, ASTM International: West Conshohocken, PA.
30. Abrahami, S.T., et al., *XPS Analysis of the Surface Chemistry and Interfacial Bonding of Barrier-Type Cr(VI)-Free Anodic Oxides.* The Journal of Physical Chemistry C, 2015. **119**(34): p. 19967-19975.
31. Alexander, M.R., G.E. Thompson, and G. Beamson, *Characterization of the oxide/hydroxide surface of aluminium using x-ray photoelectron spectroscopy: a procedure for curve fitting the O 1s core level.* Surface and Interface Analysis, 2000. **29**(7): p. 468-477.
32. McCafferty, E. and J.P. Wightman, *Determination of the concentration of surface hydroxyl groups on metal oxide films by a quantitative XPS method.* Surface and Interface Analysis, 1998. **26**(8): p. 549-564.
33. Abrahami, S.T., et al., *The role of acid-base properties in the interactions across the oxide-primer interface in aerospace applications.* Surface and Interface Analysis, 2016. **48**(8): p. 712-720.

34. Brockmann, W., et al., *Adhesion in bonded aluminium joints for aircraft construction.* International Journal of Adhesion and Adhesives, 1986. **6**(3): p. 115.
35. Semoto, T., Y. Tsuji, and K. Yoshizawa, *Molecular Understanding of the Adhesive Force between a Metal Oxide Surface and an Epoxy Resin.* The Journal of Physical Chemistry C, 2011. **115**(23): p. 11701-11708.
36. Ogata, S. and Y. Takahashi, *Moisture-Induced Reduction of Adhesion Strength between Surface Oxidized Al and Epoxy Resin: Dynamics Simulation with Electronic Structure Calculation.* The Journal of Physical Chemistry C, 2016. **120**(25): p. 13630-13637.
37. Posner, R., O. Ozcan, and G. Grundmeier, *Water and Ions at Polymer/Metal Interfaces*, in *Design of Adhesive Joints Under Humid Conditions*, M.L.F. Silva and C. Sato, Editors. 2013, Springer Berlin Heidelberg: Berlin, Heidelberg. p. 21-52.
38. Kacar, G., et al., *Hierarchical multi-scale simulations of adhesion at polymer-metal interfaces: dry and wet conditions.* Physical Chemistry Chemical Physics, 2015. **17**(14): p. 8935-8944.
39. Mohseni, M., et al., *Adhesion performance of an epoxy clear coat on aluminum alloy in the presence of vinyl and amino-silane primers.* Progress in Organic Coatings, 2006. **57**(4): p. 307-313.
40. Abel, M.-L., J.F. Watts, and R.P. Digby, *The adsorption of alkoxysilanes on oxidised aluminium substrates.* International Journal of Adhesion and Adhesives, 1998. **18**(3): p. 179-192.

CHAPTER 7

Potentiodynamic anodizing of aluminium alloys in Cr(VI)-free electrolytes

This chapter is published as a scientific paper:
van Put, M., Abrahami, S.T., Elisseeva, O., de Kok, J.M.M, Mol, J.M.C., Terryn, H.,
Surf. Interface Anal. (2015), 48(8): p. 946-952.

Abstract

The aerospace industry progressively develops alternatives for chromic acid anodizing, since Cr(VI) is known to be toxic and carcinogenic. In this work, potentiodynamic anodizing of AA1050 and AA2024-T3 clad was performed in phosphoric-sulphuric acid (PSA) and sulphuric acid (SAA). All anodizing cycles started with a linear voltage sweep, followed by a constant voltage or a dynamic voltage. Current density responses were recorded during each anodizing cycle and comprised different stages, which could be related to growth phases of the anodic oxide film. Interesting differences were found between cycles with an intermediate increase in anodizing voltage versus cycles with an intermediate decrease in voltage. Cycles including an increase in voltage resulted in higher anodic oxide formation efficiencies due to a temporary exceedance of the steady state current (recovery period) directly after the voltage step. Also, a sudden decrease in voltage led to distinct border between a fine and coarse region in the film morphology, while a sudden increase in voltage did not. For prolonged anodizing in PSA, coarsening of the upper film part was observed due to the high solubility of Al_2O_3 in phosphoric acid. Pore walls close to the outer surface did not only get thinner, but completely dissolved in the electrolyte. Consequently, anodic oxide formation efficiencies were higher for SAA than for PSA.

7.1 Introduction

Aluminium and its alloys are widely used in the aerospace industry due to their excellent properties like low density, high mechanical strength and relatively high corrosion resistance [1]. Adhesive bonding of aluminium is often preferred over alternative joining methods, since it offers a higher fatigue resistance of components, improves aerodynamics and saves weight [2]. To achieve successful long-term bonding, pre-treatment of aluminium surfaces is necessary before the application of primers and adhesives. Pre-treatment procedures consist of a number of sequential process steps, of which anodizing often is an important one. By appropriate selection of anodizing electrolyte and anodizing voltage or current, porous anodic oxides can be created with a duplex structure: a compact barrier layer on the bottom and a porous structure on top [3-6].

Keller, Hunter and Robinson [6] and Wood and O'Sullivan [4] have performed a significant amount of work studying the effect of anodizing process parameters on the morphology of the porous layer. They found that for high purity aluminium, the major film characteristics (pore diameter *d*, cell diameter *c* and barrier layer thickness *b*) are linearly dependent upon the steady-state anodizing voltage. Higher anodizing voltages lead to larger pore and cell diameters, and thicker barrier layers. Also, Rahman et al. [7] and Huang et al. [8] have shown that pore diameters (measured from top view analysis) increase with anodizing time in aggressive electrolytes. For potentiostatic anodizing, the pore widening rate was found to be constant over the duration of the anodizing process [7].

Compared to galvanostatic and potentiostatic anodizing, relatively few researchers have looked into potentiodynamic anodizing. Curioni et al. [9-11] and Ma et al. [12] recorded the current density response for linear polarization of aluminium in several electrolytes and linked different stages of the recorded *i-V* curve to growth stages of the porous oxide films. O'Sullivan and Wood [4] recorded the current response after a step-wise increase or decrease in anodizing voltage. They found that after a sudden voltage change the system needs time ('recovery time') to reach the new equilibrium current density ('steady state'). They also propose that the pore widening mechanism after a sudden voltage increase differs significantly from what that of a voltage decrease. However, more complex voltage-cycles, which include both gradual voltage changes and periods of constant voltage, have not yet been studied in-depth. This is surprising, since such voltage cycles are extensively applied in practice, for example during the 40/50V cycle of chromic acid anodizing (CAA) [13].

The aim of the current work was to study the electrical response and porous film growth in phosphoric-sulphuric acid (PSA) and sulphuric acid (SAA) under potentiodynamic anodizing conditions. Seven different voltage cycles were applied. All cycles started with a linear voltage sweep, followed by a constant voltage or a dynamic voltage. The influence

of gradual voltage changes on the current density response, anodic oxide morphology (both outer surface and cross section) and anodic oxide formation efficiency was studied. Anodizing times were also varied in order to get more insight in the effect of this parameter on the development of anodic oxide morphologies.

7.2 Experimental

7.2.1 Potentiodynamic anodizing

Anodizing in phosphoric-sulphuric acid (75 g/l H_3PO_4 and 50 g/l H_2SO_4) and sulphuric acid (50 g/l H_2SO_4) was conducted on aluminium alloys AA1050 (100x150x2.0 mm) and AA2024-T3 clad (100x100x1.0 mm; clad layer AA1230), at T=28±1 °C. AA2024-T3 clad samples were included in the study because this material is extensively used by the aerospace industry. The composition of the outer AA1230 clad layer is comparable to the composition of aluminium alloy AA1050 [14].

AA1050 specimens were masked with a polymer maskant. An area of 100x100 mm was cut out of the mask on both sides of the specimen and it was connected with a copper wire. AA2024-T3 clad specimens (not masked) were clamped in a titanium rack to be able to anodize multiple specimens simultaneously.

Prior to anodizing, all specimens were degreased in 50 g/l Metaclean T2001/4 VP2 (Chemie-Vertrieb GmbH) at 67.5 °C for 5 to 15 min. For AA2024-T3 clad specimens, degreasing was followed by etching in 35 g/l P3 Almeco (Henkel) for 5 min at 35 °C and desmutting in 150 g/l Desoxin AL (Enthone) for 15 min at 30 °C.

Displayed in Figure 7.1 are the seven different anodizing voltage cycles that were applied. The total anodizing time was 30 min for all cycles. Additionally, cycles 1, 2 and 3 have been conducted for 5 min and 15 min. All cycles were used for AA1050 anodizing, while five cycles (2, 4, 5, 6 and 7) were chosen for AA2024-T3 clad. Anodizing voltage cycles were programmed with an Aucos software system.

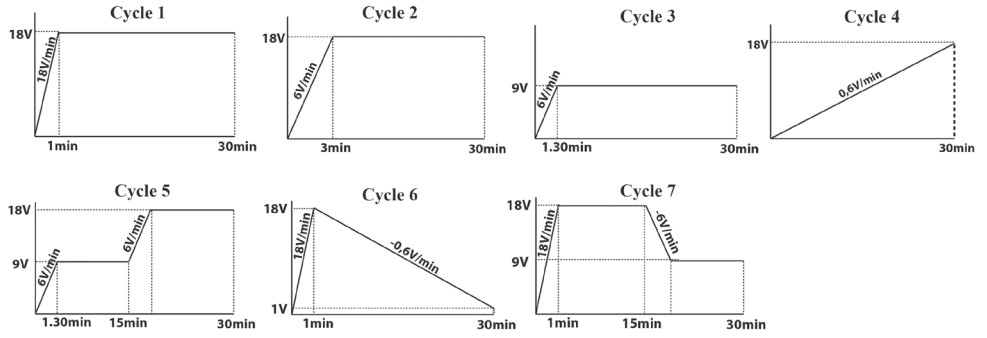

Figure 7.1: Potentiodynamic cycles applied during PSA and SAA anodizing.

An XL 120 datalogger from Yokogawa was used for recording the voltage and current flow during anodizing. After each chemical treatment the specimen was spray rinsed for 30 sec and subsequently immersion rinsed in de-ionized water for 4.30 min at ambient temperature. After pickling/de-smutting and anodizing, specimens were subsequently rinsed for 4.30 min, in two separate tanks. After the final step of anodizing and rinsing, the specimens were dried in an oven at 55 ºC and stored for analysis.

7.2.2 Surface analysis

The outer surface and cross-sections of the oxide films on AA1050 specimens were studied with a Jeol 6500-F FE-SEM. Image capturing occurred at an accelerating voltage of 5.0-6.0 keV at a working distance of 4.0-9.4 mm. A Pt coating of 2 nm was applied to prevent charging. For AA2024-T3 specimens, mirror-like cross sections were prepared by a Hitachi IM4000 ion milling system. The morphology of these cross-sections was studied with a Hitachi SEM SU-70, suitable for non-conducting samples. Image capturing occurred at an accelerating voltage of 2.0 keV, a current of 19-20 μA and a working distance of 2.0-3.4 mm. No Pt coating was applied. The image software system AnalySIS was used to measure pore and interpore distances (equal to cell diameters) close to the outer surface and close to the barrier layer.

Weight measurements (±0.1 mg) before and after stripping the oxide film were used to determine the oxide weight. This was performed on a 75x75 mm specimen by immersion in boiling (±100 °C) solution of 20 ± 0.5 g/l chromic acid and 35 ± 0.5 g/l phosphoric acid.

7.3 Results

7.3.1 Current density response

Fig. 7.2 (a) and (b) show the recorded current densities of anodizing in PSA and SAA for initial voltage sweep rates of 18 V/min and 6 V/min, respectively. The current density response showed a step-wise behaviour during the sweep period, because the system could only increase the voltage in steps of ±1V instead of linearly. The noise in the current signal is due to penetration of the electrolyte under the polymer maskant during anodizing. To clarify the general response, trend lines are included in the graph. A closer look at the initial 4 min is shown in Fig. 7.2 (c) and (d). As indicated in Fig. 7.2 (d), four different stages can be distinguished in the current curves:

1. Rise in current during the first seconds.
2. A 'current plateau' during which the current remains constant. The plateau is found at higher current densities for 18 V/min than for 6 V/min.
3. Rise in current. The rate at which the current increases is higher for 18 V/min than for 6 V/min.

4. Current reaches a peak value, after which it starts decreasing again. The peak is higher and reached earlier in time for 18 V/min than for 6 V/min. In both cases, the peak is observed before the final voltage has been reached. After the peak, the current decreases until it eventually stabilizes (steady state).

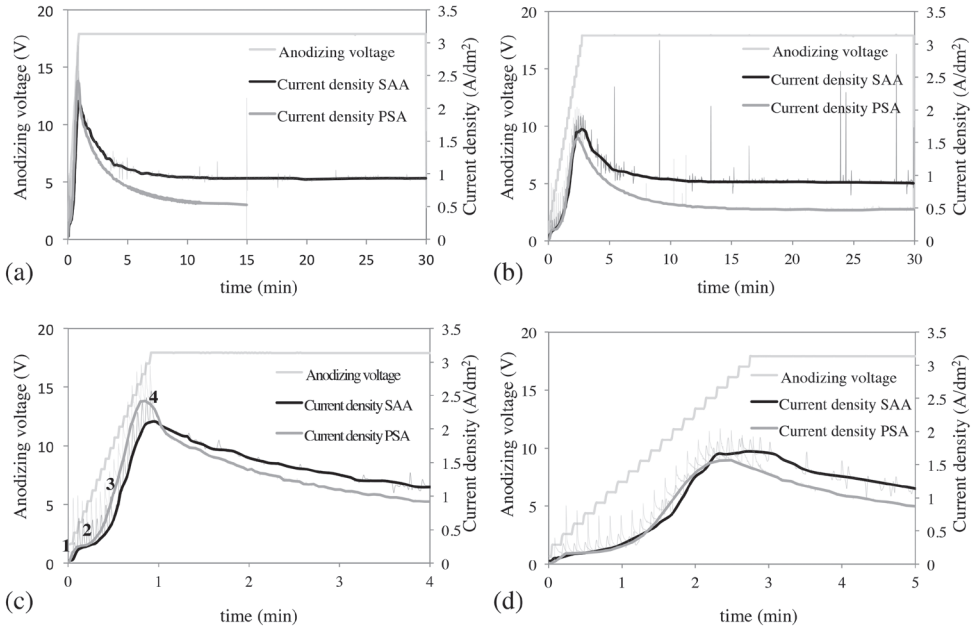

Figure 7.2: Current density response for potentiodynamic anodizing of AA1050 at 28±1 ºC for 30min in PSA and SAA with an initial voltage sweep of (a) 18 V/min or (b) 6 V/min, both up to 18 V. Images (c) and (d) show the initial 5 min of (a) and (b), respectively. Trend lines are included to clarify the general response. Please note that the 18 V/min curve for PSA is from the 15min cycle, since the 30 min curve showed much noise.

When the voltage was increased very slowly, at 0.6 V/min (not shown), no clearly defined stages were recognized in the recorded current. Instead, the current increased almost linearly with the anodizing voltage.

The steady state current density for an anodizing voltage of 18 V was found to be ±0.50 A/dm^2 for PSA and ±0.93 A/dm^2 for SAA, independently of the initial voltage sweep rate. The steady-state current density for 9V was measured during cycles 3, 5 and 7 and found to be ±0.23 A/dm^2 for PSA and ±0.38 A/dm^2 for SAA. So, steady state current densities were lower for PSA than for SAA, and current densities at 18 V were more than twice as high as at 9 V.

After 15 min of anodizing within cycle 5, the voltage was increased from 9V to 18V (at a rate of 6 V/min). Looking at the current density response in Fig. 7.3 (a), it is interesting to note that no current plateau is recorded during this intermediate voltage step, while

it was observed during the initial voltage sweep. Additionally, the recovery time (time until steady state is reached) is much shorter after the intermediate step than after the initial voltage sweep. The effect of a voltage *decrease* instead of increase is shown in Fig. 7.3 (b). A voltage decrease (18V→9V) is accompanied by a drop in the current density, for both PSA and SAA. The current increases towards a new steady state current density.

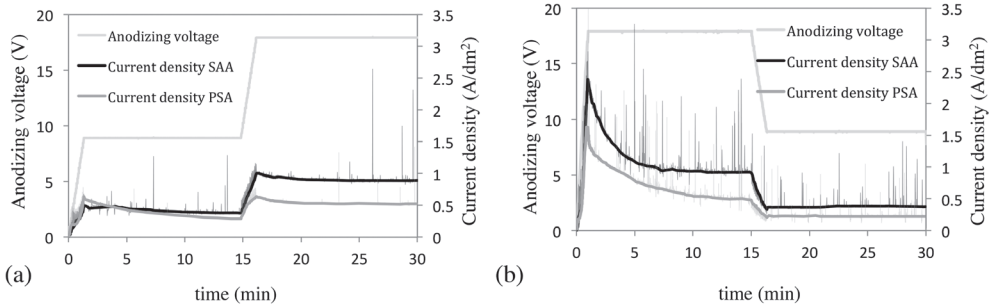

Figure 7.3: Intermediate voltage step: current density response for (a) voltage cycle 5 and (b) voltage cycle 7 for anodizing of AA1050 at 28±1°C in phosphoric-sulfuric acid (PSA) and sulfuric acid (SAA). Again, trend lines are included to clarify the general response.

7.3.2 Film Morphology

Fig. 7.4 displays cross sections of anodic films on AA1050 after 30 min of anodizing with a voltage sweep of 6 V/min up to 18 V (cycle 2). The PSA morphology is shown in Fig. 7.4 (a), SAA morphology in Fig. 7.4 (b). Note that the magnification is not the same for both images. Some general differences between the PSA- and SAA film morphologies are the following:

– The PSA film (±2.5 µm) is thinner than the SAA film (±5.7 µm);
– PSA pores and cells have larger diameters than SAA pores and cells;
– PSA pores are much larger close to the outer surface (±33 nm) than close to the barrier layer (±15 nm). The SAA morphology is more constant throughout the film thickness.

Similar differences were observed for all other voltage cycles.

It is especially interesting to compare the films prepared by voltage cycles with an intermediate dynamic step. Halfway during the process in cycle 7, the voltage was decreased from 18 V to 9 V. As a result, the film on AA2024-T3 clad exists of two distinct regions: a layer with coarse pores on top of a thin layer with much finer pores (Fig. 7.5 (b), with the boarder indicated with the dashed white arrow). For cycle 5 (9 V→18 V), one might expect to find a morphology that is inversed of cycle 7. However, Fig. 7.5 (a) shows that a distinct border between a fine-featured region and a coarse region is absent in this case.

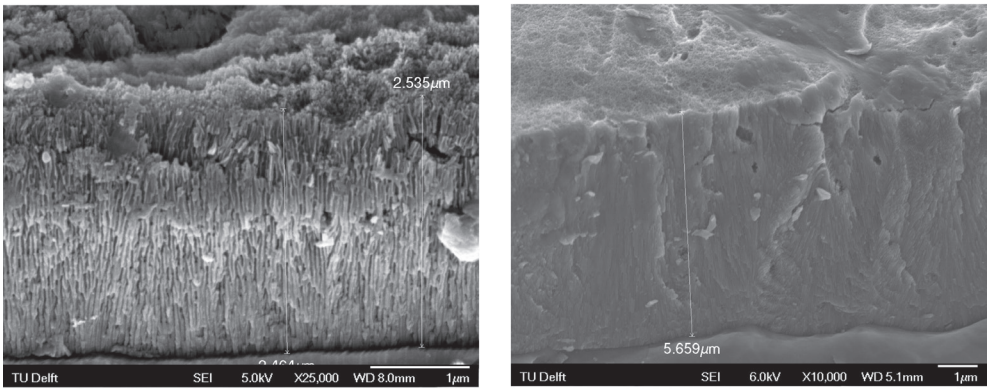

(a) (b)

Figure 7.4: FE-SEM cross-sectional images of AA1050 specimens, anodized for 30 min in (a) PSA and (b) SAA, at 28±1 ºC. These followed voltage cycle 2, with a sweep rate of 6 V/min up to 18 V. Note that the magnification is not the same for both images.

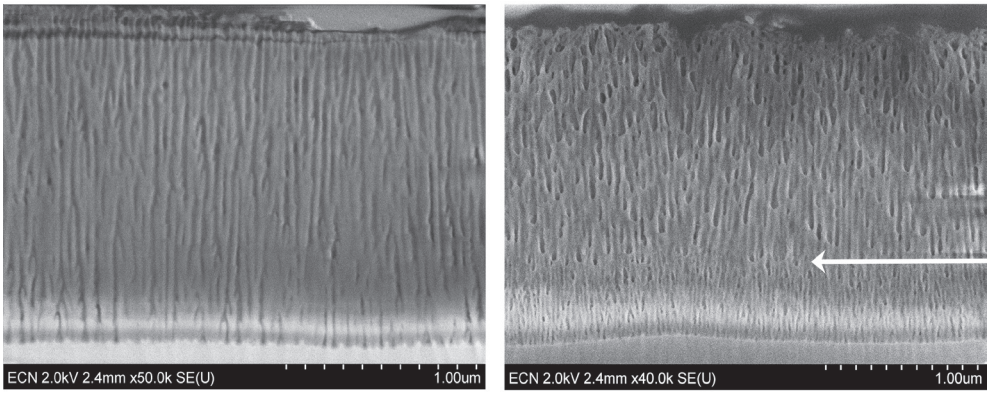

(a) (b)

Figure 7.5: SEM images of ion milled cross sections of AA2024-T3 clad specimens, anodized in PSA at 28±1 ºC for 30 min, (a) voltage cycle 5 (9 V → 18 V) and (b) voltage cycle 7 (18 V → 9 V).

Besides the cross section morphology, top view of the surface oxides was also studied with FE-SEM. When PSA is compared to SAA, differences were especially large for longer anodizing times. Fig. 7.6 displays the pore and cell diameters (for PSA and SAA) versus anodizing time. After 5 min of anodizing, the dimensions measured for PSA and SAA were still within the same order of magnitude (pore diameter 10-15 nm, cell diameter 17-27 nm). For prolonged anodizing, however, PSA dimensions increased significantly, while SAA dimensions remained the same. The 'pore widening effect' in PSA is more pronounced for voltage cycles 1 and 2 (final voltage 18 V) than for voltage cycle 3 (final voltage 9 V). Similar trends were observed for the cell diameter vs. time (not shown). The cell diameter was dependent on time for PSA, but independent of time for SAA.

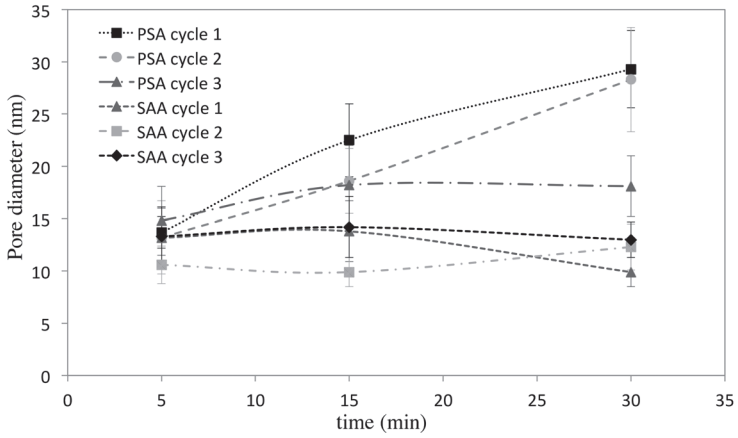

Figure 7.6: Pore diameter at outer surface of AA1050 vs. anodizing time for PSA and SAA, voltage cycle 1 (18 V/min up to 18 V), cycle 2 (6 V/min up to 18 V) and cycle 3 (6 V/min up to 9 V). Error bars represent ±1 σ.

7.3.3 Anodic Oxide Formation Efficiency

The anodic oxide formation efficiency, η_{ox}, is the ratio of the measured film mass to the theoretical mass calculated from the charge passed, using Eq. 7.1:

$$\eta_{ox} = \frac{m_2 - m_3}{\eta_{charge} \cdot \frac{M_{ox} \cdot Q(t)}{n_{ox} \cdot F}} \quad \text{Eq. (7.1)}$$

Where m_2 and m_3 are the weights of the specimen after anodizing (g dm^{-2}) and after oxide removal (g dm^{-2}), respectively, η_{charge} the charge efficiency, M_{ox} the molar mass of Al_2O_3 (102 g mol^{-1}), $Q(t)$ the cumulative charge transferred per dm^2, n_{ox} is the number of electrons associated with oxide formation (6) and F is the Faraday's constant (96 500 C mol^{-1}). Since η_{charge} is usually close to 1.0 for small anodizing systems, this value will be used for further calculations. For calculation of SAA efficiencies, both the charge and coating weight were determined from AA1050 specimens. For calculation of PSA efficiencies the charge passed Q during an AA1050-run was used while the coating weight was measured on an AA2024-T3 clad specimen. This is not ideal, but since anodic films on both alloys have shown to be almost identical, it will give a good indication of the actual efficiencies. As shown in Fig. 7.7, the anodizing efficiencies of SAA- are always higher than for PSA-processes. The anodizing efficiency is also positively related to the average anodizing voltage of a cycle. However, when the voltage cycle includes a period of decreasing voltage, the efficiency is always lower than when the voltage is increased, even though the average voltages are comparable. This is clearly seen when cycle 4 (0 →18 V) is compared to cycle 6 (18 → 0 V), and cycle 5 (9 →18 V) to cycle 7 (18 → 9 V).

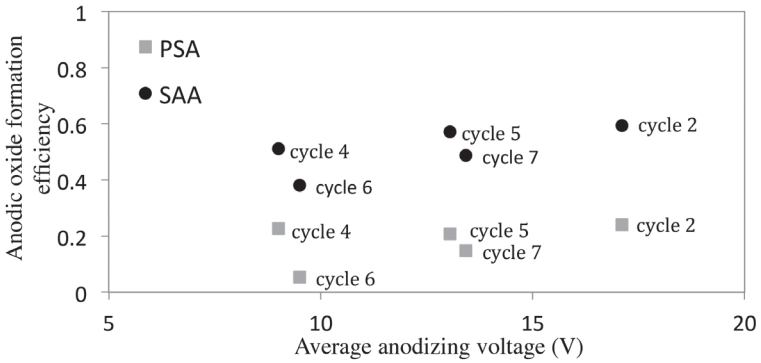

Figure 7.7: Anodic oxide formation efficiencies versus the average anodizing voltage for PSA and SAA, after 30min anodizing.

7.4 Discussion

Previous work by Curioni et al. [10] has shown that for linear polarization anodization of high purity aluminium, the current density response consists of three distinct stages, which correspond to different growth phases of the anodic oxide film. These three current density stages were also observed in this study for AA1050 anodizing (Fig. 7.2 (d)):

1. First, the current rises rapidly due to ionic conduction across the thin, pre-existing air-formed film. Aluminium ions start to move outward and oxygen ions migrate inward.
2. The current density temporarily stabilizes ('current plateau') when the barrier layer is grown at a constant thickening rate. No pores have been formed yet at this stage.
3. As soon as pores start to form at the surface of the barrier film, the current plateau ends. The presence of pores eases current flow which leads to an increased current density.

Surprisingly, a fourth current density stage was recorded in this study: a relatively broad current peak just before the voltage reaches its final value. Such broad current peaks were previously only recorded for aluminium alloys with higher amounts of alloying elements, like bare AA2024-T3 [11]. Oxidation of second phase particles is thought to be responsible for the generation of these peaks. So far, it remains unclear what mechanism causes this current peak for high purity aluminium.

A current plateau (second current density stage) is only seen after initial voltage sweeps (Fig. 7.2 (d)), not after intermediate ones (Fig. 7.3). During intermediate voltage sweeps, pores are already present at the surface and current flows not only due to barrier layer thickening but also due to displacement of oxide towards pore walls.

For SAA anodizing, the measured film features (pore diameter *d,* cell diameter *c* and barrier layer thickness *b*) were in most cases consistent with the linear relation between

morphology and anodizing voltage. Film cross sections indicated that small pores and cells developed during the time periods of low voltages, while large pores and cells developed during high voltages. Conversely for PSA films, only the bottom film sections – those close to the barrier layer – were in most cases consistent with this model. At the outer surface, rough PSA morphology with large pores was observed for all voltage cycles. As for the effect of anodizing time, outer pore and cell diameters showed to increase with time when anodizing was conducted in PSA but remained constant in SAA.

Since the only difference between PSA and SAA is the presence of phosphoric acid in the electrolyte, differences are likely to be caused by dissolution of the outer pore walls in phosphoric acid. Previous work has shown that the chemical dissolution rate of Al_2O_3 depends on the concentration of phosphoric acid in the electrolyte [1] while the solubility of Al_2O_3 in sulphuric acid is very low [15]. The results of this study show that both pore diameters and cell diameters increase with time during PSA anodizing. This suggests that the outer pore walls do not only get thinner, since this would lead only to a variation in cell diameter, but that outer walls completely dissolve in the electrolyte. Oxide film dissolution in phosphoric acid causes complete or partial disappearance of the fine-featured section that was formed during the initial voltage sweep (Fig. 7.8), resulting in an increase in cell diameter with time. Since film growth occurs at the aluminium/film interface, the recently formed bottom part of the anodic film has been in contact with the electrolyte for a very short period of time and is, therefore, less affected by dissolution. This explains why PSA film morphologies at the bottom section are more consistent with the linear model than the top section. It also explains why PSA pore diameters after 5 minutes of anodizing are similar to those of SAA.

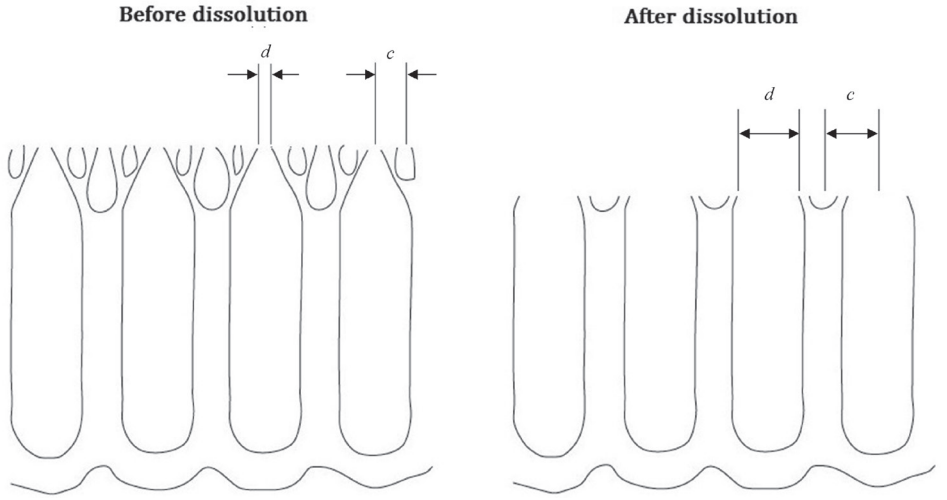

Figure 7.8: Schematic illustration of the oxide morphology after dissolution of the outer surface during prolonged anodizing in phosphoric-sulfuric acid.

O'Sullivan and Wood [4] previously described that immediately after a fast voltage change ($dV/dt \rightarrow \infty$), pore diameters have to adapt to the new voltage. Pore widening is proposed to happen through dissolution of the pore base with coalescence of the growing pores, which reduces the number of pores and increases the pore diameter. On the contrary, after a decrease in voltage, the pore walls cannot become thicker, and therefore the new pores, with smaller diameter, must initiate and develop below the pre-existing larger pores. This study shows that O'Sullivan and Wood's theory also holds for the more gradual voltage changes of 6 V/min. The film prepared with an intermediate increase in anodizing voltage (Fig. 7.5 (a)) exhibits a gradual transition between the 9 V- and 18 V-region. During this voltage increase, pore walls of small 9 V-pores partly dissolve to create the transition towards larger 18 V-pores, which are formed below them. Conversely, there is a clear border between the 9 V- and 18 V- region (Fig. 7.5 (b)) after a voltage decrease.

As expected, the results indicated a positive relation between average anodizing voltage and anodizing efficiency (Fig. 7.7). Higher anodizing voltages generally result in higher current densities. Since the current density is a direct measure of the oxide growth rate, a higher anodizing voltage generally results in a higher efficiency. More surprising is the fact that cycles including an intermediate voltage increase have higher efficiencies than cycles with an intermediate voltage decrease, even when the average voltages of both cycles are similar. This phenomenon is likely to be caused by the fact that after a voltage increase, the barrier layer is temporarily thinner than its equilibrium value. As seen in Fig. 7.3, this causes the current to temporarily exceed the steady state value. The opposite is true for the transient after a voltage decrease, when the barrier layer is temporarily thicker than the equilibrium thickness and the current temporarily drops below steady state. The current density peak after a voltage increase is expected to contribute to a higher overall current flow during the anodizing cycle, and therefore also to a higher oxide formation efficiency. The opposite accounts for a voltage decrease, where a drop in current density leads to a lower total current flow and a lower efficiency. Differences in efficiency between SAA and PSA processes are likely to be caused by the high solubility of Al_2O_3 in phosphoric acid. If the rate of dissolution is high compared to the film growth rate, which is the case for PSA anodizing, this lowers the anodic oxide formation efficiency.

7.5 Conclusions

This work has shown that current density responses, anodic film morphologies and oxide formation efficiencies are dependent on the applied voltage profile for potentiodynamic anodizing in phosphoric-sulphuric acid (PSA) and sulphuric acid (SAA). Four distinct stages were identified for the initial current response at relatively fast initial voltage sweeps (6 V/min and 18 V/min). The final current density is independent of the initial voltage sweep rate. As expected, changing the voltage during the process results in differences in oxide morphology across the film thickness. Coarse morphologies are developed at higher voltages and fine morphologies at lower voltages. Interesting differences were found between cycles with an intermediate increase in anodizing voltage versus cycles with an intermediate decrease in voltage. After a sudden voltage decrease, new pores with smaller diameters have to develop below existing pores, which result in a distinct border in the film morphology. Conversely, after a voltage increase, a transition layer with 'intermediate size pores' forms by partly dissolving walls of smaller pores. The current density peak after a voltage increase contributes to a higher overall current flow during the anodizing cycle, while a drop in current density after a voltage drop leads to a lower total current flow. Since the current density is a direct measure of the oxide growth rate, anodizing cycles including an increase in voltage have higher oxide formation efficiencies, even when the average voltage is similar to that of another cycle. For prolonged anodizing, the high solubility of Al_2O_3 in phosphoric acid significantly affects the film morphology in PSA. Finally, it was found that the anodic oxide formation efficiency is higher for SAA than for PSA.

7.6 References

1. Sheasby, P.G. and R. Pinner, *Surface Treatment and Finishing of Aluminium and its Alloys*. 6th ed. 2001., England: Finishing Publications Ltd.
2. Brockmann, W., et al., *Adhesion in bonded aluminium joints for aircraft construction.* International Journal of Adhesion and Adhesives, 1986. **6**(3): p. 115.
3. Thompson, G.E., *Porous anodic alumina: fabrication, characterization and applications.* Thin Solid Films, 1997. **297**(1–2): p. 192-201.
4. O'Sullivan, J.P. and G.C. Wood, *The Morphology and Mechanism of Formation of Porous Anodic Films on Aluminium.* Proceedings of the Royal Society of London. A. Mathematical and Physical Sciences, 1970. **317**(1531): p. 511-543.
5. Setoh, S. and A. Miyata. Scientific Papers of the Institute of Physical and Chemical Research. Vol. 317. 1932, Tokyo.
6. Keller, F., M.S. Hunter, and D.L. Robinson, *Structural Features of Oxide Coatings on Aluminum.* Journal of The Electrochemical Society, 1953. **100**(9): p. 411-419.
7. Rahman, M.M., et al., *Effect of the anodization voltage on the pore-widening rate of nanoporous anodic alumina.* Nanoscale Research Letters, 2012. **7**(1): p. 474.
8. Huang, Y., et al., *Kinetic models of controllable pore growth of anodic aluminum oxide membrane.* Metals and Materials International, 2012. **18**(3): p. 433-438.
9. Curioni, M., et al., *Optimization of anodizing cycles for enhanced performance.* Surface and Interface Analysis, 2013. **45**(10): p. 1485-1489.
10. Curioni, M., P. Skeldon, and G.E. Thompson, *Anodizing of Aluminum under Nonsteady Conditions.* Journal of The Electrochemical Society, 2009. **156**(12): p. C407-C413.
11. Curioni, M., et al., *Graded anodic film morphologies for sustainable exploitation of aluminium alloys in aerospace.* Advanced Materials Research, 2008. **38**: p. 48-55.
12. Ma, Y., et al., *Anodic Film Formation on AA 2099-T8 Aluminum Alloy in Tartaric–Sulfuric Acid.* Journal of The Electrochemical Society, 2011. **158**(2): p. C17-C22.
13. Critchlow, G.W., et al., *Strategies for the replacement of chromic acid anodising for the structural bonding of aluminium alloys.* International Journal of Adhesion and Adhesives, 2006. **26**(6): p. 419-453.
14. Hussey, R.J. and J. Wilson, *Light Alloys: Directory and Databook*. 1998, New York: Chapman & Hall.
15. Ćurković, L., M. Fudurić, and S. Kurajica. *Kinetic study of the corrosion of alumina ceramics in sulphuric acid aqueous solution*. in *1st Interantional Conference Corrosion and Material Protection*. 2007. Prag, Češka.

CHAPTER 8

The effect of Cr(VI)-free anodizing conditions on interfacial bonding strength and durability of adhesively joined aluminium

Part of this chapter was submitted as a scientific paper:
Abrahami, S.T., de Kok, J.M.M., Gudla, V.C.M Ambat, R., Terryn, H. and Mol, J.M.C. (2016).

Abstract

A robust industrial Cr(VI)-free anodizing process is needed to prepare aluminum structural parts for adhesive bonding in aerospace applications. A crucial parameter in the long-term integrity of these bonded assemblies is the durability of the joint under various environmental conditions. In this study, we investigated the relationship between the anodizing conditions in sulfuric, or a mixture of sulfuric and phosphoric acid electrolytes and the quality and robustness of bonding with an aerospace epoxy adhesive (AF163). Scanning electron microscopy (SEM) was used to characterize the pore size and film thickness. In addition, selected specimens were studied with transmission electron microscopy (TEM) coupled with energy-dispersive X-ray spectroscopy (EDS) to measure the resin concentration within structurally different porous anodic oxide layers as a function of depth. Results show that anodizing at higher temperature and higher phosphoric acid concentration leads to excessive chemical dissolution of the initially formed anodic oxide. A distinction was made between two types of morphological changes that affect adhesion. Dry peel strength indicated that a minimum pore size is important for the initial formation of a strong bond between the oxide and the adhesive. However, extended chemical dissolution was found signification for bond durability under water ingress, as it modifications to micro- and nano-roughness of the oxide/resin interface. Hence, a higher degree of dissolution during anodizing is beneficial for the adhesion, facilitating a composite-like interphase. Too much dissolution, however, reduces the resistance to bondline corrosion. Overall, the presented results illustrate the need to consider both chemical and morphological changes in the selection of Cr(VI)-free alternatives for structural adhesive bonding.

8.1 Introduction

Long-term service of adhesively bonded aircraft structures relies upon the durability of adhesion between the aluminum substrates and the adhesive. The importance of surface preparation for bond durability was directly recognized in the early days of the aerospace industry. Initially, pre-treatments for structural bonding included only chemical degreasing and etching using Cr(VI)-based solutions [1]. This combination was sufficient to primarily remove the mechanically weak surface layers, including the native oxide, and subsequently produce a new micro-rough surface oxide that is suitable for adhesion. Later on, anodizing was added to the pre-treatment procedure, mainly to increase the corrosion resistance [2]. Utilizing low pH electrolytes for anodic oxidation produces a porous self-ordered hexagonal oxide structure on top of a compact barrier layer [3]. The anodic oxidation is driven by an external voltage or current source. Hence, the oxide films produced by this method can be substantially thicker than those obtained using chemical etching.

Over the years, industrial and scientific research has greatly contributed to our understanding of the changes that take place during surface treatments of aluminum and its alloys, as well as the influence of the different processing parameters [4]. Nevertheless, the excellent adhesion and corrosion resistance that is achieved by the complete Cr(VI)-based pre-treatment process currently applied by the European aerospace industry is not easily duplicated [5]. Since strict international environmental and health regulations announced the near future ban of Cr(VI), its replacement has become a burning issue [6]. Reviewing the literature to this day, the high strength of these bonded structures is attributed to the accumulated effect of two main mechanisms: (1) mechanical interlocking and (2) chemical- and physical interactions between the oxide and the organic resin [7-9].

Since candidate Cr(VI)-free electrolytes such as phosphoric acid (PAA), sulfuric acid (SAA), and phosphoric-sulfuric acid (PSA) mixtures introduce different chemical and morphological modifications in comparison to the oxide produced by chromic acid anodizing (CAA), their effects on adhesion strength and durability are not well understood. In our previous study, we reported that the density of hydroxyl species at the surface of the oxide is closely related to the stability of bonding with an epoxy-based adhesive upon the ingress of water [10]. Since the former study has been conducted on thin, featureless barrier anodic oxide films, it does not take into account variations in the surface roughness that can lead to different levels of mechanical interlocking. Hence, in this study we explore the additional effect of changes in the oxide morphology on the resulting adhesion strength and stability. To this aim, a set of samples with anodic films having a range of pore sizes and lengths were prepared and characterized. The penetration of the resin into the various oxide pores was studied using high resolution scanning and transmission electron microscopy coupled with energy dispersive X-ray

spectroscopy and related to its resulting bonding performance measured using floating roller peel tests.

8.2 Experimental

8.2.1 Materials and Sample Preparation

The effect of anodizing conditions was studied on an AA7075-T6 alclad (clad layer AA7072). Six different combinations of phosphoric acid (H_3PO_4) and/or sulfuric acid (H_2SO_4) concentrations were used, as presented in Table 8.1. Within each electrolyte combination, three different parameters were varied: temperature (20 °C, 35 °C and 50 °C), anodizing dwell time (15 and 30 min) and voltage (preselected to yield a stable process at "low" and "high" relative voltages, see Table B1 in Appendix B for the exact values, since they varied with the electrolyte and the anodizing conditions).

Table 8.1: Electrolyte combinations applied in this study. Al^{3+} bath concentration was 2 g/l.

H_3PO_4 (g/l)	0		40		80	
H_2SO_4 (g/l)	10	50	10	50	10	50

Prior to anodizing, all specimens were degreased in 50 g/l Metaclean T2001/4 VP2 (Chemie-Vertrieb GmbH) at 67.5 °C for 15 min. This was followed by etching in 35 g/l P3 Almeco (Henkel) for approximately 5 min at 35 °C for 3-4 μm metal removal and desmutting in 150 g/l Desoxin AL (Enthone) for 15 min at 30 °C. After anodizing the panels were dried at 45 °C for 30 minutes.

Panels for mechanical testing were additionally coated with 1-2 μm of phenol formaldehyde primer layer (Redux 101, Hexel, without inhibitor) and an AF163 epoxy structural adhesive film (3M). All panels were bonded at 6 bar and cured at 125 °C for 75 minutes.

Floating roller peel tests were performed according to ASTM D3167-03a [11]. The panels were cut into 25 mm wide samples using a lint saw. After fixing the test panels in the apparatus, the unbound end of the specimen was attached to the lower head of the testing machine. The thin panel was peeled off the thicker panel at a speed of 100 mm/min. The peeling load versus head movement (or load versus distance peeled) was recorded. All tests were performed at ambient temperature. The first half of the specimen was peeled under dry (atmospheric) conditions. Water containing surfactants was then applied to the crack-tip and the second half was peeled under wet conditions. Additional bonded panels were placed in the salt cabinet for accelerated corrosion test using the standard conditions (ISO 9227) for neutral salt spray test (NSS). After 90 and

180 days of exposure, panels were tested for peel strength and visually examined for the extent of bondline corrosion.

8.2.2 Scanning Electron Microscopy (SEM)

Pore size and oxide thickness were measured from top- and cross-section view using Hitachi SEM SU-70. Image capturing occurred at an accelerating voltage of 2.0 keV, a current of 19-20 μA and a working distance of 2.0-3.4 mm. No Pt coating was applied. The image software system AnalySIS was used to measure pore and interpore distances close to the outer surface and close to the barrier layer.

A cross-section of selected panels was cut using a diamond saw and (cold) embedded. The cross-sections were then grinded and polished down to 1 μm using a diamond paste. Lamellas for TEM measurements were then prepared by focused ion beam (Helios Nanolab 600, Dual Beam FEI) milling and in-situ lift out from the interface of the adhesive joint. The lamellas of approx. 1 μm thick were further thinned down for electron transparency to an approximate thickness of 120 nm and low energy milling (2 keV) was finally performed to remove any ion beam induced artifacts and damage to the samples.

8.2.3 Transmission Electron Microscopy (TEM)

Selected panels were chosen for detailed microstructural characterization using a transmission electron microscope (Tecnai T20 G2, FEI) operating at 200 keV. The local composition of the anodic oxide and the relative concentrations of the resin in the porous structure were measured using an X-ray energy dispersive spectrometer (EDS, Oxford X-Max SDD X-ray detector) coupled to the TEM.

8.3 Results

8.3.1 Oxide Film Morphology

8.3.1.1 Film thickness and Surface Morphology

The diverse anodizing conditions that were applied in this study resulted in porous oxide layers with a broad range of morphological features. SEM measurements were used to determine the oxide thickness and pore size. Pore diameter (measured at the surface) ranges between 5 and 60 nm, with varying oxide film thicknesses of up to 6 μm. A full list of the measurements is given in Table B1 in Appendix B. The general trends are highlighted below.

Top view SEM images of selected oxides are shown in Fig. 8.1. The corresponding anodizing conditions and measured pore- and oxide thicknesses are listed in Table 8.2. A clear change in the morphology as a function of the anodizing conditions is visible. The pore size of the different oxides is generally visible in the images at high magnification.

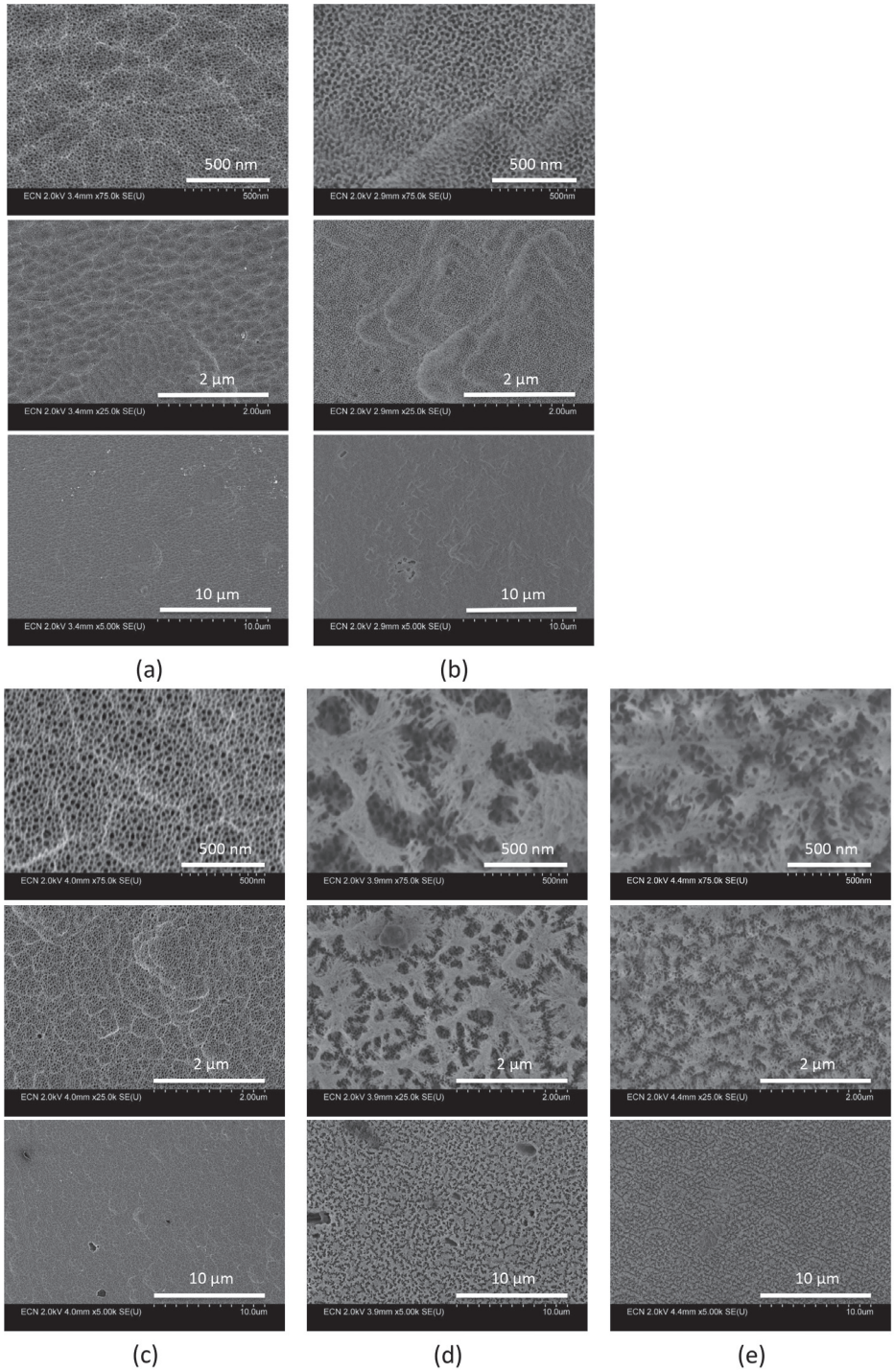

Figure 8.1: Secondary electron SEM images of the surface morphology of anodic oxides produced by anodizing in: (a) SAA20, (b) SAA50, (c) PSA20, (d) PSA35 and (e) PSA50 (full experimental conditions are listed in Table 8.2).

The SAA oxides at both 20 °C and 50 °C produce a relatively dense honeycomb porous structure with finer pores for the lower anodizing temperature (Fig. 8.1 (a) and (b) for SAA20 and SAA50, respectively). Since except for the temperature the anodizing conditions are similar, pore widening is caused by the prolonged contact with the high temperature electrolyte. When the anodizing electrolyte also contained phosphoric acid, pores were already wider at 20 °C (Fig. 8.1(c)). Finally, more aggressive anodizing conditions that include phosphoric acid and higher temperatures cause such extended dissolution that the top part of the oxide have collapsed during anodizing, exhibiting a "bird's nest"- like structure on top of the honeycomb (Fig. 8.1 (d) and (e) for PSA35 and PSA50, respectively). These additional features significantly increase the surface roughness of these oxides. This is noticeable in the images taken at lower magnifications. "Bird's nests" that extends between 0.5-2 μm in lateral size on PSA35 and PSA50 provides an extra microscopic roughness to the oxide surface. Since these "nests" are clusters of nano-sized ridges and pore walls, they also provide a nano-roughness that significantly increases the effective surface area. Conversely, the top surface of both SAA oxides and PSA20 that do not exhibit these features are relatively smooth (Fig. 8.1 (a), (b) and (c), respectively).

Table 8.2: Anodizing conditions and oxide dimensions (measured by SEM) for the selected samples in Fig. 8.1.

Abbreviation	Anodizing Temp. (°C)	H_2SO_4 (g/l)	H_3PO_4 (g/l)	Voltage (V)	Anodizing time (min)	Oxide thickness (μm)	Pore diameter (nm)
SAA20	20	10	0	19	30	1.2 ± 0.1	7 ± 2
SAA50	50	10	0	19	30	5.2 ± 0.4	24 ± 3
PSA20	20	10	80	26	15	1.0 ± 0.1	25 ± 5
PSA35	35	50	80	19	30	3.2 ± 0.1	40 ± 5
PSA50	50	10	40	23	15	2.1 ± 0.2	44 ± 4

In addition to the electrolyte composition and temperature, variations in the voltage and anodizing time were also found to affect the morphology of the produced anodic oxides. Pore size at the surface generally becomes larger with time due to the extended period of contact with the dissolving electrolyte (see Table B1 in Appendix B). The higher the anodizing temperature and the concentration of phosphoric acid, the larger the difference in pore size for short (15 min) and long (30 min) anodizing times. Similar trends were observed when a higher anodizing voltage was applied.

The extent of oxide dissolution can also be observed in Fig. 8.2, which displays the accumulated charge density, Q, (calculated from the measured current density and the time that passed during anodizing, Table B1 in Appendix B) and the final oxide thickness. The higher the anodizing temperature, the more the oxide thickness deviates from the linear relationship that is predicted using Faraday's law of electrolysis (the solid line in Fig. 8.2). In addition, this deviation is more prominent for higher phosphoric acid concentrations (not indicated).

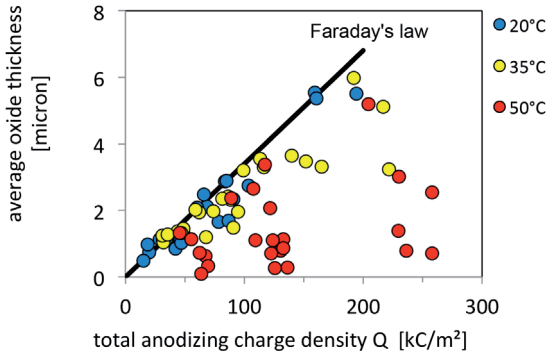

Figure 8.2: Average oxide thickness vs. the total anodizing charge density. A larger degree of deviation from Faraday's law for anodizing at 35 °C and 50 °C is related to chemical dissolution of the anodic oxide by the electrolyte.

8.3.2 High Resolution Oxide Morphology

Five different panels that were produced by varying anodizing conditions had been chosen for a detailed study using high resolution TEM. To investigate the interface area, lamellas were prepared using focused ion beam (FIB) milling from cross-sections of the samples. Fig. 8.3 shows an example of such cross-section with the site of interest marked in green at the interface between the oxide and the primer and adhesive. Also visible in Fig. 8.3 is the border between the primer layer and the adhesive. Primers are commonly used to seal the oxide immediately after the pre-treatment (and before bonding) for protection. Since primers are diluted versions of the adhesives, it is generally also presumed that they can penetrate more easily into the pores, assisting in the formation of a stable bonding. From here on, the primer and adhesive are generally referred to as the resin.

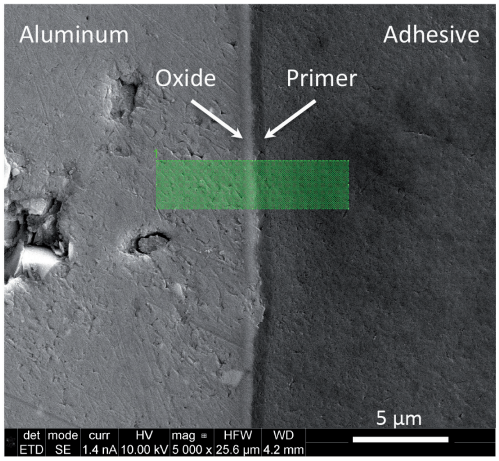

Figure 8.3: SEM image of a cross section before FIB milling. The area marked in green was chosen for lamella preparation. The separation between the primer layer (dark band) and adhesive layer (lighter region to the right of the dark band) is visible.

High-resolution TEM bright field images of the five chosen oxides are shown in Fig. 8.4. Both SAA20 and PSA20 oxides (Fig. 8.4 (a) and (c)) show a branched morphology with similar features throughout the oxide film thickness and a relatively smooth interface. Some branching with undeveloped pores can be distinguished at the surface of these oxides. This indicates of a very limited chemical dissolution during anodizing, since the "history" of the initial pore development stages is still present. Conversely, the advanced dissolution of the films prepared at 35 °C and 50 °C (Fig. 8.4 (b), (d) and (e)), resulted in oxides that are much rougher, irregular, and thinned at the oxide/resin interface. Although a relatively high anodizing temperature leads to widening of the pores at the oxide/resin interface, it seems to have little to no effect on the features in the interior of the oxide. The "birds nest" morphology that was previously observed in Fig. 8.1 (d) and (e) can be distinguished in the cross section view of the corresponding oxides (Fig. 8.4 (d) and (e)). They display a "zigzag" morphology at the upper part of the oxide. Although not visible in the SEM image in Fig. 8.1 (b), similar feature could be seen on the SAA50 oxide, but at a much lower level and density (for an example, see Fig. B1 in Appendix B). Hence, an additional micro- and nano-roughness is present at the surface of the high-temperature oxides, the extent of which clearly varies with the temperature and/or phosphoric acid concentration.

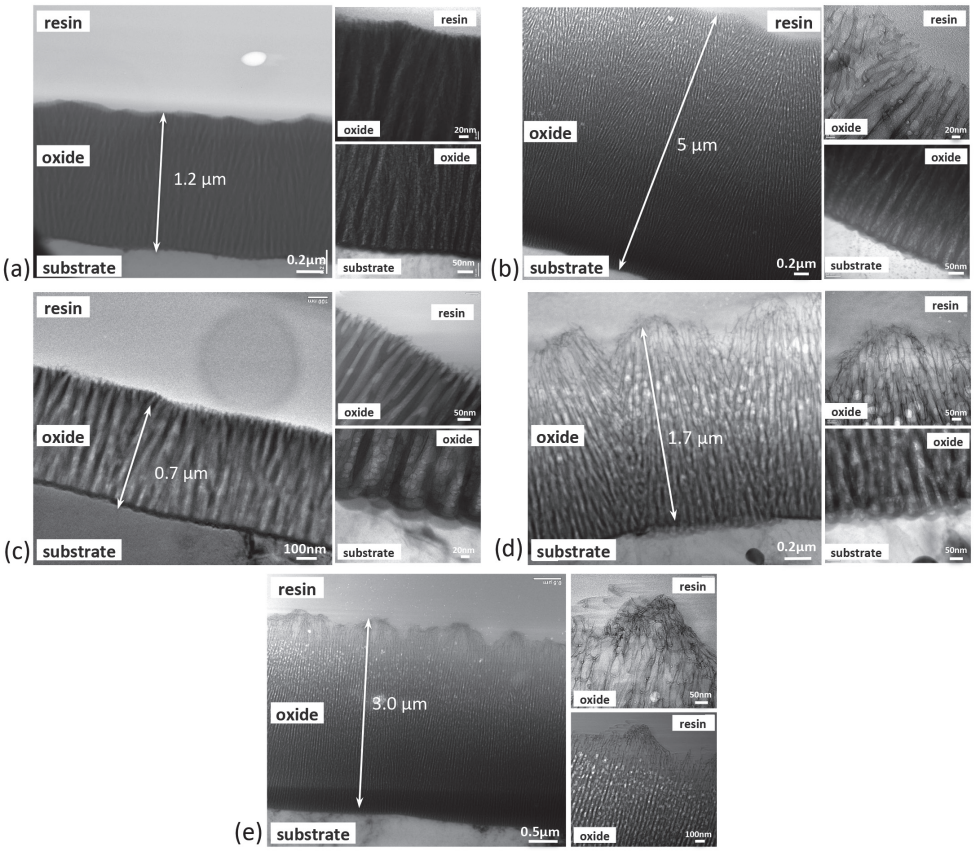

Figure 8.4: Bright field TEM micrographs of the five selected oxides. For each image: a complete cross-section (large) and zoom-in at the top- and bottom part of the oxide (smaller images) are shown. Anodizing conditions: (a) SAA20, (b) SAA50, (c) PSA20, (d) PSA35 and (e) PSA50.

Table 8.3 lists the measured morphological features that were retrieved from the TEM images in Fig. 8.4. Under the concentration and potential conditions, as in SAA20 and SAA50, the oxide thickness increases with an increasing anodizing temperature, in accordance with Schneider et al. [12]. The thickness of the barrier layer generally corresponds to the applied voltage following the 1.2 nm/V relation [4]. The relation accurately predicts the barrier layer thickness of both SAA oxides, while the measured values for PSA oxides are slightly larger than expected. Pore diameters for 20 °C oxides do not differ much at bottom and top part of the oxide. For 35 °C and 50 °C anodizing, pores are much larger at the surface due to chemical dissolution.

Table 8.3: Summary of the oxide morphology measured on the TEM images.

Annotation	Anodizing temperature	Oxide thickness (μm)	Pore diameter (nm)		Barrier layer thickness (nm)
			[Top]	[Bottom]	
SAA	20 °C	1.2	8	13	15
	50 °C	5.0	22	8	17
PSA	20 °C	0.7	22	25	30
	35 °C	3.0	28	15	20
	50 °C	1.6	30	20	26

8.4 Primer Penetration

It is of great interest to relate the oxide geometrical features to the extent at which the primer/resin is able to penetrate into the oxide. Fig. 8.5 and 6 show the concentration profiles of the main elements detected by TEM-EDS measurements on the different lamella that were shown in Fig. 8.4. The three different phases: aluminum (A), oxide (O) and resin (R) can be clearly distinguished. Except for copper that arises from the TEM sample holder (and is detected in all cases), only Al is found in the substrate region.

Some sulfur and phosphorus are detected in the relevant oxides that mainly consist of aluminum and oxygen. These arise from the incorporation of anions during anodizing in the corresponding acids and their concentration correspond to the levels previously measured by AES on barrier-type oxides [13]. Sulfur (1-3 wt.%) is detected throughout the SAA oxides and 0.0-1.0 wt.% phosphorus and 0.0- 2.0 wt.% of sulfur were detected in the PSA oxides.

The organic based resin is mostly composed of carbon and oxygen, with some inorganic additives such as silicon and bromine. Because some degree of carbon contamination is expected to be found on all anodic oxides due to ambient exposure before bonding (as well as lamella processing) [14], the most definite indicators for the presence of resin in the pores are silicon and bromine. Silicon was found mostly close to the oxide-resin interface of all specimens. Its presence suggests that silane adhesion promoters may have been incorporated into the primer chemistry. Bromine was detected in all specimens, with an initial concentration of 0.1 wt.% at the oxide/resin interface and increasingly higher concentration towards the bulk of the resin. Maximal detected concentration of bromine ranged from 5 to 12 wt.%. Although these two elements are definite indications for the presence of resin within the oxide, their concentration is very low (especially for Si, with 0.1- 0.2 wt.%). Moreover, bromine concentration profiles in Fig. 8.5 and 8.6 generally follow the same trend as the corresponding carbon profile. Carbon is therefore further used as a measure for the presence of resin within the oxides.

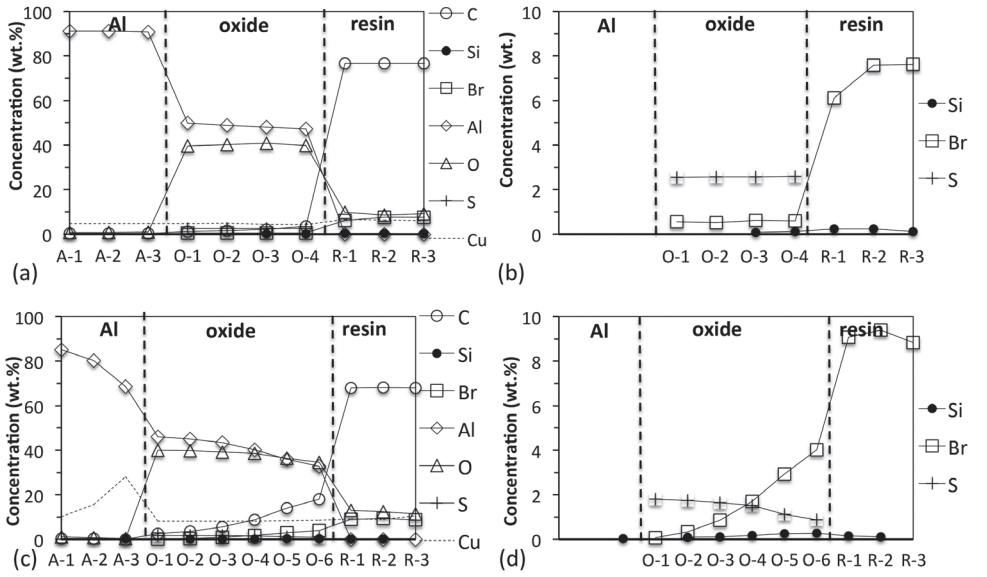

Figure 8.5: TEM-EDS concentration profile measurements (left) and a closer look at selected low-concentration elements (right). Anodizing conditions: (a) and (b) SAA20, (c) and (d) SAA50. Notice that due to differences in oxide thickness, the last measurements within an oxide, as well as the distance within two points differ between specimens.

Comparing the different profiles show that the carbon content in the bulk of the resin is similar in all specimens, ranging between 60-80 wt.% C. At the resin/oxide interface, however, differences start to emerge. For PSA35 and PSA50 oxides, carbon concentration decreases gradually until it reaches a minimum of 6-18 wt.% near the bottom of the oxide. Conversely, the carbon concentration drops abruptly at the oxide/resin interface of SAA20, SAA50 and PSA20 oxides. This observation can be assigned to differences in surface roughness at the oxide/resin interface. The presence of "bird's nests' at the interface leads to a larger transition zone.

Pore size appears to plays a role in determining the amount of resin penetration. PSA oxides that have a larger pore size near the oxide/aluminum interface display relatively high carbon concentration. Conversely, the carbon concentration within SAA oxides drops to a minimum value of 1-2 wt.% near the bottom of the oxide. This minimum concentration is significantly lower than the final carbon concentration that was detected in PSA oxides (6-18 wt.%).

8.4.1 Mechanical Performance

Since the peel test simulates the most severe type of loading on the assembly (mode I/II), it is used to evaluate the lower limit of adhesion strength [15]. When tested under dry conditions, it indicates the quality of the initial bonding. Under wet conditions, bond durability is tested, as water ingress is often cited as the main cause for environmental

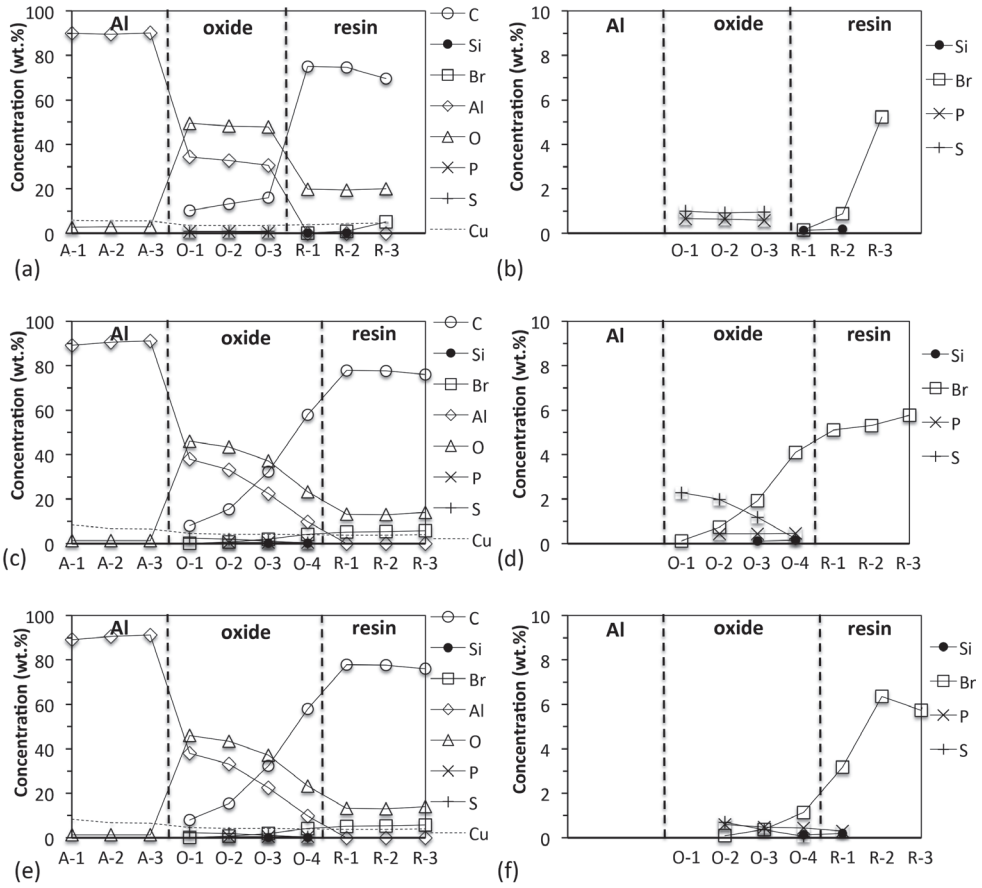

Figure 8.6: TEM EDS concentration profile measurements (left) and a closer look at selected low-concentration elements (right). Anodizing conditions: PSA20 (a) and (b), PSA35 (c) and (d) and PSA50 (e) and (f). Notice that due to differences in oxide thickness, the last measurements within an oxide, as well as the distance within two points differ between specimens.

adhesion failure [16]. Figure 8.7 (a) and (b) displays the measured dry peel strength vs. the pore diameters and the oxide thickness, respectively. It shows that, up to a certain limit, the initial peel strength increases with the pore size. Almost all oxides with pore diameters larger than 15 nm fulfill the minimum level of strength (300 N) with required cohesive fracture (shown in Fig. 8.9). Above approximately 25 nm, the dry peel strength remains relatively constant and independent of the pore size. There is, on the other hand, no correlation between oxide thickness and its dry peel strength (Fig. 8.7 (b)).

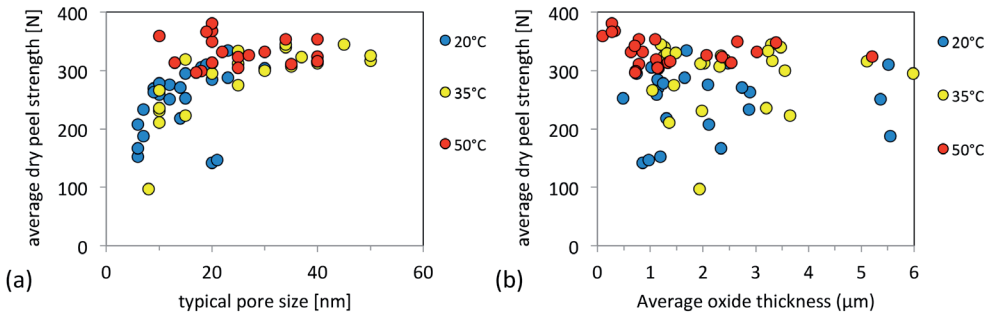

Figure 8.7: Average dry peel strength vs. the average oxide pore diameter (a) and the average oxide thickness (b), both determined by SEM.

Figure 8.8 (a) and (b) displays the trends in the measured wet peel strength vs. the measured pore diameters and the oxide thickness, respectively. In contrast to the previous results, the wet peel strengths display no clear relation to the pore size. It is interesting to note that oxides with similar pore size (at the surface) showed different mechanical performance depending on the electrolyte combination and temperature. A clear distinction is made between anodizing at 20 °C and 50 °C. Besides a single exception (that involves the highest phosphoric acid concentration), all the oxides produced at 20 °C underperform. Oxides produced at 50 °C show higher strength values than the average. This trend is also reflected in the five selected oxides in Table 8.4. The performance of oxides prepared at 35 °C varied according to the combination of the preparation conditions. Also under wet conditions, no correlation was found between the anodic oxide thickness and the measured peel strength (Fig 8.8 (b)).

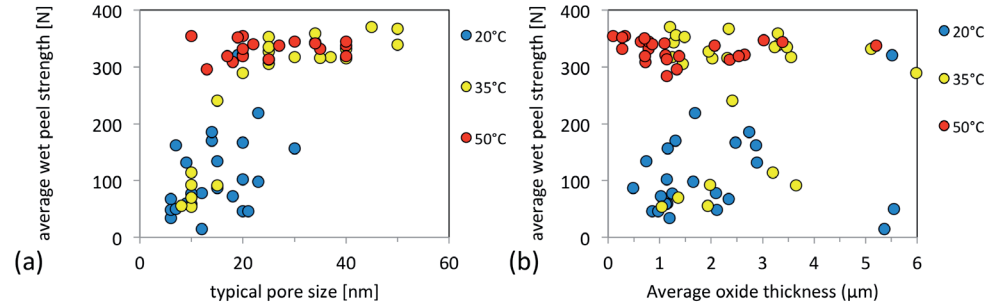

Fig. 8.8: Average wet peel strength vs. the pore diameters (a) and the average oxide thickness (b), both determined by SEM.

Generally, the wet peel strength of oxides prepared at 20 °C is much lower than their dry peel strength and they exhibited an interface (adhesive) failure in the presence of water (e.g. in Fig. 8.9 (a)). Oxides with similar pore size, but prepared at higher anodizing

temperature perform better. The wet peel strength of these panels is slightly higher than the dry peel test and they exhibited cohesive failure throughout the entire panel (e.g. in Fig. 8.9 (b)).

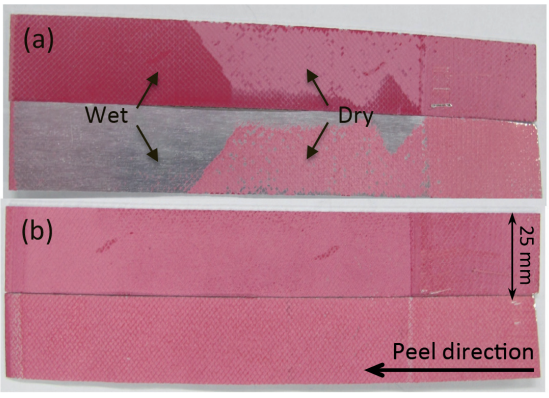

Figure 8.9: Typical failure modes of panels after floating roller peel testing under dry- and wet conditions. Oxide preparation conditions SAA20 (a) and (b) SAA50.

Table 8.4: Summary of the mechanical performance of the selected oxides.

	Floating roller peel		Average dry peel after SST		Average bondline corrosion	
Abbreviation	Dry peel [N]	Wet peel [N]	90 days [N]	180 days [N]	90 days [%]	180 days [%]
SAA20C	153	33	n.a	17	85	93
SAA50C	324	338	335	336	3	3
PSA20C	147	46	n.a.	19	75	95
PSA35C	333	335	308	315	4	1
PSA50C	326	338	333	299	5	21

8.4.2 Bondline Corrosion (BLC)

Another way to test the durability of the bond is by exposing it to harsh environmental conditions, i.e. by placing the bonded panels in a salt spray cabinet. As Zanni-Deffarges and Shanahan [17] have observed, water diffusion is often accelerated in the bonded assembly (compared to a one-side open adhesive joint configuration) due to capillary action. When this is accompanied by the presence of chloride ions, preferential corrosion of the protective clad layer can occur. As the degradation proceeds along this clad layer at the bondline, it can result in disbonding and failure [9].

This test was undertaken in here for 90 and 180 days. The amount of corrosion on the different panels was visually inspected after 90 and 180 days of exposure in the salt spray cabinet. The complete list of the results can be found in Table B.1 in appendix B and in Table 8.4 for the selected specimens. Examples of highly corroded and corrosion-resistant panels are shown in Fig. 8.10 (b) and (c) for SAA 20 °C and SAA 50 °C respectively.

In addition, post-exposure (dry) peel strengths were measured. As illustrated in Fig. 8.10 (a), there is an almost linear correlation between the amount of corrosion measured on a panel and the reduction in its peel strength. There is also a high correspondence with the anodizing temperature, but it is apparently not the only critical factor. Also in here, anodizing at 20 °C generally results in the worst performance. The only exception is the oxide that was produced at the highest concentration of phosphoric acid, anodized for 30 minutes at higher voltage. In contrast to previous results, few of the 50 °C oxides exhibited very poor mechanical performance. The observed level of performance for these oxides within each electrolyte mixture can be roughly classified as "good" for high voltage and "poor" for low voltage. However, there is no correlation to the value of the anodizing voltage itself. Most SAA and 20 °C PSA oxides performed poorly, even at relatively high voltages (Table B.1 in appendix B). Oxides prepared at 35 °C generally performed well when prepared at higher acid concentrations. These results suggest a link to the amount of dissolution of the anodic oxide by the anodizing electrolyte. Dissolution of the oxide to a certain extent seem to be beneficial, while too much of it, which may be beneficial in terms of bonding, is detrimental for the corrosion resistance.

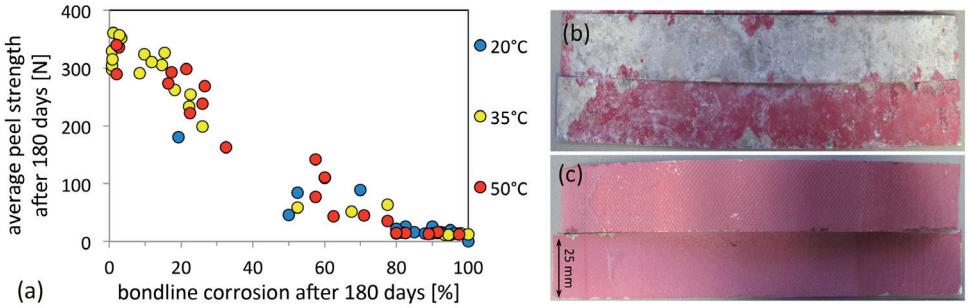

Figure 8.10: Left (a): Average peel strength after 180 days in the salt spray cabinet vs. the amount of bondline corrosion. Right: Characteristic images of the peeled panels that represented poor (b) and good adhesion (c). Oxide preparation conditions (b) 20 °C SAA and (c) 50 °C SAA.

Fig. 8.11 shows a comparison between the average peel strength after 180 days in the salt spray cabinet and the dry- and wet peel strength of the "fresh" joint. As seen in the figure, there is no clear correlation between the different tests, but severity of the tests can be ranked in the following order: bondline corrosion > wet peel > dry peel. Panels that passed in peel after a bondline corrosion test also passed the other two tests.

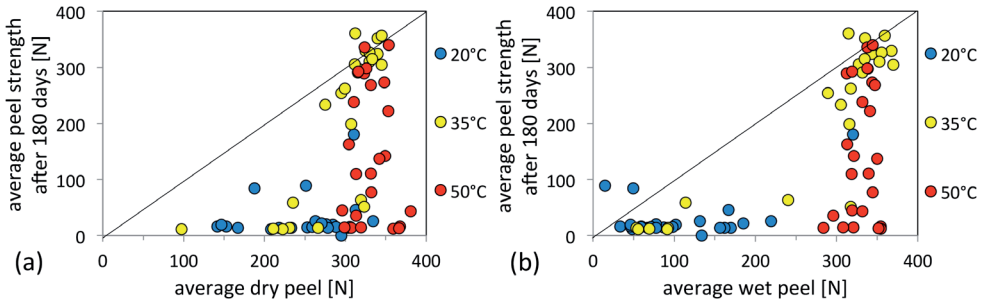

Figure 8.11: Average peel strength after180 days in the salt spray cabinet vs. average (a) dry- and (b) wet peel strength.

8.5 Discussion

The results in this study demonstrate how the anodizing conditions are affecting the morphology of porous aluminum anodic oxides. Overall, the most dominant parameters that determine the final morphology of the oxide are the electrolyte composition and the anodizing temperature. In accordance with the geometrical model that was developed by Keller, Hunter and Robinson in 1953 [18], the structural porosity is determined by the applied voltage and the nature of the electrolyte. In this study we show that the electrolyte temperature also plays an important role. In contrast to the addition of phosphoric acid, a high electrolyte temperature does not change the pore diameter close to the metal/oxide interface, which is determined by the applied voltage [19]. The higher temperature only widens the pore openings at the surface through chemical dissolution. Since the top part of the oxide is in contact with the acid for a longer period of time, it is much more affected than the interior. The resulted difference in morphology as a result of increasing the anodizing temperature is illustrated Fig. 8.12. As shown in the case of SAA20 vs. SAA50, this can make the difference between the mechanical performances of the adhesives bond.

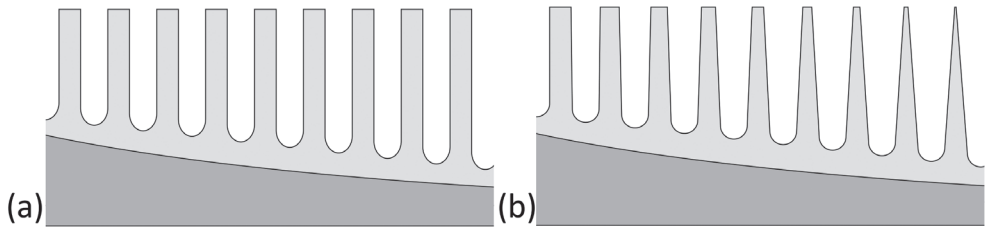

Figure 8.12: Schematic illustration of the effect of anodizing temperature on the oxide morphology, for example for SAA 20°C (a) vs. SAA 50°C (b).

Owing to the considerable dissolving action of H_3PO_4, the pore size of PSA oxides is larger than for SAA oxides. Varying the acid concentration and the anodizing conditions

(voltage, time and electrolyte temperature) can then be used to further modify the oxide morphology. This is reflected in the geometrical features, as measured by SEM and TEM. Moreover, these images reveal that changing the anodizing conditions also influences the surface roughness. A difference is then created between the relatively smooth top surface of porous oxides that are produced at lower temperatures and the micro- and nano-rough surfaces that are produced at higher electrolyte temperatures and high phosphoric acid concentration.

Mechanical tests show that good initial dry bonding between the substrate and the resin is achieved as long as the pore size exceeds a critical threshold of about 20 nm. TEM-EDS measurements indicate that these performance differences correspond to the extent in which the resin is able to fill the pores. Narrow pores that are only partly filled with the resin provide a very limited contact between the oxide and the resin. In such cases, the contact area between the two phases and the loading mode are more similar to featureless oxides, as illustrated in Fig. 8.13. The peel strength for such featureless oxides with an epoxy adhesive was previously reported in Abrahami et al. [10]. Their dry peel strength was in the same order of magnitude as porous oxides with small pores shown in here. Once the pores are large enough and the resin penetrates into the pores, sufficient bonding is achieved and no further improvements in peel strength are registered.

It can be argued that completely filled pores enhance the two main adhesion mechanisms: (1) it facilitates mechanical interlocking and (2) it provides a larger surface area for atomic and/or molecular interactions between the oxide and the resin. From a purely mechanical perspective, the fact that the contact angle between the oxide and the resin is constantly changing with respect to the direction of the exerted force already gives it an advantage over smooth surfaces or incompletely filled pores (Fig. 8.13).

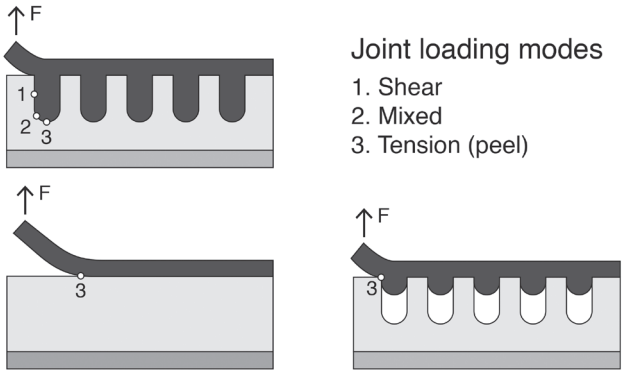

Figure 8.13: A schematic comparison between pores the extent of resin penetration and its affect on the contact area and the mechanical advantage provided by completely filled pores and a larger contact area.

In contrast to dry conditions; the anodizing temperature rather than the pore size considerably influences the peel strength under the ingress of water. These results confirm

earlier findings by Rider and Arnott [20] using ultra-milling for surface roughening. The nanoscale protrusions and microscopic "bird's nests" that are formed during high temperature anodizing produces a complex surface topography that retards the diffusion of water.

A surprising observation concerns the fact that dry- and wet peel strengths are independent of the oxide thickness. It appears that the amount of contact area between the oxide and the resin is less important than the fact that a fully cohesive interphase is formed. This has been explained by Kinloch, Little and Watts by the susceptibility of incompletely filled pores to an attack by water [21]. Moreover, this observation confirms earlier finding by Venables et al. [22], who noticed that adhesion improvements are already provided by the whisker-like protrusions of the Forest products laboratory (FPL) etch of just a few tens of nanometers long. The "bird's nest" morphology in this study provides an extended version of this whiskers protrusions. Moreover, a recent study by Ye et al. [23] and Jeong and Choi [24] found that a "birds nest" morphology to be superhydrophilic. Hence, the presence of a "bird's nest" on top of the porous oxide provides an extra advantage towards the smoother porous oxides that were prepared at lower temperatures. Comparing the carbon profiles near the oxide/resin interface, the advantage of a high surface roughness is clearly seen. Upon contact with the resin, a rough surface oxide extends the interphase to a three-dimensional resin/oxide composite. It is however also clear from the results that morphology is not the only prerequisite for good bonding. Although the carbon concentration close to the oxide/resin interface of SAA50 is approximately 4 times higher than for SAA20 (Fig. 8.5: (a) O-4 vs. (c) O-6), it is almost as low as for PSA20 (Fig. 8.6 (a) O-3), while the two exhibit very different mechanical performance. In our earlier study it was reported that interfacial bonding

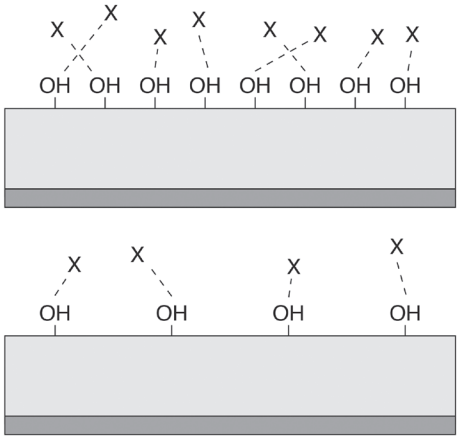

Fig. 8.14: Surface chemistry and bonding density illustration. Hydroxyl groups on the surface oxide and hydroxyl groups in epoxy adhesive (represented by an 'x') form molecular bonding, probably through hydrogen bonds.

between anodic oxides and epoxy resin proceeds through the hydroxyl groups at the surface of the oxide [10]. It was found that the density of hydroxyl groups at the surface of SAA oxide is larger than for PSA oxides (approximately double, depending on the anodizing conditions) [13]. Therefore, higher peel strengths can be achieved with less surface area. Hence, performance differences are also related to changes in the oxide chemistry, as illustrated in Fig. 8.14.

8.6 Conclusions

The results in this study demonstrate that the anodizing conditions, especially temperature and phosphoric acid concentration, are significantly affecting the morphology of the anodic oxides. Morphological changes were distinguished between geometrical modifications that affect the pore size and changes in the surface roughness that was caused by extended chemical dissolution. It was shown using TEM-EDS that resin penetration is affected by both morphological aspects. Consequentially, bond mechanical performance is closely related to oxide morphology. While the dry peel strength was, up to a certain limit, correlated to the pore size, the durability of bonding is more closely related to surface roughness. Both adhesion mechanisms: adsorption and mechanical interlocking seem to contribute to the adhesion in these structural bonds. This study provides an insight into the relation between the anodizing conditions, the oxide morphology and adhesion properties, which is significant in the design of an optimal Cr(VI)-free anodizing process for aerospace adhesive bonding.

8.7 References

1. Wegman, R.F. and J. Van Twisk, *2 - Aluminum and Aluminum Alloys*, in *Surface Preparation Techniques for Adhesive Bonding (Second Edition)*, R.F. Wegman and J.V. Twisk, Editors. 2013, William Andrew Publishing. p. 9-37.
2. Higgins, A., *Adhesive bonding of aircraft structures.* International Journal of Adhesion and Adhesives, 2000. **20**(5): p. 367-376.
3. Sheasby, P.G. and R. Pinner, *Surface Treatment and Finishing of Aluminium and its Alloys*. 6th ed. 2001., England: Finishing Publications Ltd.
4. Sulka, G.D., *Highly Ordered Anodic Porous Alumina Formation by Self-Organized Anodizing*, in *Nanostructured Materials in Electrochemistry*. 2008, Wiley-VCH Verlag GmbH & Co. KGaA. p. 1-116.
5. Critchlow, G.W., et al., *Strategies for the replacement of chromic acid anodising for the structural bonding of aluminium alloys.* International Journal of Adhesion and Adhesives, 2006. **26**(6): p. 419-453.
6. Yendall, K.A. and G.W. Critchlow, *Novel methods, incorporating pre- and post-anodising steps, for the replacement of the Bengough–Stuart chromic acid anodising process in structural bonding applications.* International Journal of Adhesion and Adhesives, 2009. **29**(5): p. 503-508.
7. Kollek, H., *Some aspects of chemistry in adhesion on anodized aluminium.* International Journal of Adhesion and Adhesives, 1985. **5**(2): p. 75-80.
8. Packham, D., *Theories of Fundamental Adhesion*, in *Handbook of Adhesion Technology*, L.M. da Silva, A. Öchsner, and R. Adams, Editors. 2011, Springer Berlin. p. 9-38.
9. Brockmann, W., et al., *Adhesion in bonded aluminium joints for aircraft construction.* International Journal of Adhesion and Adhesives, 1986. **6**(3): p. 115.
10. Abrahami, S.T., et al., *Effect of Anodic Aluminum Oxide Chemistry on Adhesive Bonding of Epoxy.* The Journal of Physical Chemistry C, 2016. **120**(35): p. 19670-19677.
11. ASTM, *ASTM D3167-03a, Standard Test Method for Floating Roller Peel Resistance of Adhesives*. 2003, ASTM International: West Conshohocken, PA.
12. Schneider, M., et al., *Interplay between parameter variation and oxide structure of a modified PAA process.* Surface and Interface Analysis, 2013. **45**(10): p. 1503-1509.
13. Abrahami, S.T., et al., *XPS Analysis of the Surface Chemistry and Interfacial Bonding of Barrier-Type Cr(VI)-Free Anodic Oxides.* The Journal of Physical Chemistry C, 2015. **119**(34): p. 19967-19975.
14. McCafferty, E. and J.P. Wightman, *Determination of the concentration of surface hydroxyl groups on metal oxide films by a quantitative XPS method.* Surface and Interface Analysis, 1998. **26**(8): p. 549-564.
15. Hart-Smith, L.J., *A peel-type durability test coupon to assess interfaces in bonded, co-bonded, and co-cured composite structures.* International Journal of Adhesion and Adhesives, 1999. **19**(2): p. 181-191.
16. Posner, R., O. Ozcan, and G. Grundmeier, *Water and Ions at Polymer/Metal Interfaces*, in *Design of Adhesive Joints Under Humid Conditions*, M.L.F. Silva and C. Sato, Editors. 2013, Springer Berlin Heidelberg: Berlin, Heidelberg. p. 21-52.
17. Zanni-Deffarges, M.P. and M.E.R. Shanahan, *Diffusion of water into an epoxy adhesive: comparison between bulk behaviour and adhesive joints.* International Journal of Adhesion and Adhesives, 1995. **15**(3): p. 137-142.

18. Keller, F., M.S. Hunter, and D.L. Robinson, *Structural Features of Oxide Coatings on Aluminum.* Journal of The Electrochemical Society, 1953. **100**(9): p. 411-419.
19. Wood, G.C. and J.P. O'Sullivan, *The anodizing of aluminium in sulphate solutions.* Electrochimica Acta, 1970. **15**(12): p. 1865-1876.
20. Rider, A.N. and D.R. Arnott, *The Influence of Adherend Topography on the Fracture Toughness of Aluminium-Epoxy Adhesive Joints in Humid Environments.* The Journal of Adhesion, 2001. **75**(2): p. 203-228.
21. Kinloch, A.J., M.S.G. Little, and J.F. Watts, *The role of the interphase in the environmental failure of adhesive joints.* Acta Materialia, 2000. **48**(18–19): p. 4543-4553.
22. Venables, J.D., et al., *Oxide morphologies on aluminum prepared for adhesive bonding.* Applications of Surface Science, 1979. **3**(1): p. 88-98.
23. Ye, J., Q. Yin, and Y. Zhou, *Superhydrophilicity of anodic aluminum oxide films: From "honeycomb" to "bird's nest".* Thin Solid Films, 2009. **517**(21): p. 6012-6015.
24. Jeong, C. and C.-H. Choi, *Single-Step Direct Fabrication of Pillar-on-Pore Hybrid Nanostructures in Anodizing Aluminum for Superior Superhydrophobic Efficiency.* ACS Applied Materials & Interfaces, 2012. **4**(2): p. 842-848.

CHAPTER 9

Conclusions & recommendations

9.1 Introduction

For more than six decades, chromic acid anodizing (CAA) has been the central process in the surface treatment of aluminium for adhesively bonded aircraft structures. This process, known for producing a readily adherent oxide with an excellent corrosion resistance, is no longer acceptable from a health and environmental risk perspective. Replacing this traditional process in a high-demanding and high-risk industry such as aircraft construction requires an in-depth understanding of the underlying adhesion mechanisms at the oxide/resin interface resulting from alternative processes. This fundamental understanding will be crucial in controlling and predicting the performance and limitations of the system in practice.

From the literature reviewed in Chapter 2 it was concluded that, although two adhesion mechanisms are generally acknowledged to contribute to the adhesion in structural bonds, only relatively little is known about the influence of surface chemistry. This is surprising, especially because it has been widely reported that anodizing in candidate electrolytes (SAA, PAA and PSA) lead to the incorporation of anion species. Yet, their presence at the interface was never explicitly taken into account in adhesion studies. Hence, the main focus of this PhD thesis was set to understand how changes in the surface chemistry affect adhesion. Additionally, it attempts to understand how fundamental properties of the process are related to the oxide morphological properties and its affinity for polymer adhesion and interfacial durability.

9.2 The Influence of Oxide Chemistry on Adhesion and Durability of an Adhesive Bond

The initial hypothesis was that anion incorporation would change the acid-base properties of the oxides. This was studied in Chapter 3 using FTIR, XPS and Auger parameter. FTIR spectra of the anodic oxides all show similar Al-O bands, with a small shoulder in case of the presence of phosphate and sulphate species. Only the hydrothermal oxide deviated, exhibiting features that are typical for pseudoboehmite (AlOOH). Shifts in the binding energies of O1s and Al2p were measured with XPS to evaluate the acid-base properties. Despite the incorporation of anions, results showed no significant net changes in the acid-base properties of the anodic oxides. The hydrothermally produced oxide, on the other hand, presented a shift of more than 0.4 eV from this group, indicating a more basic character. This was explained by the fact that the localized coordination structure in this oxide is different from the other oxides. Nevertheless, all oxides present the same Auger parameter (including the hydrothermally produced one).

It was therefore decided to proceed in Chapter 4 with a quantitative analysis of the different surface species. This was accomplished after an extended model was developed to account for the presence of phosphates and sulphates at the surface. Calculations then

showed that the choice of electrolyte significantly affects the oxide chemistry, giving rise to varying amounts of O^{2-}, OH^{-}, PO_4^{3-} and SO_4^{2-} surface species. It was established that the incorporation of phosphate and sulphate anions comes at the expense of surface hydroxyl groups. The concentration of hydroxyls generally increases in the order: PAA < PSA, HcPSA < SAA < CAA < Alkaline < Hydrothermal. This trend was consistent across the different anodizing temperatures.

One of the main challenges in the study of adhesion is the detection of interactions at the buried interface. To overcome this limitation and to investigate the type of bondings that are formed, model molecules that represent aerospace adhesive functionalities were studied initially. This allowed probing the interactions between the oxide and the molecules on an atomic and molecular level. Hence, adsorption studies of two types of phenol molecules were reported in Chapter 3. FTIR results showed that both the pre-treatments and the choice of molecule play a role in the formation of the interface. The more acidic phenol group in 4-EP exhibited selectivity for interaction based on the pre-treatment. The thin layers formed on hydrothermal, alkaline and CAA oxides displayed hydrogen bonds to a surface site of decreased basicity, while the other oxides showed no significant interactions. On the other hand, the adsorption of 4-HbA displayed no preference to the type of pre-treatment and films were formed on all oxides. In both cases, most interactions were reversible in nature, with negligible irreversible adsorption to unsaturated aluminium cations.

Further in Chapter 4, the adsorption of DETA, an amine hardener that is typically used for epoxy curing, was studied. FTIR measurements revealed nitrogen on the surface of all oxides, even after rinsing in pure THF solvent. In XPS, nitrogen showed three different types of interactions with all oxides: weak hydrogen bonds and/or non-bonded excessive nitrogen atoms, stronger hydrogen bonds to surface hydroxyl and phosphates in PAA/PSA and Brønsted type interactions with surface oxygen. The basic amine exhibited a larger amount of stronger hydrogen interactions with the oxides prepared in phosphoric acid. This was attributed to the acidic nature of phosphate groups at the surface. In general, adsorption studies in Chapters 3 and 4 indicate that even though there is no net change in the acid-base properties of the anodic oxides, local changes in the acidity of surface species can influence interfacial bonding on a molecular level. Hence, the aim in the following chapters was to study the effect of changes in the surface chemistry, as measured in the previous chapters, on the adhesion with industrial adhesives. As opposed to model molecules, adhesive films undergo curing at elevated temperatures and pressures and typically contain extra additives. Since mechanical tests in Chapters 5 and 6 were performed with featureless oxides, they provide an empirical method to evaluate the contribution of adsorptive interactions as a single adhesion mechanism.

Results with FM 73 epoxy adhesive in Chapter 5 and 6 show that significant initial adhesion strength can be achieved without mechanical interlocking, and independent of the type of (anodizing) electrolyte. All joints presented a cohesive failure within the

adhesive, indicating that bonds across the interface are stronger than bonds within the adhesive. Conversely, the ingress of water caused interfacial failure. Wet peel strength was found to depend on the surface chemistry, linearly increasing with the amount of surface hydroxyls. These two observations are summarized in Fig. 9.1 (a). Because the amount of hydroxyls is reduced by the incorporation of phosphates and sulphates, wet adhesion strength is also inversely correlated with their presence of at the surface.

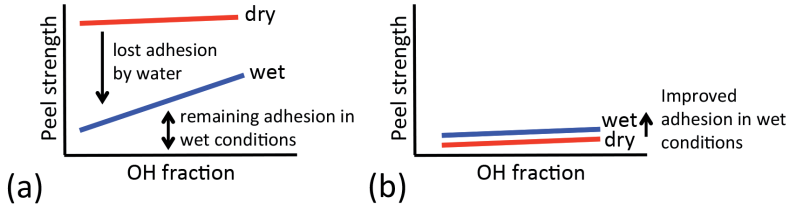

Figure 9.1: Schematic illustration of the relation between the peel strength and the hydroxyl fraction of featureless oxides bonded with FM73 epoxy (a) and Redux 775 vinyl phenol (b) adhesive films.

This dependency on the amount of hydroxyls and the fact that water lead to interfacial failure (irrespective of the bond strengths), suggests that bonding with epoxy proceeds through these surface groups. Hence, the incorporation of anions does not change the bonding mechanism; it only affects the amount of groups available for bonding. This conclusion is illustrated in Fig. 9.2. Since phosphates and sulphates at the surface did not appear to contribute to bonding, they are not included in the illustration. Even though the presence of phosphates at the surface was found to be beneficial for the interaction with the amine hardener in Chapter 4, only the density of available hydroxyl groups at the surface eventually determines the extent of bonding with epoxy under water ingress. The higher the density, the more bonds needed to be simultaneously displaced by water molecules before complete delamination occurs, explaining the correlation.

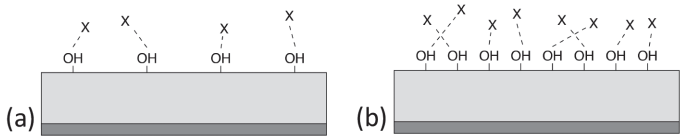

Figure 9.2: Schematic illustration of the affect of hydroxyl density on interfacial bonding with FM-73 epoxy (represented by x).

Generally, adsorptive interactions can be divided into two classes: primary and secondary (Chapter 2). The previous results indicated that epoxy/oxide interactions are mainly secondary in nature, providing relatively low bond strengths. It was demonstrated in Chapter 6 that the capability to form covalent bonds across the oxide/adhesive interface could be used to improve adhesion strength, especially under wet conditions. The

presence of Al-O-Si boding, provided by a silane coupling-agent, was shown to approach the level of adhesion provided by porous oxides.
As a comparison, the adhesion of phenolic-based aerospace adhesive (Redux 775) was investigated in Chapter 6. In contrast to the previous results with epoxy, very low bond strengths were achieved with featureless oxides bonded with Redux 775 and it generally did not exhibited sensitivity to changes in the surface chemistry. This is illustrated in Fig. 9.1 (b). These results correspond well with previous observations made by adsorption studies. As presented in Chapter 3, the adsorption of 4-HbA (the first product of phenol curing) displayed no preference to certain oxides and interfacial interactions were mainly reversible. Although the initial dry peel was low, strength increased slightly under wet conditions, indicating of a temporary adhesion improvement in the presence of water. Although this was not expected from studying molecular interactions, it can be linked to the observations made by bondline corrosion tests, also in Chapter 6. The stability of the oxide/adhesive interface is determined by the chemical compatibility between the oxide and adhesive. Hence, the nature of the oxide *and* the adhesive should be considered. From the literature it is known that the two adhesives differ in their chemical constitution. While epoxy is slightly alkaline, phenol (as seen earlier) has slightly acidic properties. Under the ingress of water, components from the adhesive may leach out and reach the interface. The acidic phenol components can stabilize the interactions with basic surface hydroxyls (Chapter 3). However, since these reactions are reversible, delamination eventually occurs. Alternatively, the alkaline environment created by the leaching of epoxy additives (e.g. amine) was shown to be detrimental in corrosion perspective (Chapter 6).
Generally, the results obtained by molecular adsorption studies and mechanical tests agree well, showing that these model systems adequately represent the real interface. In the absence of silane additives, both adhesives relay on relatively weak secondary bonds, which not stable in the presence of water. Enhancing the durability of these bonds is therefore needed by a higher degree of adhesive crosslinking, or alternatively inhibiting additives. Nevertheless, while both adhesives were found to form mainly hydrogen bonds, peel strength results display two different trends with respect to changes in the surface chemistry. The cause for these differences is still not completely clear and further research is recommended in section 9.4.

9.3 The Influence of Oxide Morphology on Adhesion and Durability of an Adhesive Bond

The second part of this work investigated the relation between the anodizing conditions and the adhesion on porous oxides. Studies related to the anodizing scheme were discussed in Chapter 7. One of the main findings was the dramatic effect the nature of the electrolyte has on the final film morphology. Coarsening of the upper part of

the oxide was only observed in PSA. The high solubility of Al_2O_3 in phosphoric acid increased the pore- and cell diameters at the outer surface. The fact that cell diameters were changing indicates that that pore walls did not only get thinner, but also partly dissolved in this electrolyte. A significant implication of these findings concerns the extent to which the processing history (the initial anodizing ramp and the etching step) is reflected in the final oxide morphology.

Potentiodynamic anodizing was also considered as a method to control the oxide morphology, possibly providing an alternative for a two-step anodizing process. SEM images showed that complex oxide morphologies could be made by dynamically changing the voltage during anodizing. A distinction was observed between an intermediate voltage increase or decrease step. After a sudden voltage decrease, new pores with smaller diameters had to develop below existing pores, which resulted in a distinct border between the two morphologies. Conversely, a transition layer forms by partly dissolving walls of smaller pores after a voltage increase. Recorded current density responses show that directly after a voltage increase, the current density temporarily exceeds the steady state value. Because the current density is a direct measure of the oxide growth rate, anodizing cycles including an increase in voltage have higher oxide formation efficiencies, even when the average voltage is similar to that of another cycles.

The following Chapter 8 presents the results of a broad empirical investigation on the relation between the anodizing conditions, oxide morphology and adhesion. Results demonstrate that the anodizing conditions, especially temperature and phosphoric acid concentration, are significantly affecting the final oxide morphology. A distinction was made between geometrical modifications to the pore size and changes in the surface roughness. It was shown using TEM-EDS that resin penetration is affected by both aspects. As a consequence, mechanical performance was closely related to oxide morphology.

Dry peel strength was mostly dependant of the pore size. As illustrated in Fig. 9.3, the contact area between oxide with very narrow pores and resin is more comparable to the area provided by featureless oxides due to poor resin penetration into the pores. Mechanical test results also indicate that the two provide similar level of peel strengths. Consequently, anodizing at higher temperatures and phosphoric acid concentrations are beneficial since it leads to a higher dissolution rate during anodic oxidation and to wider pores. These observations were supported by TEM-EDS profiles, showing differences in the extent of carbon concentration within pores of different dimensions. Above approximately 25 nm, the dry peel is generally independent of the pore size. According to these observations, it is not possible to conclude which is the dominating adhesion mechanism. Both mechanical interlocking and a larger contact area could provide this improvement in strength.

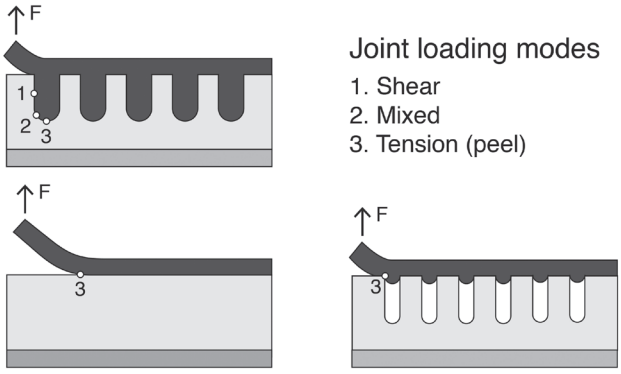

Figure 9.3: Schematic illustration of the mechanical advantage provided by completely filled pores. The larger surface area provides additional contact area for interactions, as well as possible interlocking with the adhesive.

On the contrary, peel tests under wet conditions display no distinct relation to the pore size. It does, however, provide a clear distinction between oxides prepared under different conditions. It appears that the increased roughness of the interface at higher anodizing temperature and/or phosphoric acid concentration plays a crucial role in the durability of the bond. This was explained by the complex topographies that retards the diffusion of water at the interface, especially in the presence of a 'bird's nest' morphology.

There was, however, an upper limit to the beneficial amount of anodic dissolution above which it negatively affects the resistance to bondline corrosion. This was found to be the most critical factor in determining the long-term performance of the joint in this study. The fact that bondline corrosion failure occurred at high temperature oxides that were prepared at lower voltages possibly indicates of a relation to the barrier-layer thickens. Further electrochemical studies are needed to confirm this suggestion.

A surprising observation concerns the fact that both dry- and wet peel test results are independent of the oxide thickness. If the adhesion was only controlled by adsorptive interactions, a larger surface area provided by pores with similar diameters but much longer, is expected to withstand a larger peel force (assuming that the resin fully penetrated into the pores). Hence, bond strength and durability both appear to be closely related to the ability of the oxide and the resin to form a cohesive interphase. Mechanical interlocking is considered to contribute in here, but there is no conclusive evidence for its dominance. Also for porous oxides, surface chemistry appears to be important, contributing to the differences in adhesion performance between SAA and PSA oxides. Overall, the results illustrate the need to consider both chemical and morphological changes in the selection of Cr(VI)-free alternatives for a strong and durable adhesive bonding.

9.4 General remarks and recommendations

"No complex system could be known in its entirety, and any system that could be known in its entirety is merely a subset of a larger one". Considering this definition by the Austrian mathematician Kurt Gödel (1931), adhesion in structural adhesive bonding can be considered a complex system. Although the results in this study provide insight into various fundamental aspects of adhesion in structural joints, there are still many questions to be answered and the performance of the system in practice seem to rely on multiple contributions. Based on the knowledge acquired in this thesis about the two adhesion mechanisms and the complete system, further studies can be suggested to obtain a deeper understanding of the underlying phenomena.

A puzzling observation concerns the fact that, even though both adhesives interact mainly through hydrogen bonds, they show different trends in respect to changes in the surface chemistry. Therefore, further research is needed to fully understand interfacial processes at a molecular- and atomic level. A better insight on the formation and delamination of the bonds at the interface could be provided by in-situ monitoring the interfacial chemistry during curing and upon water exposure using FTIR-ATR measurements in Kretschmann configuration. This might help in revealing the difference in the observed performance of epoxy and phenolic-base adhesives. Alternatively, computational modelling the affinity for interactions at this scale is also recommended. Modelling the potentials for the different interations on an atomic-scale can possibly show the cause for the selectivity for hydroxyl groups, rather than the phosphate and sulphate species.

The main aim in this work was to study the changes that are introduced by candidate Cr(VI)-free electrolytes (PAA, SAA and PSA) and evaluate their performance. Experimental results show that (by selecting the right conditions), it is possible to produce joints that match and even outperform the current CAA oxides. Because anodizing in PAA, SAA and PSA present disadvantage regarding surface chemistry, it is recommended to further explore the addition of a post-treatment step like immersion in alkaline solution. This option presents a relatively easy way to maximize the amount of surface hydroxyls after anodizing in the aforementioned electrolytes. Additionally to the chemical enhancement, this step could be beneficial to open the (in case of SAA) dense oxide structure and remove the history of the initial pre-treatment and anodizing steps. Moreover, because both classes of aerospace adhesives were found to form secondary interactions with the different oxides, the use of silanes to promote adhesion is highly recommended.

To gain more insight into the effect of mechanical interlocking, it is suggested to isolate its contribution in future studies. One such possibility is to produce porous layers that are not capable of interacting with the adhesive. This can be achieved by inhibiting the OH group with an inert to the adhesive specie. Additionally, it is suggested to test

the joint under shear and/or mixed loading conditions. Under these conditions the importance of mechanical interlocking should be more pronounced.
Lastly, a simplification made in this work was using (relatively) pure aluminium substrates. This choice was deliberately made to avoid the additional electrochemical influence of diverse alloying elements on oxide formation during anodizing and, accordingly, its influence on the resulting morphology. Nevertheless, many aerospace structures apply aluminium alloys in its bare form and therefore, the influence of the alloying elements should be considered. Morphological effects may make it more challenging to find the optimal processing conditions that lead to both adequate adhesion and corrosion resistance.

Appendix A

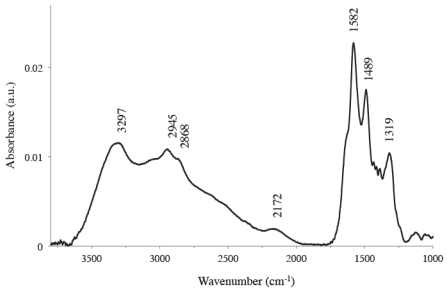

Figure A1: FTIR spectrum after DETA adsorption and rinsing on PSA oxide. The appearance of bands at 1489 cm^{-1} and 1582 cm^{-1} represents N-H bending and C-N stretching. Stretching of the N-H bond is also observed at 3297 cm^{-1}, possibly indicating hydrogen bonding. This type of spectrum appeared on all oxides.

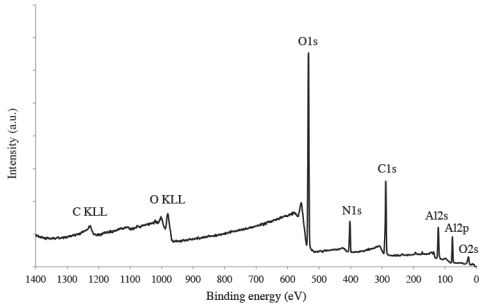

Fig. A2: XPS survey spectra after DETA adsorption on PSA oxide. The appearance of the N1s peak is characteristic for the adsorption of amine on the surface of the oxide.

$$c(COOX) = I_{COOX}/\sigma_c\lambda_c \sin\theta \left(1 - e^{\left(\frac{-t_{cont}}{\lambda_c \sin\theta}\right)}\right) \quad \text{Eq. 4(a)}$$

$$c(CO) = I_{CO}/\sigma_c\lambda_c \sin\theta \left(1 - e^{\left(\frac{-t_{cont}}{\lambda_c \sin\theta}\right)}\right) \quad \text{Eq. 4(b)}$$

$$c(PO_4^{3-}) = I_{PO_4^{3-}}/\sigma_P\lambda_P \sin\theta \left(e^{\left(\frac{-t_{cont}}{\lambda_P \sin\theta}\right)}\right) \quad \text{Eq. 4(c)}$$

$$c(SO_4^{2-}) = I_{SO_4^{2-}}/\sigma_S\lambda_S \sin\theta \left(e^{\left(\frac{-t_{cont}}{\lambda_S \sin\theta}\right)}\right) \quad \text{Eq. 4(d)}$$

$$c(O^{2-}) = I_{O^{2-}}/\sigma_O\lambda_{O(oxide)} \sin\theta \left(e^{\left(\frac{-t_{cont}}{\lambda_{O(oxide)} \sin\theta}\right)}\right) \quad \text{Eq. 4(e)}$$

$$c(OH^-) = \left[\frac{I_{OH^-} - \sigma_O\lambda_{O(cont)}(2(c(COOX)+c(CO)) \left(1 - e^{\left(\frac{-t_{cont}}{\lambda_{O\,(cont)} \sin\theta}\right)}\right)}{\sigma_O\lambda_{O(oxide)} \left(e^{\left(\frac{-t_{cont}}{\lambda_{O(oxide)} \sin\theta}\right)}\right) - 4c(PO_4^{3-}) - 4c(SO_4^{2-})}\right] \quad \text{Eq. 4(f)}$$

Appendix B

Table B1: Summary of the anodizing conditions, oxide morphology measurements (SEM), Floating roller peel test results (dry, wet and after salt spray test (SST)) and bondline corrosion. The five specimens chosen for detailed analysis are indicated with grey shading. The designated abbreviations used in the paper are also mentioned (n.a. = not available).

Anodizing conditions						**Morphology**		**Peel strength**		**Peel strength after SST**		**Corrosion after SST**		
Acid 1	Acid 2	Temp.	Voltage	Anodizing time	Measured current [A]	Oxide thickness [µm]	Pore size (top) [nm]	Dry [N]	Wet [N]	90 days [N]	180 days [N]	90 days [%]	180 days [%]	Abbreviation
10 g/l H_2SO_4	0 g/l H_3PO_4	20 °C	19 V	15 min	13	0.7	15	295	134	n.a.	0	100	100	
				30 min	12	1.2	6	153	33	n.a.	17	85	93	SAA20
			27 V	15 min	20	1.3	14	218	170	n.a.	14	88	98	
				30 min	19	2.3	6	167	67	n.a.	14	83	97	
		35 °C	15 V	15 min	24	1.0	10	266	53	n.a.	14	90	98	
				30 min	23	1.9	8	97	56	n.a.	12	83	94	
			23 V	15 min	35	2.0	10	231	93	n.a.	14	90	80	
				30 min	35	3.6	15	223	92	n.a.	12	88	95	
		50 °C	10 V	15 min	35	1.3	13	313	296	n.a.	35	70	78	
				30 min	32	2.4	25	323	312	326	289	4	2	
			19 V	15 min	57	2.7	20	349	321	172	142	30	58	
				30 min	55	5.2	40	324	338	335	336	3	3	SAA50
50 g/l H_2SO_4	0 g/l H_3PO_4	20 °C	12 V	15 min	23	1.2	9	269	59	n.a.	17	90	95	
				30 min	24	2.1	6	208	48	n.a.	11	88	95	
			19 V	15 min	42	2.9	7	233	162	n.a.	14	83	98	
				30 min	41	5.5	7	187	50	41	84	40	53	
		35 °C	7 V	15 min	31	1.4	10	211	69	n.a.	12	73	100	
				30 min	30	2.4	15	319	240	223	64	35	78	
			13 V	15 min	63	3.2	10	235	114	83	59	25	53	
				30 min	64	6.0	20	295	289	290	255	2	23	
		50 °C	4 V	15 min	40	1.1	unclear	307	284	291	14	40	90	
				30 min	40	1.1	unclear	319	321	239	15	50	83	
			8 V	15 min	78	3.4	unclear	348	344	372	274	5	16	
				30 min	70	3.0	unclear	331	347	352	269	4	27	

Anodizing conditions						Morphology		Peel strength		Peel strength after SST		Corrosion after SST		
Acid 1	Acid 2	Temp.	Voltage	Anodizing time	Measured current [A]	Oxide thickness [µm]	Pore size (top) [nm]	Dry [N]	Wet [N]	90 days [N]	180 days [N]	90 days [%]	180 days [%]	Abbreviation
10 g/l H_2SO_4	40 g/l H_3PO_4	20 °C	25 V	15 min	13	0.5	15	253	87	n.a.	15	78	92	
				30 min	12	1.1	20	285	102	n.a.	19	83	90	
			31 V	15 min	15	0.9	20	142	46	n.a.	16	88	85	
				30 min	17	1.7	23	288	98	n.a.	16	82	92	
		35 °C	20 V	15 min	31	1.3	37	323	318	n.a.	51	85	68	
				30 min	31	2.0	40	312	315	332	361	9	1	
			28 V	15 min	41	2.3	35	307	316	218	199	28	26	
				30 min	39	3.3	50	316	339	359	297	0	1	
		50 °C	13 V	15 min	63	0.6	30	332	344	311	77	15	58	
				30 min	62	0.8	35	311	332	202	238	33	26	
			23 V	15 min	86	2.1	27	326	338	333	299	5	21	PSA50
				30 min	84	1.4	40	316	319	340	293	1	17	
50g/l H_2SO_4	40g/l H_3PO_4	20 °C	16 V	15 min	21	1.1	10	259	59	n.a.	15	90	94	
				30 min	19	2.1	12	276	78	n.a.	20	83	91	
			22 V	15 min	34	2.9	9	263	131	n.a.	26	88	83	
				30 min	33	5.4	12	251	15	n.a.	89	48	70	
		35 °C	11 V	15 min	36	1.4	25	275	305	316	233	12	22	
				30 min	34	2.0	25	312	327	359	305	6	15	
			17 V	15 min	61	3.6	30	300	318	362	262	1	18	
				30 min	57	5.1	40	316	332	349	291	14	8	
		50 °C	6 V	15 min	53	0.7	18	299	308	n.a.	15	78	80	
				30 min	50	0.7	17	296	319	n.a.	45	65	71	
			11 V	15 min	90	1.1	25	305	313	306	163	20	33	
				30 min	87	2.5	20	313	319	400	110	1	60	

Anodizing conditions						Morphology		Peel strength		Peel strength after SST		Corrosion after SST		
Acid 1	Acid 2	Temp.	Voltage	Anodizing time	Measured current [A]	Oxide thickness [µm]	Pore size (top) [nm]	Dry [N]	Wet [N]	90 days [N]	180 days [N]	90 days [%]	180 days [%]	Abbreviation
10 g/l H_2SO_4	80 g/l H_3PO_4	20 °C	26 V	15 min	17	1.0	21	147	46	n.a.	19	75	95	PSA20
				30 min	16	1.2	30	304	157	155	14	50	88	
			34 V	15 min	22	1.0	18	306	72	n.a.	15	70	82	
				30 min	20	1.7	23	334	219	n.a.	26	78	90	
		35 °C	17 V	15 min	40	1.3	34	340	343	390	324	9	10	
				30 min	40	1.2	45	345	370	372	305	5	1	
			29 V	15 min	62	2.3	50	325	367	374	330	0	1	
				30 min	56	3.5	72	340	335	381	352	2	3	
		50 °C	8 V	15 min	78	0.3	20	368	354	n.a.	16	78	92	
				30 min	75	0.3	20	381	332	n.a.	44	73	63	
			18 V	15 min	120	1.1	34	353	341	300	222	18	23	
				30 min	115	0.8	40	354	344	386	340	5	2	
50 g/l H_2SO_4	80 g/l H_3PO_4	20 °C	18 V	15 min	22	1.3	10	278	77	n.a.	14	90	96	
				30 min	21	2.5	20	313	167	n.a.	46	45	50	
			25 V	15 min	40	2.7	14	271	185	n.a.	22	80	80	
				30 min	38	5.5	19	310	320	266	180	11	19	
		35 °C	11 V	15 min	38	1.3	unclear	330	356	329	326	15	15	
				30 min	37	1.5	25	330	353	349	311	4	12	

	19 V	15 min	68	3.3	34	345	359	320	357	4	3	
		30 min	70	3.2	25	333	335	308	315	4	1	PSA35
50 °C	5 V	15 min	63	0.1	10	359	355	196	12	45	98	
		30 min	62	0.3	19	367	352	67	13	75	89	
	11 V	15 min	105	0.9	22	332	340	191	111	40	60	
		30 min	107	0.7	unclear	342	350	277	138	15	48	

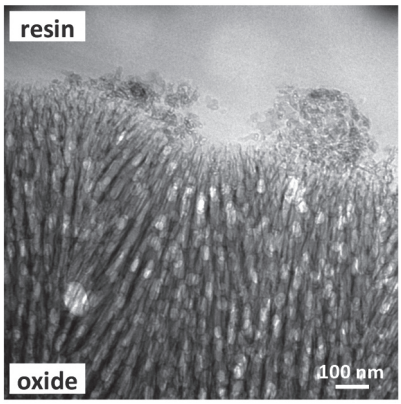

Fig. B1: Evidence of a “bird’s nest” on top of SAA 50 °C.

Acknowledgments

This dissertation is the product of a 4-year research project in the framework of the Materials innovation institute (M2i). I would like to thank M2i for giving me this opportunity and for the financial support of this project.
Making it to this point is the result of direct and indirect contribution, support, guidance and inspiration of many people. This has been an important period of my life from both professional and personal point of views and I would like to express my gratitude to everyone who helped me along the way.
First and foremost I would like to thank my promoters Prof. Herman Terryn and Dr. Arjan Mol. It has been a great pleasure to work with you and to learn from you both. Your tremendous commitment, engagement and passion for research have been a great motivation for me. You have always provided me the attention and guidance I needed to move forward and your full support at difficult times. You also made sure to keep things fun, which was reflected in a great atmosphere in the group and made for some unforgettable moments at conferences.
I also wish to thank Dr. John de Kok from Fokker Aerostrucutres for the fruitful collaboration and the constant support through the course of this project. Your guidance and feedback lead to many interesting discussions and contributed to the quality of this work. I would like to thank Vincent van den Heuvel for always willing to help and to Rob Leonard for the execution of the floating roller peel tests. To Arnold, Olga, Maria, Yulia and many more who contributed in one way or another. I am very grateful to Marloes van Put for the excellent work performed during her Master thesis that produced the results presented in Chapter 7.
A large amount of the measurements were performed at the Vrije Universiteit Brussel (VUB). I am grateful to Oscar Steenhaut (VUB) for his time and patience to answer every question and show me how to work with the XPS and the AES. I would like to thank Dr. Tom Hauffman from VUB for the valuable support in everything related to the XPS model. To Kees Kwakernaak (TU Delft) for his help with the XPS measurements for the Auger parameter in Chapter 3. To Dr. Visweswara (Chakri) Gudla and Prof. Rajan Ambat from Technical University of Denmark (DTU) for the opportunity to perform TEM-EDS measurements on the oxides in Chapter 8.
I am very thankful to all my colleagues at the Materials Science and Engineering (MSE) department, and especially to my colleagues at the corrosion technology and electrochemistry (CTE) group during these years: Yaiza, Jose, Farid, Önnaz, Peyman, Peter, Majid, Mats, Laura-Lynn, Joost, Soheil, Uma, Ali and Aytac. A special thanks goes to two amazing ladies for their technical support in the lab: Agnieszka and Maria. To my colleagues at VUB who made my frequent stays in Brussels very pleasant, as well as helping me develop my taste for Belgium beers.

To my awesome former housemates at GLL1, thank you for the incredible years together. Goncalo, thanks for the frequent motivational quotes as well as the occasional kick in the butt when it was needed. A special thanks goes to Merijn who was always willing to help with design questions and for making the illustrations in Chapters 8 and 9. To my Delft sister- Lily, thank you for being there for me at all times. Alexandara, thank you for the daily coffee breaks and pep up talks. Among many friends I would like to express my gratitude to Leni, David, Adam, Ioanna, and Zohar for being part of my Delft-family. To Hadar and all my dear friends in Israel, thanks for the continuous support and fun times at the kibbutz.

I am grateful for Ruthi who has been an immense source of support and inspiration for me. Your enthusiasm and love are contagious. To Wil, although I didn't call you oma, you have been one for me in every sense of that word. Thanks you both for the constant support since I moved to the Netherlands.

Last, but certainly not least, I would like to dedicate this book to my parents and grandparents, my four sisters and their families. I am very lucky to have you all in my life. In spite of living far away from you for almost ten years, you are a valuable support system and a big loving presence in every step of the way.

List of publications

Journal articles

S.T. Abrahami, J.M.M. de Kok, V.C. Gudla, R. Ambat, H. Terryn and J.M.C Mol, Reduced Adhesion Between Anodic Aluminum and Organic Reins caused by Fluoride contamination (tentative title), in preparation.

S.T. Abrahami, J.M.M. de Kok, H. Terryn and J.M.C Mol, *Towards Cr(VI)-free Anodization of Aluminum Alloys for Aerospace Adhesive Bonding Applications: A Review. Frontiers in Chemical Science and Engineering*, 2016, *submitted (invited)*.

S.T. Abrahami, J.M.M. de Kok, H. Terryn and J.M.C Mol, Interfacial bonding strength and stability of epoxy and phenol resins on different aluminium oxide and silane chemistries*, submitted*.

S.T. Abrahami, J.M.M. de Kok, V.C. Gudla, R. Ambat, H. Terryn and J.M.C Mol, The effect of Cr(VI)- Free Anodizing Conditions on the Adhesion and Durability of Adhesively Bonded Aluminium, *submitted*.

S.T. Abrahami, T. Hauffman, J.M.M. de Kok, J.M.C Mol, and H. Terryn, Effect of Anodic Aluminum Oxide Chemistry on Adhesive Bonding of Epoxy., J *The Journal of Physical Chemistry C,* 2016, 120(35): p. 19670-19677.

S.T. Abrahami, T. Hauffman, J.M.M. de Kok, J.M.C Mol, and H. Terryn, *The role of acid-base properties in the interactions across the oxide-primer interface in aerospace applications.* Surface and Interface Analysis, 2016. 48(8): p. 712-720.

M. van Put, S.T. Abrahami, O. Elisseeva, J.M.M de Kok, J.M.C Mol, H. Terryn, *Potentiodynamic anodizing of aluminum alloys in Cr(VI)-free electrolytes,* Surface and Interface Analysis, 2016. 48(8): p. 946-952.

S.T. Abrahami, T. Hauffman, J.M.M. de Kok, J.M.C Mol, and H. Terryn, XPS analysis of the surface chemistry and interfacial bonding of barrier-type Cr(VI)-free anodic oxides, *The Journal of Physical Chemistry C*, 2015 119 (34) 19967-19975.

S.T. Abrahami, Y. Xiao and Y. Yang, Rare-earth elements recovery from post-consumer hard-disc drives, *Mineral Processing and Extractive Metallurgy*, 2015. 124(2): p. 106-115.

Conference presentations

S.T Abrahami, J.M.M de Kok, J.M.C Mol, H. Terryn, *Influence of anodized oxide films on adhesive bonding properties*, Symposium Elektrochemie Anodisieren - Symposium Anodisieren 2016 2016, 24-25 November 2016, Fraunhofer IKTS, Dresden, Germany (invited).

S.T Abrahami, J.M.M de Kok, V.C. Gudla, *T. Hauffman,* R. Ambat, J.M.C Mol, H. Terryn, *Cr(VI)-Free Aluminium Pre-treatment for Aerospace Structural Adhesive Bonding: Mechanical Interlocking versus Chemical Bonds,* **Greener Aviation conference**, 11-13 October 2016, Brussels, Belgium.

S.T Abrahami, J.M.M de Kok, V.C. Gudla, *T. Hauffman,* R. Ambat, H. Terryn, J.M.C Mol, *Cr(VI)-free anodizing for structural adhesive bonding in the aerospace industry,* **16th Technical symposium of the International Hard Anodizing Association (IHAA)**, 5-7 October 2016, Düsseldorf , Germany (invited).

S.T Abrahami, J.M.M de Kok, V.C. Gudla, R. Ambat, H. Terryn, J.M.C Mol, *The effect of anodic oxide chemistry and morphology on adhesion and durability in aerospace structural adhesive bonding*, **EUROCORR 2016**, 11-15 September 2016, Montpellier, France.

S.T. Abrahami, T. Hauffman, J. de Kok, J.M.C Mol, and H. Terryn, *Advanced XPS analysis of Cr(VI)-free anodic oxide surface chemistry and its effect on oxide-resin bonding,* **16th European Conference on Applications of Surface and Interface Analysis (ECASIA)**, 28 September – 1 October 2015, Granada, Spain.

S.T. Abrahami, T. Hauffman, J. de Kok, J.M.C Mol, and H. Terryn, *The corrosion and adhesion performance of barrier-type anodic aluminium oxides prepared in different electrolytes,* **EUROCORR 2015**, 6-10 September 2015, Graz, Austria.

M. van Put, S.T. Abrahami, O. Elisseeva, J.M.M de Kok, J.M.C Mol, H. Terryn, *Potentiodynamic anodizing of aluminium alloys in Cr(VI)-free electrolytes,* **VII Aluminium Surface Science and Technology (ASST),** 17-21 May 2015, Madeira, Portugal.

S.T. Abrahami, J. de Kok, J.M.C Mol, and H. Terryn, *The influence of pretreatment on the acid-base interactions across the oxide-primer interface in aerospace applications,* **VII Aluminium Surface Science and Technology (ASST),** 17-21 May 2015, Madeira, Portugal.

M. van Put, S.T. Abrahami, O. Elisseeva, J.M.M de Kok, J.M.C Mol, H. Terryn, *Complex oxide morphologies by potentiodynamic anodizing of aluminium*, **EUROCORR 2014**, 8-12 September 2014, Pisa, Italy.

S.T. Abrahami, J. de Kok, J.M.C Mol, and H. Terryn, *The role of anodic oxide chemistry in the interfacial bonding of aluminium in the aerospace industry*. **2nd International symposium on Anodizing Science and Technology (AST),** 4-6 June 2014, Sapporo, Hokkaido, Japan

Curriculum Vitae

Shoshan Tamar Abrahami
Born on November 10th, 1983
Haifa, Israel

Education

2013 - 2016 **Ph.D. in Materials Science and Engineering**. Delft University of Technology, Delft, The Netherlands

2010 - 2012 **MSc in Materials Science and Engineering**. Delft University of Technology, Delft, The Netherlands

2007 - 2011 **BSc in Molecular Science & Technology.** Delft University of Technology, Delft, The Netherlands

1995 - 2001 **Full matriculation**, Hof HaCarmel high school in Maagan-Michael, Israel

Working experience

2011 **Researcher.** Material innovation institute, Delft, The Netherlands

2011 **Internship.** TNO, Eindhoven, The Netherlands

2004 - 2005 **Quality Control**. PLASSON Ltd, Maagan-Micahel, Israel

2002 - 2004 **Meteorologists.** Israeli Air Force (IAF)